Non-Destructive Evaluation of a Deep Foundation Test Section at the Northwestern University National Geotechnical Experimentation Site
A Report Submitted to the Federal Highway Administration

Dr. Richard J. Finno
Sarah L. Gassman
Peter W. Osborn

Northwestern University
Evanston, Illinois

June 1997

- List of figures
- List of tables
- List of symbols
- Chapter 1. Introduction
- Chapter 2. Review of non-destructive testing methods
- Chapter 3. National geotechnical experimentation site
- Chapter 4. Evaluation of impulse response tests at NGES
- Chapter 5. Uncertainties in impulse response results caused by concrete age and equipment effects
- Chapter 6. Numerical analysis of impulse response signals
- Chapter 7. Parallel seismic testing
- Chapter 8. Summary and conclusions
- References
- Appendix A
- Appendix B

List of Figures

Figure 2.1. Wavefronts of Compression, Shear and Rayleigh Waves Produced by a Point Impact on a Surface.
Figure 2.2. Theoretical Variation of the Two Compression-Wave Velocities and the Shear-Wave Velocity with Confining Pressure, as Calculated from the Biot (1956) Theory (from Hardin, 1961), (after Richart et. al., 1970).
Figure 2.3. Force-Time Function of Elastic Impact of a Sphere on a Solid (after Sansalone and Carino, 1986)
Figure 2.4. Frequency Spectrum of Force-Time Function (after Sansalone and Carino, 1986)

Figure 2.5. Reflection and Transmission of a Stress Wave at an Impedance Change
Figure 2.6. Reflection and Refraction of an Incident Compression Wave at an Interface
Figure 2.7. Mode Conversion of an Incident Compression Wave at an Interface
Figure 2.8. Testing Setup for Surface Reflection Techniques: Accessible-Head and Inaccessible Head
Figure 2.9. Response Curve for SM-6 Digital Grade Geophone (adapted from Sensor Nederland b.v Literature)
Figure 2.10. Ideal Impulse Response Result
Figure 2.11. Electric Analogue of a Pile Segment (after Davis & Dunn, 1974)
Figure 2.12. Electric Analogue for a Defective Pile (after Davis & Dunn, 1974)
Figure 2.13. Ideal Resolution Chart
Figure 2.14. Ideal Sonic Echo Result: Velocity versus Time
Figure 2.15. Typical Testing Arrangement for Parallel Seismic Testing (adapted from Stain, 1982)
Figure 2.16. Idealized Parallel Seismic Profile

Figure 3.1. Plan of the National Geotechnical Experimentation Site (NGES) at Northwestern University
Figure 3.2. Soil Profile with CPT Data
Figure 3.3. Geotechnical Characteristics of NGES Soils
Figure 3.4. NDE Test Section, Plan View
Figure 3.5. Shear and Compression Wave Velocities of NGES Soils
Figure 3.6. Profile View of NGES Test Section
Figure 3.7. Detailed Schematic of Shaft 1 - Accessible Head Condition
Figure 3.8. Detailed Schematic of Shaft 2 - Accessible Head Condition
Figure 3.9. Detailed Schematic of Shaft 3 - Accessible Head Condition
Figure 3.10. Detailed Schematic of Shaft 4 - Accessible Head Condition
Figure 3.11. Detailed Schematic of Shaft 5 - Accessible Head Condition
Figure 3.12. Detailed Schematic of Shaft 1 - Inaccessible Head Condition
Figure 3.13. Detailed Schematic of Shaft 2 - Inaccessible Head Condition
Figure 3.14. Detailed Schematic of Shaft 3 - Inaccessible Head Condition
Figure 3.15. Detailed Schematic of Shaft 4 - Inaccessible Head Condition
Figure 3.16. Detailed Schematic of Shaft 5 - Inaccessible Head Condition
Figure 3.17. Unconfined Compression Test Results on Concrete Cylinders
Figure 3.18. Correlation between Propagation Velocity and Compressive Strength of Typical Concrete (after Davis and Robertson, 1975)
Figure 3.19. Change in Propagation Velocity with Concrete Age - Determined from UC and UPV Tests

Figure 4.1. Impulse Response Result - Shaft 3: Time Domain and Frequency Spectrum
Figure 4.2. Impulse Response Result - Shaft 3: Mobility Plot up to 2000 Hz
Figure 4.3. Impulse Response Result - Shaft 3: Mobility Plot up to 1000 Hz
Figure 4.4. Impulse Response Result - Shaft 4: Time Domain and Frequency Spectrum
Figure 4.5. Impulse Response Result - Shaft 4: Mobility Plot
Figure 4.6. Impulse Response Result - Shaft 5: Time Domain and Frequency Spectrum
Figure 4.7. Impulse Response Result - Shaft 5: Mobility Plot

Figure 4.8. Impulse Response Result - Shaft 1: Time Domain and Frequency Spectrum
Figure 4.9. Impulse Response Result - Shaft 1: Mobility Plot
Figure 4.10. Impulse Response Result - Shaft 2: Time Domain and Frequency Spectrum
Figure 4.11. Impulse Response Result - Shaft 2: Mobility Plot
Figure 4.12. Effect of Soil-Filled Joint on Mobility Plot: Comparison of Shafts 1 & 3
Figure 4.13. Effect of Neck Defect on Mobility Plot: Comparison of Shafts 2 & 4
Figure 4.14. Experimentally Determined Low-Strain Stiffness, K' as a Function of (a) Soil Conditions at Shaft Toe, and (b) Shaft Diameter
Figure 4.15. Impulse Response Result - Shaft 3 with Pile Cap: Time Domain and Frequency Spectrum
Figure 4.16. Impulse Response Result - Shaft 3 with Pile Cap: Mobility Plot
Figure 4.17. Impulse Response Result - Shaft 4 with Pile Cap: Time Domain and Frequency Spectrum
Figure 4.18. Impulse Response Result - Shaft 4 with Pile Cap: Mobility Plot
Figure 4.19. Impulse Response Result - Shaft 5 with Pile Cap: Time Domain and Frequency Spectrum
Figure 4.20. Impulse Response Result - Shaft 5 with Pile Cap: Mobility Plot
Figure 4.21. Impulse Response Result - Shaft 1 with Pile Cap: Time Domain and Frequency Spectrum
Figure 4.22. Impulse Response Result - Shaft 1 with Pile Cap: Mobility Plot
Figure 4.23. Impulse Response Result - Shaft 2 with Pile Cap: Time Domain and Frequency Spectrum
Figure 4.24. Impulse Response Result - Shaft 2 with Pile Cap: Mobility Plot
Figure 4.25. Center of Pile Cap Test - Pile Cap 1
Figure 4.26. Center of Pile Cap Test - Pile Cap 3

Figure 5.1. Propagation Velocity from Velocity-Time Plots versus Concrete Age
Figure 5.2. Propagation Velocity from Mobility Plots versus Concrete Age
Figure 5.3. Propagation Velocity from Embedded Geophone vs. Concrete Age
Figure 5.4. Propagation Velocity from All Field and Laboratory Tests as a Function of Concrete Age
Figure 5.5. Average Shaft Mobility versus Concrete Age
Figure 5.6. Low-Strain Stiffness versus Concrete Age
Figure 5.7. Resolution versus Concrete Age
Figure 5.8. Comparison of Rycon and Epoxy Couplants - Shaft 3
Figure 5.9. Comparison of Rycon and Epoxy Couplants - Shaft 5
Figure 5.10. Temperature Effects on Rycon Grease - Shaft 4
Figure 5.11. Comparison of Rycon and Duct Seal Couplants - Shaft 3

Figure 6.1. "Best Estimate" Numerically-Simulated and Experimental Mobilities: Shaft 3
Figure 6.2. "Best Estimate" Numerically-Simulated and Experimental Mobilities: Shaft 4
Figure 6.3. "Best Estimate" Numerically-Simulated and Experimental Mobilities: Shaft 5
Figure 6.4. "Best Estimate" Numerically-Simulated and Experimental Mobilities: Shaft 1
Figure 6.5. "Best Estimate" Numerically-Simulated and Experimental Mobilities: Shaft 2
Figure 6.6. "Best Fit" Numerically-Simulated and Experimental Mobilities: Shaft 3

Figure 6.7. "Best Fit" Numerically-Simulated and Experimental Mobilities: Shaft 4
Figure 6.8. "Best Fit" Numerically-Simulated and Experimental Mobilities: Shaft 5
Figure 6.9. "Best Fit" Numerically-Simulated and Experimental Mobilities: Shaft 1
Figure 6.10. "Best Fit" Numerically-Simulated and Experimental Mobilities: Shaft 2
Figure 6.11. Numerical Simulation of Shaft 1 with Varying Pile Cap Diameter
Figure 6.12. Numerical Simulation of Shaft 2 with Varying Pile Cap Diameter
Figure 6.13. Numerical Simulation of Shaft 3 with Varying Pile Cap Diameter
Figure 6.14. Numerical Simulation of Shaft 4 with Varying Pile Cap Diameter
Figure 6.15. Numerical Simulation of Shaft 5 with Varying Pile Cap Diameter
Figure 6.16. Factor to Determine "Effective" Area from Tributary Area of Pile Cap
Figure 6.17. Resolution of NGES Shafts Compared to Ideal Resolution Chart
Figure 6.18. Effect of Concrete Density Variation on Resolution
Figure 6.19. Effect of Soil Density Variation on Resolution
Figure 6.20. Effect of Embedment Layer Soil Stiffness of the Mobility Resolution
Figure 6.21. Resolution Chart for a Two-Layer Subsurface Profile, L/D = 10
Figure 6.22. Resolution Chart for a Two-Layer Subsurface Profile, L/D = 15
Figure 6.23. Resolution Chart for a Two-Layer Subsurface Profile, L/D = 20
Figure 6.24. Resolution Chart for a Two-Layer Subsurface Profile, L/D = 25
Figure 6.25. Resolution Chart for a Two-Layer Subsurface Profile, L/D = 30
Figure 6.26. Comparison of Cutoff Frequencies

Figure 7.1. Compiled Parallel Seismic Profile: Shaft 3 Access Hole 3
Figure 7.2. Compiled Parallel Seismic Profile: Shaft 1 Access Hole 1
Figure 7.3. Compiled Parallel Seismic Profile: Shaft 4 Access Hole 2
Figure 7.4. Compiled Parallel Seismic Profile: Shaft 5 Access Hole 2
Figure 7.5. First Arrival Times versus Depth: Shaft 1
Figure 7.6. First Arrival Times versus Depth: Shaft 2
Figure 7.7. First Arrival Times versus Depth: Shaft 3
Figure 7.8. First Arrival Times versus Depth: Shaft 4
Figure 7.9. First Arrival Times versus Depth: Shaft 5
Figure 7.10. First Arrival Time versus Distance from Shaft: Shaft 1
Figure 7.11. First Arrival Time versus Distance from Shaft: Shaft 2
Figure 7.12. First Arrival Time versus Distance from Shaft: Shaft 3
Figure 7.13. First Arrival Time versus Distance from Shaft: Shaft 4
Figure 7.14. First Arrival Time versus Distance from Shaft: Shaft 5
Figure 7.15. Comparison of Compression Wave Velocities from Results of Cross-Hole and Parallel Seismic Tests
Figure 7.16. Travel Path for Direct Wave
Figure 7.17. Travel Path for Refracted Wave

List of Tables

Table 2.1. Typical Propagation Velocities from Various Materials

Table 2.2. Range of Input Frequencies for Impulse Hammer Tips
Table 2.3. Analogous Relationships between Mechanical and Electrical Systems (after Richard, et al. (1970))

Table 3.1. Field Investigations at the Northwestern NGES
Table 3.2. NDE Test Section Details
Table 3.3. Summary of Casing and Liner Dimentions
Table 3.4. Length of Sonic Logging Access Tubes
Table 3.5. Spacing between Sonic Logging Access Tubes
Table 3.6. Cased Borehole Dimentions
Table 3.7. Dimensions of Pile Caps
Table 3.8. Average Density of Concrete Cylinders

Table 4.1. Summary of Impulse Response Results - Accessible-Head (Day 28)
Table 4.2. Summary of Accessible- and Inaccessible-Head Impulse Response Results

Table 6.1. Average Soil Parameters at NGES
Table 6.2. Summary of Shaft Parameter Changes for "Best Estimate" to "Best Fit" Simulations
Table 6.3. Summary of Soil Parameter Changes for "Best Estimate" to "Best Fit" Simulations
Table 6.4. Summary of "Best Estimate" Simulated and Experimental Mobility Results
Table 6.5. Summary of Resolution for Accessible-Head Impulse Response Tests
Table 6.6. Overconsolidation Ratio Exponent, K (after Hardin and Drnevich, 1972)
Table 6.7. Constant K_2 as a Function of Void Ratio or Relative Density (after Seed and Idriss, 1970)
Table 6.8. Resolution Prediction from Two Layer Resolution Charts
Table 6.9. "Cutoff" Frequencies for Inaccessible Head Tests
Table 6.10. Cutoff Frequencies from Experimental and Empirical Methods
Table 6.11. Parameter Effects for Achieving "Best Fit Simulations

Table 7.1. Distance between Drilled Shafts and Access Holes (m)
Table 7.2. Summary of Results within 3 m of a Drilled Shaft
Table 7.3. Summary of Propagation Velocities in Concrete (m/s)
Table 7.4. Compression Wave Velocities from Parallel Seismic and Cross-Hole Seismic Tests

List of Symbols

Roman Letter Symbols

A, A_c = cross-sectional area of concrete shaft

A_i = amplitude of normal incident stress wave

A_R = amplitude of reflected stress wave

A_T = amplitude of transmitted stress wave

B = depth of pile cap or grade beam

C = capacitance (electrical analogue)

d = travel distance

D = diameter

D_r = relative density

e = void ratio

E, E_c = Young's Modulus (elastic concrete modulus)

E' = apparent stiffness of pile head

f = frequency

f_c = cutoff frequency

Df = change in frequency between resonant peaks

F = force

G = shear modulus

i_c = critical angle of incidence

I = electrical current (electrical analogue)

K' = low-strain shaft head dynamic stiffness

L = length

L_D = length to depth of anomaly

L, L', l = inductance (electrical analogue)

M_p = mass of shaft

m = point on mobility curve

N = mobility; mean value of V/F

P = maximum peak resolution

Q = minimum peak resolution

q_u = unconfined compressive strength

q_c = CPT tip resistance

r = radius

R = resistance (electrical analogue)

t = time

Dt = time increment

t_c = contact time of impact

t_d = travel time for the direct wave

t_h = travel time for refracted wave

u = displacement

v = wave velocity

v_{var} = compression wave velocity in a rod

v_c = compression wave velocity

v_{conc} = propagation velocity in concrete

v_o = partical velocity

v_p = longitudinal wave velocity

v_R = Rayleigh wave velocity

v_s = shear wave velocity

V/F = modility (mechanical admittace) of shaft head

x = space

Dx = distance between shaft and access hole

Z = mechanical impedance

Greek Letter Symbols

α = angle of refraction

α_p = refraced angle of compressive wave

α_s = refraced angle of shear wave

α_s = factor for pile cap plan area

α_t = factor for relative thickness of pile cap

β = damping factor

ν = Poisson's ratio

λ = wavelength

λ_c = wavelength where wave propagation in a rod is no longer one-dimensional

ρ = material density

ρ_c = concrete density

ρ_s = bulk density of soil surrounding shaft

σ = attenuation factor

σ_o' = mean normal effective stress

σ_v' = effective overburden stress

θ = angle of incidence

θ_p = compression wave angle of incidence

θ_s = shear wave angle of incidence

Table of Contents

Chapter 1. Introduction

Non-destructive evaluation (NDE) techniques have been used for a number of years to provide quality control of construction procedures for drilled shafts and driven concrete piles. In particular sonic echo and impulse response methods have been used extensively to check lengths and continuity of newly-installed foundations. In recent years, the need to evaluate conditions of in-service foundations has arisen as a result of rehabilitation studies of existing structures and the federally-mandated inspection of bridges. In some cases, the latter task involves identifying unknown bridge foundation types because plans for older structures have been lost over the years. Evaluation of existing foundations differs from the usual methods of NDE in that structures now cover the tops of deep foundations, and this structure alters the results of a NDE test as compared to one which was conducted atop the deep foundation.

To provide an opportunity to analyze the applicability of non-destructive testing methods to evaluate deep foundations under inaccessible-head conditions in a controlled environment, a test section was constructed at the National Geotechnical Experimentation Site (NGES) at Northwestern University. The test section consists of five drilled shafts with lengths between 12.2 and 27.4 m (40 to 90 ft) and diameters between 610 and 914 mm (2 to 3 ft). Two of the shafts were constructed purposely with defects, a reduced cross-section in one shaft and a thin, soil-filled joint in another. The former defect represents a typical construction deficiency while the latter represents a performance-related defect induced by excessive lateral loads. Eight weeks after the drilled shafts were constructed, reinforced concrete caps were cast to form three groups of shafts. Two groups of two shafts are connected with pile caps and one single shaft was also constructed with a cap.

The shafts were appropriately instrumented to conduct various non-destructive tests. Access tubes for sonic logging were placed in two of the shafts, and five cased bore holes were installed in the vicinity of the pile caps so that parallel seismic tests could be conducted. Each shaft had a geophone embedded near its bottom to directly measure the propagation velocity. Sixty cylinders were made from the concrete as it was placed to determine the strength and propagation velocity variations over time.

After the five shafts were constructed, sonic echo and impulse response tests were conducted on each shaft with its top exposed, herein called an accessible-head condition. After the reinforced concrete pile caps were poured, these tests were again conducted from the tops of the pile caps, herein called an inaccessible-head condition. Parallel seismic tests were also conducted at that time.

Extensive field and laboratory testing have been conducted to determine subsurface conditions and geotechnical parameters for the various soil strata. Field investigations include soil borings with standard penetration, field vane, cone and piezocone penetration, Menard pressuremeter, dilatometer, and cross-hole seismic tests. Laboratory tests include index property, consolidation, direct shear,

triaxial compression and extension, and plane strain compression tests.

The purpose of this work is to evaluate the capabilities of sonic echo, impulse response and parallel seismic tests to determine the conditions of drilled shafts under inaccessible-head conditions. To accomplish this goal, construction of the shafts was closely monitored so that the geometries of the shafts could be known as much as possible. The shafts were tested using the sonic echo and impulse response methods under both accessible- and inaccessible-head conditions. Because the interpretation of NDE tests in general is an inverse problem, the accessible- and inaccessible-head impulse response tests were numerically simulated to help define the predictive capabilities of the method. Parallel seismic tests were conducted only under inaccessible-head conditions.

This report reviews pertinent literature related to NDE testing of deep foundations, describes the construction of the test section, presents the results of the sonic echo and impulse response tests under both accessible- and inaccessible-head conditions, compares the results of observed and numerically simulated impulse response tests, presents the results of the parallel seismic testing, and draws conclusions concerning the applicability of these NDE techniques.

CHAPTER 2 reviews the sonic echo, impulse response and parallel seismic methods used in this study and presents the background information necessary to understand the application of these methods to deep foundations. For each method, the required equipment, conventional data interpretation techniques, and limitations are presented.

In CHAPTER 3, site characterization conducted at the NGES at Northwestern University and construction details of the test section built to evaluate non-destructive testing methods for deep foundations in a controlled environment are presented. The soils at the location of the NDE test section site have been well characterized by laboratory and field investigations. Construction of the test section was closely controlled, and careful observations were made of the shaft dimensions, as-built depths and drilling procedures.

CHAPTER 4 summarizes the results of impulse response and sonic echo tests performed at the NGES test site. Tests were performed on five drilled shafts, both when the shaft heads were exposed, the accessible-head condition, and when the shaft heads were obscured by pile caps, the inaccessible-head condition. The ability of the method to help evaluate concrete integrity and identify anomalies in drilled shafts is discussed, and the effects of pile caps on the interpretation of signals obtained from sonic echo and impulse response tests is presented.

In CHAPTER 5, the effect of concrete age and how it affects the interpretation of conventional sonic echo and impulse response results is discussed. The wave propagation velocity through concrete was determined in the laboratory using ultrasonic pulse velocity tests and correlations with compressive strength from concrete cylinders taken from the concrete mix used to construct the shafts. It was also measured in the field using impulse response and sonic echo techniques on the five concrete shafts at the site. Additionally, the results of a study on various couplants used to fix the geophone to the concrete surface are presented.

CHAPTER 6 presents two numerical analysis techniques used to evaluate the impulse response results. First, numerical simulations of impulse response signals for the accessible and inaccessible shafts are presented, and comparisons are made between the numerical simulations and the observed

results. The chapter continues with the development of resolution charts for both homogeneous subsurface conditions and layered soil systems, and concludes with a discussion of the observed signal resolution of the impulse response signals of the NGES shafts.

The results of the parallel seismic testing program are presented in CHAPTER 7. In addition to the usual data obtained, the depth and type of the deep foundation, the compression wave velocities of the soils adjacent to the shafts have been determined from the results of the parallel seismic testing.

The non-destructive testing program conducted at the NGES at Northwestern University is summarized and conclusions are drawn in CHAPTER 8.

Funds for this project have been provided by the infrastructure Technology Institute (ITI) at Northwestern University and the Federal Highway Administration (FHWA), grant number DTFH61-95-P-0816. The support of Mr. David Schulz, Director of ITI, and Mr. Al DiMillo of the FHWA is greatly appreciated.

Table of Contents

Chapter 2. Review of Non-Destructive Testing Methods

- 2.1 Introduction
- 2.2 Stress wave principles
  - 2.2.1 Wave propogation velocity
  - 2.2.2 Wave propagation in long thin rods
  - 2.2.3 Wave propagation in soils
  - 2.2.4 Frequency content of stress waves from impact
  - 2.2.5 Reflection and transmission of stress waves at an impedance change
- 2.3 Surface reflection methods
  - 2.3.1 Impulse response method
  - 2.3.2 Sonic echo method
- 2.4 Direct transmission methods: parallel seismic test
  - 2.4.1 Testing equipment
  - 2.4.2 Conventional testing procedure
  - 2.4.3 Data interpretation
  - 2.4.4 Limitations of the parallel seismic method
- 2.5 Summary

2.1 Introduction

Non-destructive testing techniques used to evaluate deep foundations are either surface reflection or direct transmission methods. The most common surface reflection methods include the sonic echo and impulse response tests. For these tests, compression waves are generated at the surface of a concrete drilled shaft, pile or pier by means of a hammer impact, and reflections are received at the surface with a transducer (geophone or accelerometer). The most common direct transmission method used to evaluate in-service deep foundations is the parallel seismic test. In the parallel seismic method, the direct transmission time of compression waves generated at the top of a foundation element are measured by a hydrophone in a water-filled borehole adjacent to the deep foundation. Several other NDE testing methods exist in practice today, including sonic logging, gamma-gamma logging, ground radar, and resistivity, but they were not considered in this report.

This chapter reviews several non-destructive testing methods and provides the background information necessary to understand the application of these methods to deep foundations. First, the basic principles of stress wave propagation in solids are reviewed, including a description of the

various types of waves and a discussion of the characteristics of these waves traveling in infinite media, long thin rods, and soils. The nature of waves imparted into a structure by mechanical impact, and the reflection and transmission of stress waves at impedance change interfaces are discussed. Finally, both the surface reflection and direct transmission methods are described, focusing on the equipment needed, conventional interpretation techniques used for data analysis, and limitations of each method.

2.2 Stress Wave Principles

One of the fundamental equations of mechanics is the one-dimensional wave equation given by the following partial-differential equation:

$$\frac{\delta^2 u}{\delta t^2} = v^2 \frac{\delta^2 u}{\delta x^2} \qquad (2.1)$$

where v is the propagation velocity, u is displacement, t is time and x is space. Some systems which can be described by this equation include transverse vibrations of taut strings, rods in longitudinal or torsional vibration, and pressure waves in ideal fluids along an axis of a container. Details of the development of the equations of motion can be found in detail by many authors including Timoshenko and Goodier (1951), Richart, et. al. (1970), and Graff (1975).

Non-destructive testing methods use stress waves to evaluate the integrity of various structural media. There are, in general, three types of stress waves generated from a disturbance that is applied suddenly to an elastic solid and cause physical distortion to the media through which the waves travel. These waves which radiate in all directions from the point of disturbance include waves of dilation, waves of distortion and surface waves. Waves of dilation are often called compression waves, and are also known as primary waves (P-wave), longitudinal waves, plane waves in infinite elastic media, or "bar" waves in long thin rods. Waves of distortion are commonly known as shear waves, secondary waves (S-wave), or transverse waves. Also, on the surface of an elastic body, waves are generated which propagate over the surface and penetrate a relatively small depth into the interior of the body. These waves are know as Rayleigh surface waves (R-waves).

As illustrated in FIGURE 2.1, compression and shear waves are distinguished by the direction of particle motion with respect to the direction which the wavefront is propagating. Compression waves propagate parallel to the direction of particle motion, whereas shear waves have particle motion perpendicular to the direction of propagation. Compression waves can travel through all types of media, whereas shear waves can only propagate through media which have shear stiffness. The Rayleigh wave propagates along a surface with particle motion that is elliptical in nature and retrograde (counter clockwise) with respect to the direction of propagation. The amplitude of the Rayleigh wave motion decreases exponentially away from the surface impact point.

2.2.1 Wave Propagation Velocity

The velocity of propagation of stress waves through infinite elastic media is a function of the material properties of the media, and depends upon the elastic modulus of the material, E, Poisson's

ratio, ν, and the material density, ρ. In an infinite elastic solid, the compressive wave velocity, v_p, (also called plane wave or longitudinal wave velocity) is given by the equation:

$$v_p = \sqrt{\frac{E(1-\nu)}{\rho(1+\nu)(1-2\nu)}} \qquad (2.2)$$

This equation for the compression wave velocity is appropriate for the sonic logging method because the impulse generated at a depth near the perimeter of the shaft has a significantly shorter wavelength than the dimensions of the medium in which it is traveling. It is also the proper equation for calculating the speed of compression waves traveling through soil strata, as is needed for the parallel seismic method.

Shear waves cause vibration of particles in the concrete to occur perpendicular to the direction of wave propagation. The wave propagation velocity of shear waves, v_s, is expressed by the following equation:

$$v_s = \sqrt{\frac{G}{\rho}} \qquad (2.3)$$

where G is the shear modulus given by the following equation:

$$G = \frac{E}{2(1-\nu)} \qquad (2.4)$$

Values of shear wave velocity in many elastic solids are generally slightly less than half the compression wave velocity. For a Poisson's ratio of 0.2 to 0.3, a typical range in concrete, the shear wave velocity is 0.61 to 0.54 times the compression wave velocity traveling through an infinite medium.

In an elastic half-space, a third wave type, the Rayleigh wave, is generated with a motion which is confined to a zone near the boundary of the half-space. Rayleigh surface wave particle motion is two-dimensional: the particles follow an elliptical path in a vertical plane parallel to the direction of propagation. The influence of the Rayleigh wave decreases rapidly with depth. The propagation velocity of Rayleigh waves, v_R, can be determined from the following approximation (Achenbach, 1975):

$$v_R = \frac{0.862 + 1.14\nu}{1+\nu} v_s \qquad (2.5)$$

As poisson's ratio, ν , varies from 0 to 0.5, the Rayleigh wave velocity increases from $0.862v_s$ to $0.955v_s$.

Representative values of density, compressive wave velocity and shear wave velocity are listed in TABLE 2.1 for selected materials. The Rayleigh wave velocity for a given material can be computed from the shear wave velocity presented in TABLE 2.1 and EQUATION 2.5.

The compression wave velocity in good quality concrete is often taken in practice to be 4000 m/s (13,124 ft/s). Typical compressive wave velocities in concrete may range from 3500 m/s to 4500 m/s (11484 ft/s to 14765 ft/s), depending upon the age, condition, and composition of the concrete (Popovics, 1994). For poor quality concrete, the propagation velocity reduces to 2000 m/s to 3000 m/s (6562 ft/s to 9843 ft/s) for honeycombed concrete, soil inclusions, gravel, sand, and mud, so that the presence of these defects or extraneous materials is obvious (Davis & Robertson, 1975) when evaluating the results of NDE.

2.2.2 Wave Propagation in Long Thin Rods

When a wave propagates through a long thin rod, as in the case of a drilled shaft, the equation for compression wave velocity can be simplified. For rod-like structures, compression wave speed is independent of Poisson's ratio if the rod diameter is much less than the propagating wavelengths because the stress component perpendicular to the axis of the rod becomes negligible (Timoshenko and Goodier, 1970). In this case, the compressive wave velocity in a rod, v_c or v_{bar}, is given by:

$$v_c = v_{bar} = \sqrt{\frac{E}{\rho}} \qquad (2.6)$$

This velocity is also called the propagation velocity in literature related to non-destructive evaluation of deep foundations. Comparison of EQUATIONS 2.2 and 2.6 reveals that the compression wave will travel faster in an infinite medium than in a rod. This physically occurs because lateral displacements are possible in the rod due to the cylindrical boundary effects, whereas no boundaries exists in an infinite medium to generate lateral displacements. For a Poisson's ratio of 0.2 to 0.3, a typical range in concrete, the compression wave velocity in a long thin rod is approximately 5 to 15% less than the compression wave velocity in an infinite medium. Recall that typical compressive wave velocities may range from 3500 m/s to 4500 m/s (11484 ft/s to 14765 ft/s) in concrete, thus, the bar wave velocity is 5 to 15% lower than these values for waves traveling through long thin cylinders.

2.2.3 Wave Propagation in Soils

By their inhomogeneous nature, soils have special characteristics which cause their wave propagation behavior to differ from ideal solids. Soils are composed of three phases, solid, liquid and gas, which gives rise to a complex dynamic behavior. The wave propagation velocity of a soil mass is contingent upon which materials (water, air, or mixtures of fluids) fill the pores of a soil mass. In a

saturated cohesionless soil, seismic methods which rely upon measuring the first arrival time of a wave will often identify the velocity of the compression wave in water rather than in the soil structure (Richart, *et. al*., 1970). Water has a compression wave propagation velocity of about 1480 m/s (5000 ft/s), thus it behaves as a hard material when compared to the behavior of loosely confined soils.

Richart, et. al., (1970) presented several studies of wave propagation in porous saturated solids including a detailed study performed by Biot in 1956. From a three-dimensional consideration of shear and compressive wave propagation in a fluid-saturated porous medium, Biot determined the effect of structural coupling between the fluid and the solid on the wave propagation properties. The findings showed that two different compression waves were transmitted in a saturated porous medium: a compression wave through the fluid and a compression wave through the elastic structure. The two waves are coupled through the stiffness of the fluid and solid components, in addition to a coupling effect produced from the motions of the solid and fluid. In contrast, no structural coupling between the elastic structure and the fluid exists for a transmitted shear wave because the fluid has no shearing stiffness. Thus, field measurements of shear waves in saturated soils can be confidently used to determine the shear wave velocity in the soil structure.

To further examine the wave propagation in saturated solids, Richart, et. al., (1970) presented Hardin's work from 1961 where Biot's theory was applied to a water-saturated body of quartz sand. The results from the study are presented in FIGURE 2.2 showing the variation of the two compression wave velocities and the shear wave velocity with confining pressure. Biot's theory illustrates the existence of these three types of waves and their relative velocities. The compression wave in the fluid had the highest velocity which is actually higher than that in water alone due to a "push" produced from the vibrating elastic structure. In the elastic structure, the compression wave velocity was determined to be lower than that observed in the dry condition because the water in the pores creates a drag effect. Also, it was observed that the shear wave has the lowest velocity.

For deep foundations seated on rock, wave propagation characteristics for rock masses must be determined. It is important to understand that propagation velocities through rock masses are substantially affected by jointing and weathering. In general, jointing changes rock mass stiffness which influences the propagation velocity. The range of propagation velocities for heavily jointed to non-jointed limestone and granite are presented in TABLE 2.1.

2.2.4 Frequency Content of Stress Waves from Impact

For the surface reflection techniques and the parallel seismic methods, stress waves are introduced into the structure by means of a hammer impact. Upon impact to a surface, stress waves are generated and a wavefront is created. The wavefront results in spherical compression- and shear-wavefronts and a cylindrical Rayleigh-wavefront, as illustrated in FIGURE 2.1.

Mechanical impact is used in nondestructive testing of concrete to generate low frequency stress pulses. Stress waves generated by mechanical impact are limited in their effectiveness for NDE of concrete structures by the depth of signal penetration in concrete. Piezoelectric ultrasonic transducers generate controlled, high frequency (1 MHz or greater) stress pulses which cannot penetrate deeply into concrete (Sansalone & Carino, 1991).

The frequency content of an impact is a function of the duration and magnitude of the impact. Upon applying the Fourier transform, the force-time function of elastic impact of a sphere on a solid shown in FIGURE 2.3 is equivalent to the summation of a number of continuous sinusoidal force-time functions with different frequencies, amplitudes and phase shifts (Sansalone and Carino,1986). Thus, a range of frequencies, or a range of waves with different wavelengths, is imparted into the structure by impact. The force-time function can be approximated by a half-cycle sine curve, given by the following equation:

$$F = F_{max} \sin \pi \frac{t}{t_c} \qquad 0 \le t \le t_c \qquad (2.7)$$

where F_{max} is the maximum force and t_c is the contact time of the impact. Both F_{max} and t_c are recorded in a force-time history for the impulse response method used in this study. By examining the frequency spectrum of the force-time function shown in FIGURE 2.4, the frequency content of the impact can be determined. The time of contact between a impact source and an impacted surface determines the frequency content of the impact. Also, the significant contribution of energy imparted by an impact is found at frequencies approximately below the inverse of the contact time. For a contact time of 0.9 msec, typical for the testing performed in this study, the significant energies imparted to the structure would be less than 1200 Hz. Note that as the contact time of impact becomes shorter, the range of frequencies containing significant energy increases.

The ability of stress wave propagation methods to detect defects depends on the frequencies (wavelengths) contained in the propagating wave and on the size of the defect. In general, a stress wave will reflect from a defect if the size of the defect is on the order of or greater than the wavelength of the propagating wave. Given the relationship between wave velocity, v, frequency, f, and wavelength, λ:

$$v = f\lambda \qquad (2.8)$$

and assuming a wave propagation velocity of 4000 m/s with a frequency range of 0 to 2000 Hz (typical of the input from the impulse hammer described in SECTION 2.3.1.1), the shortest wavelength, λ, introduced by an impact to the head of a deep foundation is on the order of 2 m (6.6 ft). Relatively low frequency waves must be used to evaluate concrete to ensure that the propagating wavelengths are larger than the size of the aggregate. For example, the highest frequency that can be used for concrete with aggregate of 76 mm (3 in.) is 50,000 Hz. Unfortunately, the use of these relatively low frequencies reduces the sensitivity to detect small defects; thus, there is an intrinsic limitation in the detectable defect size within concrete which is defined by the wavelength of the propagating wave.

2.2.5 Reflection and Transmission of Stress Waves at an Impedance Change

When a stress wave is generated at the surface with the impact hammer, a compression zone is

formed which results in stress waves that will travel down the shaft until a reflector is met. Typically a reflector consists of a change in mechanical impedance, which can be a change in material, such as occurs at the toe of the shaft, a change in cross-sectional area of the shaft, or even a break in the shaft. When the stress wave encounters an impedance change, part of the wave is reflected back up the shaft and part is transmitted down. After the wave has been reflected, it will travel back to the shaft head where it can be recorded with a geophone.

Any point at which the stress waves are observed moves with particle velocity, v_o, and transmits an axial force, F. Their ratio is termed mechanical impedance, Z, or shaft wave resistance, and is given by the expression:

$$Z = \frac{F}{v_o} \qquad (2.9)$$

Impedance can also be expressed by the following relationship:

$$Z = \rho_c v_c A = A\sqrt{\rho_c E} \qquad (2.10)$$

where A is the cross-sectional area, and E elastic modulus. Therefore, changes in density, elastic modulus, or cross-sectional area of a concrete shaft produce changes in impedance. Accordingly, reflections can arise from changes in impedance between materials and from defects within a material, if the size of the defect is on the order of or greater than the wavelength of the propagating wave, as discussed in SECTION 2.2.4.

The portion of an incident longitudinal wave that is reflected at an interface between two media depends on the specific impedances of each medium. The amplitude of the reflected stress wave, A_R, relative to the amplitude of the normal incident stress wave, A_I, can be found from (Graff, 1975):

$$\frac{A_R}{A_I} = \left[\frac{Z_2 - Z_1}{Z_2 + Z_1}\right] = \left[\frac{\rho_2 v_{p2} - \rho_1 v_{p1}}{\rho_2 v_{p2} + \rho_1 v_{p1}}\right] \qquad (2.11)$$

where Z_1 and Z_2 are the specific mechanical impedances of media 1 and 2, respectively. The amplitude of the transmitted stress wave, A_T, relative to the amplitude of the normal incident stress wave, A_I, is determined from:

$$\frac{A_T}{A_I} = \left[\frac{2Z_1}{Z_2+Z_1}\right] = \left[\frac{2\rho_1 v_{p1}}{\rho_2 v_{p2}+\rho_1 v_{p1}}\right] \qquad (2.12)$$

FIGURE 2.5 illustrates the reflection and transmission characteristics at an interface of a compression wave traveling through media with Z_1 and Z_2. As indicated in the figure, if Z_1 is greater than Z_2 then the reflected wave will change phases. If an incident longitudinal wave is compressive, the stress in the reflected wave will be tensile. Boundary conditions also affect wave transmission and reflection at interfaces. Consider the cases of fixed end and free end rods. Reflection of an incident wave from a free end, where $Z_1>Z_2$, results in a stress reversal such that a compression wave reflects as a tension wave, and vice versa. On the other hand, when $Z_2>Z_1$, such as when an incident wave reflects from a fixed end, both the reflected and transmitted waves maintain the sign of an incident wave. Also note that the maximum amplitude in a reflected wave occurs when an incident wave is normal to an interface.

For cases where an incident wave is not normal to an interface, Snell's Law (Graff, 1975, and Richart, et. al.,1970) is used to determine the angle of refraction, α, given by the following equation:

$$\sin\alpha = \frac{v_2}{v_1}\sin\theta \qquad (2.13)$$

where θ is the angle of incidence and v_1 and v_2 are the wave propagation velocities for medium 1 and 2, respectively. Thus, the angle at which a reflected or refracted wave leaves the interface depends on the angle at which the incident wave approached the interface and the ratio of the wave velocities of the two media. FIGURE 2.6 illustrates the reflection and refraction of an incident wave at an interface. For an incident compression wave, as illustrated in FIGURE 2.7, there will be four resultant waves, a reflected and a refracted compression wave and a reflected and a refracted shear wave, as a result of mode conversion at the interface. Snell's Law is used to determine angles for both the reflected and refracted compression and shear waves:

$$\frac{\sin\theta_p}{v_{p1}} = \frac{\sin\theta_s}{v_{s1}} = \frac{\sin\alpha_p}{v_{p2}} = \frac{\sin\alpha_s}{v_{s2}} \qquad (2.14)$$

where θ_p is the angle of incidence for the compression wave; θ_s is the reflected angle of the shear wave; λ_p and λ_s are the refracted angles for the compression and shear waves, respectively; and v_{p1}, v_{s1}, v_{p2}, and v_{s2} are the compression and shear wave propagation velocities for medium 1 and 2, respectively. To determine the amplitude of the resulting reflected and refracted waves, refer to Achenbach (1975), Graff (1975), or Richart, *et. al*. (1970) for a detailed presentation of the

governing equations and graphical solutions of amplitude ratio versus incident angle.

Attenuation of a stress wave occurs as it propagates down a shaft. The amount of attenuation is affected by the concrete quality, the shaft cross-sectional area, and the soil surrounding the shaft. Briard (Davis and Dunn, 1974) defined a soil attenuation factor, σ:

$$\sigma = \frac{\rho_s v_s}{\rho_c v_c r} \qquad (2.15)$$

where ρ_s is the bulk density of the surrounding soil, v_s is the shear wave velocity of the soil surrounding the shaft, ρ_c is the density of the concrete, v_c is the compression wave velocity of the shaft medium, and r is the shaft radius. Attenuation is greater for shafts in stiff soils than in soft soils and, for a given soil, attenuation is reduced by increasing concrete quality and cross-sectional area. Also, any change within the propagating material, such as an impedance change will further attenuate stress waves in that the amplitude of the reflected wave will be less than the wave before it encountered the impedance change.

2.3 Surface Reflection Methods

Surface reflection methods used for nondestructive evaluation of deep foundations include the sonic echo and impulse response tests. For these tests, stress waves are generated at the surface of a deep foundation, for example, a concrete drilled shaft, by means of a hammer impact. These stress waves travel the length of a shaft and reflect from impedance changes at depth, such as defects and the shaft toe. The reflections are sensed at the surface with a transducer, either a geophone or an accelerometer.

2.3.1 Impulse Response Method

The impulse response method is a surface reflection technique which relies on the identification of compression wave reflections. The method was developed as a means to quickly and inexpensively evaluate shaft integrity with minimal pile head preparation. Its beginnings can be traced back to the late 1970's in France, when it arose as an extension of a vibration test which involved harmonically vibrating a known mass at frequencies up to 2000 Hz at the head of a shaft, and measuring the shaft response with a geophone (Higgs and Robertson, 1979).

The test involves impacting the top of a drilled shaft with an impulse hammer, which induces transient vibrations with frequencies as high as 2000 Hz. Both the impact force and particle velocity are measured on the impacted surface. Shaft response is recorded in the time domain with a geophone, and the signal is digitally converted to the frequency domain for analysis.

2.3.1.1 Testing Equipment

The testing equipment necessary to perform impulse response tests is schematically shown in FIGURE 2.8. The figure also illustrates a typical testing arrangement for performing tests on

concrete shafts where the top of the shaft is accessible and when access to the shaft head is obscured by a pile cap, grade beam, or other existing structure. The equipment includes a portable computer equipped with a data acquisition board and signal conditioning card, an impulse hammer and a geophone. The portable PC is used for acquiring, analyzing, and storing the data. An IBM-compatible, Intel chip based 486 computer running at a clock speed of 33 MHz with a math coprocessor and 4 MByte of RAM was used for this study. The computer is equipped with an LCD screen with VGA display suitable for use in an outdoor environment with its attendant sunlight intensity.

Impulse Hammer

An impulse hammer is required to strike a drilled shaft head to induce transient vibrations. The impulse hammer used for this study was a PCB Piezotronics Model No. 086M54. It is equipped with a load cell and is capable of generating transient vibrations with frequencies as high as 2000 Hz, depending on the material at the tip of the hammer. The head of the hammer tip is 5.1 cm (2 in.) in diameter and can induce a force with a magnitude as high as 22 kN (5000 lb). Each hammer is modally tuned to eliminate multiple impacts.

The force measurement is recorded with an integral quartz force transducer mounted on the striking end of the hammer head. This quartz transducer is a piezoelectric material that develops an electrical charge proportional to applied pressure or deformation. A micro-electric amplifier circuit is incorporated into the transducer housing to improve the output signal-to-noise ratio. The sensitivity of each hammer varies slightly and was determined by the manufacturer. The hammer used for this testing program had a sensitivity of 0.20 mV/N (0.90 mV/lb). The magnitude of the force created by a hammer impact is calculated by dividing the measured voltage by the sensitivity.

The hammer has four interchangeable plastic tips of varying stiffnesses. Each tip stiffness creates a different impact duration which allows the user to control the frequency input range of an impact. The frequency range for the various hammer tips is listed in TABLE 2.2. This flexibility provides the ability to get a better low or high frequency response depending on the structural testing needs. Frequency content and energy level of an impact are interrelated. Generally speaking, the material at the hammer tip affects the hammer impulse frequency content, and the hammer mass and velocity at impact will affect both the frequency content and the energy level. The most common hammer tip used in deep foundation concrete integrity evaluation is the hardest plastic tip which induces a full 2000 Hz frequency range. The softer hammer tips induce ranges of frequencies from 0 to 600, 650, or 800 Hz, depending on the tip stiffness.

Digital Grade Geophone

Vibrations at the shaft head can be recorded by either a geophone (velocity transducer) or an accelerometer (acceleration transducer). For this testing program, a vertical geophone was used, specifically, a SM-6 Geophone Model B by Sensor Nederland b.v. This geophone has a natural frequency rated at 4.5 ± 0.5 Hz. The sensitivity is rated at 28.8 ± 5% V/m/s (0.73 V/in/s). The frequency response curve for the geophone is shown in FIGURE 2.9. Notice that the curve response does not begin to flatten out until approximately 30 Hz; therefore, a calibrated damping series-parallel resistor network is added to the geophone. The effect of this damping resistor network is to extend the low frequency response down to about 8 Hz, and reduce the sensitivity to a calibrated

value of 20 V/m/s (0.51 V/in/s).

The geophone is activated upon a hammer impact by a triggering device within a data acquisition card and signal conditioning unit in a portable PC to which both the hammer and geophone are connected. The voltage response of the geophone is stored digitally for processing. The magnitude of the velocity recorded by the geophone is calculated by dividing the measured velocity voltage by the geophone sensitivity.

Amplifier/Signal Conditioning Card

The amplifier/signal conditioning card was custom built by STS Consultants, Ltd. and housed in an expansion slot of the portable computer. Both the impulse hammer and geophone are directly connected to the card. The card uses the +12V power supply of the computer and doubles it to 24 V to power the hammer load cell micro-electronics at a constant current of 4 mA. The card ensures proper voltage (not to exceed 300 V) and current (not to exceed 20 mA) for the impulse hammer. Amplifications of low voltage signals are achieved with an amplifier filter present on the card which has switch-selected gain ranges of x1, x2, x5, x10 and x20. This allows optimization of the signal to noise ratio to improve low voltage signal resolution. A gain of x20 was typically used for this project.

Data Acquisition Card

A data acquisition card is required to capture the force and velocity responses. The card is housed on one of expansion slots of the portable computer and is directly accessible by the data acquisition software. The card used for this testing program was the DAS-58, manufactured by Keithly MetraByte. The card is an extremely high-speed 12 bit analog-to-digital converter board for use in PC computers. The board features 1 Megasample/sec throughput and 1 Megaword of onboard memory. The board has eight analog input channels, an auto-zero feature to ensure accurate measurements, and a simultaneous sample-and-hold capability when used with the Keithley MetraByte SSH-58 accessory.

The SSH-58 allows the DAS-58 to operate in a simultaneous sample and hold mode where up to eight single-ended inputs are sampled within ±20 ns of each other. Channels 0 to 3 or channels 4 to 7 are sampled with less than 300 picoseconds of inter-channel skew. The SSH-58 uses the burst mode feature to burst sample all channels at 1 µs per channel once they have been held. The maximum aggregate sample rate for 8 channels is 889,000 samples/sec.

2.3.1.2 Conventional Testing Procedure

To perform an impulse response test, the equipment was set up as indicated in FIGURE 2.8. Testing setups are shown for performing tests on concrete shafts where the top of a shaft is both accessible and inaccessible.

Before testing can be conducted, two locations on the shaft head must be prepared; one for the geophone and one for the hammer impact point. For conventional accessible head tests, the impact point should be located at the center of the shaft and the geophone should be located near the perimeter approximately 7.6 to 15.24 cm (3 to 6 in) from the edge, within the reinforcing cage. Both

locations should be prepared such that a smooth concrete surface exists and is free of any debris.

A coupling agent is used to fix the geophone to the concrete surface and the shaft head is struck at the hammer impact point. Most tests were done using either Amoco Rycon grease or Castrol water pump grease. Vibrations at the shaft head are recorded by the vertical geophone which is activated upon hammer impact by means of a triggering device in a portable PC to which both the hammer and geophone are connected. The force, velocity and mobility signals are immediately displayed on the PC screen for viewing. Both the velocity and force time traces are stored electronically for processing and viewing at a later date.

2.3.1.3 Conventional Data Analysis

Results of an impulse response test provide a measure of the homogeneity of concrete in the shaft and information about the shaft performance (Higgs and Robertson, 1979). The analyses of the data is conducted in the frequency domain. A fast Fourier transform (FFT) is performed on both the force and the velocity signals to convert them from the time to the frequency domain. The velocity spectrum is divided by the force spectrum (called mobility) and is plotted against frequency. Various filtering techniques may be used to remove noise from the data at frequencies which obscure identification of significant reflections. For this study, the mobility curve was filtered by applying a lowpass Blackman window filter which smoothed fluctuations between 2 adjacent data points in the mobility plot which were spaced at intervals of 19.5 Hz.

An ideal graph of mobility versus frequency is shown in FIGURE 2.10. Quantitative information concerning the shaft length, low-strain stiffness and impedance can be obtained from this plot. Because of its rod-like shape, elastic theory indicates that a deep foundation has a consistent change in frequency between resonant peaks that is a function of the shaft length and compression wave velocity. Resonant peaks usually can be easily identified, and by measuring the frequency change, Df, between these peaks, the length from the geophone to the source of the reflection, L, can be found from:

$$L = \frac{v_c}{2\Delta f} \qquad (2.16)$$

where v_c is the compression (bar) wave velocity in concrete.

From the low frequency portion of the mobility curve, the low strain stiffness, K', can be calculated. At low frequencies, the pile-soil system behaves as a spring, resulting in a linear increase in mobility with increasing frequency until the onset of resonance. Shaft head stiffness is known to be a function of the pile geometry, concrete density, and the soil beneath and surrounding the shaft. This parameter has been correlated to the initial stiffness in an axial load test (Davis and Robertson, 1975; Stain, 1982). At a given site, shafts with lower than average pile stiffnesses can be selected from the group of shafts tested to produce a rational, rather than random, method for selecting piles for full-scale load tests. The low-strain stiffness is found from:

$$K' = \frac{2\pi f_m}{V/F_m} \qquad (2.17)$$

where f_m and V/F_m are the frequency and mobility, respectively, at point m. The point m is selected on the initial linear portion of the mobility curve when the shaft-soil unit behaves like a spring, as shown in FIGURE 2.10.

To help evaluate the computed stiffness values, Davis and Dunn (1974) derived the theoretical minimum and maximum stiffnesses, K_{min} and K_{max}, respectively, for a shaft embedded in soil as:

$$K_{max} = \frac{AE}{L}\sqrt{\frac{P}{Q}}\coth^{-1}\sqrt{\frac{P}{Q}} \quad ; \quad K_{min} = \frac{AE}{L}\sqrt{\frac{Q}{P}}\coth^{-1}\sqrt{\frac{P}{Q}} \qquad (2.18)$$

where A is the shaft cross-sectional area, E is the elastic modulus of the shaft, P is the maximum value of mobility and Q is the minimum value of mobility. K_{max} represents the shaft head stiffness when a shaft is supported on a rigid base while K_{min} corresponds to a shaft with no base support behaving as if it had been cut off at depth. These two values provide limiting stiffness values with which the actual measured stiffness may be compared.

The characteristic admittance or mobility is also measured for a shaft. The shaft mobility, N, is found by taking the geometric mean of the height of the resonant peaks (= $\sqrt{PQ}$; see FIGURE 2.10) in the portion of the mobility curve where the shaft response is in resonance. It can also be defined theoretically as (Davis and Robertson, 1975; Stain, 1982):

$$N = \frac{1}{\rho_c v_c A} \qquad (2.19)$$

where r_c is the density of concrete. If the actual N is greater than the theoretical value, it is likely that there is a defect in the shaft due to a smaller than anticipated cross-section (i.e. a neck) or poor concrete quality (low r_c or v_c).

2.3.1.4 Simulation of Impulse Response Signals

Numerical simulation of impulse response signals is useful for aiding the interpretation of signals obtained in the field. The mobility curves obtained from drilled shafts in the field are seldom as clear as the ideal curve for a perfect pile shown in FIGURE 2.10. This observed response may be due to numerous factors including variations in the pile diameter, the concrete quality within the pile, and

the soil stiffness surrounding the pile (Davis and Dunn, 1974). Therefore, numerical analysis techniques are useful to improve the interpretation of the results. One such numerical simulation technique arises from an analogue that exists between mechanical wave propagation and electrical transmission lines. The analogous relationships between the two systems are listed in TABLE 2.3.

Simulation of shaft response subjected to a hammer impact can be accomplished by taking advantage of these analogous relationships. Davis and Dunn (1974) demonstrated this analogue for a steady state vibration applied to the head of a shaft. When a perfect cylindrical unit length segment of a pile is considered, the force, F, applied to the top of the segment may be represented by current, I, and the maximum particle velocity at the shaft head, v_o, by the voltage, V, as shown by a schematic electrical analogue element in FIGURE 2.11. Therefore, the mechanical impedance, v_o/F, of the pile segment corresponds to the electrical admittance I/V.

To model a cylindrical concrete pile that is embedded in soil using the aforementioned analogue, the mechanical properties for both the soil and the concrete pile must be converted to their electrical equivalents. To account for the pile mass, the mass of the pile per unit length is represented by the electrical equivalent, capacitance:

$$C = \pi r^2 \rho_c \qquad (2.20)$$

where r is the radius of the pile and r_c is the density of the concrete. The soil stiffness per unit length is represented by an inductance, L_s, and given by the following equation:

$$\frac{1}{L_s} = \pi \rho_s v_s^2 \qquad (2.21)$$

where r_s is the soil density, and vs is the soil shear wave velocity. The stiffness per unit length of pile is represented by an inductance, L_c, given by the equation:

$$\frac{1}{L_c} = \frac{\pi r^2 E_c}{l^2} \qquad (2.22)$$

where E_c is the modulus of the concrete and *l* is the unit length of a pile segment. The damping lost per unit length of the soil can be represented by the admittance

$$\frac{1}{R} = 2\pi r \rho_s v_s \qquad (2.23)$$

of resistance R. The stiffness at the base of the shaft is represented by an inductance, L', where the base stiffness is determined by

$$\frac{1}{L'} = 1.84 r \left(\frac{E_{(B)}}{1 - \nu^2_{(B)}} \right) \qquad (2.24)$$

and $E_{(B)}$ is the modulus of elasticity and $\nu_{(B)}$ is the Poisson's ratio, both for the soil at the base of the shaft. FIGURE 2.12 shows how several electrical analogue elements can be combined to simulate a defective pile. This example illustrates the modelling of a necking defect as well as a bulging imperfection, in a two-layer soil system with a rigid base.

To simulate a result from an impulse-response test, a shaft can be modelled as a cylinder surrounded by "infinitely" extending horizontal soil layers. Input parameters for the shaft include shaft length, diameter and concrete density. The soil parameters required are the shear wave velocity and density. With a numerical procedure, multiple layers with any parameter combination can be simulated for a given shaft. This is advantageous for simulating complex soil conditions and changes in shaft cross-sectional area. Also, this information is useful to quantify the percentages of the wave that are reflected and transmitted at the toe of the shaft, or at other impedance changes. Assumptions made for modelling layered soil deposits include parallel and horizontal interfaces between soil layers and elastic, isotropic and homogeneous soil layers.

2.3.1.5 Resolution of Impulse Response Signals

Resolution of impulse response signals can be defined in terms of the ratio of P/Q, the minimum and maximum mobilities as identified on the ideal mobility plot shown in FIGURE 2.10. When the P/Q ratio approaches 1.0, no resonance frequencies can be identified and thus one cannot expect to locate the bottom of a drilled shaft under those conditions. Higher signal resolution makes the resonant peaks easier to distinguish and, thus, makes it easier to interpret pile length and location of apparent defects. For a shaft in a homogeneous, elastic soil, the resolution is primarily a function of the length-to-diameter ratio, the ratio of the shear wave velocity of the soil to that of concrete, and the ratio of soil density to concrete density. It is important to remember that drilled shafts are not perfect cylinders and surrounding soils are rarely homogeneous.

Following the theoretical development of signal resolution presented by Paquet (1968) and Caputo (1994), maxima P_i and minima Q_i are respectively equal to:

$$P_i = N\coth\beta \qquad Q_i = N\operatorname{th}\beta \qquad (2.25)$$

and the ratio of P_i over Q_i is constant and depends only on a damping factor, β:

$$\frac{P_i}{Q_i} = \coth^2\beta \qquad (2.26)$$

where β is defined as :

$$\beta = \frac{b \cdot L}{2 \cdot \sqrt{k \cdot M}} \qquad (2.27)$$

and b, k (pile stiffness), and M (pile mass) are defined as:

$$b = 2 \cdot \pi \cdot r \sqrt{G \cdot \rho_s}; \qquad k = \frac{E_c \cdot A_c}{L}; \qquad M = \rho_c \cdot A_c \cdot L \qquad (2.28)$$

where r is the shaft radius, E_c is Young's Modulus of the concrete, G is the shear modulus of the soil, A_c is the cross-sectional shaft area, L is the shaft length, and r_c is the concrete density. Thus, a full expression for P/Q can be derived as follows:

$$\frac{P_i}{Q_i} = cth^2\left(\frac{2\pi \cdot r \cdot L\sqrt{G \cdot \rho_s}}{2\sqrt{\frac{E \cdot A}{L} \cdot \rho_c \cdot A \cdot L}}\right)$$

$$= cth^2\left(\pi \cdot r \cdot L\sqrt{\frac{G \cdot \rho_s}{E \cdot A^2 \cdot \rho_c}}\right) \qquad (2.29)$$

$$= cth^2\left(\frac{L}{r}\sqrt{\frac{v_s^2 \cdot \rho_s \cdot \rho_s}{v_c^2 \cdot \rho_c \cdot \rho_c}}\right)$$

$$= cth^2\left(\frac{L}{r} \cdot \frac{v_s}{v_c} \cdot \frac{\rho_s}{\rho_c}\right)$$

FIGURE 2.13 shows an ideal resolution chart giving P/Q as a function of L/D, and v_s/v_c for given values of r_s/r_c, . The chart was developed for shaft length-to-diameter, L/D, ratios of 15, 20, 25, 30, and 35. The density of the soil was held constant at 1920 kg/m^3 (120 pcf) as was the density of the concrete at 2400 kg/m^3 (150 pcf), typical for materials in this study. These values yield a constant ratio of soil density to concrete density (r_s/ r_c) of 0.8. For each L/D ratio, the v_s/v_c ratio was varied until the calculated resolution approached 1.0.

The chart is useful in determining the resolution which can be expected for a given impulse response test. When the dimensions of a drilled shaft are known and an estimate of the soil and concrete properties can be made, an estimate of the resolution, P/Q, can be determined from the chart for a given L/D and v_s/v_c ratio. Generally, it is accepted in current practice that the toe of a drilled shaft cannot be identified when the L/D ratio is greater than 30. From the resolution chart, it can be clearly seen that the identification of the toe is dependent upon the soil and concrete properties. For a judicious combination of soil and concrete parameters, the toe of a shaft can be identified for L/D ratios greater than currently expected.

2.3.1.6 Limitations of the Impulse Response Method

Interpretation of impulse response data requires knowledge of either the as-built drilled shaft length or the concrete compression wave velocity. Uncertainty in interpretation arises when the exact length of a drilled shaft is unknown and/or the concrete compression wave velocity must be assumed.

Determining the location and size of defects is limited by the type and frequency content of the propagating waves. Low frequency waves (appropriate frequency is a function of the shaft length, but usually below 1000 Hz) are needed to identify the bottom of drilled shafts. Higher frequency waves are needed to detect smaller concrete defects. However the wavelengths need to be larger than

the shaft diameter to assure that the wave propagation is essentially one-dimensional and the shaft will behave like a rod-like structure, instead of an infinite elastic medium where compression waves will reflect from all shaft boundaries (Hearne et al., 1981).

A major restriction is the limiting length-to-diameter ratio (L/D) which is further impacted by the soil conditions surrounding the concrete shaft. Highly attenuating soils, such as stiff soils, contribute to attenuation of the compression waves for shafts with high L/D ratios. As the critical L/D ratio is approached, the resolution of the mobility curve, defined by the ratio of P/Q, i.e., the maximum and minimum mobilities, will approach 1.0 as a result of the peaks flattening out to a point where resonant peaks are not discernable due to attenuation effects. Thus, one can not expect to be able to locate the bottom of a drilled shaft under those conditions. The limiting L/D ratio depends upon the surrounding soils, but typically the value in a medium stiff clay is about 30:1. The amplitude of the reflection is also dependent on the impedance contrast at the toe of the shaft between the concrete and the soil/rock bearing strata. The greater the similarity between the toe material and the shaft concrete, the smaller the reflected wave amplitude (EQUATION 2.11).

It can be difficult to locate defects present near the toe of the shaft. These defects may produce sufficient reflection that could be easily interpreted as the toe itself. This problem is further complicated by the uncertainties associated with knowing the exact value of the compression wave velocity. Moreover, if the actual length of the shaft is unknown, it is difficult to draw a distinction between the toe and a defect near the toe.

Accurate determination of the source of a reflection is limited by the types of defects present in the shaft. For example, necking and poor concrete both produce reductions in impedance and distinguishing between the two can be complicated. Also, a defect with a gradual decrease in cross-sectional area may go undetected because a distinct reflection may not be generated. On the other hand, if a bulb (a local increase in cross-sectional area) is present in a shaft, the reflection generated may cause the shaft to be considered defective, when in actuality a bulb does not decrease the shaft integrity. In addition, very stiff soils, will also produce reflections similar to those of increases in impedance, causing additional uncertainty in shaft integrity analysis. Surface waves also create problems for interpretation of impulse response signals, especially for tests made under inaccessible-head conditions. The large amplitude of the surface waves can mask the lower amplitude reflections from the toe and defects within the shaft.

2.3.2 Sonic Echo Method

The sonic echo test was the first low-strain method used in practice to determine pile integrity. In practice, the test is called various names, including the TNO method (Holland), the PIT test (Pile Integrity Test, Pile Dynamics Inc., USA) and the Impact-Echo test (Centre Experimental de Recherche et des Etudes du Bftiment et des Travaux Publics-CEBTP, France). The sonic echo test is a stress wave reflection method which, similar to that of the impulse response method, relies on the measurement of compression wave velocities to verify shaft integrity. However, the analysis of the sonic echo results is conducted in the time domain only and the impact force of the hammer is not measured.

2.3.2.1 Testing Equipment

The typical test set up for the sonic echo method is similar to the impulse response method shown in FIGURE 2.8, except that the hammer is not necessarily equipped with a load cell to measure the impact force with time. The equipment used for the work done in this study was the same as that described in SECTION 2.3.1.1.

2.3.2.2 Testing Procedure

For this test, a compression wave is generated by means of an impact to the shaft head and the particle velocity there is recorded by a geophone fixed to the shaft head surface with a coupling agent. The impact is generated using an impulse hammer with a triggering device which activates the computer to start recording the geophone response. The compression wave propagates down the shaft and is reflected off the toe at the concrete-soil interface. If discontinuities such as changes in cross-section area or cracks are present in the shaft, these may also cause reflections. The sonic echo method can be applied to accessible shaft heads as well as inaccessible shaft heads.

2.3.2.3 Data Interpretation

The analysis of the sonic echo data is conducted in the time domain. An idealized plot of a sonic echo test result is illustrated in FIGURE 2.14. The figure shows the shaft head velocity as measured by a geophone versus time. The difference in time between the point of hammer impact and the reception of the echo can be determined. Knowing that the wave has to travel down the shaft and back up, the pile length is calculated from the following equation:

$$L = \frac{v \Delta t}{2} \qquad (2.30)$$

where L is the pile length, v_c is the estimated concrete compression wave velocity, and Dt is the time from the initial impact to the time an echo is received. Conversely, if the length of the pile is known, the compression wave velocity can be determined. This velocity, along with a correlation between compression wave velocity and concrete strength, is used to estimate concrete quality.

2.3.2.4 Limitations of the Sonic Echo Method

The sonic echo method shares most of the same limitations associated with the impulse response method because they are both surface reflection methods and rely on measuring reflected responses at the surface of a structure. While the frequency-based analysis of the impulse response method considers deep foundations with varying cylindrical cross-sections, the sonic echo method is best suited for precast and permanently cased piles due to the straight-sided shafts these structures provide (Stain, 1982). Variations in cross-section that often exist in drilled shafts create multiple reflections which can interfere with shaft toe identification in the velocity-time history. Therefore, the sonic echo test is most useful for determining linear continuity of a shaft, but provides no quantifiable information about the shaft cross-section or behavior under load.

2.4 Direct Transmission Methods: Parallel Seismic Test

The parallel seismic method is a direct transmission method developed in France in the mid 1970's to evaluate the integrity of drilled shafts and piles under existing structures (Davis and Hertlein, 1993). A typical testing arrangement for parallel seismic testing is shown in FIGURE 2.15. To perform the test, a bore hole adjacent to and slightly deeper than the shaft must be drilled. Then, the exposed structure is struck with a hammer close to the foundation to generate stress wave energy, some of which travels down the shaft and through the soil where the compression wave passage is monitored by a hydrophone in an adjacent water-filled bore hole. The transit time of the stress wave is measured between the point of impact and the receiver for each probe location. The probe is initially located at the bottom of the borehole, and is raised a short distance after each hammer strike until the entire depth has been sensed. Examination of the first arrival time versus depth for a continuous shaft in a homogeneous soil should contain a linear increase in arrival time with depth. If a defect is encountered, the travel time will increase accordingly, indicating the depth of the defect. The same change will occur as the shaft toe is encountered, thus providing a measurement of the shaft depth. Currently, the parallel seismic method is the most popular technique used to evaluate foundations covered by a superstructure, although costly boreholes must be drilled and the exact location of the piles or drilled shafts must be known.

2.4.1 Testing Equipment

The equipment required for the parallel seismic test includes an impulse hammer (typically a 4 or 12 lb impulse hammer), a hydrophone receiver, and a portable computer with appropriate analytical software. The impulse hammer and the hydrophone receiver are connected to a data acquisition card installed in the computer. To signal the data acquisition cycle to begin upon impact, the hammer is outfitted with a trigger. Once impact is made the hydrophone receives the signal and it is recorded by the computer where it can be viewed and stored in the field. The portable computer and data acquisition card used in this study was described in SECTION 2.3.1.1. The parallel seismic amplifier unit was custom built by STS Consultants and is used to adjust the strength of the received hydrophone signal. For this study, a 4 pound sledge hammer with an impact trigger switch was used. The hydrophone receiver probe is capable of withstanding hydrostatic pressures greater than 2.96 kPa/ft (0.43 psi/ft) of depth. For a 30.5 m (100 ft) core hole, the pressures can exceed 296 kPa (43 psi). The analytical software used to acquire and process the data for this study was developed by STS Consultants.

2.4.2 Conventional Testing Procedure

The test procedure first involves the installation of an access hole. The access hole is constructed near the foundation element in question at a distance typically within 2 m (6.5 ft) and is drilled deeper than the suspected depth of the foundation element in question. To determine the appropriate depth for the access hole for cases of unknown foundations, a static analysis may be performed to estimate the suspected depth of foundation and the hole could then be constructed to a depth 3 m (10 ft) greater than estimated. Once the hole is drilled, a closed end tube (either steel or PVC) is placed to the bottom of the hole. Typically a 50 mm (2 in.) or larger inside diameter tube is utilized. The tube is filled with water to provide a coupling medium through which the compression wave can travel. It is critical that the access hole be drilled plumb. The void between the casing and the soil should be properly grouted to obtain acoustic coupling between the water filled tube and the surrounding natural soil. Grouting should be conducted in accordance with ASTM D 4428/D 4428M

standard for cross hole seismic testing.

Once the access hole is properly installed, testing may begin. A typical testing arrangement is shown in FIGURE 2.15. The first step in testing is to properly set up the computer and attach the hydrophone to the signal processor which in turn is connected to the computer. The receiver probe is then lowered to the bottom of the hole and the test is begun by striking the structure with the impulse hammer. Upon impact, the impulse hammer triggers the data acquisition cycle to begin.

Once received, the stress wave signal is recorded and displayed on the computer monitor. At this point the gain control is set to best identify the first arrival. The option of adjusting the gain control is available for each signal acquired, but since relative strength gain is a useful test parameter, it is not advisable to alter the gain control setting once a test profile has begun. The operator then has a choice of accepting the data, rejecting the data and re-striking the shaft for new data, or adding a signal to the data set for that depth increment. Adding signals from a particular depth increment amplifies the first arrival and cancels out some of the random noise in the signal. Once the signal is accepted, the probe is raised the predetermined depth interval and the test is repeated. These steps are repeated until a profile of signals is acquired for the entire depth of the access hole.

Vertical impacts are best for generating compression waves. Horizontal impacts may also be imparted to generate flexural waves if one is using an array of geophones in the access hole, rather than a hydrophone. A second opposing horizontal impact may be imparted to reverse the polarity of the shear wave to enhance its identification Olson (1995).

Testing has also been conducted in other ways. Open hole parallel seismic testing has been conducted, but requires the use of mechanical clamping geophones. There also is a risk of losing the geophone should collapse of the hole occur. The clamped three component geophone has also been used with some success. Olson (1995), utilized the three component geophone in an attempt to better examine the wave propagation behavior with reduced tube wave energy noise. Where the geophone is used, the casing should be dry when conducting the test. In fully saturated conditions below the water table, the use of geophones and grouting is not as critical. A number of tests have been performed by Olson (1995) with a hydrophone receiver in slotted plastic casing and no grouting. This method was effective since the water acts as a coupling agent for the compression waves through the soil to the hydrophone receiver in the water-filled borehole and casing. In partially saturated soils, Olson (1995) reported the practice of pouring loose sand to fill the void between the soil and the casing.

For parallel seismic testing, a high energy, short duration impact is required to generate a clean wave pulse that is easily identified when detected by the receiver. For cases where the impact point is some distance from the head of the foundation, or a very deep foundation is suspected, high energy is required. Thus, a steel sledge hammer is utilized to generate the necessary energy in the right frequency range. For relatively shallow depth tests, where the impact can be delivered directly onto a pile cap or grade beam, an aluminum tipped hammer can be used, similar to the PCB hammer described in SECTION 2.3.1.1. The parallel seismic test system is triggered by a piezoceramic impact switch that can be easily attached to the shaft of an ordinary steel sledge hammer. For the parallel seismic test, the hammer energy is used only as a trigger and is not actually measured (Hertlein, 1995).

2.4.3 Data Interpretation

The standard method of interpretation of data from the parallel seismic test is fairly straight forward. The tests conducted result in a compiled profile of signals for the various shots taken at each depth increment. A compiled profile from the NGES test section at Northwestern University is shown in FIGURE 2.16. From this compiled profile, the linear increase in arrival times with depth may be easily distinguished. Where the receiver probe passes below the bottom of the shaft or a defect in the shaft is encountered, a change in the slope of the arrival time with depth line will occur. As shown in FIGURE 2.16, the compiled profile indicates that the toe of the shaft is at a depth of approximately 13.5 m (44.3 ft). Often the data is not clear due to noise, and it may be necessary to analyze each signal separately to determine the time of first arrival and plot depth versus time of first arrival. The same general principles will apply whereby a change in the linear increase in arrival times with depth will indicate a change in the medium through which the stress wave is traveling. The slope of the depth versus first arrival line provides an estimate of the wave speed of the pile material where the receiver probe is adjacent to the pile.

2.4.4 Limitations of the Parallel Seismic Method

A major disadvantage of the parallel seismic test is the cost of coring and installing the access hole needed for the hydrophone. Another disadvantage is determining the type of defect encountered when a slope change of arrival time occurs. It is only known that the arrival time increases as a result of a lower propagation velocity, which could be caused by several factors including changes in concrete quality, cracks, and soil inclusions.

By employing the general method of data analysis described above and considering only the plot of depth versus first arrivals, the method is limited to cases where the soil profile is fairly consistent. Where there is a substantial change in the soil profile, there may be an associated increase or decrease in the wave speed of the soil through which the stress wave is traveling and the result of plotting depth versus first arrivals may be inconclusive in determining the depth of the foundation element and/or the location of defects in the shaft, especially if the borehole is not very close to the deep foundation.

The analytical software used for this study also puts limits on the analysis of parallel seismic data. The propagation velocity of concrete is typically about 4000 m/sec, therefore an impulse will pass through 1.0 m of concrete in about 0.25 milliseconds. For trigger and signal acquisition, the program requires about 0.26 milliseconds. This makes it impossible to capture the true arrival time of a signal traveling less than about one meter. Since the propagation velocity of concrete can vary significantly, parallel seismic data from depths of less than about 1.5 m (5 ft) should be used with caution. In practice this limitation is rarely a factor since the upper 2 m (6 ft) of soil around the parallel seismic access tube is usually loosened or disturbed to such an extent that the signal from the foundation is too attenuated to be detected (Hertlein, 1995).

2.5 Summary

Two types of low-strain, non-destructive testing methods for deep foundation integrity testing have been presented, surface reflection techniques (sonic echo and impulse response) and direct transmission methods (parallel seismic). A basic description of the stress wave principles underlying

the theory of the methods was presented. The testing procedures for each method were described, the conventional data interpretation methods were presented, and the limitations of each method were summarized. The surface reflection techniques are simple and quick to perform and are lower in cost relative to the parallel seismic method.

Table of Contents

Chapter 3. National Geotechnical Experimentation Site

- 3.1 Introduction
- 3.2 Subsurface conditions
  - 3.2.1 Cone penetrometer tests
  - 3.2.2 Soil wave propagation velocities
- 3.3 Drilled shaft test section
  - 3.3.1 Overview
  - 3.3.2 Construction details
- 3.4 Summary

To provide an opportunity to analyze the results of non-destructive testing methods in a controlled environment, a test section was constructed at the National Geotechnical Experimentation Site (NGES) at Northwestern University. Extensive field and laboratory testing have been conducted to determine subsurface conditions and geotechnical parameters for the various soil strata.

The National Geotechnical Experimentation Site (NGES) at Northwestern University is located in Evanston, Illinois on the northeast corner of campus adjacent to Lake Michigan on 1.5 acres of reclaimed land. This site was selected by the National Science Foundation (NSF) and the Federal Highway Administration (FHWA) as a National Geotechnical Experimentation Site in 1992. The purpose of these sites is to allow full scale field experimentation at locations where the subsurface conditions have been well characterized.

To date, three full scale test sections have been constructed at the site: a test section to evaluate axial capacity of four types of deep foundation elements, a drilled shaft test section for non-destructive evaluation of deep foundations, and a pressure-grouted micropile test section. The locations of these three test sections are shown in FIGURE 3.1 which is a map of the NGES at Northwestern. Also shown on the map are the locations of all site characterization bore holes. Utility lines are clearly marked on the map and electrical outlets and a hydrant for water hookup are available at the site.

The axial capacity test section was constructed in conjunction with the 1989 Foundation Engineering Congress held at Northwestern. For this event, a priori predictions of the axial capacity and load transfer characteristics of four types of deep foundations, both driven steel piles and cast-in-place concrete drilled shafts, were compared to a series of pile load tests conducted over a 43-week period (ASCE, R.J. Finno, ed. 1989).

A drilled shaft test section was constructed in fall of 1994 to provide a controlled, full scale site where different non-destructive evaluation (NDE) methods could be conducted to evaluate their ability to determine the integrity of inaccessible deep foundations. A complete description of this test section is found in SECTION 3.3.

To evaluate constructability and axial load behavior of multiple expanded tip micropiles, a test section was constructed in the fall of 1996. The work was done in recognition of the need to develop techniques to construct non-traditional deep foundation elements under restricted access conditions to allow in-place rehabilitation of structures while maintaining functional capabilities. In cooperation with GEOBASE, Inc., four reaction piles and seven test piles were installed using various grout mix designs. The piles were tested in compression and extension to evaluate the axial load behavior. After load testing, each micropile was excavated and visually inspected.

3.2 Subsurface Conditions

The stratigraphy at the test section location and a typical piezocone result are shown in FIGURE 3.2. With increasing depth from the ground surface, the soils consist of 0.6 m (2 ft) of topsoil, 8.2 m (27 ft) of hydraulically-placed fine grained sand fill, 12.5 m (41 ft) of soft to medium clay, and 6.1 m (20 ft) of hard silt and clay (glacial till) with trace gravel. Beneath the silt, Niagaran dolomite bedrock is encountered. The water table is approximately 4 m (12 ft) below ground surface and fluctuates with the water level of adjacent Lake Michigan.

Comprehensive laboratory and field testing has been conducted to characterize the geotechnical properties of the various soil strata at the site. The site was first extensively characterized in 1988 and 1989 as part of the pile prediction symposium. Laboratory investigations include index property tests, standard oedometer tests, direct shear tests, and triaxial tests. Field investigations include soil borings with SPT, field vane (FV), cone penetrometer tests (CPT), Menard pressuremeter tests (PMT), and dilatometer tests (DMT). Details of the in situ and laboratory site characterization tests performed were presented by Finno (1989) and also can be found on the NGES data base located on the internet at the web site address: http://www.unh.edu/nges/.

More recently, field testing in the vicinity of the NDE test section comprised of two soil borings with SPT, cross-hole seismic testing and nine cone penetrometer tests (CPT& PCPT). A plan showing the location of the borings and soundings relative to the NDE test section is given in FIGURE 3.1. Two soil borings, B-2 and B-3, were conducted on May 5, 1993 and December 9, 1994 respectively. Soil boring B-2 was drilled with nearly continuous sampling SPT in the sand and the glacial till, and 76 mm (3 in.)-diameter tube samples in the clay. Soil boring B-3 was drilled with nearly continuous sampling SPT in the sand and the glacial till and alternating 76 and 127 mm (3 and 5 in.)-diameter tube samples in the clay. The 127 mm (5 in.)-diameter tube samples were retrieved using an Osterberg piston sampler. A summary of all the field investigations conducted at the Northwestern NGES are presented in TABLE 3.1.

From the field and laboratory investigations conducted to date at the site, basic geotechnical characteristics for the stratigraphic data are presented in FIGURE 3.3. The sand at the site is a fill that was placed in 1966 by Northwestern University to expand its facilities. In general, the sand is fine-grained and medium dense to dense with SPT blow counts ranging from 5 to 35. The cohesive soils at the site consist of soft to medium clays of low plasticity (CL) overlying hard, glacially-

deposited silt and clay. The water content of the soft clay is several percentage points above the plastic limits indicating the soil has been overconsolidated. Results of the consolidation tests indicate that the softer clays are normally to slightly overconsolidated under the present vertical effective stresses. The variation of the clay's undrained shear strength with depth is also presented in FIGURE 3.3.

3.2.1 Cone Penetrometer Tests

Cone penetrometer (CPT) and piezo-cone penetrometer (PCPT) tests were performed by the Louisiana Transportation Research Center at Louisiana State University (LTRC/LSU) in August 1996 at the Northwestern NGES. Nine CPT/PCPT tests were performed at the site. The location of each test is indicated on FIGURE 3.1 by the labels CPT1 to CPT9. Both a friction cone and a dual-piezocone penetrometer were used for the testing. A friction cone penetrometer was used in the upper unsaturated sand fill and a dual-piezocone penetrometer was used below the water table. The friction cone penetrometer, developed by Fugro-McClelland Engineers B.V., The Netherlands, has a cross-sectional area of 15 cm^2, friction sleeve area of 200 cm^2 and 60 degrees cone apex. The dual-piezocone penetrometer is similar to the friction cone; however, it is capable of measuring pore pressures at the cone tip (mid face) and behind the friction sleeve. The tests were performed using a standard penetration rate of 2 cm/sec.

The penetration data from hole CPT7 is presented in FIGURE 3.2. The figure shows the tip resistance, sleeve friction, friction ratio and tip and sleeve pore pressures plotted versus depth. The tip resistance profile is indicative of a sand overlying a clay, with the transition occurring around 8.8 m. Tip and sleeve pore pressures are significant in the clay layer. A second transition occurs around 21.7 m, indicating a hard clayey-silty material by the increased tip resistance and high tip pore pressures. The other eight CPT soundings had similar profiles confirming a relatively uniform soil stratigraphy in the tested area. In addition to the penetration tests, pore water dissipation data was collected during two of the tests at 3.05 m (10 ft) intervals in the soft clay and two depths in the hard till. Dissipation tests for hole CPT1 were conducted at depths of 12.12 m, 15.22 m, and 18.68 m and for hole CPT9 at depths 12.22 m, 15.24 m, 18.38 m, 21.56 m and 22.64 m.

3.2.2 Soil Wave Propagation Velocities

Cross-hole seismic tests were performed by STS Consultants Ltd. in December, 1994 to measure the velocity of compressive (P) and shear (S) waves through the various soil strata. An EG&G E 1225 Exploration Seismograph, with 12 digital data acquisition channels was used to acquire the data.

To conduct the test, two boreholes were predrilled to 27.4 m (90 ft) and cased with 10.2 cm (4 in.) diameter PVC pipe to accommodate the receiver probes. A third borehole was advanced at the time of testing to provide access for the wave source. All three holes were in line and equidistantly spaced at 4.6 m (15 ft). with the source hole at one end of the line. The alignment of the holes can be seen in FIGURE 3.4 which shows the plan of the NDE test section. The two receiver probes were placed in holes CHS2 and CHS3 and the impact source was created in hole CHS1.

To run the test, the 3-D velocity transducers, were placed in the predrilled boreholes at a desired depth. The source borehole was drilled to about a foot above the same depth and then a split-barrel sampler was driven by hammer blows to the same level as the receivers. The drill rod was then

struck with a hammer equipped with a trigger device to initiate the test. The seismic waves radiated through the surrounding soils from the tip of the split-barrel sampler to the receiving probes and were recorded on the seismograph.

Tests were conducted at interval depths of 1.52 m (5 ft) in the sand fill, 3.05 m (10 ft) in the soft clay, and 1.52 m (5 ft) in the hard till. The velocities for the different waves at each testing depth were calculated from the measured transit time and known distance between the source and the receivers. FIGURE 3.5 illustrates the variation of the compression (P) wave and shear (S) wave velocity with depth. The test results indicated a variable velocity profile. The shear and compressive wave velocities are the lowest in the sand fill with average values of 180 m/s and 1500 m/s, respectively. In the soft clay, the shear wave velocity averaged 220 m/s and the compression wave velocity about 2000 m/s. An increase in the shear wave velocity to 400 m/s was observed in the deepest portion of the clay layer, most likely reflecting the presence of a stiffer, gravelly layer. The largest values were observed in the hard till layer where the shear wave velocities varied from 300 to 500 m/s and compressive wave velocities ranged from 2000 to 2500 m/s. Note that shear and compression wave velocities were not obtained for the tests performed at 1.52 m (5 ft) and 3.05 m (10 ft) depths. Also, the compression wave was not identifiable at a depth of 6.1 m (20 ft). This was in part due to inadequate grouting of the PVC tubing in the upper surficial sand layer.

The results and interpretation of non-destructive evaluation of deep foundations are affected by the shear and the compression wave velocities of the soil. For example, the travel time measured for an impact during a parallel seismic test is a function of the propagation velocity in concrete as well as the compression wave speed in the adjacent soil. In an impulse response test, the variation of the shear wave velocity has a substantial effect on the resolution (P/Q) of the mobility plot. These effects will be discussed in detail in CHAPTER 6.

3.3 Drilled Shaft Test Section

3.3.1 Overview

A test section consisting of five drilled shafts in three groups was constructed at the National Geotechnical Experimentation Site at Northwestern University to provide a controlled site where various non-destructive testing techniques could be performed to evaluate their applicability for determining the integrity of inaccessible deep foundations. As illustrated by the plan view shown in FIGURE 3.4, the test section consists of five drilled shafts with lengths of 12.19, 21.33 and 27.43 m (40, 70 and 90 ft) and diameters of 61.0, 76.2 and 91.4 cm (2, 2.5 and 3 ft). A profile view of the site is presented in FIGURE 3.6. The main variables considered in the test section are the shaft length to shaft diameter (L/D) ratio, the pile cap height to shaft diameter (B/D) ratio, and the soil condition at the shaft toe including soft clay, hard silt or dolomite bedrock. Two of the shafts were constructed purposely with defects: a reduced cross-section and a thin, soil-filled joint. The former defect represents a typical construction deficiency while the latter represents a performance-related defect induced by excessive lateral loads. Details of the test section are summarized in TABLE 3.2.

After the drilled shafts were constructed, reinforced concrete caps were cast to form 3 groups of shafts. Two groups of two shafts are connected with pile caps and one single shaft was also constructed with a cap. Pile cap 1 was constructed atop shafts 1 and 2, pile cap 2 above shaft 3, and pile cap 3 above shafts 4 and 5. The dimensions (length x width x height) of the pile caps are 4.11 x

1.52 x 0.61 m (13.5 x 5 x 2 ft), 1.52 x 1.52 x 1.52 m (5 x 5 x 5 ft), and 4.11 x 2.13 x 0.91 m (13.5 x 7 x 3 ft), respectively. The drilled shafts were constructed by Case Foundation in August of 1994 and the pile caps were constructed by DeGraf Concrete Construction in October of 1994.

The shafts were appropriately instrumented to conduct various non-destructive tests. Access tubes for sonic logging were placed in two of the shafts, and five cased boreholes were installed so that parallel seismic tests could be conducted. Each shaft had a geophone embedded near its bottom to directly measure the longitudinal wave speed. Sixty cylinders were made from the concrete as it was placed to determine the strength and longitudinal wave speed variations over time.

After the five shafts were constructed, a period of six weeks was used to non-destructively evaluate the shafts using the impulse response, sonic echo and sonic logging methods. Thereafter the reinforced concrete caps were poured and these tests were again conducted from the tops of the pile caps. Parallel seismic tests were also conducted at that time.

3.3.2 Construction Details

Case Foundation Company constructed the drilled shafts. Mobilization began at the NGES site on August 29, 1994 when a Manitowoc crane was assembled at the site. The location to construct the test section was selected in a relatively level area at the NGES site close to boring B-2 made in May 1993. The site was mapped out noting the locations of water lines, electric lines, manholes, and sewer lines. Before drilling began, a trench was dug approximately 0.91 m (3 ft) down from grade in a T-shape with a front end loader.

Care was taken to construct the shafts with uniform cross-sections. To accomplish this, construction began by drilling through the sand fill layer under a slurry head, placing an oversized casing for temporary support into the underlying clay, removing the slurry and drilling the remainder of the hole in the dry with earth augers. After a permanent liner was placed through the sand layer and driven a few feet into the clay layer, a reinforcing cage was set to the bottom of the drilled hole and the concrete was placed by the free-fall method. The concrete was then let to cure at least 1 day after which the 15.24 cm (6 in.) annulus between the corrugated liner and temporary casing was backfilled with sand, placed by free-fall, as the temporary casing was pulled. The shaft dimensions, as-built depths, and drilling procedures were carefully noted.

The reinforcing steel cages were constructed with nominal steel to allow for attachment of instrumentation including PVC tubing, embedded geophones and the wires, and sand bag defects. Reinforcement for each shaft consisted of four No. 7 vertical bars with No. 5 spiral ties at 61.0 cm (24 in.) spacing. Note for shaft 2, the spacing of the spiral ties was 30.5 cm (12 in.) in the area of the defect to allow for adequate attachment of the sand bags to the cage.

After each shaft was poured, the concrete surface was leveled with a trowel to create a smooth, flat surface. This minimized the surface preparation by mechanical grinding often necessary for performing integrity testing which requires a level, smooth surface for transducer coupling and hammer impact locations.

3.3.2.1 Drilled Shafts

Shaft 1

As shown in FIGURE 3.7, shaft 1 was constructed 12.2 m (40.0 ft) long and 61 cm (2 ft) in diameter and included a soil-filled joint built into the shaft. Note that all dimensions shown in FIGURES 3.7, 3.8, 3.9, 3.10, 3.11, 3.12, 3.13, 3.14, 3.15, and 3.16 are as-built dimensions. The shaft was drilled on September 1, 1994 and 7.8 m (25.7 ft) of concrete was placed the same day, such that the shaft was filled to a depth of 4.4 m (14.3 ft). To construct a joint within the shaft, pieces of soft clay, 5 to 10 cm (2 to 4 in.) in size, were dropped into the shaft to form a 10 cm (4 in.) soil layer. Sand was also poured into the shaft to fill in the gaps between the clay pieces. Subsequent concrete placement the next day resulted in a mixture of soil and concrete which simulates a break in the shaft caused by excessive lateral loading whereby soil is introduced into the cracked portion of concrete. Three access tubes were placed along the length of the reinforcing cage for sonic logging testing. Concrete was poured from three trucks and twelve 15.24-cm-diameter by 30.48-cm-long (6-in. by 12-in.) concrete cylinders were cast, four from each truck. Note that the depths of the corrugated permanent liner, temporary casing, embedded geophone and shaft toe were all carefully observed during the construction.

Shaft 2

As indicated in FIGURE 3.8, shaft 2 was constructed 21.33 m (70 ft) in length and 91.44 cm (3 ft) in diameter. The shaft was drilled and the concrete was placed on September 2, 1994. Three 3.81 cm (1.5 in.) diameter PVC access tubes were placed along the length of the reinforcing cage for sonic logging testing. Concrete was poured from three trucks and twelve 15.24-cm-diameter by 30.48-cm-long (6-in. by 12-in.) concrete cylinders were cast, four from each truck.

A reduced cross section, or neck, was built into the shaft to simulate a typical construction deficiency caused by a side cave-in or squeeze-in, as can occur if an insufficient concrete head is maintained in a temporary casing as it is being extracted. This reduced cross section area was built into shaft 2 by tying sandbags to the reinforcing cage at depths between 3.76 and 4.47 m (12.33 and 14.67 ft), resulting in a defect length of 0.71 m (2.33 ft). The sand bags were made using Poly-Tarp heavy duty polyethylene plastic. The tarp was cut into 91.4 cm by 30.5 cm (3 ft by 1 ft) sections and two sections were sewn together around the perimeter. A 15.2 cm (6 in.) opening remained for filling the bags with sand. The sand bags were placed around the outside of the reinforcing cage and attached with 6.35 mm (0.25 in.) nylon rope and contractors duct tape. Bags were also placed on the inside of the cage creating a 25% reduction in cross-sectional area. As the cage was lifted to be placed into the hole, the bags shifted in position and sand leaked from at least one of the bags. The sand bulged in the bottom of the bags slightly changing the dimensions of the defect from that measured while the cage was lying on the ground.

Shaft 3

Shaft 3 was drilled on August 31, 1994. It was the second shaft drilled. The slurry was made with soft clay removed from the first hole drilled, thus a denser mix was made to adequately support the walls of the hole allowing for drilling of a more uniform shaft. As shown in FIGURE 3.9, the shaft is 12.2 m (40 ft) long, 61.0 cm (2 ft) in diameter, and the upper 10.5 m (33.75 ft) is cased with a permanent corrugated liner. An inclinometer casing was cast in the full length of the shaft for measurements of lateral deflection induced by a lateral load test to be conducted as part of future

work. Concrete was poured from one truck and twelve 15.24-cm-diameter by 30.48-cm-long (6-in. by 12-in.) cylinders were made.

Shaft 4

Shaft 4 was drilled to 32 feet on August 30, 1994 and completed to 21.33 m (70 ft) on August 31, 1994. Chatter in the rod was noted at 5.5 m (18 ft) and 8.5 m (28 ft) indicating hard drilling conditions. Since shaft 4 was the first shaft drilled, soft clay was not available to make an adequate slurry. Thus, bentonite was added to water to provide the slurry. As illustrated in FIGURE 3.10, the shaft was constructed 21.33 m (70 ft) long and 76.2 cm (2.5 ft) in diameter and the upper 10.67 m (35 ft) is permanently cased with a corrugated liner. Concrete was poured from two trucks and twelve 15.4-cm-diameter by 30.48-cm-long (6-in. by 12-in.) concrete cylinders were cast, six from each truck.

Shaft 5

Details of shaft 5 showing all shaft dimensions and liner and casing depths are shown in FIGURE 3.11. Shaft 5 is 27.49 m (90.2 ft) in length, 91.44 cm (3 ft) in diameter and is lined with a corrugated liner in the uppermost 11.81 m (38.75 ft). Drilling for Shaft 5 began August 31, 1994 and was completed September 1, 1994. During drilling, the drill rod walked substantially in the sand and had to be re-centered, thus creating a large diameter at the top of the hole. A good slurry was made with soft clay. The temporary liner was not long enough to sufficiently extend into the soft clay layer. The hole was advanced until hard drilling conditions were encountered at 27.5 m (90.2 ft) from grade, suggesting the soil/rock interface had been reached. Concrete was poured from four trucks and twelve 15.24-cm-diameter by 30.48-cm-long (6-in. by 12-in.) concrete cylinders were cast, four from each of the first three trucks. The fourth truck supplied only 1.5 yds of concrete for the top of the shaft.

Permanent Liners

To minimize unplanned defects, the shafts were cased with permanent steel liners through the sand layer. This eliminated the formation of enlarged cross-sections in the upper portion of the shafts which may occur as a result of overbreaks in the surficial sand layer caused by overdrilling, implied from the chatter in the drill rod, and collapse of the drilled hole from insufficient slurry pressure. The permanent liners are corrugated, thus the outer diameters are 2.54 cm (1 in.) larger than the inner diameters of 61.0, 76.2, and 91.4 cm (2, 2.5 and 3 ft) due to the corrugation. The permanent liners are gauge 16 and accordingly have a thickness of 1.588 mm (0.0625 in.). The length of the liners varies from 9.6 m to 11.81 m (31.5 to 38.75 ft). A summary of the dimensions of the temporary casings and permanent liners used during the construction of each shaft are presented in TABLE 3.3. The temporary casings were 31.5 cm (1 ft) larger in diameter than the permanent liners and for most cases were similar in lengths. The exception was the temporary casing for shaft 5 which was 3 m shorter than the permanent liner. Also, the permanent corrugated liners are drawn and dimensioned in the schematics for each shaft shown in FIGURES 3.7, 3.8, 3.9, 3.10, and 3.11.

3.3.2.2 Instrumentation

The shafts were instrumented to perform impulse response, sonic echo, sonic logging and parallel seismic tests. Each shaft has a geophone embedded near the bottom of the shaft to directly measure the one-way travel time of longitudinal stress waves. Three access tubes for sonic logging were placed in shafts 1 and 2. Five cased boreholes for parallel seismic testing were placed near the shafts. One inclinometer casing was included in shaft 3 to analyze a lateral load test to be performed as a part of future research.

Access Tubing

Three access tubes were placed along the length of each reinforcing cage in shafts 1 and 2 for sonic logging testing. The access tubes were schedule 80 PVC, 3.81 cm (1.5 inch) inner diameter cut in 3.05 m (10 ft) long segments. First, three 3.05 m (10 ft) sections of PVC pipe with sealed capped ends were attached loosely with wire to the bottom portion of the reinforcing cage spaced approximately at 120° intervals around the perimeter. The ends of the PVC pipe were capped and sealed using a generous application of PVC solvent cement and several layers of contractors duct tape.

The distance from the end of the reinforcing cage to each of the three capped ends of PVC pipe was measured while the cage was lying on the ground to determine the depth of the bottom of the PVC tubes in the concrete shaft. Once the tubing was attached to the bottom of the cage, the cage was lifted off the ground into the air and lowered into the drilled hole. While the cage was lifted, the reinforcing cage twisted and the PVC pipe shifted position. As the cage was lowered into the hole, additional length of PVC pipe were spliced onto the in-place sections in 3.05 m (10 ft) increments. At each increment, the connections were made using a coupling PVC section, generous application of PVC cement, and layers of contractors duct tape. The PVC tubes were filled with cold water before the concrete was placed to prevent the tubes from "floating" in the wet concrete. Even though extreme care was taken to seal the ends and connections of the PVC access tubing segments, two of the access tubes in shaft 2, 2W and 2S, were unable to hold water after several days, indicating a slow leak probably caused by a broken seal or puncture somewhere on the length of the PVC tubing, presumably near the bottom.

For analysis of sonic logging data, it is necessary to know the depths of the probes and the spacing between the probes within the access tubing. Each length of PVC access tubing is given in TABLE 3.4. The lengths are measured from the top of the pile cap to the bottom of the PVC tubing. The spacing between each tube is a measure of the length the ultrasonic wave travels from the source probe to the receiver probe. TABLE 3.5 contains the measured spacing data between each of the access tubes. Note that the spacing between each of the tubes was measured center to center and was assumed to be constant with depth in the shaft. However, twisting of the PVC tubing was observed during construction as the reinforcing cage was placed in the drilled hole.

Embedded Geophones

A geophone was tied to the lower end of each reinforcing cage and, subsequently, was embedded near the bottom of each shaft to measure the one-way travel time of the longitudinal compression wave. The geophones were housed in a sealed 15.24 cm (6 in.) diameter metal casing and attached to the reinforcing cage with wire and contractors duct tape. The distance of each geophone from the bottom of the reinforcing cage was measured. The wires from the geophones were taped along the

length of the reinforcing cage to be accessed at the surface of the shafts. Immediately after the shafts were poured, the geophone wires were placed into a capped 30.5 cm (1 ft) long 5.08 cm (2 in.) diameter PVC pipe protruding from the concrete surface to house the wires. The final depths of each geophone are noted in the as-built schematics for shafts 1 to 5, FIGURES 3.7, 3.8, 3.9, 3.10, and 3.11, respectively.

Cased Boreholes for Parallel Seismic

Five cased boreholes for parallel seismic testing were included in the test site. The location of the cased boreholes are shown in FIGURE 3.4. Three of the holes, PS1, PS2 and PS5, were initially used to conduct the cross-hole seismic tests to evaluate the compression and shear wave velocities of the soil at the site. Details of the boreholes are presented in Table 3.6. Boreholes PS2 and PS5, used for the receiving probes during cross-hole seismic testing, were drilled 12.7 cm (5 in.) in diameter and were cased with 10.16 cm (4 in.) diameter PVC. Boreholes PS1, PS3 and PS4 were drilled 7.6 cm (3 in.) in diameter and are cased with 5.08 cm (2 in.) diameter PVC. The depths of the boreholes ranged from 22.41 to 28.84 m (73.54 to 94.63 ft).

The boreholes were drilled under slurry head through the sand fill layer. An oversized casing was placed through the sand layer for temporary support, and the slurry was removed so that the remainder of the hole could be drilled in the dry. The PVC casings were placed in the holes and the annular space between the hole wall and casing was filled with grout. The temporary casing was pulled after the grout was placed in the hole. Note that cross-hole seismic and parallel seismic results indicated that grouting of the casing in the surficial sand fill layer was inadequate. This was suggested by a lack of received signal by the hydrophones at shallow depths within the sand layer.

Inclinometer Casing

To analyze a lateral load test to be performed as a part of future research, one inclinometer casing was included in shaft 3. The flush casing, manufactured by Slope Indicator Company, was 69.85 mm (2.75 in.) OD (outer diameter) and 12.89 m (42.3 ft) in length (full length of drilled shaft and pile cap). The casing was capped at the bottom end and filled with water prior to placing the concrete.

3.3.2.3 Pile Caps

Three reinforced concrete pile caps were constructed on October 27, 1994 by DeGraf Concrete Construction, Inc., to form three groups of shafts. Two groups of two shafts are connected with pile caps and one single shaft was also constructed with a cap. TABLE 3.7 lists the dimensions of the three pile caps and indicates which shafts are grouped together.

Before the pile caps were constructed, all PVC pipe extending from the top of each shaft was raised so they would be flush with the surface of the top of the cap. Flush mount PVC caps were installed to access the full-length PVC tubing for sonic logging on shafts 1 and 2 and the geophone wires housed in PVC pipes in all the shafts.

To ensure a level, smooth pile cap bottom surface, a hand compactor was used to compact the sand fill around the exposed shaft heads. While the formwork was placed, careful measurements were

taken to center the shaft heads within the pile caps. The pile caps were reinforced with 1 layer of #6 reinforcing bars spaced 30.48 cm (12 in.) on center each way at the top and bottom of each cap. The concrete, supplied from three mixing trucks, was poured and a concrete vibrator was used to evenly distribute the concrete within the formwork. Thirteen 15.24-cm-diameter by 30.48-cm-long (6-in. by 12-in.) concrete cylinders were made from samples taken from the three trucks. To produce a smooth, even surface and rounded edge, the top of each concrete cap was troweled. After the concrete cured for one day, the formwork was removed and the space between the concrete cap and soil trench wall was backfilled with sand.

Upon completion of the pile cap construction, the heads of the five drilled shafts were no longer accessible for non-destructive testing. Thus, all future testing programs would be carried out from atop the pile caps. Schematics for the drilled shafts with the pile caps are shown in FIGURES 3.12, 3.13, 3.14, 3.15, and 3.16.

3.3.2.4 Concrete Specifications

Concrete was used to construct the drilled shafts and the pile caps. The concrete was specified to be a ready-mix concrete with 21 MPa (3000 psi) strength, 76 to 127 mm (3 to 5 in.) slump and a fly ash to water ratio (FAWR) of 4.25.

All concrete for the drilled shafts was placed by the free-fall method and mechanical vibration was not employed. To avoid segregation during placement, concrete was prevented from striking the reinforcing cage by directing the concrete down the center of the hole by a drop-chute section hung in reverse from the concrete truck trough. The concrete for the pile caps was also placed using a drop-chute section. Mechanical vibration was used to evenly distribute the concrete within the formwork.

Samples were taken from each batch of concrete used to construct the test section. Sixty concrete cylinders were made from the concrete used for the drilled shafts and twelve cylinders were made from the concrete placed for the pile caps. Concrete was taken directly from the truck drop chute from the middle of each pour and the cylinders were cast at the site following the casting procedure outlined in ASTM standard C-31 (ASTM, 1987). After the concrete had set for at least 24 hours, the molds were removed and the cylinders were placed in a controlled, high humidity curing room.

To determine the strength and wave propagation velocity of the concrete cylinders, unconfined compression tests and ultrasonic pulse velocity (UPV) tests were performed. Sets of concrete cylinders were tested at 7, 14 and 28 days after casting. In addition, a final set of cylinders was tested a year and a half (564 to 566 days) after casting.

Concrete Compressive Strength Testing

The compressive strength of the concrete cylinders was determined in accordance to the method specified by ASTM C-39 (6x12) standards (ASTM, 1986). A Material Testing Service (MTS) 1000 kip servo-hydraulic testing machine was used to test the 15.24 cm-diameter by 30.48 cm-long (6 in. x 12 in.) concrete cylinders under compression. The length and diameter were measured for every cylinder. Each cylinder was also weighed to compute the density of the concrete. All of the tested cylinders were capped one day before testing using a sulfur mortar capping compound, CYCLAP, manufactured by DFC Ceramics. The tests were performed in stress control mode at a loading rate of

242 kPa/sec (35 psi/sec). Specimens were loaded until catastrophic failure of the concrete occurred.

For each concrete cylinder, the maximum load was recorded at failure and the compressive strength was calculated based on the measured cross-sectional area of the cylinder. Three cylinders from each shaft were tested 7, 14, and 28 days after the concrete was cast in the molds. In addition, a final set of cylinders, two from each shaft, was tested 565 days after casting to determine the long-term properties of the concrete. The cylinders made from the pile cap concrete were tested 26 and 509 days after casting. The results from the concrete cylinder testing program are plotted in FIGURE 3.17 showing compressive strength versus time. The compressive strengths varied an average of 300 kPa on a given testing day. It is important to note that while the 28 day strength is usually used to determine the properties of concrete, the concrete exhibits an increase in strength with time as shown by the increased strengths of the specimens tested 565 days after casting. For the concrete tested for the drilled shafts, the compressive strength increased 22 to 38% from 28 to 565 day strengths. The concrete cylinders for the pile caps increased in strength 49% over the same period.

Unconfined Compressive Strength Correlation to Propagation Velocity

A means to estimate the compression wave propagation velocity through concrete is by correlating the unconfined compression strength of concrete cylinders to the propagation velocity. One such correlation was suggested by Davis and Robertson (1975) and was used for this study to estimate the compression wave velocity in the concrete cylinders. This correlation of propagation velocity to compressive strength is reproduced in FIGURE 3.18. Using this correlation with compressive strength, a compression wave velocity for the concrete was estimated from the compressive strength of the cylinders. These unconfined compression tests were conducted at various times throughout the year; therefore, these results were used to evaluate the increase in the longitudinal wave speed in concrete with time. The propagation velocity for each compression test was estimated from the correlation presented in FIGURE 3.18 and the results are shown in FIGURE 3.19. The increase in strength of the cylinders tested 565 days after casting corresponds to a 2 to 3% (approximately 100 m/s) increase in propagation velocity over that measured at 28 days, according to the Davis and Robertson correlation. Therefore, the age of a deep foundation should be considered when estimating the concrete wave propagation velocity to ensure accurate determination of the depth of a reflection.

Ultrasonic Pulse Velocity Method

Before the cylinders were capped for compression testing, ultrasonic pulse velocity (UPV) tests were conducted on each of the 15.24 cm-diameter by 30.48 cm-long (6 in x 12 in.) cylinders to estimate the longitudinal wave velocity. A portable ultrasonic pulse velocity unit developed by James Electronics Inc. was used in this program. The pulser/receiver unit was used to measure the wave transmission time through the specimen according to the specifications of ASTM standard C-597 (ASTM, 1990). Prior to conducting the tests, the timing unit was calibrated with a standard rod. The frequency of the source wave was 54 kHz. Once the emitter and receiver were attached to each end of the cylinder, the transmission time between the emitter and the receiver was displayed digitally in µsec on the unit. Rycon grease was used to couple the emitter and receiver to the specimen. Tests were performed both 14 and 28 days after the casting date for the cylinders made from the concrete for the drilled shafts and at 26 days for the cylinders from the pile cap concrete.

Results from the UPV tests are presented in FIGURE 3.19 along with the results computed from the

unconfined compression strength correlation. The wave speeds determined by this method are approximately 10% higher than those from the compressive strength correlation. This is due to the nature of the pulse velocity test. The frequency of the source wave was 54 Hz producing a source with a wavelength much smaller than the diameter of 15.24 cm (6 in.) for the concrete cylinder specimen. Therefore, the wave was traveling in an infinite medium instead of a long thin rod. As discussed in SECTION 2.2.2, compression waves traveling in long thin rods generally have wave speeds 5 to 15% less than those waves traveling in an infinite medium.

Concrete Density

Density was determined by weighing each cylinder and measuring the length and diameter to calculate the volume. The average density determined for the cylinders from the five shafts and pile caps is presented in TABLE 3.8. For the cylinders from the five shafts, the density had an average of 2405 kg/m^3 (150 pcf) and a standard deviation of 98 kg/m^3 (6.1 pcf). These results are consistent with a concrete density of 2400 kg/m^3 (150 pcf), typical for good quality concrete. Two observations are made about the variation of concrete density for each shaft. First, the cylinders cast from shaft 5 had an average density of 2238 kg/m^3, significantly lower than the average density of cylinders from the other shafts. As a result, the average density for all shafts is misleading. Thus, the average concrete density for shafts 1 to 4 was 2450 kg/m^3 which is higher than the total average density for all shafts. Second, the densities for cylinders from shafts 1 and 2 were more variable than the other shafts with standard deviations of 56 and 61 kg/m^3. Cylinders from shafts 1 and 2 also had the highest densities. Cylinders from the pile caps had an average density of 2390 kg/m^3.

3.4 Summary

This chapter summarized the site characterization conducted at the Northwestern University NGES and described the construction details of a test section built to evaluate non-destructive testing methods for deep foundations in a controlled environment. The soils at the location of the NDE test section site have been well characterized by laboratory and field investigations, including cross-hole seismic tests, nine CPT tests and two soil borings. Construction of the test section was controlled, and careful observations were made of the shaft dimensions, as-built depths and drilling procedures. The finished NDE test section consists of five drilled shafts with lengths varying from 12.19 to 27.43 m (40 to 90 ft) and diameters ranging from 61.0 to 91.4 cm (2 to 3 ft). The five shafts were arranged in three groups. The pile caps vary in thickness from 61.0 to 152.4 cm (2 to 5 ft). At this test section, one can conduct parallel seismic, sonic logging, sonic echo and impulse response tests on inaccessible drilled shafts. Before the pile caps were constructed, sonic logging, sonic echo and impulse response test were conducted on the five shafts such that both accessible and inaccessible shaft results have been obtained.

Table of Contents

Chapter 4. Evaluation of Impulse Response Tests at NGES

- 4.1 Introduction
- 4.2 Accessible-head tests
  - 4.2.1 Testing procedure
  - 4.2.2 Impulse Response / sonic echo results
  - 4.2.3 Summary of accessible-head tests
- 4.3 Inaccessible-head tests
  - 4.3.1 Testing procedure
  - 4.3.2 Sonic echo / impulse response results
  - 4.3.3 Summary of effects of intervening structure
- 4.4 Summary

4.1 Introduction

One of the most common techniques used to analyze the integrity of drilled shafts is the impulse response method. This method is a surface reflection technique which relies on the identification of compression wave reflections. The procedure involves impacting the top of a concrete shaft with a modal hammer and measuring both the impact force and the particle velocity on the impacted surface. The impulse response method was described in detail in SECTION 2.3.

This chapter presents impulse response and sonic echo results from tests performed at the NGES test site on five drilled shafts, both when the shaft heads were exposed, the accessible-head condition, and when the shaft heads were obscured by pile caps, the inaccessible-head condition. First, the accessible-head results are presented with a discussion of the ability to evaluate concrete integrity and identify defects for drilled shafts using the impulse response and sonic echo methods. Next, the inaccessible-head results are presented and compared to the accessible-head results. Finally, the effects of the pile caps on the concrete integrity determination are examined.

4.2 Accessible-Head Tests

4.2.1 Testing Procedure

Prior to construction of the pile caps, impulse response tests were performed on the shafts in the accessible-head condition. The equipment used for this testing program was presented in SECTION

2.3.1.1. Both force and velocity were measured with time and digitally stored for analysis. Tests were performed each day for seven days after the concrete was placed and then approximately 14, 28 and up to 56 days after construction. During this period before the pile caps were constructed, the effects of concrete age and couplant performance were investigated to determine the influence of each factor on the impulse response tests conventionally performed in the accessible-head condition. The results of the effects of these variables will be presented in SECTION 5.3.

For all the tests performed, the hammer strikes were located in the center of the shaft and the geophone was placed 7.6 cm (3 in.) from the edge of the shaft, inside the reinforcing cage. Each hammer and geophone location on the concrete shaft surface was smoothed with a hand-held mechanical grinder. Rycon couplant was used for all accessible-head tests, except for the study of couplant performance to be presented in SECTION 5.3.

The sonic echo and impulse response results presented herein for the five drilled shafts in the accessible-head condition were performed 28 days after the concrete was placed in each drilled shaft. At this time the concrete had reached its "28 day strength" to coincide with industry and laboratory testing standards for concrete. Hence, it was assumed that the material properties of the concrete had become constant. However, the compression tests performed on the concrete cylinders presented in SECTION 3.3.2.4 indicated that the strength of the concrete increased for at least 1.5 years after casting, resulting in an increase in correlated propagation velocity of 2 to 3% from 28 to 565 days (1.5 years).

4.2.2 Impulse Response / Sonic Echo Results

Analysis for the sonic echo method is completed in the time domain by examining the velocity-time trace. In contrast, the impulse response method uses the frequency spectrum of the force and velocity functions to produce a mobility curve for analysis. For each drilled shaft, both a time domain analysis (sonic echo) and a frequency domain analysis (impulse response) were performed. In the time domain, only the velocity-time trace was examined to identify reflections from the shaft toe or other reflector, such as a defect. For the frequency domain analysis, both the force- and velocity-time functions were used to produce the mobility curve for analysis. A fast fourier transform was performed on both the force and the velocity signals to convert them from the time to the frequency domain. Then, the velocity spectrum was divided by the force spectrum, and the resulting quantities were filtered by applying a lowpass Blackman window filter which smoothed fluctuations between 2 adjacent data points in the mobility plot which were spaced at intervals of 19.5 Hz.

For each shaft, the average mobility was determined by calculating the geometric mean of the maximum mobilities, P_i, and the minimum mobilities, Q_i. The average mobilities were then compared to the range of expected theoretical mobility values determined using equation 2.16, assuming a propagation velocity, v_c, range of 3500 to 4500 m/s (11484 to 14765 ft/s) and a concrete density, r_c, of 2400 kg/m^3. The ratio of P/Q was also calculated to determine the signal resolution. The low-strain stiffness, K', was determined according to EQUATION 2.17 from the low frequency portion of the each mobility curve to provide an indication of the load deflection response at low-strains. These values were compared to a theoretical range of stiffness values using EQUATION 2.18. This range was calculated using the diameter of each shaft and the P, Q, and v_c values determined from the experimental mobility curves.

As one might expect for shafts made under controlled conditions with L/D ratios less than 30, the impulse response results were quite clear for most cases. Reflections from the toe of each shaft were distinctly observed. In addition, the planned defects were clearly identifiable in the impulse response test results.

4.2.2.1 Shafts without Planned Defects

Shaft 3

Sonic echo and impulse response tests were performed at numerous times on shaft 3, at times up to 56 days after construction of the shaft. The testing schedule for all accessible-head tests performed on shaft 3 is located in APPENDIX A. As shown in the schematic of the constructed drilled shaft on FIGURE 3.9, the drilled shaft passes through the sand fill layer and is embedded into the soft clay layer. The shaft length is 12.19 m (40 ft) and its diameter is 0.61 m (2 ft); thus, the L/D ratio is 20.

The results of the impulse response tests performed on shaft 3, 28 days after concrete placement, are presented in detail to show the typical response for this shaft. The observed force and velocity time-traces for shaft 3 are shown in FIGURE 4.1A and 4.1B, respectively. The duration of the force impact was about 1 msec. As discussed in SECTION 2.2.4, this implies that significant frequencies up to 1000 Hz are contained in this impulse. The velocity trace is characterized by a quickly decaying peak velocity which was generated by the impact force. It is followed by two clearly defined reflections at 11.9 and 18.3 msec, which correspond to a Dt = 6.3 and Dt = 6.4 msec, respectively. A time-domain analysis of this signal indicates that these larger reflections originate from the toe of the shaft and using equation 2.30 with the as-built length of 12.19 m (40 ft), the propagation velocity is determined to be 3810 m/s (12500 ft/s).

Also shown on the figure are the fast fourier transforms (FFT) of the force and velocity data in FIGURE 4.1C and 4.1D, respectively. The force spectrum indicates that the hammer blow imparts significant frequencies below about 1000 Hz. This result implies that the mobility plot would provide significant data only below 1000 Hz, since the force would be small compared to the velocities above this frequency and thus the mobility would be spuriously affected by small variations in the force. The frequency domain of the velocity signal can be used to identify the resonant frequencies. The velocity spectrum shows regularly occurring resonant peaks below about 1200 Hz.

FIGURES 4.2 and 4.3 present the mobility plot for shaft 3. FIGURE 4.2 shows the mobility for frequencies below 2000 Hz, and FIGURE 4.3 shows a plot for frequencies below 1000 Hz. These plots were made by taking the fast fourier transform of the force and velocity time traces, and dividing the resulting velocity spectrum by the force spectrum. Consistent with the careful design and construction procedures for shaft 3, resonant peaks are clearly visible in the mobility plot up to 1300 Hz. However, the signal becomes distorted around 1000 Hz because the response at higher frequencies is dominated by the effects of surface wave reflections, the low magnitude of force at higher frequencies, and imperfect coupling between the geophone and the concrete surface. Thus, the mobility plots of the remaining shafts will only be presented for frequencies less than 1000 Hz, wherein significant energy is contained.

The information for the shaft toe is found at the lower frequencies, as shown on FIGURE 4.3. Discounting the first peak at about 50 Hz, as is typically done in an impulse response test, there are six clearly identifiable reflections below 1000 Hz. The first five reflections have about the same amplitude, and hence mobility. The average change in frequency between these five peaks is 156 Hz. For a shaft length of 12.19 m (40 ft), this corresponds to a velocity of 3810 m/s (12500 ft/s). The average mobility from these five peaks, as determined by the geometric mean of the minimum and maximum mobilities for each peak is 3.8×10^{-7} m/s/N. This mobility is within the theoretical range of 3.6 to 4.1×10^{-7} m/s/N for a 0.61 m (2 ft) diameter shaft made of good quality concrete.

The resolution of the mobility signal was determined by the ratio of the maximum mobility, P, to the minimum mobility, Q, as illustrated in FIGURE 2.10. For shaft 3, the resolution was determined to be 1.9. This high resolution of the signal was observed as a result of both the uniformly-cylindrical shape of the shaft (it was cased almost its entire length) and the presence of the loose backfill sand surrounding the shaft, which has a relatively low shear wave velocity.

The low-strain stiffness, K', for shaft 3 was calculated from the low frequency portion of the each curve to provide an indication of the low-strain, soil-foundation interaction. Using EQUATION 2.18, the theoretical range of stiffness values was determined to be 0.35 to 0.67 MN/mm for K_{min} and K_{max}, respectively. This range was determined for a 0.61 m (2 ft) diameter shaft using P, Q, and v_c from the experimental result. The experimental low-strain stiffness was determined from equation 2.17 and found to be 0.68 MN/mm. This stiffness is equal to the theoretical K_{max} which suggests that the shaft is seated on a rigid base. This 12.19 m (40 ft) deep shaft is seated in the soft clay deposit.

Shaft 4

After construction of shaft 4, sonic echo and impulse response tests were performed numerous times up to 56 days after concrete placement. The schedule for all tests performed on shaft 4 in the accessible-head condition is located in APPENDIX A. Details of the constructed shaft are shown in FIGURE 3.10. Shaft 4 has a length of 21.33 m (70 ft) and diameter of 0.76 m (2.5 ft), thus an L/D ratio of 28. The shaft passes through both the sand fill and the soft clay layers and is embedded in the hard silt and clay layer.

The impulse response results for shaft 4 conducted in the accessible-head condition are shown in FIGURES 4.4 and 4.5. These are results from the tests performed 28 days after concrete placement, and are characteristic of all impulse response tests performed on shaft 4. FIGURE 4.4A indicates the contact time of the force impact was about 1 msec. The velocity time-trace is shown in FIGURE 4.4B. A reflection from the toe of the shaft is apparent at 16.2 msec which corresponds to a Dt = 10.6 msec. Using the sonic echo analysis in the time-domain indicates the propagation velocity through the concrete to be 4025 m/s (13210 ft/s) for the 21.33 m (70 ft) shaft. Additionally, a second reflection occurring at 11.1 msec signifies a unexpected change in impedance, most likely a bulge at a depth of 11 m (35 ft) (v_c = 4025 m/s) in the shaft, as will subsequently be described.

The fast fourier transforms of the force and velocity data are shown on FIGURE 4.4C and 4.4D, respectively. The force spectrum suggests that the hammer impact introduced significant frequencies below about 1200 Hz; therefore, the frequency domain analysis will focus within this frequency

range. The velocity spectrum in FIGURE 4.4D shows three clear resonant peaks below about 400 Hz, followed by peaks that are forced into pairs between 400 and 1000 Hz, and eventually becoming a broader single peak after 1000 Hz. This pairing of peaks corresponds to the reflection seen in the velocity time trace at 11.1 msec and is best explained by examining the mobility plot.

The mobility plot for shaft 4 is shown in FIGURE 4.5. Nine resonant peaks are visible in the mobility plot up to 1000 Hz. As discussed in the velocity spectrum analysis, three clear peaks exist below 400 Hz, after which, a secondary response is observed that begins around 500 Hz as the resonating peaks are forced into pairs. The first three peaks result from resonances from reflections off the bottom of the shaft, and have an average change in frequency of 93 Hz which corresponds to a velocity of 3960 m/s (12990 ft/s) for a shaft length of 21.33 m (70 ft).

The secondary response, shown by the pairing of peaks, has a change in frequency of 200 Hz, which was measured from the center of the two peaks forming two superimposed secondary resonances observed between 400 to 600 Hz and 600 to 800 Hz. This indicates an unplanned anomaly located at a depth around 11 m (35 ft) which corresponds to the bottom of the permanent liner. The secondary response was not observed in the frequency range below 400 Hz because the unplanned anomaly is located at 11 m (35 ft) which is half the distance to the toe of the shaft at 21.33 m (70 ft), therefore it is possible for the resonances to coincide and not be apparent throughout the entire frequency range in the mobility plot.

As will be shown by numerical simulations in SECTION 6.2, the unplanned anomaly is a bulge that corresponds to a locally increased cross-sectional area of about 140%. The average mobility from the first three peaks, as determined by the geometric mean of the minimum and maximum mobilities for each peak, is 1.96×10^{-7} m/s/N. This mobility is slightly lower than the theoretical range of 2.0 to 2.6×10^{-7} m/s/N for a 0.76 m (2.5 ft) diameter shaft made of good quality concrete. This may be a result of the increased cross-sectional area of the bulge, a better than expected quality of concrete, or a combination of both. The resolution of the mobility signal was determined to be 1.2.

As noted on FIGURE 4.5, the low-strain stiffness, K', for shaft 4 was found to be 1.21 MN/mm. K_{min} and K_{max} were determined to be 0.92 and 1.1 MN/mm for a 0.76 m (2.5 ft) diameter shaft using P, Q, and v_c from the experimental mobility curve. This stiffness is greater than the theoretical K_{max} which suggests that the shaft is seated on a rigid base. This shaft is seated on the top of the glacial till stratum.

Shaft 5

Before the pile caps were constructed, sonic echo and impulse response tests were performed on shaft 5 at times up to 55 days after concrete placement, including the day the shaft was poured. The testing schedule for all accessible-head tests performed on shaft 5 is presented in APPENDIX A. Details of constructed shaft 5 were shown in FIGURE 3.11. The shaft has a length of 27.49 m (90.2 ft) and a diameter of 0.91 m (3 ft), thus a L/D ratio of 30. The shaft passes through the sand fill, soft clay and glacial till layers and is seated on Dolomite bedrock.

FIGURES 4.6 and 4.7 show the impulse response results for the accessible-head tests performed on

shaft 5. The observed force and velocity time-traces are shown in FIGURE 4.6A and 4.6B, respectively. The contact time during impact was 0.95 msec, as indicated in FIGURE 4.6A. Unlike the velocity time traces for shaft 3 and 4, no strong reflections from depth are identifiable in the time domain, although small reflections are observed at 19.4 msec and 12.0 msec, corresponding to Dt =13.8 msec and Dt = 6.4 msec, respectively. These reflections correspond to a reflection from the shaft toe and an anomaly near the midpoint of the shaft, respectively. Given the low magnitude reflections in the velocity time trace, a frequency domain analysis is necessary to quantify these reflections. Hence, the force and velocity spectrums are shown in FIGURE 4.6C and 4.6D, respectively. The force spectrum indicates significant hammer impact frequencies less than 1100 Hz producing resonances in the velocity spectrum also below 1100 Hz.

As shown in FIGURE 4.7, the mobility plot for shaft 5 contained indications of resonances from the bottom of the shaft, although not as clear as the other shafts. There are four identifiable reflections between 200 and 500 Hz. The average change in frequency between these peaks is 71.7 Hz. For a shaft length of 27.49 m (90.2 ft), this corresponds to a velocity of 3940 m/s (12920 ft/s). In addition to the toe reflection, a stronger reflection appears to be coming from a depth of 12.8 m (42 ft), as seen by the more pronounced reflections at 225 and 380 Hz with an average change in frequency of 155 Hz. This reflection causes a non-uniform amplitude in the resonating peaks. It is likely that this reflection originates from a possible cross-sectional area change at the depth of the bottom of the permanent liner. Also, the transition from soft clay to hard till marks an increase in the attenuation characteristics of the surrounding soil for the lowest 6.1 m (20 ft) of the shaft, creating an impedance change, which would cause a reflection at this depth.

The average mobility from the first four peaks below 500 Hz is 1.4×10^{-7} m/s/N. This mobility is equal to the lower limit of the theoretical range of 1.4 to 1.8×10^{-7} m/s/N for a 0.91 m (3 ft) diameter shaft, indicating better than expected concrete quality, a larger cross-sectional area than expected, or a combination of both. In addition, the resolution of the mobility signal was determined to be 1.05. The low-strain stiffness, K', for shaft 5 was determined from EQUATION 2.17 and found to be 1.65 MN/mm which is greater than the theoretical range of stiffness values determined to be 1.39 to 1.5 MN/mm for K_{min} and K_{max}, respectively.

4.2.2.2 Shafts with Planned Defects

Shaft 1

Sonic echo and impulse response tests were performed on a number of days between 4 to 54 days after construction of the shaft. Tests could not be performed on the first three days after concrete placement because the temporary casing extended several feet above the shaft head which prevented access to the top of the shaft. A summary of the impulse response testing schedule for shaft 1 is presented in APPENDIX A. As shown in the schematic of the constructed drilled shaft on FIGURE 3.7, the shaft passes through the sand fill layer and is embedded into the soft clay layer. It was constructed 12.19 m (40 ft) in length and 0.61 m (2 ft) in diameter with a soil-filled joint at 4.37 m, giving a L/D ratio of 20.

The results of the accessible-head impulse response tests performed 28 days after concrete placement are presented to show the typical response for shaft 1. The observed force and velocity traces for

shaft 1 are shown in FIGURE 4.8A and 4.8B, respectively. The contact time of the force impact is about 0.9 msec. The velocity trace is characterized by a quickly decaying peak velocity followed by several strong reflections from the soil-filled joint located at 4.37 m. The first two reflections are located at 7.8 msec and 10 msec corresponding to a Dt of 2.2 msec. To identify the toe of the shaft from this data was somewhat difficult due to the stronger multiple reflections from the defect. This lack of clear reflection in the velocity trace emphasizes the advantages of using the frequency domain to identify the resonant frequencies. The fast fourier transforms of the force and velocity data are also shown in FIGURE 4.8C and 4.8D, respectively. The force spectrum indicates that the hammer blow imparted significant frequencies below about 1200 Hz, hence, the mobility plot would provide significant data only below this frequency. The velocity spectrum shows four regularly occurring resonant peaks below about 1600 Hz with two lesser pronounced peaks occurring around 270 Hz and 460 Hz.

FIGURE 4.9 presents the mobility plot for shaft 1. The response is dominated by several large resonances with an average change in frequency of 430 Hz between these peaks. This corresponds to a reflection from a depth of 4.4 m (14.4 ft), the location of the soil-filled joint. Less pronounced peaks were identified at 120 and 275 Hz originating from the shaft toe. Resonances from the toe are obscured by the stronger resonances from the soil-filled joint, causing difficulty in the determination of concrete integrity for the full length of the shaft. A propagation velocity of 3810 m/s (12500 ft/s) was determined for a shaft length of 12.19 m (40 ft). Given that the toe was somewhat discernable in the mobility plot, it is clear that a small percentage of the compression wave is traveling through the soil layer and being reflected back from the toe.

For this shaft, resonances from the soil-filled joint controlled the mobility response for the shaft. In this case, the average mobility for the first three dominating peaks was 6×10^{-7} m/s/N; whereas, the average mobility for the peak identifying the shaft toe was 1.6×10^{-7} m/s/N, which had obviously been distorted by the governing resonances from the defect. Neither of these values are consistent with the expected average mobility of an intact shaft constructed with similar dimensions and good quality concrete, thus the existence of the soil-filled joint was evident. Also, the resolution of the resonance originating from the defect was around 9, whereas, the resolution of the toe resonance was only 1.2.

As noted on FIGURE 4.9, the low-strain stiffness, K', for shaft 1 was found to be 0.57 MN/mm. A range of K_{min} and K_{max} was determined to be 0.35 and 0.67 MN/mm for shaft 3 which has the same dimensions as shaft 1, yet was constructed without a defect. The experimental K' for shaft 1 is within this range, suggesting that the actual shaft base is between a free and rigid support. However, this value of 0.57 was lower than the low-strain stiffness of shafts 3, 4, and 5 constructed without defects, suggesting that the reduced stiffness reflects the discontinuity at 4.4 m (14.4 ft).

Shaft 2

Sonic echo and impulse response tests were performed directly on the accessible shaft head beginning the day after the concrete was poured (day 1) through day 54, just before the concrete pile caps were constructed. A summary of the impulse response testing schedule for shaft 2 is presented in APPENDIX A. As shown in FIGURE 3.8, shaft 2 was constructed 21.33 m (70 ft) in length and 0.91 m (3 ft) in diameter with a necking defect located between the depths of 3.76 and 4.47m (12.33 to 14.67 ft). The shaft passes through both the sand fill and the soft clay layers and is embedded in

the hard silt and clay layer.

The results from the impulse response testing performed on shaft 2 in the accessible-head condition are presented in FIGURES 4.10 and 4.11. These are results from the tests performed 28 days after concrete placement, and are characteristic of all impulse response tests performed on shaft 2. FIGURE 4.10A and 4.10B show the digitized force and velocity time traces. Examination of the velocity-time trace, indicates a reflection from the toe occurring at 16.5 msec (Dt=10.9 msec). A clear reflection from the neck defect was found at 7.9 msec or Dt=2.3. The corresponding force spectrum and velocity spectrum are shown in FIGURE 4.10C and 4.10D, respectively. The force spectrum indicates that the hammer impact imparted significant frequencies below 1000 Hz. The velocity spectrum shows four clear resonant peaks below about 400 Hz, followed by a secondary response indicated by 3 larger, broader peaks between 400 and 1600 Hz which eventually completely mask the smaller resonant peaks observed below 800 Hz. This secondary response corresponds to the necking defect located between 3.76 and 4.47m (12.33 and 14.67 ft) within the shaft.

The mobility plot for the impulse response tests performed on shaft 2 is shown in FIGURE 4.11. The toe of shaft 2 is clearly identifiable in the mobility plot by the eight peaks below 800 Hz. However, only the first four resonances that are equally spaced an average of 93 Hz are relatively unaffected by the larger secondary response identified by the peaks at 560 and 1010 Hz. This secondary response with peaks spaced an average of 470 Hz corresponds to reflections from the planned necking defect around 4.2 m. The first four peaks were used to determine the propagation velocity and the shaft mobility because they were minimally affected by the dominating secondary response. A propagation velocity of 3960 m/s (12990 ft/s) was determined for a shaft length of 21.33 m (70 ft). The average mobility from these four peaks, as determined by the geometric mean of the minimum and maximum mobilities for each peak, is 1.22×10^{-7} m/s/N. This mobility is lower than the theoretical range of 1.4 to 1.8×10^{-7} m/s/N for a 0.91 m (3 ft) diameter shaft made of good quality concrete. However, the response was governed by the larger peaks occurring at 560 Hz and 1010 Hz which have an average mobility of 3×10^{-7} m/s/N which is larger than the theoretical mobility, most likely as a result of the reduced cross-sectional area of the shaft in the neck region. Therefore, these latter average mobility values were not as expected for an intact drilled shaft constructed with similar dimensions and good quality concrete. The resolution of the mobility signal was determined by the ratio of the maximum mobility, P, to the minimum mobility, Q. The resolution of the first four peaks is 1.3; whereas, the resolution of the part of the signal dominated by the neck defect is 2.8.

The low-strain stiffness, K', for shaft 2 was determined from EQUATION 2.17 and found to be 1.57 MN/mm. Using EQUATION 2.18, the theoretical range of stiffness values was determined to be 1.05 to 1.36 MN/mm for K_{min} and K_{max}, respectively. This range was determined for a 0.91 m (3 ft) diameter shaft using P, Q, and v_c from the first four peaks observed in the experimental mobility curve.

4.2.3 Summary of Accessible-Head Tests

4.2.3.1 Analysis of Defects

Defects were included in shaft 1 and shaft 2 to determine the ability of surface reflection methods to determine the location, size and shape of typical construction defects. Common construction

anomalies include necks and bulbs which result in a decrease or an increase in the cross-sectional area of the shaft, respectively. Note that the latter anomaly does not adversely affect the load carrying ability of the shaft and as such is not a defect. Both anomalies, the soil-filled joint and the neck, were detected by the sonic echo and the impulse response methods. To quantify the size and shape of the defects, numerical simulations which considered the as-built shaft geometries were performed. The results of the simulation study are presented in SECTION 6.2.

Planned Defects

The mobility plots for shafts 1 and 3, the two 12.19 m (40 ft) long, 0.61 m (2 ft) diameter shafts, are shown in FIGURE 4.12. A comparison of the two mobility signals illustrates the effect the soil-filled joint had on the shaft response. The reflections from the toe of shaft 3 were nearly ideal as a result of the careful construction procedures, whereas the bottom of shaft 1 with the planned soil-filled joint was barely discernible. For frequencies less than 200 Hz, both signals had about the same average mobility, but the resonant peaks had shifted to lower frequencies as a result of the defect. At frequencies above 200 Hz, the larger resolution and higher average mobility of the signal for shaft 1 masked the reflections from the toe of the shaft, which indicated that the reflections from the soil-filled joint dominated the response.

FIGURE 4.13 shows the mobility plots for shafts 2 and 4, the two 21.33 m (70 ft) shafts with diameters of 0.91 m (3 ft) and 0.76 m (2.5 ft), respectively. Reflections from the bottom of both shafts were clearly visible at frequencies below 600 Hz. Reflections from the neck in shaft 2 were also identifiable by the peaks at 540 and 1000 Hz. Also, a secondary response from shaft 4 was identified around 500 Hz where the resonating peaks were forced into pairs.

Unplanned Anomalies

In addition to the planned defects, indications of unplanned anomalies were observed in the impulse response results. Most noticeably, unexpected reflections were observed in the mobility plots for shafts 4 and 5, shown in FIGURES 4.5 and 4.7, respectively. These reflections correspond to bulges in the shaft, which occurred at the depths of the permanent liners due to the construction procedure. It is possible that these bulges are also present in shafts 1, 2, and 3; however, they are most likely of a lesser magnitude or are masked by the neck and soil-filled joint, given that they were not observed in the velocity-time trace or the mobility curve. The observed changes in cross-section are consistent with the construction technique of overexcavating from the ground surface to approximately 1.5 m (5 ft) into the soft clay, placing a temporary liner to drill the remaining part of the hole in the dry, and finally placing the permanent liner. Concrete could have easily filled up to one or two feet of the overexcavated annulus between the permanent liner and the temporary liner.

4.2.3.2 Theoretical Mobility

As summarized in TABLE 4.1, the average mobility was calculated from each mobility plot and compared to a theoretical range that was calculated based on EQUATION 2.16, assuming a wave propagation velocity range of 3500 to 4500 m/s (11484 to 14765 ft/s) and a concrete density of 2400 kg/m^3 (150 pcf). The magnitude of the average mobility for shaft 3 was in the middle and for shafts 4 and 5 was near the lower limit of the theoretical range for the accessible-head condition as shown

in TABLE 4.1. This indicates that the as-built shaft impedance for these shafts was greater than or equal to the design value as a result of better than expected concrete quality, the increased cross-sectional area of unplanned bulges (shafts 4 and 5), or a combination of both. In contrast, the mobility of the defects for shafts 1 and 2 was not consistent with the expected average mobility of an intact shaft constructed with similar dimensions and good quality concrete. For these two shafts, the anomalous average mobility corresponded to the inferior concrete forming the soil-filled joint in shaft 1 and the reduced cross-sectional area of the necking defect in shaft 2.

4.2.3.3 Low-Strain Stiffness

The low-strain stiffnesses, K', for each shaft, calculated from the low frequency portion of each mobility curve to provide an indication of the low-strain load-deflection responses of the shafts are shown in TABLE 4.1. The measured stiffness values are theoretically a function of pile stiffness and the resolution of the impulse response signal, P/Q. A shaft supported on a rigid base has a larger stiffness than an unsupported shaft. As shown in FIGURE 4.14A, the experimentally-determined low-strain stiffness, determined for the five NGES shafts, increased with increasing soil stiffness at the toe of the shaft. Shafts 1 and 3, the two 12.19 m (40 ft) shafts tipped in the soft clay, have lower stiffnesses than shafts 2 and 4, the two 21.33 m (70 ft) shafts tipped in the hard till. The larger stiffness values apparently reflect a more rigid support at the bottom of the shaft. Accordingly, the stiffness of the 27.49 m (90.2 ft) shaft seated on Dolomite bedrock was the largest of the five.

However, a more appropriate assessment of the stiffness is made by comparing the shaft diameter to the experimentally-determined low-strain stiffness. As shown in FIGURE 4.14B, the measured low-strain stiffness increased as the diameter of the shaft increased. Thus, the diameter of the shaft, which reflects the axial stiffness (EA) of the shaft, governs the measured low-strain stiffness more so than the soil at the bottom of the shaft. Presumably the modulus of elasticity, E, is similar for all five shafts and the only difference is the shaft diameter. Therefore, it is more instructive when evaluating the soil conditions at the shaft toe to compare low-strain stiffness values determined from impulse response results from shafts which have the same axial stiffness.

Comparison of the two 12.19 m (40 ft) shafts indicates that shaft 1 with the soil-filled joint has a smaller low-strain stiffness than does shaft 3. Both shafts have the same shaft cross-sectional area and L/D ratio of 20. This difference in stiffnesses can be mostly attributed to the presence of the defect in shaft 1. Also, the density of the sand backfill surrounding the upper portion of each shaft affected the stiffness value.

It is observed that the defect in shaft 2 also decreased the low-strain stiffness value as shown by the comparison of shaft 2 and 5 in FIGURE 4.14B. Both shafts 2 and 5 have the same diameter, 0.91 m (3 ft), but shaft 2 has an L/D ratio of 23.3 and shaft 5 has an L/D = 30. For shaft 2 with the neck, the low-strain stiffness was 1.57 MN/mm, which was lower than 1.65 MN/mm for shaft 5. Additionally, the cylinders from shaft 5 had a density of 2240 kg/m^3, which was less than the average density of 2450 kg/m^3 for shafts 1 through 4, suggesting that the actual modulus of elasticity, E, and low-strain stiffness, K', were lower for shaft 5. Therefore, if the modulus of elasticity for shaft 5 was the same as the modulus of elasticity for shafts 1 through 4, then a larger difference between shaft 2 and 5 would have been observed due to the neck in shaft 2. Furthermore, four of the five shafts had K' values larger than the theoretical maximum value corresponding to a rigid base, dotted line on FIGURE 4.14B. Because the end conditions of the five shafts varied from being tipped in soft clay to

resting on dolomite, the low-strain stiffness depends on conditions through the entire depth of the shaft and not just the conditions at the bottom of the shaft. As such, one would expect a stiffer response for a shaft with a smaller L/D ratio given the same bottom conditions. This can be seen by comparing shaft 2 and shaft 4, both having the same length equal to 21.33 m (70 ft) and hence the same bottom conditions, but different L/D ratios. The higher K' value for shaft 2 suggests that the L/D ratio governed the stiffness of the response, more than the bottom conditions or the neck defect.

4.3 Inaccessible-Head Tests

4.3.1 Testing Procedure

After the accessible-head tests were completed, the pile caps were constructed rendering the shaft heads inaccessible. Consequently, all subsequent testing was conducted from atop the pile caps. Impulse response and sonic echo tests were conducted by impacting the pile cap and recording the vibrations with a geophone mounted to the pile cap surface directly above the drilled shaft. In the case of inaccessible-head shaft tests, additional reflections of the longitudinal stress waves were generated by the interface between the bottom of the pile cap and the shaft, as well as surface waves from the perimeter boundaries of the cap.

The testing procedure was similar to the procedure used for the accessible-head tests as described in SECTION 2.3.1.2. Also, the same equipment was used as described in SECTION 2.3.1.1. All hammer strikes for the data presented herein were located directly above the center of the shaft on the pile cap (FIGURE 2.8). The geophone was mounted to the pile cap surface near the projection of the shaft perimeter, specific locations will be noted in the discussion for each inaccessible-head shaft result. Rycon grease was used for the couplant. Processing of the digitized force and velocity signals was similar to the technique used for the accessible-head tests as described in SECTION 4.2.2. However, the higher frequency data, particularly in the velocity spectrum, was used to identify reflections emanating from the pile cap boundaries.

The sonic echo and impulse response results presented herein for the five drilled shafts in the inaccessible-head condition were performed on November 15, 1994. This was 19 days after the pile caps were constructed and 74 to 77 days after the drilled shaft were constructed.

4.3.2 Sonic Echo / Impulse Response Results

4.3.2.1 Shafts without Planned Defects

Shaft 3 with Pile Cap

A schematic of shaft 3, constructed 12.19 m (40 ft) in length and 0.61 m (2 ft) in diameter, which illustrates the inaccessible-head condition, is shown in FIGURE 3.14. The pile cap which was constructed atop shaft 3 has dimensions 1.52 m (5 ft) long, 1.52 m (5 ft) wide, and 1.52 m (5 ft) high. Thus, the length-to-diameter (L/D) ratio is 20 and the pile cap thickness-to-shaft diameter (B/D) ratio is 2.5. The distance between the top of the cap and the top of the shaft is 0.72 m (2.36 ft), therefore, the total length of the shaft and cap is 12.91 m (42.36 ft).

To perform the impulse response tests on the inaccessible shafts, the cap was impacted with the impulse hammer on the top surface of the pile cap. The hammer impact location was in the center of the pile cap, directly above the center of the shaft. The geophone was attached to the concrete surface just outside the perimeter of the projection of the shaft. This geophone location minimized surface wave reflections while capturing reflections from the toe of the shaft.

The results for the inaccessible-head impulse response tests performed on shaft 3, 19 days after the pile cap was constructed, are shown in FIGURES 4.15 and 4.16. The accessible-head results are also shown for comparison. The digitized force time-traces for shaft 3 in both the accessible- and inaccessible-head condition are shown for comparison purposes in FIGURE 4.15A. The force signal is clean for both conditions, but the input force for the inaccessible-head test has a larger magnitude and a shorter contact time, resulting in a broader frequency range shown in FIGURE 4.15C. The larger amplitude of force input was needed for the inaccessible-head tests to provide enough energy to penetrate through the cap, reach the shaft toe and reflect back to the cap surface.

Comparison of the velocity-time traces, shown in FIGURE 4.15B, for the accessible- and inaccessible-head cases, indicates that the interpretation of the velocity-time signal alone, as is done with the sonic echo test, requires considerable judgement for the inaccessible-head case. As discussed in SECTION 4.2.2.1, the toe reflection for shaft 3 in the accessible-head condition was strong and clear, and analysis of the shaft length was straightforward. For the inaccessible-head test, reflections from a combination of the pile cap boundaries and surface waves are identified in the velocity-time trace, spaced at 0.83 msec. These reflections govern the response and mask reflections arriving from the shaft toe. Therefore, the velocity spectrum, shown in FIGURE 4.15D, must be used to analyze the integrity of shaft 3 in the inaccessible condition. The velocity spectrum indicates several trends. For frequencies lower than 600 Hz, there is resonance (however, of low resolution) for the inaccessible-head tests which corresponds to reflections off the bottom of the shaft. The second observation is the strong resonance at 1200 Hz for the inaccessible-head test. This represents a combination of reflections from the interface between the bottom of the pile cap and the shaft, and reflections from the surface waves.

The mobility plot for shaft 3 is shown in FIGURE 4.16. Both the accessible- and inaccessible-head tests are shown in FIGURE 4.16A, whereas a close up of the lower frequency range for the inaccessible-head test alone is shown in FIGURE 4.16B. As shown in the figures, reflections from the shaft toe are apparent for both accessible- and inaccessible- conditions, although the resonances for the inaccessible case were significantly less pronounced than the accessible case. This is because there was a lack of signal transmitted past the pile cap interface into the shaft. The most notable difference in the mobility plot for the inaccessible-head case is the character of the low frequency portion of the curve. In contrast to the constant magnitude of the resonating peaks up to 1000 Hz for the accessible-head response, the peaks in the inaccessible-head case follow an exponentially decreasing trend between 100 and 600 Hz. This response is a function of the increased mass atop the shaft from the pile cap, as will be shown by results of numerical simulations in section 6.2.2.

Comparison of the accessible and inaccessible cases indicates several trends in the mobility signals. The average mobility decreased from 3.8×10^{-7} m/s/N for the accessible case to 0.5×10^{-7} m/s/N for the inaccessible case, as expected due to the increased mass from the pile cap. Another notable difference between the accessible and inaccessible mobility curves is the rise in the mobility signal which develops around 1200 Hz. This rise is largely due to the strong reflection from a depth of 1.52

m (5 ft) at the bottom of the pile cap, as well as the surface waves. For the inaccessible case, the resolution, P/Q, was 1.2 at frequencies below 600 Hz; whereas, for the accessible-head condition the resolution was 1.9 and resonant peaks from the shaft toe were clearly identified up to 1000 Hz. Also note that the inaccessible-head low-strain stiffness equal to 1.32 MN/mm was greater than the accessible-head low-strain stiffness of 0.68 MN/mm.

Shaft 4 with Pile Cap

After a pile cap was constructed atop shaft 4 to form a group of two shafts with shaft 5, impulse response tests were again performed, this time from atop the pile cap surface. A detailed schematic of the constructed shaft and pile cap is shown in FIGURE 3.15. The cap is 4.11 m (13.5 ft) long, 2.13 m (7 ft) wide, and 0.91 m (3 ft) thick. Shaft 4 is 21.33 m (70 ft) in length and 0.76 m (2.5 ft) in diameter, thus, the length-to-diameter (L/D) ratio is 28 and the pile cap thickness-to-shaft diameter (B/D) ratio is 1.2. The total length of the shaft and cap is 21.95 m (72.0 ft), given that the distance between the top of the cap and the top of the shaft is 0.62 m (2.0 ft).

FIGURES 4.17 and 4.18 show the impulse response results for shaft 4 after the pile cap was constructed compared to the results when the top of the shaft was accessible. The inaccessible results are from tests performed 19 days after the pile cap was constructed and are characteristic of all impulse response tests performed on shaft 4 with a pile cap. For this test, the hammer impact location was directly above the center of the shaft and the geophone was attached to the concrete surface just inside the projection of the reinforcing cage.

The observed force and velocity time-traces for shaft 4 in both the accessible- and inaccessible-head condition are shown for comparison purposes in FIGURES 4.17A and 4.17B, respectively. The input force for the inaccessible-head test has a larger magnitude and a shorter contact time, resulting in a broader frequency range shown in FIGURE 4.17C.

The interpretation of the velocity-time signal alone is difficult for the inaccessible-head case, given the additional spurious reflections from the pile cap. Therefore, the velocity spectrum, shown in FIGURE 4.17D, was examined but didn't reveal any resonances in the lower frequency range to identify the shaft toe. However, resonances were observed above 1000 Hz, indicating surface waves reflected off the sides of the pile caps.

Examination of the mobility curve, shown in FIGURE 4.18 for the inaccessible-head tests for shaft 4, indicates that no reflections from the shaft toe are identifiable. Clearly, the increased mass from the pile cap atop the shaft prevented enough energy from reaching the shaft toe and returning to the top of the shaft to be recorded by the geophone and identified in the velocity time trace or the mobility plot. The low frequency portion of the mobility curve for the inaccessible-head case is characterized by an exponentially decreasing trend between 60 and 460 Hz with no resonating peaks, which differs from the accessible curve which has relatively constant-magnitude resonating peaks up to 700 Hz. Numerical simulations in section 6.2.2. will demonstrate that this is due to the increased mass atop the shaft from the pile cap.

The presence of the pile cap had several notable effects on the analysis of the impulse response result. First, the average mobility of 0.6 m/s/N E-7 for the inaccessible-head condition is substantially less than 1.9 m/s/N E-7 for the accessible condition. Secondly, the resolution, P/Q,

approached 1.0 to the point where no resonances from the toe could be identified; whereas, for the accessible-head condition the resolution was 1.2 and resonant peaks from the shaft toe were clearly identified. Apparently, the combination of a L/D ratio of 28, the damping arising from the soils adjacent to the 21.33 m (70 ft) long shaft, the interference caused by the cap width, and a B/D ratio of 1.2 resulted in enough reduction of energy being transmitted along the shaft to prevent reflections being measured atop the cap. Also, the low-strain stiffness increased from 1.21 for the accessible case to 1.54 MN/mm for the inaccessible case.

Shaft 5 with Pile Cap

Shaft 5 was constructed in a group with shaft 4 by constructing a pile cap atop the two shafts. FIGURE 3.16 shows a detailed schematic of the construction details for shaft 5 with the pile cap. The pile cap is 4.11 m (13.5 ft) long, 2.13 m (7 ft) wide, and 0.91 m (3 ft) thick. Recall that the shaft is 27.49 m (90.2 ft) in length, 0.91 m (3 ft) in diameter and the pile cap is 0.91 m (3 ft) thick creating an L/D ratio of 30 and a B/D ratio of 1.0. The distance between the top of the cap and the top of the shaft is 0.6 m (1.97 ft), therefore, the total length of the shaft and cap is 28.08 m (92.14 ft).

FIGURES 4.19 and 4.20 show the results for the impulse response tests performed on shaft 5 for the inaccessible-head testing conditions, 19 days after the pile cap was constructed. For this test, the hammer impact location was directly above the center of the shaft and the geophone was attached to the concrete surface just inside the projection of the reinforcing cage. Both the observed force and velocity time-traces for the accessible- and inaccessible-head cases performed on shaft 5 are shown in FIGURE 4.19A and 4.19B, respectively. Neither the velocity-time trace nor the velocity spectrum (FIGURE 4.19C) indicated reflections from the shaft toe.

A study of the inaccessible-head mobility curve in FIGURE 4.20A and 4.20B, shown for a frequency range up to 2000 Hz and 1000 Hz also indicates that no reflections from the toe are identifiable. Given that it was somewhat difficult to identify toe reflections in the accessible-head case with an L/D ratio of 30, the absence of reflections from the toe in impulse response tests after the cap was added is understandable. As seen for shafts 3 and 4, the low frequency portion of the mobility curve for the inaccessible-head case is characterized by an exponentially decreasing trend between 60 and 500 Hz, as a result of the pile cap mass.

The mobility response is similar to shaft 4 in which the mobility decreased, and the resolution approached 1.0. More specifically, the average mobility of 0.5 m/s/N E-7 for the inaccessible-head condition is substantially less compared to 1.4 m/s/N E-7 for the accessible condition, and the resolution approached 1.0 to the point where no resonances from the toe could be identified; whereas, for the accessible-head condition the resolution was 1.05 and resonant peaks from the shaft toe were discernable, however slightly. As expected from the addition of the pile cap, the low-strain stiffness increased from 1.65 to 1.93 MN/mm for the inaccessible-head condition.

4.3.2.2 Shafts with Planned Defects

Shaft 1 with Pile Cap

After a pile cap was constructed atop shaft 1 to form a group of two shafts with shaft 2, impulse

response tests were again performed, this time from the top of the pile cap. The pile cap is 4.11 m (13.5 ft) long, 1.52 m (5 ft) wide, and 0.61 m (2 ft) thick. As shown in FIGURE 3.11, the shaft is 12.19 m (40 ft) in length and 0.61 m (2 ft) in diameter creating a length-to-diameter (L/D) ratio of 20 and a pile cap thickness-to-shaft diameter (B/D) ratio of 1.0. There is a soil-filled joint at a depth of 4.86 m (15.9 ft) from the top of the pile cap. The total length of the shaft and cap is 12.68 m (41.6 ft), given that the distance between the top of the cap and the top of the shaft is 0.49 m (1.6 ft).

In FIGURES 4.21 and 4.22, the results for the impulse response tests performed on shaft 1 for inaccessible-head testing conditions are presented. The inaccessible-head tests were performed 19 days after the pile cap was constructed. For this test, the geophone was attached to the concrete surface just inside the projection of the reinforcing cage and the hammer impact location was directly above the center of the shaft. The results for the accessible test are shown for comparison. The force and velocity time traces are shown in FIGURE 4.21A and 4.21B, respectively, and the resulting force spectrum and velocity spectrum are shown in FIGURE 4.21C and 4.21D. As for all the shafts, the magnitude of the force input for the inaccessible test was larger than the accessible test. The velocity-time trace indicates many reflections originating from surface waves reflecting off the sides of the pile cap. Both these reflections and the reflections originating from the soil-filled joint, most noticeably identified for both the accessible and inaccessible cases at 7.5 msec (Dt=2.2 msec), mask the reflection from the toe. Therefore it was constructive to analyze the velocity spectrum in FIGURE 4.21D which indicated toe resonances in the lowest frequency portion of the curve around 100 and 260 Hz.

Larger resonances at higher frequencies were noted at 900, 1270 and 1500 Hz, however they are not equally spaced, and thus would suggest a defect located anywhere from 5.4 m (17.7 ft) to 8.7 m (28.5 ft). It is possible that these resonances suggest reflections from the soil-filled joint located at 4.9 m but were distorted in shape and frequency content at these higher frequencies due to the presence of the three-dimensional pile cap. However, it is more probably that these resonances are from surface wave interactions from the sides of the pile cap.

The mobility plot for the impulse response tests performed on shaft 1 with a pile cap are presented in FIGURE 4.22. Both the accessible and inaccessible-head tests are shown up to 2000 Hz in FIGURE 4.22A, whereas, a close up of the lower frequency range is shown in FIGURE 4.22B. Resonances from the toe are identified only in the lowest frequency portion of the curve at 108 and 264 Hz corresponding to a change in frequency of 156 Hz and a velocity of 3960 m/s for a length of cap and shaft of 12.68 m (41.6 ft). Resonances from the soil-filled joint may be present at the higher frequencies around 900, 1270, and 1500 Hz as noted in the velocity spectrum discussion.

Similar to the other shafts, the average mobility decreased from 1.2 m/s/N E-7 to 0.7 m/s/N E-7 and the low-strain stiffness increased from 1.57 to 1.83 MN/mm for the inaccessible condition. As seen for the accessible-head case, the resolution, P/Q, was also dominated by the defect for the inaccessible case, making it difficult to identify toe resonances, except at the frequencies lower than 250 Hz as shown in the mobility plot. This is because a strong signal was reflected from the soil-filled joint in the accessible case and both the joint and the bottom of the cap in the inaccessible case, leaving less energy for the full length of the shaft. Since the response from the toe was subdued in the inaccessible-head condition, reduction of energy to the shaft precluded identification of a reflection from the toe in the velocity response as well.

Shaft 2 with Pile Cap

Shaft 2 was constructed in a group with shaft 1 by constructing a pile cap atop the two shafts. The pile cap is 4.11 m (13.5 ft) long, 1.52 m (5 ft) wide, and 0.61 m (2 ft) thick. A schematic of shaft 2 in the inaccessible-head condition is shown in FIGURE 3.13. The shaft is 21.33 m (70 ft) in length and 0.91 m (3 ft) in diameter. This yields an L/D ratio of 23 and B/D ratio of 0.7. A neck was built into the shaft at a depth of 4.95 m (16.2 ft) from the top of the pile cap. The distance between the top of the shaft and the top of the cap is 0.48 m (1.58 ft), therefore, the total length of the shaft and cap is 21.82 m (71.58 ft).

FIGURES 4.23 and 4.24 show the results for the impulse response tests performed on shaft 2 with a pile cap, 19 days after the pile cap was constructed, compared to those tests performed on the shaft when the top of the shaft was accessible. For the inaccessible test, the hammer impact location was directly above the center of the shaft and the geophone was attached to the concrete surface just inside the projection of the reinforcing cage.

The digitized force time-traces and force spectrum for shaft 2 are shown in FIGURE 4.23A and 4.23C, respectively. Comparison of the velocity-time traces, shown in FIGURE 4.23B, for the accessible- and inaccessible-head cases, indicates that reflections from the neck defect are clear for both cases around 8 msec, but reflections from the shaft toe, around 16.7 msec, are not quite as obvious for the inaccessible-head case. As observed in the velocity spectrum in FIGURE 4.23D, the reflection from the neck observed at 8 msec in the velocity-time trace corresponds to the resonance around 420 Hz, yet multiples of this resonance are not apparent. Four clear resonating peaks below 500 Hz from the shaft toe are clear for both the accessible and inaccessible cases. The three larger, broader resonances observed between 400 and 1600 Hz in the accessible-head result are possibly observed in the inaccessible-head result between 600 and 1300 Hz. However, the peaks are not equally spaced, suggesting that the presence of the three-dimensional pile cap caused distortion in shape and frequency content at these higher frequencies. It is more likely that these and the spurious resonances above 1400 Hz originate from surface wave reflections from the sides of the pile cap.

Comparison of the accessible and inaccessible mobility signals, shown in FIGURE 4.24, indicates that the toe of shaft 2 was detected for tests with and without the pile cap atop the shaft, although the resonances for the inaccessible case were slightly less pronounced than the accessible case. This is because a strong signal was reflected from both the reduced cross-section defect and the bottom of the cap in the inaccessible case, leaving less energy to be transmitted down the full length of the shaft. The mobility response up to 2000 Hz is shown in FIGURE 4.24A, whereas, a close up of the lower frequency range is shown in FIGURE 4.24B.

Five resonating peaks from the shaft toe are clearly visible at frequencies below 500 Hz in the inaccessible-head result compared to nine resonances below 800 Hz in the accessible-head result. The average change in frequency between these peaks is 89 Hz and for a total shaft and cap length of 21.8 m (71.58 ft), the propagation velocity, v_c, is 3900 m/s (12800 ft/s). The reflection from the planned defect, the neck, that was clearly identifiable by peaks at 540 and 1000 Hz in the accessible-head response is possibly apparent in the inaccessible result by the peaks at 630 and 960 Hz. This corresponds to a change in frequency equal to 330 Hz for the resonance generated from the neck located 4.95 m (16.2 ft) below the cap surface, However, at these higher frequencies, the signal was distorted in shape and frequency content, likely due to the effects of the three-dimensional pile cap,

which resulted in a mobility signal without equally spaced, multiple resonances from the neck. Thus the propagation velocity calculated to be 3270 m/s (10720 ft/s) (Df=330 Hz and L= 4.95m) is less than expected when compared to 3900 m/s (12800 ft/s) determined from the five resonating peaks below 500 Hz. Therefore, it is more likely that these resonances are products of surface wave reflections from the sides of the pile caps, than only from the neck itself.

Similar to the results for all five shafts, the presence of the pile cap created a decrease in the average mobility from 1.2 m/s/N E-7 to 0.7 m/s/N E-7; a decrease in resolution, P/Q, from 1.3 to 1.2 for the resonances from the shaft toe; and an increase in low-strain stiffness from 1.57 to 1.83 MN/mm for the accessible and inaccessible cases, respectively. Accordingly, the resonances from the defect also exhibited a decrease in mobility and resolution.

4.3.2.3 Center of Pile Cap Tests

Pile Cap Response at Lower Frequencies

Impulse response tests were conducted by placing the geophone and hammer strike locations at positions on the pile cap not above the center of a drilled shaft to quantify the effects of the pile cap alone. One such test, performed on pile cap 1, between shafts 1 and 2 is presented in FIGURE 4.25. This test was performed by striking the hammer in the center of the pile cap and placing the geophone 0.46 m (18 in.) from the center position, along the short axis and then the long axis. The tests performed on both axes are shown, as well as the tests performed directly above shaft 2. Comparison of the tests performed in the center of the cap to the tests above shaft 2 indicates a significantly different response below 1000 Hz. Resonances from the toe of the shaft are seen for the test above the shaft, whereas the tests in the center of the cap are characterized by a broad peak of higher mobility occurring around 200 Hz and no toe resonances are observed. Also, the responses from the short and long axis geophone locations deviate around 450 Hz, as a result of the cap boundaries. The short axis is 1.52 m (5ft) long and the long axis is 4.11 m (13.5 ft) long. Placing the geophone on the shorter axis, closer to an edge, resulted in stronger resonances between 450 and 1000 Hz.

In contrast, no significant deviations below 1000 Hz between the short and long axis responses were seen in the mobility plot for tests performed on the center of cap 3, between shafts 4 and 5, as shown in FIGURE 4.26. Pile cap 3 has the same long axis as pile cap 1, but a longer short axis of 2.13 m (7 ft). As for cap 1, the mobility curve below 500 Hz for the tests performed on the center of the cap is characterized by a broad peak at 220 Hz, whereas the test above shaft 4 indicated an exponentially decreasing signature from 60 to 460 Hz. Above 500 Hz, both the tests in the center and above shaft 4 have similar responses as seen by the peaks at 600 and 840 Hz with similar shape and average mobility. Thus, the effects of the cap are seen for both conditions only at these frequencies.

Identification of Pile Cap/Shaft Interface at Higher Frequencies

Information concerning the inaccessible-head condition can also be obtained by examining the higher frequency portion of the velocity spectrum. At these higher frequencies, resonant frequencies corresponding to the shallow depths of the structural interfaces can be identified. Thus, the lack of force data above the significant frequencies can be overcome. This is best illustrated by examining the velocity spectrum for the inaccessible-head test on shaft 3, shown in FIGURE 4.15D, which

showed a strong single resonance at 1200 Hz. This corresponds to a reflection from a depth of 1.52 m (5 ft) at the bottom of the pile cap for a propagation velocity of 3700 m/s. This propagation velocity is less than the propagation velocity of 4080 m/s determined by using the correlation from unconfined compression strength presented in 3.3.2.4 for the cylinders cast from the concrete of the pile caps, tested for a 28 day strength, indicating that a strong resonance should be observed around 1300 Hz. However, the inaccessible-head tests presented herein were performed 19 days after concrete placement and thus the lower propagation velocity of 3700 m/s is plausible.

Given the limits of the impulse hammer used for this study which input frequencies up to 2000 Hz (significant frequencies up to 1200 Hz), the interface between the cap and the shaft for pile caps 1 and 3 was not detected by examining the velocity spectrum. A strong resonance was expected around 3350 Hz for pile cap 1, which is 0.61 m (2 ft) deep. This was determined using a wave propagation velocity of 4080 m/s correlated from the unconfined compression strength for the cylinders cast from the concrete of the pile caps. This resonant frequency is greater than the limit of 2000 Hz which was input by the impulse hammer, thus resonances from the bottom of the pile cap were not seen in the velocity spectrum (FIGURES 4.21D and 4.23D for shafts 1 and 2, respectively). For pile cap 3, 0.91 m (3 ft) deep, a strong resonance was expected around 2230 Hz, but similar to the reasons for pile cap 1, the bottom of pile cap 3 could not be identified in the velocity spectrum (FIGURE 4.17D and 4.19D for shafts 4 and 5, respectively). Therefore, additional testing needs to be performed on pile caps 1 and 3 with a hammer that inputs a higher frequency range to identify the interface between the pile cap and shafts.

4.3.3 Summary of Effects of Intervening Structure

The purpose of this testing program was to evaluate the effects of intervening structure, in this case pile caps, on the results of impulse response and sonic echo tests. A summary of the impulse response analysis of accessible and inaccessible results is shown in TABLE 4.2 for all five shafts.

The presence of the pile cap had two notable effects on the impulse response result. For all five shafts tested, the average mobility decreased and the resolution decreased. These two effects are attributed to the presence of the increased mass from the pile cap. This creates an impedance change at the interface between the cap and shaft which causes reflections from the incident wave and results in less energy being transmitted down the shaft. The response for the inaccessible-head tests is characterized in the mobility plot by peaks which follow an exponentially decreasing trend in the lower frequency region, in contrast to the constant magnitude of the resonating peaks for the accessible-head tests. Collectively, the responses of the inaccessible tests can also be considered in light of the deviation from one-dimensional wave propagation to a more complicated, three-dimensional response from the geometries of the pile caps, which are not axi-symmetric members. At higher frequencies, the wavelengths are not necessarily greater than the pile cap dimensions whereas they were for the dimensions of the shafts, which leads to deviations from the normally-assumed 1-D wave propagation conditions.

It was shown that information concerning a shaft in the inaccessible-head condition can be obtained from examining both the mobility plot and the velocity spectrum. The accurate use of the mobility plot is limited by the frequency content of the force impulse because the mobility is the result of dividing the velocity by the force. The lack of force data at higher frequencies can be overcome by using the velocity spectrum where resonances can be identified at higher frequencies corresponding to structural interfaces. This was feasible for pile cap 2 with a depth of 1.52 m (5 ft), but not for pile

caps 1 and 3 with shallower depths of 0.61 m (2 ft) and 0.91 m (3 ft), respectively, given the range of hammer input frequencies used for this study. For these two caps, further testing is needed to identify the interface between the pile cap and shaft using a hammer that inputs a higher frequency range.

From this study of accessible-head and inaccessible-head impulse response tests, the limits of the method were defined for the conditions at the NGES at Northwestern University. Using the impulse response method on shafts obscured by pile caps, the toes of shafts 1, 2, and 3 were identified, whereas the toes of shafts 4 and 5 were not. This can be explained by the L/D and B/D ratios for each shaft, as well as the surrounding soil conditions. Shafts 4 and 5 had L/D ratios of 28 and 30, both of which are near the limits of the conventional testing method, and B/D ratios of 1.2 and 1, respectively. The three shafts in which the toe was identified had L/D ratios of 20, 23, and 20 for shafts 1, 2 and 3 and B/D ratios of 1, 0.67 and 2.5, respectively. These three shafts have similar L/D ratios, but shaft 3 has the largest B/D ratio. The B/D ratios for shafts 4 and 5 are in the middle of the ratios tested for this study. Therefore, the limits of the impulse response method for detecting the toe of a shaft with a pile cap are a combination of the L/D ratio and B/D ratio, as well as the soil conditions adjacent to a shaft. This study determined that the toe of the shaft could be identified for inaccessible shafts with L/D ratios as high as 23 with a B/D ratio of 0.67 and with L/D ratios as high as 20 with a B/D ratio of 2.5.

4.4 Summary

The results from the impulse response testing program at the NGES at Northwestern University have been presented. Impulse response tests were performed when the drilled shaft heads were accessible, and when the heads of the shafts were obscured by the presence of a pile cap. As expected for shafts made under controlled conditions, the impulse response results conducted in the accessible-head condition were quite clear for most cases. Both defects, the soil-filled joint and the neck were clearly identifiable in the impulse response results. Evaluation of the effects of intervening structure on the impulse response signals indicated that the limits of the impulse response method applied to inaccessible-head shafts are a function of both the L/D ratio and B/D ratio. The addition of the pile cap resulted in a decrease in the average mobility, a decrease in the resolution and an increase in low-strain stiffness. These effects were a result of the increased mass of the pile cap and strong reflections from the impedance change at the pile cap/shaft interface.

Table of Contents

Chapter 5. Uncertainties in Impuse Response Results Caused by Concrete Age and Equipment

---

- 5.1 Introduction
- 5.2 Effect of concrete age
  - 5.2.1 Concrete propagation velocity
  - 5.2.2 Average mobility
  - 5.2.3 Low-strain stiffness
  - 5.2.4 Resolution
- 5.3 Equipment effects: couplants
  - 5.3.1 Preliminary couplant investigations
  - 5.3.2 NGES couplant investigations
  - 5.3.3 Discussion
- 5.4 Summary

5.1 Introduction

The results of impulse response testing performed on both accessible- and inaccessible-head shafts were presented in CHAPTER 4. In this chapter, the conventional impulse response method will be evaluated in light of several testing variables that affect the results and interpretation of impulse response signals. First, the effect of concrete properties will be examined, with a focus on the age of the concrete and how it effects the interpretation of sonic echo and impulse response results. The age of concrete is related to the propagation velocity used to determine the depths of reflectors, either a shaft toe or an anomaly, and it affects the interpretation of velocity-time traces and mobility plots in terms of average mobility, shaft head stiffness and signal resolution. Additionally, the results of a study on various couplants used to fix the geophone to the concrete surface are presented.

5.2 Effect of Concrete Age

The age of the concrete affects the material properties of the concrete. As the concrete ages, the wave propagation characteristics of the concrete changes. The calculation of the shaft length and the shaft mobility are both dependent upon the wave propagation velocity through concrete, v_c. Furthermore, the results of this study can be used to determine the time after placing concrete in a drilled shaft when non-destructive testing methods can be performed with reasonable certainty in the concrete properties.

5.2.1 Concrete Propagation Velocity

The age of the concrete is indicative of the wave propagation velocity through the concrete. Generally, as the concrete ages, the propagation velocity increases. To investigate this behavior, laboratory and field tests were performed at various times after the test section was constructed to evaluate the compression wave velocity with the age of the concrete in each shaft. Laboratory tests performed included unconfined compression tests and ultrasonic pulse velocity (UPV) tests. Using a correlation to compressive strength, a propagation velocity for the concrete was estimated from the compressive strength of each cylinder.

Field velocity measurements were made using the sonic echo, impulse response methods and the geophones embedded near the toe of each shaft. The sonic echo and impulse response methods determine a two-way velocity based on interpretation of the observed signals obtained by a geophone coupled at the surface, given the depths of each shaft. Conversely, the propagation velocity determined by the embedded geophones is a one-way velocity in that the wave only travels one length of the shaft to be recorded by the geophone near the toe of the shaft.

5.2.1.1 Wave Velocity from Laboratory Tests on Cylinders

The results from the laboratory tests on the concrete cylinders cast from the concrete used to construct the drilled shafts and pile caps were presented in SECTION 3.3.2.4. Two methods were used to determine the propagation velocity using the concrete cylinders: a correlation between unconfined compressive strength and propagation velocity (after Davis and Robertson, 1975) and ultrasonic pulse velocity (UPV) tests. As shown in FIGURE 3.19, the propagation velocity was determined at 7, 14, 28, and 565 days after concrete placement from the unconfined compression strength correlation. The results showed that propagation velocity increased with concrete age. The tests performed at 565 days indicated a 2 to 3% increase of about 100 m/s in the propagation velocity from the 28 day tests. The propagation velocity was determined at 14 and 28 days after concrete placement using the UPV method. As shown in FIGURE 3.19, this method also showed an increasing trend with concrete age; however, the values were approximately 10% higher than those from the compressive strength correlation, due to the nature of the high frequency input source which had a wavelength much smaller than the diameter of the concrete cylinders. Theoretically, the compressive wave velocity in an infinite medium is approximately 5 to 15 % greater than that in a cylinder.

5.2.1.2 Wave Velocity from Field Tests at NGES

Sonic echo and impulse response tests were performed numerous times on the five shafts in the accessible-head condition, up to 56 days after concrete placement, to determine the effect of concrete age on the measured wave propagation velocity. The methods of analysis for the impulse response and sonic echo methods were described in SECTION 2.3.1 and 2.3.2, respectively. The propagation velocity determined from these two methods is a two-way velocity because the wave has to travel the length of the shaft, reflect off the shaft toe and return to the top of the shaft to be recorded by a geophone. The propagation velocity determined from the tests using the embedded geophone is a one-way velocity, thus both the one-way and two-way compression wave travel times in the shaft were determined, providing a means to compare the various methods.

Two-Way Velocity from Sonic Echo Analysis

The propagation velocity measured from the sonic echo tests for shafts 2, 3, and 4 is shown as function of concrete age in FIGURE 5.1. Clear toe reflections were seen in the velocity time traces for these three shafts. The propagation wave velocities for shafts 1 and 5 were not included in the figure because the soil-filled joint defect masked the toe response for shaft 1 and the toe reflection for shaft 5 was not clear due to this shaft's L/D ratio of 30 and the relatively large damping from the hard, glacial till soil layer adjacent to the bottom 6.8 m (22.3 ft) of the shaft. The relationship between propagation velocity and concrete age indicated a rapid increase in velocity for the shafts tested up to 10 days, after which the propagation velocity slowly increased. The propagation velocity for shaft 4 was the largest of the three shafts, whereas the propagation velocity for shaft 2 initially was higher than shaft 3, but after 28 days, the two had approximately the same velocity. After 28 days, the propagation velocity for the three shafts ranged from 3810 to 4100 m/s (12500 to 13460 ft/s) which corresponds to an average of 3950 m/s (12960 ft/s) and a standard deviation of 91 m/s (299 ft/s). Recall that the design unconfined compression strength (q_u) for this mix was 21 MPa (3000 psi) and that the average q_u from the cylinder tests was 42 MPa (6000 psi) at 28 day strength.

Two-Way Velocity from Mobility Analysis

In FIGURE 5.2, the propagation velocity determined from the impulse response tests for shafts 2, 3, and 4 is shown as function of concrete age. Clear resonances from the shaft toe were seen in the mobility plots for these three shafts. The wave propagation velocity for shaft 1 was not included in the figure because the resonances were affected by the lower propagation velocity of the soil-joint defect. Also, shaft 5 was not included in the figure because the resonances were not always identifiable due to this shaft's L/D ratio of 30 and its embedment in the hard till soil layer. The relationship between propagation velocity and concrete age indicated a gradually increasing v_c up to 28 days, after which the propagation velocity essentially remained constant. After 28 days, the propagation velocity for the three shafts ranged from 3750 to 4080 m/s (12305 to 13400 ft/s) having an average of 3880 m/s (12730 ft/s) and a standard deviation of 111 m/s (366 ft/s). This scatter is larger than that found in the sonic echo analysis, partially due to the resolution between data points of the digitized fourier transform. For the data acquisition rates used for this work, 10,000 points/sec, the change in frequency between data points in the fourier transform is 9.75 Hz. This limited the interpretation of the 'true' frequency at which each resonance peaked.

One-Way Velocity from Embedded Geophones

A geophone was embedded near the toe of each shaft to determine the one-way wave propagation velocity in the five shafts. To receive a signal from the embedded geophone, a four pound sledge hammer with an attached triggering device was used to impact the shaft. The sledge hammer generated larger wave energies than the 2000 Hz impulse hammer, so that the stress wave would mobilize the geophone and housing. The calculation of the shaft length and the shaft mobility are both dependent upon the velocity of the compression wave through the concrete, v_c.

Tests were conducted on the five shafts using the embedded geophone on 7, 14 and 28 days after concrete placement. A time-domain analysis was performed to determine the first arrival of the propagating wave to the embedded geophone. The measured one-way propagation velocities are

shown in FIGURE 5.3 as a function of concrete age. Tests performed on 7 and 28 days show the propagation velocity increased during this time and corresponded very well to the range of velocities determined from the laboratory tests and both the two-way velocity field tests. However, the velocities determined from the 14 day tests were lower than both the 7 and 28 days and do not fall within the range of the other testing results; thus the data is anomalous, possibly a result of equipment or operator error.

The propagation velocity for all five shafts tested on day 28 ranged from 3653 to 4075 m/s (11985 to 13370 ft/s) which corresponds to an average of 3879 m/s (12726 ft/s) and standard deviation of 175 m/s (576 ft/s). However, shaft 5 had the lowest propagation velocity of the five shafts. This was expected because the cylinder density determined in section 3.3.2.4 was 8.6% lower than the average of the cylinders from the other four shafts. Also, the propagation velocity for shaft 1 was lower than shafts 2, 3, and 4 as expected due to the lower propagation velocity of the soil-filled joint. Thus, the scatter in the results using all five shafts is misleading. Examination of shafts 2, 3, and 4 at 28 days indicated the propagation velocity ranged from 3909 to 4075 m/s (12825 to 13370 ft/s) having an average of 3997 m/s (13113 ft/s) and standard deviation of 83 m/s (274 ft/s), which is more representative of the concrete for the well-constructed shafts.

5.2.1.3 Discussion

The propagation velocity determined from all laboratory and field methods is summarized in FIGURE 5.4 as a function of concrete age. Only the results for shafts 2, 3, and 4 are compared because the propagation velocity was determined for these three shafts using all the laboratory and field tests. Comparison of the five methods indicated that there were different apparent velocities depending on the manner in which it was measured. In general, the correlation from unconfined compression strength resulted in propagation velocities that were higher than the velocities determined using the three field methods. This is possibly due to higher strengths in the cylinders than the shaft concrete as a result of casting the cylinders and curing them in a humidity controlled room compared to the free-fall placement of the concrete into the shafts and curing in the field. Also, since concrete is a highly variable material with properties that depend on the type of aggregate and admixtures, correlations with strength, such as that of Davis and Robertson, are specific to the concrete tested for a given study.

At 28 days after concrete placement, the propagation velocity for the three shafts determined from the three field methods and the correlation to strength ranged from 3750 to 4150 m/s (12305 to 13615 ft/s) and has a standard deviation of 118 m/s (280 ft/s) from the average which was equal to 3990 m/s (13090 ft/s). This average corresponds quite well to a value of 4000 m/s (13124 ft/s) which is commonly used as an estimate for the propagation velocity through good quality concrete when a means to measure the velocity is absent. The scatter in the data for shafts 2, 3, and 4 indicates that the uncertainty in determining the length of a shaft 28 days after construction from propagation velocities can be ±5% depending on whether the velocity is measured, estimated, or found from correlations with strength.

For many quality control operations, tests are conducted as soon as possible after a shaft is poured and the uncertainties in the propagation velocity are larger during the first 14 days. Note that clear signals were obtained within a day after each shaft was poured. Significant increases occur in propagation velocity during the first two weeks after pouring, as much as 1000 m/s, or 25% of the final value. Since the inferred length of a shaft is directly proportional to the assumed propagation

velocity, significant errors can arise in estimated lengths unless the time-dependence of the propagation velocity is considered in the analysis of tests conducted within a week after concrete placement. The following equations were developed from the data shown on FIGURE 5.4, excluding the UPV data, to allow one to estimate the effects of concrete age on propagation velocity:

$$\begin{aligned} Age < 14\ days: \quad & v_c\,(m/s) = 217 * \ln\,(Concrete\ Age\,(days)) + 3339 \\ Age > 14\ days: \quad & v_c\,(m/s) = 12 * \ln\,(Concrete\ Age\,(days)) + 3887 \end{aligned} \qquad (5.1)$$

5.2.2 Average Mobility

FIGURE 5.5 illustrates the effect of concrete age had on the average mobility, N, determined from the impulse response results for shafts 2, 3, and 4. As the concrete aged up to 56 days, the average mobility generally decreased for the three shafts. This was expected because the average mobility is theoretically a function of the concrete density, r_c, the propagation velocity,v_c, and the cross-sectional area, A, of the shaft as shown in EQUATION 2.19. Note that the propagation velocities increased up to 28 days, but essentially remained constant thereafter, since the concrete density and shaft cross-sectional area will not change, the average mobility should essentially reflect the time-dependence of the propagation velocities. As the concrete ages, the propagation velocity increases which subsequently decreases the average mobility. This effect was most pronounced in shaft 3 which had the smallest diameter, 0.61 m (2 ft), and had a decrease in average mobility of 37%, 56 days after concrete placement. Shaft 4 had a decrease in the average mobility equal to 20% and shaft 2 and the lowest decrease equal to 14%. Thus, the percentage decrease in mobility was inversely proportional to the shaft diameter.

The magnitude of the average mobility determined from the experimental tests is somewhat suspect because the values after day 28 were lower than the expected range of theoretical mobility which accounted for the permanent steel liner in the upper portion of the shafts and the overdrilling in the soft clay. While the average mobility is theoretically a function of the concrete propagation velocity, density and cross-sectional area, it is also experimentally a function of the hammer strike. If the hammer head was not hit square to the shaft head surface, the energy transmitted to the shaft would be lower than what was recorded by the load cell in the hammer; therefore, the velocity spectrum would be divided by a force spectrum with a larger magnitude than was actually imparted to the shaft, resulting in a lower than expected average mobility. This would suggest a quality shaft had been constructed better than specified in design, but may be misleading given the possibility of an inadequate hammer blow. Thus, it is imperative that the operator of an impulse hammer be skilled to provide a consistent, square hammer strike. To overcome this method limitation, work is currently underway to develop an input device which is independent of the operator and not subject to such potential errors.

5.2.3 Low-Strain Stiffness

The low-strain stiffness, K', was calculated from the low frequency portion of the each curve as described in SECTION 2.3.1.3 to provide an indication of the low-strain, soil-foundation interaction. The results are provided in FIGURE 5.6 showing the low-strain stiffness as a function of concrete

age for the five NGES shafts. The stiffness values rapidly increased in the first 7 days after the concrete was poured. This was because as the concrete cured, it became more stiff, thus changing the interaction between the impulse hammer and the concrete surface. Also, the soil surrounding the shafts likely stabilized after construction which also caused the stiffness to increase. After 7 days, the stiffness value for each shaft gradually increased. As seen in the figure, shafts 2 and 5, both having the largest diameters, 0.91 m (3 ft) of the group, had the largest stiffnesses. Accordingly, shafts 1 and 3, both having the smallest diameters of 0.61 m (2 ft), had the lowest stiffnesses. Thus, the measured low-strain stiffness was greater for the larger diameter shafts. Note that improper hammer blows would cause a higher than expected experimentally-determined stiffness, and thus only the relative magnitudes for the five shafts should be compared.

5.2.4 Resolution

For each impulse response test performed on the accessible-head shafts, the resolution was determined by selecting the maximum and minimum mobilities from the portion of the mobility curve in resonance, and dividing the two quantities. In FIGURE 5.7, the resolution of the mobility signals for the shafts 2, 3, and 4 is presented to show the effect of concrete age on the values of the maximum and minimum mobilities. The first 6 peaks were used to determine P and Q from the mobility curves for shaft 3. For shafts 2 and 4, P and Q were determined using only the first 3 peaks to minimize the effect of the strong reflection from the neck in shaft 2 and the reflection from the bulge in shaft 4.

The resolution of a mobility curve is theoretically a function of the propagation velocity and density of the concrete, as well as the shaft dimensions and surrounding soil properties as explained in SECTION 2.3.1.5 and shown in EQUATION 2.29. Thus, as the concrete ages and the propagation velocity increases, the resolution of the mobility also increases. This was most clearly seen in the results for shaft 3 which had an increase of 25% in the resolution from day 1 to day 56. This shaft had the smallest diameter, 0.61 m (2 ft) of the five, and as such, the response was affected the greatest by changes in concrete properties. The resolution for shaft 2 increased 3.5% and shaft 4 increased 3.1%.

The resolution of shaft 3 was the largest of the three shafts shown in FIGURE 5.7 as expected because it had the lowest L/D ratio equal to 20. Higher resolution is associated with lower L/D ratios for given soil conditions as shown in FIGURE 2.10. Accordingly, the resolution for shaft 2 was higher than shaft 4 given the L/D ratios of 23.3 and 28 for shafts 2 and 4, respectively.

5.3 Equipment Effects: Couplants

Variations in the equipment used to perform impulse response tests, such as different greases used for couplants, different hammer tip stiffnesses and various locations of geophone placement on the concrete surface may affect the interpretation of shaft integrity. In particular, this study investigated the effect of various couplants on the interpretation of sonic echo and impulse response results.

Many non-destructive testing techniques require attachment of a transducer to a specimen to measure vibrations. With any transducer it is necessary to adequately couple it to the tested material, such that energy emitted from a specimen as a result of induced stress waves can be received unadulterated or unattenuated. To accurately receive the wave reflections, it is essential for the transducer (a

geophone was used in this study) to be mechanically as well as acoustically coupled to the head of the pile (Bray and McBride, 1992). Attaching the transducer mechanically allows it to remain in place when exposed to an external force. More important is appropriate acoustical coupling which prescribes the amount of energy received by the transducer compared to the actual energy generated from within the tested specimen.

Couplants become of great concern in non-destructive testing when the wavelenghs of the stress waves are small compared to the thickness of the couplant, and is especially a concern for ultrasonic testing. It has been shown (Halmshaw, 1991) that if the couplant layer is one-quarter of the wavelength of the incoming signal, the resulting reflections in the couplant will broaden the width of the incoming pulses; thereby, damping out the signal. In deep foundation testing, the wavelengths induced by the impulse response method greatly exceed the width of the couplant layer.

It is clear that proper preparation of the pile head is essential to achieve accurate impulse response results. Unlike many non-destructive testing applications which often involve steel or plastics, concrete drilled shafts are very rough and non-homogeneous. Therefore, preparation of the pile head may be required before testing can be conducted. An ideal pile head surface for impulse response testing would be perfectly flat (perpendicular to the cylindrical axis), smooth, dry, and free of debris. This may be achieved by using a trowel to smooth the concrete surface after it is poured, and subsequent use of a hand-held grinder to smooth areas for the impact surface and geophone mounting surface. For quality control testing of drilled shafts, it is often uneconomical to prepare pile heads in this manner due to excessive time requirements of grinding. In that case, it is the goal of the couplant to reduce this deficiency in surface smoothness to as great of an extent as possible.

For the geophone used for impulse response testing, it has been thought that inadequate geophone coupling and geophone resonance are contributors to a rise in the mobility plot causing a distortion of the results above 1000 Hz. This phenomena has not yet been completely quantified. To examine the source of this behavior, various couplants under different environmental conditions were used to couple the geophone to the concrete surface. From this testing, the performance of each coupling medium was evaluated to quantify the geophone rise phenomena.

5.3.1 Preliminary Couplant Investigations

A small scale research project at Northwestern University was undertaken as part of an NSF summer research program to determine the most suitable couplant under various laboratory and field testing conditions. The laboratory portion of the testing program investigated temperature effects and surface preparation of 15.24 cm-diameter by 30.48 cm-long (6 in. by 12 in.) concrete test cylinders. Given that the cylinders were 30.48 cm (12 in.) in length, a small 1 lb modal hammer was used to allow frequencies up to10 kHz to be input into the cylinder. Various couplants were also tested under field conditions on a 0.91 m (3 ft) diameter, 18.9m (62 ft) long (L/D = 20.7) drilled shaft to evaluate the dependance of surface preparation on the couplant performance was investigated. The soil conditions at the site consisted of 5.49 m (18 ft) of fill overlying silty clays and clayey silts, both fairly stiff layers. Couplants were attached to a smooth concrete surface (achieved by a hand-held grinder) and to a rough concrete surface (created by a chipping hammer). The latter surface is typical of the preparation of concrete shafts for quality control field testing. The results of the study indicated that the epoxy performed the best for most conditions, yet the field practicality of epoxy is limited by its drying time and expense. For ease of use, an oil-based grease was recommend, given that its performance rivaled that of the epoxy. Upon comparing the results of tests on smooth and

rough surfaces, an increase in amplitude of the mobility plot was noted in the rough surface tests indicating the benefits of a smooth, ground surface.

5.3.2 NGES Couplant Investigations

To further investigate the dependence of accurate impulse response results on the couplant used to affix the geophone to a concrete surface, various couplants were used when performing impulse response tests on the five NGES test shafts in the accessible-head condition. The couplants used in this study included Devcon 5 minute epoxy (epoxy), Amoco Rycon premium grease number 3 (Rycon), and duct seal. The performance of Rycon grease was compared to the performance of both the epoxy and duct seal. Additionally, the effects of various environmental conditions on the oil-based Rycon grease were examined.

5.3.2.1 Performance of Rycon Grease versus Epoxy

To verify the findings from the preliminary couplant investigation that epoxy was a superior couplant, both the epoxy and the Rycon grease were used as couplants on the same day, temperature, and geophone attachment location on the shaft head. The tests were performed 36 days after concrete placement. The consistency of the Rycon grease was noted to be quite stiff.

The performance of the epoxy couplant was governed by the setting time needed to achieve a good mechanical bond. When using the epoxy couplant, the geophone and epoxy had to be pried from the concrete surface, whereas the geophone was easily removed from the surface when using Rycon grease. It was noted that the epoxy around the edge of the geophone had set, but the epoxy underneath the geophone was still wet. Therefore, while good mechanical coupling was achieved, the acoustic coupling was still in question.

FIGURE 5.8 shows the results from the impulse response testing on shaft 3 using both the Rycon grease and epoxy. FIGURE 5.8A shows the two force spectrums which are characterized by the same response, although the test with Rycon has a slightly higher magnitude compared to the test with epoxy. Both force spectrums indicate significant frequencies up to 1200 Hz. As shown in FIGURE 5.8B, the two velocity spectrums indicate similar responses up to 800 Hz, however, the resolution and magnitude of the velocity spectrum for the epoxy test are slightly lower than the Rycon test as expected due to the lower magnitude force input. Significant deviation between the two responses begins around 800 Hz where the average magnitude of the resonating peaks for the epoxy result was smaller than the Rycon result. In the frequency spectrum, the epoxy couplant recorded 9 resonances up to 1500 Hz, whereas the Rycon grease couplant only recorded 8 resonances up to 1400 Hz. The significance of this response is seen in the mobility plot shown in FIGURE 5.8C which also evidences a deviation between the two responses around 800 Hz. The test with Rycon grease indicates a strong resonance which peaks at 1270 Hz and the test with epoxy has a strong resonance which peaks at 1420 Hz. These resonances might suggest reflections from a depth near 1.6 m (5.2 ft) and 1.4 m (4.5 ft) for the Rycon and epoxy tests, respectively. A possible resonance could arise from low soil confinement near the shaft head, but presumably the resonance would be consistent for all tests performed, thus, the discrepancy in resonances can be attributed to the mechanical and acoustical performance differences between the two couplants.

A similar response was observed for shaft 5 as shown in FIGURE 5.9, as well as the other three

shafts. For the tests performed on shaft 5 using both couplants, the force spectrums were ideally identical as shown in FIGURE 5.9A and indicated significant frequencies up to 1200 Hz. A deviation between the velocity spectrum results for the two couplants in FIGURE 5.9B was noted around 600 Hz, the same point the average mobility in FIGURE 5.9C began to increase. This rise peaked around 1290 Hz in the velocity spectrum for the Rycon test and 1445 Hz for the epoxy test. Consequently, analysis of the mobility plot would indicate a reflection originating from 1.5 m (5 ft) and 1.4 m (4.5 ft), for the Rycon and epoxy tests respectively, neither of which were expected as a result of the uniform cross-sectional area in the region of the permanent steel liner. Thus, the discrepancy in resonances can again be attributed to the mechanical and acoustical performance differences between the two couplants.

5.3.2.2 Performance of Rycon Grease with Temperature

Rycon (Amoco Rycon premium grease number 3) was the primary couplant used for the impulse response testing of the NGES accessible-head shafts. It is an oil-based grease, and has a viscosity which is highly temperature-dependent. Observations of the performance of the grease in the field indicated that when the grease was warm, it became runny, almost liquid-like, and coupling a geophone to a concrete surface was difficult. In contrast, when the temperature was cold, the grease was very stiff and served as an excellent couplant.

Working within a period of 56 days when the shaft heads were exposed provided time to evaluate the performance of each couplant in various environmental conditions. Within this period, the concrete was still curing as the environmental temperature decreased with time, and thus limited the opportunity to compare testing results with Rycon grease at various environmental conditions with constant concrete properties.

Two tests performed on shaft 4 in which the couplant was observed to be either warm or cold, as a result of temperature effects, are compared in FIGURE 5.10. The two tests were performed on day 28 and 56 after concrete placement for warm and cold couplant consistencies, respectively. The force spectrums in FIGURE 5.10A are quite similar, but deviate slightly below 600 Hz and above 1200 Hz. As shown in FIGURE 5.10B, the velocity spectrums are quite different. They both show similarly-shaped resonating peaks, however the amplitude of the peaks deviates significantly around 450 Hz. The resonating peaks for the response using the warm Rycon began to increase in magnitude around 450 Hz and reached a peak at 1270 Hz , whereas the peaks using cold Rycon decreased consistently up to 1500 Hz.

The two mobility plots for the cold and warm Rycon are shown in FIGURE 5.10C. Below 1000 Hz, the effects of concrete age are observed: the peaks are not directly aligned and the average mobility for the cold Rycon is less than the warm Rycon. This is because the concrete was curing during the period in which these tests were performed, thus the propagation velocity of the concrete was still increasing with time. The effect of the various couplant temperatures was seen in the non-constant amplitude of the resonating peaks. Each successive peak, beginning around 300 Hz has a higher amplitude of mobility for the peak, P_{i+1}, than the previous peak, P_i. This "rise" in the mobility signal affects the quantification of the average mobility using peaks below 1000 Hz and identification of possible reflections at shallower depths which resonate at higher frequencies than the toe.

When the Rycon couplant was stiff, hence more viscous in the cold temperatures, the peak magnitude of the rise in the mobility curve occurred around 1500 Hz and had a smaller amplitude than that for the warm conditions. In comparison, the warm Rycon tests showed a peak rise in mobility around 1300 Hz. Thus, less distortion of the mobility signal was observed for the stiffer Rycon (cold) than the warm conditions. Therefore, Rycon grease performs well, both mechanically and acoustically, when kept at a cold temperature. It is recommend to keep the couplant away from direct sunlight when using during the warm summer months. Colder temperatures keep the grease stiff, which makes for excellent mechanical coupling.

5.3.2.3 Performance of Rycon Grease versus Duct Seal

FIGURE 5.11 shows the impulse response results on shaft 3 using both the Rycon grease and duct seal. The test with Rycon grease was performed on day 28 after concrete placement and the consistency of the couplant was noted to be warm; whereas the test with duct seal was performed on day 27 by STS Consultants, having similar temperature conditions as day 28. FIGURE 5.11A shows the two force spectrums which are characterized by similar responses, although the test with Rycon has a slightly higher magnitude compared to the test with duct seal. Both force spectrums indicate significant frequencies up to 1200 Hz. As shown in FIGURE 5.11B, the two velocity spectrums indicate similar responses up to 800 Hz, however, the magnitude of the resonating peaks in the velocity spectrum for the duct seal test is slightly higher than the Rycon test. The significant deviation between the two responses occurs around 800 Hz where the average magnitude of the resonating peaks for the duct seal result decreased as those from the Rycon result increased. In the frequency spectrum, the duct seal couplant recorded 10 resonances up to 1550 Hz (with some electrical interference between 1200 and 1300 Hz), whereas the Rycon grease couplant only recorded 9 resonances up to 1450 Hz.

Analysis of the mobility plot shown in FIGURE 5.11C indicates similar resonances up to 1000 Hz, however the average mobility of the duct seal test is 3.9×10^{-7} m/s/N which is higher than the test with warm Rycon grease having an average mobility of 3.4×10^{-7} m/s/N. A second deviation between the two responses begins around 1000 Hz. The test with Rycon grease indicates a strong resonance which peaks at 1270 Hz and the test with duct seal has a strong resonance which peaks at 1420 Hz. This discrepancy in resonances can be attributed to the mechanical and acoustical performance differences between the two couplants. The duct seal is superior to the Rycon grease in the ability to mechanically attach to the concrete surface. However, it was noted that in colder temperatures, the duct seal becomes difficult to mold to create a thin layer between the geophone and a concrete surface. Therefore, better performance can be expected for duct seal in warm weather and Rycon grease in cold weather.

5.3.3 Discussion

A good mechanical bond was achieved using the epoxy, duct seal and cold Rycon grease. However, the acoustical differences were seen in the higher frequencies of the velocity spectrums which resulted in differing locations of the peak rise in the mobility plot. This frequency shift is also a function of the Rayleigh wave speed for surface waves. As the concrete aged, the propagation velocity of the Rayleigh waves increased, consequently, the peak in mobility was observed at higher frequencies. Thus, the rise observed in the mobility plot is a function of the type of couplant used as well as surface wave effects.

It can be concluded that the type of couplant used to affix the geophone used for this study to a concrete shaft surface affects the interpretation of an impulse response result, particularly at frequencies greater than 800 Hz. Thus, analysis of mobility signals in the lower frequency range are reliable, whereas the interpretation of the higher frequency portion is affected by couplant effects.

5.4 Summary

This chapter presented the results from several investigations into factors which affect the interpretation of sonic echo and impulse response results. First, the effect of concrete age on the interpretation of impulse response results was presented. The increase in wave propagation velocity with time for the concrete used in this study, was evaluated based on the results of unconfined compression tests and UPV tests on concrete cylinders, in conjunction with results of sonic echo and impulse response tests were analyzed. The effect of concrete age, especially less than 7 days after pouring, limits the confidence in the analysis procedure. For example, tests at 7 days using the embedded geophones indicated a variation in propagation velocity of ±5% which decreased to ±2% for 28 day tests. In addition to these time effects, there were different apparent velocities depending on the manner in which the propagation velocity was measured. The scatter in all of the data indicates that the uncertainty in the wave propagation velocity through the concrete used in length calculations can be as much as ±5%, depending on whether the velocity is measured, estimated, or found from correlations with strength. The use of different couplants to attach a geophone to a concrete surface affects the interpretation of shaft integrity. Inadequate coupling of the geophone to the concrete surface contributed to distortion of mobility plots above 800 Hz which interfered with the interpretation of mobility signals above these frequencies.

Table of Contents

Chapter 6. Numerical Analysis of Impuse Response Signals

- 6.1 Introduction
- 6.2 Simulation of impulse response signals
  - 6.2.1 Simulation of nges accessible shafts
  - 6.2.2 Simulations of nges inaccessible shafts
- 6.3 Resolution of impulse response signals
  - 6.3.1 Homogeneous subsurface conditions
  - 6.3.2 Layered subsurface conditions
- 6.4 Frequency ranges for inaccessible head conditions
- 6.5 Summary

6.1 Introduction

Impulse response tests performed on drilled shafts in the field do not always generate mobility curves which are easy to interpret as a result of variations in the shaft diameter, concrete quality, or soil stiffness. For this reason, numerical analyses are often useful to assist in the interpretation of field-obtained signals. One such numerical analysis technique used in this study is based on the analogous relationships between mechanical and electrical systems presented in SECTION 2.3.1.4. The other technique, described in SECTION 2.3.1.5, uses resolution charts which were developed from theoretical relationships to quantify the effect of the foundation-soil interaction on the impulse response results.

This chapter presents numerical analyses of signals obtained from the impulse response tests conducted at the NGES test site. First, numerical simulations of impulse response signals for the accessible and inaccessible shafts are presented, and comparisons are made between the numerical simulations and the observed results. Shaft and soil parameters are examined to achieve the best fit between the experimental and simulated mobility curves. The chapter continues with the development of resolution charts for both homogeneous subsurface conditions and layered soil systems, and concludes with a discussion of the observed signal resolution of the impulse response signals of the NGES shafts.

6.2 Simulation of Impulse Response Signals

The simulation program used for this study was the Siminteg Simulation Program developed by

Centre Experimental de Recherche et des Etudes du Batiment et des Travaux Publics-CEBTP of Paris, France and revised by STS Consultants, Ltd. The program utilizes the analogue existing between mechanical wave propagation and electrical transmission lines presented in SECTION 2.3.1.4.

6.2.1 Simulation of NGES Accessible Shafts

A two-step procedure was used to determine the best correlation between a numerically-simulated signal and a field-observed signal for the five shafts at the NGES test site. First, the accessible-head shafts were simulated using the comprehensive test section data for as-built shaft dimensions, concrete properties, and soil properties determined from extensive site and laboratory investigations. These are termed "best estimate" simulations. Following the initial simulations, the parameter inputs were modified to more accurately match the impulse response curves. These are called "best fit" simulations.

6.2.1.1 Simulations using "Best Estimate" Parameters

Shaft Parameters

The simulation parameters required for the drilled shafts were the shaft length and diameter, and the density and propagation velocity of the concrete. Considering the careful construction procedures, the as-built shaft lengths are reliably known, as are the diameters of the permanently cased lengths of the shafts. Thus, the dimensions of the shafts for the initial simulations were based on the as-built dimensions for the accessible-head condition as exhibited in FIGURES 3.7, 3.8, 3.9, 3.10, and 3.11. for shafts 1 to 5, respectively. The relative elevations of each shaft head, toe, and defect relative to the surrounding soil layers are summarized in FIGURE 3.6. The density and compression wave velocity for the concrete were determined from field and laboratory tests, as discussed in SECTION 3.3.2.4. The density of the sixty concrete cylinders, cast from the concrete used to construct the five drilled shafts, was determined by weighing and measuring the dimensions of each cylinder. Based on the results, a concrete density of 2450 kg/m^3 (153 pcf) with a standard deviation of 48 kg/m^3 (3 pcf) was used for the simulations for shafts 1 to 4 and a concrete density of 2240 kg/m^3 (140 pcf) with a standard deviation of 11 kg/m^3 (0.7 pcf) for shaft 5. The propagation velocities used for these simulations were determined from time domain analyses of tests performed 28 days after concrete placement, using the geophones embedded at the toe of each shaft. Thus, the velocities were determined for a wave which traveled one length of the shaft and was recorded near the shaft toe. These one-way travel time velocities were presented in SECTION 5.2.2.2.

Soil Parameters

The soil parameters required for simulations include the soil density, the soil shear wave velocity, and the thickness of each soil layer. The soil profile used for simulating the accessible shafts at the NGES was based on two boring logs, B-2 and B-3 located within a few feet of the test section, identified on FIGURE 3.1. As shown in FIGURE 3.2, the soil profile at the NGES test site generally consists of four layers: sand fill, soft clay, hard glacial till, and Dolomite bedrock.

The soil properties used for these numerical simulations are shown in TABLE 6.1. The average

density for each soil stratum was determined based on the geotechnical characterization of the soils at the site presented in SECTION 3.2. TABLE 6.1 also lists the shear wave velocities for each soil layer based on the cross-hole seismic testing presented in SECTION 3.2.2. These are average values representative of each soil layer, and are used to simplify the numerical simulation process. A more detailed profile of the soil shear wave velocities was presented in FIGURE 3.4. The shear wave velocity was determined up to a depth of 27.4 m (90 ft), and thus the shear wave velocity of the Dolomite bedrock was not measured.

Shafts without Defects

Shaft 3

The experimental and simulated mobility curves for shaft 3 are presented in FIGURE 6.1. The experimental curve is described in detail in SECTION 4.2.2.1. Shaft 3 provided an opportunity to model the response of an almost "ideal" drilled shaft because the permanent liner provided a constant cross-sectional area for a length of 10.5 m (34.5 ft) of the 12.2 m (40 ft) total length, therefore leaving only the bottom 1.7 m (5.5 ft) of the shaft to contain possible unknown changes in cross-section.

As shown in FIGURE 6.1, the shaft was modelled with constant concrete properties throughout the length of the 12.2 m (40 ft) shaft. The diameter was 0.61 m (2 ft), the propagation velocity was 4006 m/s and the concrete density was 2450 kg/m^3. The soil surrounding the shaft was divided into four layers. The first layer accounted for the 0.3 m (1 ft) stickup of the shaft above the ground surface. The next two layers accounted for the sand fill, both above and below the water table, and the final layer was soft to medium clay. Evaluation of the two signals shows that the resonant peaks are in good alignment, indicating that the experimental propagation velocity, suggested by the impulse response result, was similar to the one-way velocity determined from the embedded geophones, and that the shaft length was as expected. Also, the simulated signal has an average mobility of 3.7 x 10^{-7} m/s/N which is slightly lower than the experimental signal which has an average mobility equal to 3.8 x 10^{-7} m/s/N. This indicates that the quality of the concrete was as expected and the as-built shaft dimensions are accurate. The most obvious difference between the simulated and experimental mobility curves is the signal resolution (P/Q). The resolution of experimental signal is 1.9 compared to 1.24 for the simulated signal, which indicates that the damping properties of the soil surrounding the shaft were less than expected. Also, the larger stiffness of the simulated curve, 1.09 MN/mm, compared to that of 0.68 MN/mm for the experimental curve, further suggests the smaller damping caused by the in situ soil.

Shaft 4

FIGURE 6.2 shows the experimental and simulated mobility curves using the "best estimate" parameters for shaft 4. The experimental curve is described in detail in SECTION 4.2.2.1. The shaft was modelled with uniform concrete properties throughout the length of the 21.3 m (70 ft) shaft. As shown in FIGURE 6.2, the diameter was 0.76 m (2.5 ft), the propagation velocity was 4075 m/s and the concrete density was 2450 kg/m^3. The soil surrounding the shaft was divided into seven layers. The first layer accounted for the 0.3 m (1 ft) stickup of the shaft above the ground surface. The six soil layers are, from the ground surface down, sand fill above and below the water table, soft to

medium clay, clay with gravel, medium clay, and hard glacial till.

The resonant peaks from the simulated signal are in reasonable agreement with the experimental signal. This suggests that the experimental propagation velocity, indicated by the impulse response results, was similar to the one-velocity determined from the embedded geophones, and also the shaft length is as expected. Several differences between the two curves are quite obvious. First, the average mobility, N, of the simulated signal is 2.3 x 10^{-7} m/s/N which was greater than the experimental signal that has an average mobility of 1.96 x 10^{-7} m/s/N, at least for frequencies less than 600 Hz. This may be due to better than expected concrete quality, an increased cross-sectional area, or both. The experimental signal begins to rise around 600 Hz, possibly in response to surface waves and inadequate geophone coupling. Another difference between the two curves was the measured signal resolution. The resolution of the simulated signal was 1.04, in contrast to a resolution of 1.2 for the experimental signal with well-defined peaks; thus, the simulated soil parameters attenuated the signal more than the actual soil parameters. The shape of the two signals are dissimilar as shown by the "pairing" of peaks in the experimental signal between 400 and 1000 Hz. This secondary response has a change in frequency of 200 Hz, which was measured from the center of the two peaks forming the two superimposed secondary resonances observed between 400 to 600 Hz and 600 to 800 Hz. This suggests a possible anomaly in the shaft at a depth of 11 m (35 ft), not accounted for in the "best estimate" parameters. Finally, the experimental low-strain stiffness value, 1.21 MN/mm, was less than that of the simulated response, 1.64 MN/mm, again suggesting smaller damping caused by the in situ soil.

Shaft 5

The experimental and simulated mobility curves for shaft 5 are presented in FIGURE 6.3. The experimental curve is described in detail in SECTION 4.2.2.1. As shown in FIGURE 6.3, the shaft was modelled with constant concrete properties throughout the length of the 27.5 m (90.2 ft) shaft, having a diameter of 0.91 m (3 ft). The one-way propagation velocity was 3653 m/s and the concrete density was 2240 kg/m^3. Seven layers were used to model the surrounding soil conditions. The first layer accounted for the 0.3 m (1 ft) stickup of the shaft above the ground surface. From the ground surface down, the idealized stratigraphy included the sand fill, above and below the water table, soft clay, clay with gravel, medium clay, and hard glacial till.

Comparison of the simulated and experimental curves shows that the resonant peaks were not in good alignment. In fact, resonances from the toe at 27.5 m (90.2 ft) were not identified in the simulated signal. The simulated signal does not capture the reflection indicated by the stronger resonance at 230 Hz in the observed signal. This resonance indicates a possible defect in the shaft or a reflection from a highly confining soil layer, neither of which are accounted for in the "best estimate" simulation. Additional dissimilarities between the two signals are quite apparent. First, the average mobility, N, of the simulated signal was 1.9 x 10^{-7} m/s/N which was greater than the experimental signal that has an average mobility of 1.4 x 10^{-7} m/s/N. As a result, the shaft may contain an increased cross-sectional area, be cast of better than expected concrete quality, or a combination of both. Furthermore, the resolution of the simulated signal was essentially 1.0 compared to 1.05 for the experimental signal suggesting that the in situ soil has smaller attenuating characteristics than assumed in the simulation. Also, the low-strain stiffnesses were not in agreement. The experimental result was 1.65 MN/mm, while that of the simulated result was 1.77 MN/mm. Thus, soil-structure interaction at the toe and along the shaft was not adequately modelled in the "best estimate" simulation.

Shafts with Defects

Shaft 1

Shaft 1 was simulated with "best estimate" parameters to model the impulse response result that was described in detail in SECTION 4.2.2.2. The experimental and simulated mobility curves for shaft 1 are presented in FIGURE 6.4. With the exception of the soil-filled joint, the shaft was modelled with constant concrete properties throughout the length of the 12.2 m (40 ft) shaft with a diameter of 0.61 m (2 ft) and concrete density of 2450 kg/m^3. The soil surrounding the shaft was divided into four layers to model the shaft head stickup, sand fill, both above and below the water table, and soft to medium clay.

To simulate the soil-filled joint, an estimate of 1000 m/s was made for the propagation velocity through the joint, to reflect the fact that during free fall placement of the concrete, the concrete mixed together with the clay pieces placed in the shaft to form a soil-filled joint. The velocity of the concrete for the full length of the shaft was computed to be 3775 m/s, based on the one-way velocity determined from the embedded geophone of 3750 m/s, and estimating the thickness of the joint to be 10 cm (4 in.).

Comparison of the two curves suggests that peaks from the soil-filled joint are aligned and the toe reflection is verified at 300 Hz, as suggested in section 4.2.2.2. The average mobility, determined by the peaks governed by the defect (between 400 and 1000 Hz), for the simulated mobility curve was 4.6 x 10^{-7} m/s/N, slightly less than the average mobility of 6 x 10^{-7} m/s/N determined for the experimental curve. Similar to the other shafts, the resolution of the simulated signal was less than the experimental signal. Also, the low-strain stiffnesses computed as 0.95 MN/mm for the simulated mobility curves was greater than 0.57 MN/mm for the experimental curve.

Shaft 2

FIGURE 6.5 shows the experimental and simulated mobility curves using the "best estimate" parameters for shaft 2. The experimental test is described in detail in SECTION 4.2.2.2. The shaft was modelled with uniform concrete properties throughout the length of the 21.3 m (70 ft) shaft with a concrete density of 2450 kg/m^3 and a propagation velocity of 3909 m/s. Similar to shaft 4, the soil surrounding the shaft was divided into seven layers to model the shaft head stickup, and from the ground surface downward, sand fill both above and below the water table, soft to medium clay, clay with gravel, medium clay, and hard glacial till.

The reduced cross-section defect (neck) was estimated to be a 25% reduction in the cross-sectional area based on construction procedures at the site (SECTION 3.3.2.1). The shape of the sandbags was carefully observed during the free-fall placement of the concrete, and thus the defect geometry before concrete placement was approximately known. As a first approximation, the neck was simulated as a constant reduction in cross-sectional area with a diameter of 0.76 m (30 in.) between 3.76 m (12.3 ft) and 4.47 m (14.7 ft).

Evaluation of the two signals indicated that the reduced cross-section defect (neck) was clearly

identifiable by the peaks around 560 and 1010 Hz, as were seven clear toe reflections below 700 Hz in the mobility simulation. However, the average mobility of the simulated curve for the first four peaks identifying the shaft toe was greater than the experimental curve, computed as 1.6 x 10^{-7} m/s/N and 1.2 x 10^{-7} m/s/N, respectively. The average mobility for the defect resonance around 600 Hz was 1.8 x 10^{-7} m/s/N compared to 3 x 10^{-7} m/s/N for the experimental signal. The average mobility for the experimental resonance around 1000 Hz was not matched by the simulated response. As for all five shafts, the resolution of the simulated mobility was lower than the experimental curve, indicating that the in situ soil adjacent to the shaft has lower damping properties than estimated for this simulation. Similar to the other shafts, the simulated low-strain stiffness for shaft 2, 1.73 MN/mm, was greater than the experimental value, 1.57 MN/mm.

6.2.1.2 "Best Estimate" to "Best Fit" Simulations

To more accurately simulate the accessible-head shafts, changes to the input parameters were made to find a "best fit" simulation. These best fit simulations accounted for irregularities in shaft geometry and soil and concrete properties resulting from construction procedures that might not necessarily be known or quantifiable at the time integrity tests are conducted. In general, the changes made to each of the parameters consisted of modifying the propagation velocity in the concrete, v_c, to align the frequency of the resonant peaks; increasing cross-sectional areas to decrease the average mobility and capture reflections from unplanned defects; and most effectively, decreasing the shear wave velocities and densities of the soils to increase the resolution and decrease the stiffness of the simulated mobility curves.

The first parameter changed for each simulation was the propagation velocity of the concrete. This was done to align the resonating peaks by increasing or decreasing the propagation velocity, depending on the experimental shaft response. Next, the average mobilities were matched. For three of the shafts, shafts 2, 4, and 5, it was necessary to decrease the average mobility by increasing the cross-sectional area. Decreasing the average mobility can also be achieved by increasing the concrete density or the propagation velocity. However, in most cases only the cross-sectional area was increased, because variations of the concrete density within the range determined for each shaft in SECTION 3.3.2.4 had a minimal effect on the mobility, and changes in the propagation velocity misaligned the resonating peaks.

The increased cross-sectional area can be justified in several ways. First, the diameter of shaft was increased in the permanently-lined portion of the shaft to account for the added diameter of the shaft created by the corrugation of the steel liner. Also, an effective area based on equivalent impedances was computed to include the effects of the steel liner. For a 1/16 inch thick liner, the effective diameter of a nominally 0.61, 0.76, and 0.91 m (2, 2.5, and 3 ft) concrete shaft was computed be 0.63, 0.78, 0.94 m (2.07, 2.57, 3.07 ft), respectively, to account for the combined effects. Also, the diameter of shaft was increased through the soft to medium clay layer to account for over-drilling. Increased cross-sectional areas (bulges) were also added at the temporary casing interfaces to account for construction procedures.

The most significant change was to vary the soil parameters to increase the resolution of the simulated mobility curves. For all five shafts, both the soil density, r_s, and soil shear wave velocity, v_s, were decreased to increase the P/Q resolution of the mobility signal and match the low-strain stiffness, K'. This was reasonable for the sand fill layer because the backfill sands placed in the

annulus between the temporary and permanent liners were not compacted. This resulted in a fill surrounding the upper most portion of each shaft which was looser than the sand between the boreholes used in the cross-hole seismic testing. These changes had the effect of reducing the signal attenuation of the propagating wave. Specific changes for each shaft are discussed in the following sections.

Shafts without Defects

Shaft 3

The "best fit" simulation for shaft 3 is shown in FIGURE 6.6. The experimental curve as well as simulated data for changes to both the sand and clay layers and the sand layer only are presented. The "best estimate" simulation was improved by first decreasing the propagation velocity, v_c, from 4006 m/s to 3950 m/s to align frequency of peaks. Excellent agreement in peak alignment was achieved up to 1000 Hz. To match the average mobility, the diameter was increased from 0.61 m (24 in.) to 0.64 m (25 in.) along the length of the shaft to accommodate the effects of the permanent liner and over-drilling in the soft clay. The average mobility of the two curves are a good match up to about 400 Hz, after which the observed curve begins to deviate from a constant average mobility. This rise in the signal can be attributed to inadequate geophone coupling and surface waves which can not be accounted for in the simulation.

The parameters for the soil surrounding the shaft required the most changes to model the observed resolution and low-strain stiffness. Due to the uncompacted backfilling of the sand around each shaft, the actual shear wave velocity and density of the sand backfill in the upper portion of the shaft were less than those indicated by the site investigation. Also, while disturbance from drilling would reduce the stiffness of the clay, the magnitude of the reduction was not quantified during site investigations. To achieve the best signal resolution match, the soil shear wave velocity, v_s, of the backfill sand was decreased from 177 m/s to 110 m/s and its density, r_s, was decreased from 1800 kg/m^3 to 1550 kg/m^3. For the "best fit" case, the depth to the bottom of the sand layer was extended to the depth of the temporary casing instead of the depth to the sand/clay interface as determined from site investigations at boring B-3. This depth was 2.3 m (7.5 ft) deeper than the "best estimate" case, to account for the placement of the temporary casing a few feet into the soft clay and filling the annulus with loose backfill. Also, the shear wave velocity and density of the soft clay were decreased from 222 m/s to 170 m/s and 2035 kg/m^3 to 1900 kg/m^3, respectively, to match the signal under 200 Hz. For comparison, the simulated response for changes to the sand layer only, using the "best estimate" clay parameters, is also shown on FIGURE 6.6, and indicates that the additional changes to the clay layer were required to increase the resolution of the signal. The "best fit" simulated soil parameters also provided a good low-strain stiffness match of 0.68 MN/mm, compared to 0.66 MN/mm for the observed curve.

Shaft 4

To achieve the "best fit" simulation shown in FIGURE 6.7, the "best estimate" simulation was improved by modifying the input parameters. This was accomplished by first increasing the propagation velocity, v_c, from 4075 m/s to 4100 m/s to align the frequency of peaks, which was

achieved up to 1000 Hz. To match the average mobility, the diameter was increased from 0.76 m (30 in.) to 0.81 m (32 in.) along the permanently-lined length of the shaft to accommodate the effects of the permanent liner. To account for over-drilling in the clay and till layers, the shaft diameter was increased from 0.76 (30 in.) to 0.86 m (34 in.). Additionally, an increased cross-section (bulge) of dimensions 0.61 m (2 ft) in length and 0.94 m (37 in.) in diameter, a 140% increase in cross-sectional area, was added at a depth of 10.1 m (33 ft), near the bottoms of the temporary casing and permanent liner. This caused a slight decrease in the mobility, but most effectively, it forced the peaks into pairs above 500 Hz to account for the unplanned anomaly created at the permanent liner interface. The combined effects of these three cross-sectional increases created a decrease in mobility to an average of 2.1 m/s/N which was closer to the observed mobility of 1.96 m/s/N than 2.3 m/s/N from the "best estimate" simulation. The rise in the observed mobility curve, beginning around 600 Hz, was not replicated in the simulation.

The parameters for the soil surrounding the shaft were adjusted to model the observed resolution and low-strain stiffness. To achieve the "best fit" resolution, the shear wave velocity, v_s, was decreased from 177 m/s to 100 m/s and the density, r_s, was decreased from 1800 kg/m^3 to 1550 kg/m^3 for the length of the shaft surrounded by the backfill sand. Also, the depth to the bottom of the loose sand layer coincided with the depth of the temporary casing, which was 1.4 m (4.5 ft) deeper than the "best estimate" case to account for the placement of the temporary casing and backfill. The shear wave velocity was decreased from 222 m/s to 200 m/s for the soft to medium clay layer, from 363 m/s to 320 m/s for the clay layer with gravel, from 247 m/s to 220 m/s for the second soft to medium clay layer, and from 434 m/s to 375 m/s for the glacial till layer. Also, the density was decreased from 2035 kg/m^3 to 2000 kg/m^3 for the three clay layers, and from 2245 kg/m^3 to 2150 kg/m^3 for the glacial till layer. These changes achieved a good match for the resolution of the peaks below 400 Hz and matched the low-strain stiffness to the observed curve with a stiffness of 1.21 MN/mm.

Shaft 5

In FIGURE 6.8, the resulting "best fit" simulated response and the experimental response are presented. Agreement in peak alignments was somewhat achieved below 400 Hz by increasing the propagation velocity, v_c, from 3653 m/s to 3950 m/s. To more closely simulate the average mobility, the diameter was increased from 0.91 (36 in.) to 0.97 m (38 in.) along the permanently-lined length of the shaft to accommodate the effects of the steel liner, and the shaft diameter was increased from 0.91 (36 in.) to 1.0 m (40 in.) to account for over-drilling in the clay and till layers. These cross-sectional increases created a decrease in mobility to an average of 1.5 m/s/N which was closer to the observed mobility of 1.4 m/s/N than 1.9 m/s/N from the "best estimate" simulation. As for shafts 3 and 4, the simulation did not reproduce the rise in the observed mobility curve which began around 500 Hz. The strong peak observed at 230 Hz was a reflection from the permanent liner interface at a depth around 11.9 m (39 ft). At this depth, there are two sources of reflection: the transition from the loose backfill to the clay layer; and the enlarged cross-sectional area due to over-drilling in the clay.

As was done for shaft 3 and 4, the parameters for the soil surrounding the shaft were adjusted to model the observed resolution and low-strain stiffness. The shear wave velocity, v_s, was decreased from 177 m/s to 115 m/s and the density, r_s, was reduced from 1800 kg/m^3 to 1550 kg/m^3 for the sand backfill. For the "best fit" case, the depth to the bottom of the loose sand layer corresponded to the depth of the temporary casing, which was 3.7 m (12 ft) deeper than the "best estimate" case.

Also, the shear wave velocity and density of the clay and glacial till layers were reduced to the same values as they were for shaft 4 to better simulate the resolution of the peaks below 400 Hz. The low-strain stiffness determined from the "best fit" curve was 1.46 MN/mm, a closer match to the value of 1.65 MN/mm for the observed response than the value of 1.77 MN/mm for the "best estimate" case.

Shafts with Defects

Shaft 1

The "best fit" simulated response and the observed response for shaft 1 are shown in FIGURE 6.9. Excellent agreement in the peak alignments from the soil-filled joint defect at 480 and 900 Hz was achieved by increasing the propagation velocity from 3775 m/s to 3900 m/s in the portion of the shaft with good quality concrete, and decreasing the propagation velocity from 1000 m/s to 700 m/s in the soil-filled joint. These changes also aligned the resonant peaks from the toe of the shaft observed at 120 and 275 Hz. Resonances from the toe at higher frequencies are masked by the stronger resonances from the soil-filled joint.

Similar to shaft 3, the diameter was increased from 0.61 m (24 in.) to 0.64 m (25 in.) along the length of the shaft to match the average mobility by accounting for the effects of the permanent liner and over-drilling in the soft clay. The average mobility of the two curves were a good match up to about 720 Hz, after which the observed curve has a slightly higher average mobility than the simulated response.

The parameters for the soil surrounding the shaft were adjusted in the same way as those for shaft 3. The soil shear wave velocity, v_s, was decreased from 177 m/s to 110 m/s and the soil density, r_s, from 1800 kg/m^3 to 1550 kg/m^3 for the length of the shaft surrounded by the backfill. Also, the depth to the bottom of the loose sand layer coincided with the bottom of the temporary casing, which was 2.1 m (6.8 ft) deeper than the "best estimate" case to account for the placement of the temporary casing and backfill. Also, the shear wave velocity and density of the soft clay were decreased from 222 m/s to 170 m/s and 2035 kg/m^3 to 1900 kg/m^3, respectively. These simulated soil parameters resulted in a low-strain stiffness of 0.59 MN/mm, a good match with the 0.57 MN/mm of the observed curve.

Shaft 2

In FIGURE 6.10, the"best fit" simulated response and the experimental response for shaft 2 are shown. To align the resonating peaks, the propagation velocity was increased from 3909 m/s to 3960 m/s, which resulted in a good agreement in peak alignment up to 740 Hz. Additionally, two resonances from the secondary response caused by the necking defect were clearly reproduced in the simulation at 560 and 1040 Hz.

Because the peaks in the "best estimate" simulation were in reasonable alignment, the geometry changes were modelled first. Similar to the other shafts, the diameter was increased from 0.91 (36 in.) to 0.97 m (38 in.) along the permanently-lined length of the shaft to simulate the effects of the steel liner. The simulated geometry of the necking defect was modified to account for the bulging of the sand bags which occurred during installation of the reinforcing cage. During construction, the

sand bags bulged at the bottoms when the reinforcing cage was lowered into the hole. Thus, the defect was modelled in two parts. The top 0.41 m (16 in.) of the defect was modelled with a diameter of 0.84 m (33 in.) and the bottom 0.3 m (12 in) was modelled with a diameter of 0.58 m (23 in.). This geometry resulted in a more accurate representation of the resonating peaks from 200 to 700 Hz. Additionally, the diameter was increased from 0.91 (36 in.) to 1.0 m (40 in.) for the shaft length passing through the soft clay to match the shape of the peaks between 120 and 400 Hz to account for likely over-excavation.

To achieve the "best fit" resolution, the parameters for the soil surrounding the shaft were adjusted in a similar way as those of shaft 4. The value of v_s was decreased from 177 m/s to 110 m/s and r_s was reduced from 1800 kg/m^3 to 1550 kg/m^3 for the sand backfill, which was extended 1.4 m (4.5 ft) deeper to the bottom of the temporary casing. The shear wave velocity was decreased from 222 m/s to 200 m/s for the soft to medium clay layer, from 363 m/s to 320 m/s for the clay layer with gravel, from 247 m/s to 220 m/s for the second soft to medium clay layer, and from 434 m/s to 375 m/s for the glacial till layer. Also, r_s was decreased from 2035 kg/m^3 to 2000 kg/m^3 for the three clay layers, and from 2245 kg/m^3 to 2150 kg/m^3 for the glacial till layer. These changes resulted in a match of the resolution of the experimental and simulated response. The low-strain stiffness was simulated as 1.35 MN/mm, close to that of the observed stiffness of 1.57 MN/mm.

Summary of Accessible-Head Simulations

The changes made to achieve the "best fit" simulations from the "best estimate" simulations are summarized in TABLES 6.2 and 6.3 for the shaft and soil parameters, respectively. To achieve the "best fit" simulations, the propagation velocity was changed -1.4 to 8.1% for all five shafts. From the data shown in FIGURE 5.4, variations in propagation velocity can be ±5%, depending on whether the velocity is measured, estimated, or found from correlations with strength. Thus the magnitudes of these adjustments are consistent with the normally-expected variations of the propagation velocity.

The concrete density was not changed, except for the soil-filled joint in shaft 1 and for shaft 5, where it was increased 7.1%. The density for shaft 5 was increased from 2240 kg/m^3 based on cylinders obtained from shaft 5, to 2400 kg/m^3, which was much closer to the average density of 2450 kg/m^3 for all other cylinders. This change suggests that the cylinder samples from shaft 5 were either not representative of the majority of the concrete, or a systematic error occurred while sampling or testing the cylinders.

Adjustments in shaft diameter for the permanent casing ranged from 4.9 to 6.6% and the overdrilling in the soft to medium clay ranged from 9.9 to 13.2%. The magnitude of the overdrilling is consistent with data presented by Stas and Kulhawy (1984) where average diameters of drilled shafts installed in sands with slurry exceed design values by 15% while those installed in soft clays exceed design values by 5%, as a result of imperfect centering of the auger during drilling or sloughing of the sides of the holes in sands, which result in a larger diameter drilled hole.

The largest changes in shaft parameters required to match the experimental signals were needed for the shafts 1 and 2, both with defects. Specifically, a 30% reduction in propagation velocity and a 10% increase in the density was required to simulate the soil-filled joint. This relatively large correction is the result of a rough estimation of the joint properties in the "best estimate" simulation,

and is to be expected because of the nature of the as-built defect, a mixture of clay and concrete. In shaft 2, the neck defect was divided into two sections for the "best fit" simulation rather than the single section used for the "best estimate" simulation, wherein the diameter was increased by 10.5% in the upper portion and decreased by 23.7% in the lower portion.

As shown in TABLE 6.3, the greatest changes to the soil parameters for all five shafts were made to the surficial sand layer, which required a 35 to 44% decrease in the shear wave velocity and a 14 to 17% reduction in the soil density to account for the loose backfill placed around the shafts. Changes made to the soft to medium clay layer included a 10 to 23% reduction in shear wave velocity and a 2 to 7% decrease in density. Softer clays are more susceptible to disturbance from augers than stiffer clays, as observed by the respective reductions in shear wave velocities and densities for the two layers. The deepest clay layer and glacial till layer were modified the least. An 11% reduction in the soil shear wave velocity and a 2% decrease in density was needed for the deepest clay layer, and a 14% decrease in the soil shear wave velocity and a 4% reduction in the density was made to the hard glacial till layer. The modified shear wave velocities and densities fall within the range of values for each parameter, as presented in Table 2.1 for sands and clays. Reported shear wave velocities for sands range from 850 m/s to 100 m/s for densities ranging from 2100 kg/m^3 to 1500 kg/m^3 (Peck, 1974). Thus an 88% reduction in shear wave velocity and a 28% reduction in density are possible over the range of values. The changes made to the shear wave velocities and densities in the best fit simulations fall well within these ranges of values.

A summary of the analysis of the "best estimate" and "best fit" simulated mobility curves for the five shafts is presented in TABLE 6.4. For all five shafts, the "best estimate" simulated signal resolution, P/Q, was less than the experimental resolution indicating that the soil surrounding the drilled shaft had attenuating properties (v_s and r_s) smaller than the values determined by site investigations. This was mostly due to the loose backfill surrounding the permanently-lined portion of the shafts. These higher values of v_s and r_s also contributed to the higher low-strain stiffness values calculated for the simulated curves. The simulated average mobility was higher than expected for all shafts, except shaft 3 which had a similar value. In general, the "best estimate" simulations provided a reasonable estimate for the shapes of the observed mobility curves, including a good estimate of the observed responses for the two shafts with defects. In practice, the lower N values for the experimental curves would indicate that an acceptable drilled shaft had been constructed. This conclusion arises primarily because the cross-sectional areas of the shafts are slightly larger than the design values.

The "best fit" simulations were achieved by altering the wave propagation velocity to align the peaks, locally increasing the cross-sectional area to account for construction techniques, and reducing the attenuating properties of the soils. As summarized in TABLE 6.4, the peaks were aligned and the resolution and low-strain stiffness values were matched for all five shafts. The average mobility was modelled well for shafts 1, 2, and 3; whereas, for shafts 4 and 5, the simulated average mobility was slightly higher than the observed. Since the average mobility is a function of the shaft cross-sectional area, propagation velocity and concrete density, increasing any of these parameters would decrease the average mobility. However, there is no basis to further increase the values of these shaft parameters because all the known effects from construction techniques were modelled. Therefore, this slight discrepancy may be attributed to equipment effects, such as inferior geophone coupling or improper hammer hits. If the hammer head was not hit square to the shaft head surface, the energy transmitted to the shaft would be lower than what was recorded by the load cell in the hammer; therefore, the velocity spectrum would be divided by a force spectrum with a larger

magnitude than was actually imparted to the shaft, resulting in a smaller average mobility.

It can be concluded that to accurately simulate results of an impulse response test on a drilled shaft and by implication to interpret the results of such a test, construction details must be known. The study presented herein has shown that variations in the as-built dimensions and surrounding soil conditions created by construction procedures have a substantial effect upon impulse response results. Results at the NGES site indicate disturbance caused by loosely placing backfill in the annulus between the temporary casing and the permanent liner resulted in a 35 to 44% reduction in v_s. Disturbance from drilling in the soft to medium clay resulted in a 10 to 23% reduction in v_s. Using a corrugated permanent liner in the upper portion of the shafts increased the effective diameter by 4.9 to 6.6% and overdrilling in soft to medium clays created an increase in diameter from 9.9 to 13.2%.

6.2.2 Simulations of NGES Inaccessible Shafts

After the "best fit" shaft and soil parameters were determined by simulations of the five accessible-head shafts, the inaccessible-head conditions were analyzed. Simulations for each inaccessible shaft were based on the "best fit" parameters discussed in SECTION 6.2.1.2 and the as-built lengths as exhibited in FIGURES 3.12, 3.13, 3.14, 3.15, and 3.16 for shafts 1 to 5, respectively. These simulations are approximations of the actual conditions because the pile caps have rectangular geometries, and thus the pile cap-shaft system is not axisymmetric. As discussed in SECTION 2.3.1.4, the existing simulation program is based on one-dimensional wave propagation through a cylindrical rod, and as such, is strictly valid for only axisymmetric conditions.

As a first approximation of the inaccessible-head condition, each pile cap was modelled as an axisymmetric member. The cap geometry was translated to an "equivalent" cylinder by determining an "effective" diameter for each cap. This was accomplished using the "best fit" accessible shaft simulations and adding a concrete cylinder of variable radius and as-built depth to the top of the shaft. The radius of the cylinder was then increased until a good match was found between the experimental and simulated mobility traces.

Pile Cap 1

FIGURE 6.11 shows the effect of increasing the "effective" pile cap diameter for pile cap 1 above shaft 1. The pile cap was modelled with a depth of 0.61 m (2 ft) and a range of diameters from the diameter of the shaft up to 2.75 m (108 in.). For a cap diameter of 0.91 m (36 in.), the toe of the shaft was seen at 280 Hz and the defect was clearly observed at 400 and 800 Hz. As the diameter of the pile cap was increased, the resolutions corresponding to the toe and the defect decreased. Also, the average mobility of the signal decreased in response to the larger pile cap diameter. An effective diameter of 2.29 m (90 in.) resulted in the best fit for the experimental and simulated signals. The resolution and average mobility of the toe resonance were matched at 280 Hz. The best fit and experimental signals were a good match up to 400 Hz, and only the resonance from the defect at 380 Hz was matched. The resonances seen in the experimental result above 400 Hz can therefore be attributed to the actual rectangular geometry of the pile cap not accounted for in the axisymmetric approximation of the cap, the surface wave reflections from the edges of the pile cap, or, more likely, a combination of the two.

The effect of increasing the diameter for the simulations of pile cap 1 above shaft 2 is shown in FIGURE 6.12. An excellent match between the simulated and the observed signals was achieved up to 460 Hz with an effective diameter of 2.29 m (90 in.), the same diameter as for shaft 1. Three resonances from the shaft toe below 400 Hz and one resonance from the defect at 420 Hz were observed in the simulation. Similar to the simulated response for shaft 1, only the first resonance from the defect was matched because the experimental curve deviated from the simulated curve around 460 Hz.

As previously discussed in SECTION 4.3.2.2, the resonances between 500 and 700 Hz for the test conducted directly above the shaft matched the resonances observed in the test performed on the center of the pile cap with the geophone placed along the short axis of the cap, as shown in FIGURE 4.24. A similar trend was observed for tests performed on shaft 1. Therefore, the difference between the experimental and simulated curves at 460 Hz was caused by reflections of surface waves which arise from the rectangular geometry of the pile cap, which was not possible to simulate with an axisymmetric approximation.

For shafts 1 and 2, the pile cap response was best modelled with an effective diameter of 2.29 m (90 in.). This diameter corresponds to an equivalent area of approximately half of the pile cap contributing to the response for each shaft. For cap 1, the tributary area of the pile cap above each shaft had a width, W_{trib}, equal to 1.52 m (5 ft) and a length, L_{trib}, equal to 2.06 m (6.75 ft). Thus, the tributary area is 3.14 m^2 (33.8 ft^2), which is less than the effective area of 4.1 m^2 (44.2 ft^2), determined for the effective diameter of 2.29 m (90 in.) from the simulations. The ratio of the tributary area to the effective area is equal to 0.76.

Pile Cap 2

Pile cap 2, atop shaft 3, was modelled as a cylinder with a depth of 1.52 m (5 ft) and a diameter varying from 0.63 to 1.83 m (25 to 72 in.). The results for the simulated responses from each diameter are shown in FIGURE 6.13. As the simulated diameter of the cap was increased, the resolution of the peaks decreased and the average mobility of the signal decreased exponentially in the frequency range of 60 to 700 Hz. The best match of the simulated and observed signals was achieved with a pile cap diameter of 1.73 m (68 in.) at least up to about 600 Hz, where the two signals began to diverge. Both these signals identified four resonating peaks below 600 Hz with similar resolution and average mobility, and possibly two additional peaks up to 1000 Hz. Thus, the effective area for cap 2 was determined to be 2.34 m^2 (25.2 ft^2), essentially equal to the as-built area of the pile cap of 2.32 m^2 (25 ft^2). Spurious resonances were not observed in the experimental result for cap 2 below 1000 Hz as they were for pile cap 1 and 3 above 460 and 420 Hz, respectively, because the square cap was essentially axisymmetric, and thus well-modelled in the simulation.

Pile Cap 3

For both shafts 4 and 5, the inaccessible-head condition was simulated by placing a 0.91 m (3 ft) deep pile cap atop each shaft and varying the diameter from the diameter of the shaft up to 2.75 m (108 in.). The simulation results are shown in FIGURES 6.14 and 6.15 for shafts 4 and 5, respectively. Similar to the effects of pile caps 1 and 2, as the diameter of the cap was increased, the resolution of the signal decreased and the average mobility decreased exponentially. For both shafts,

an effective diameter of 2.59 m (102 in.) for the pile cap produced the best fit inaccessible-head simulation at least up to 420 Hz after which the experimental curve deviated from the simulated response. In this case, it is clear that the larger width of pile cap 3, and hence the larger effective diameter, precluded identification of the toe for shafts 4 and 5 compared to pile caps 1 and 2. As shown in FIGURE 4.25, the response from the pile cap alone matched the experimental response above shaft 4 at frequencies greater than 420 Hz. Thus, the difference between the experimental and simulated curves at 420 Hz was caused by reflections of surface waves which arise from the actual rectangular geometry of the pile cap, which was not possible to simulate with an axisymmetric approximation.

Similar to pile cap 1, the equivalent area determined for the best fit simulation corresponded to an area approximately half of the pile cap. For shafts 4 and 5, the pile cap response was best modelled with an effective diameter of 2.59 m (102 in.). Thus, the effective area was determined to be 5.27 m^2 (56.7 ft^2). The tributary area of the pile cap above each shaft had a width, W_{trib}, equal to 2.06 m (6.75 ft) and a length, L_{trib}, equal to 2.13 m (7 ft). Thus the tributary area is 4.4 m^2 (47.3 ft^2), which is less than the effective area of 5.27 m^2 (56.7 ft^2) determined from simulations. The ratio of the tributary area to the effective area is equal to 0.83.

Effective Area

For a given pile cap geometry, the "effective" area, $A_{effective}$, of a cap can be determined by applying a factor to the calculated tributary area, $A_{tributary}$, of the pile cap atop a shaft. This factor, F, is applied in the following equation:

$$A(Effective) = \frac{A(Tributary)}{F} \qquad (6.1)$$

The tributary area is defined as the tributary width, W_{trib}, multiplied by the tributary length, L_{trib}; where L_{trib} is the greater dimension. F was determined from the simulations of the three NGES pile caps, and the relationship between F and the ratio of the tributary width to the tributary length, W_{trib}/L_{trib}, is shown in FIGURE 6.16. As the ratio of the tributary width to tributary length approaches 1.0, the factor approaches 1.0, thus a square pile cap atop a single shaft yields a geometry which is essentially axisymmetric.

6.3 Resolution of Impulse Response Signals

Resolution charts were generated for various subsurface profiles to delineate stratigraphy effects and quantify attenuation characteristics of impulse response tests on drilled shafts and driven concrete piles. The resolution of an impulse response signal is defined by the ratio of P and Q, the maximum and minimum mobilities, as illustrated in FIGURE 2.10. When this ratio approaches 1.0, no resonant frequencies can be identified and thus one can not expect to be able to locate the bottom of a drilled

shaft under those conditions. Using the theoretical equations developed in SECTION 2.3.1.5, closed form solutions for the resolution of mobility signals for accessible-head situations were developed for uniform soil conditions. Solutions for multi-layer soil conditions were developed based on results of numerical simulations made with the code described in SECTION 2.3.1.4. The resolution for a given soil system (ideally homogeneous), is primarily a function of the L/D ratio, the ratio of the shear wave velocity of the soil to that of concrete, and the ratio of soil density to concrete density.

6.3.1 Homogeneous Subsurface Conditions

As discussed in SECTION 2.3.1.5, closed form solutions were developed from the theoretical equations to create resolution charts for ideal uniform soil conditions. The chart was developed for length-to-diameter, L/D, ratios of 15, 20, 25, 30, and 35. The resolution chart for the ideal case was first introduced in FIGURE 2.13 and is reproduced in FIGURE 6.17 to compare the resolution determined from the experimental mobility curves for each of the three shafts with no planned defects.

The resolutions of the impulse response signals for the five NGES shafts were determined by selecting the values of P and Q from the experimental mobility plots. Based on the analysis in SECTION 4.2.2, the calculated resolution (P/Q) and length-to-diameter (L/D) ratios for each of the five shafts is summarized in TABLE 6.5. For the shafts with planned defects, the resolution is given for the full length of the shaft, as well as the resolution of the defect.

The calculated resolution for shafts 3, 4, and 5 are plotted at their respective L/D ratios in FIGURE 6.17. For each shaft, the soil shear wave velocity to concrete propagation velocity ratio, v_s/v_c, was determined using the P/Q and L/D ratios. Using the propagation velocity determined from the mobility curves for each shaft, a soil shear wave velocity can be determined. This shear wave velocity is an "effective" velocity which incorporates the attenuation effects from all the soil layers surrounding the shafts.

The highest observed resolution for a non-defective shaft was for shaft 3 with a P/Q ratio of 1.9, as a result of both the uniformly-cylindrical shape of the shaft (it was cased almost its entire length) and the presence of the sand backfill surrounding the shaft, which had a relatively low shear wave velocity. Also, this shaft had the lowest L/D ratio, 20, of the five shafts. From the resolution chart, the v_s/v_c ratio for shaft 3 was determined to be 0.029. Using the propagation velocity, v_c = 3810 m/s, found from the analysis of the mobility curve, the effective soil shear wave velocity, v_s, was calculated to be 110 m/s. This value is close to the effective shear wave velocity equal to 118 m/s which was determined by weighting the shear wave velocity for each layer from the "best fit" simulations to the length of the shaft through that layer. Also this average value is less than the effective shear wave velocity equal to 183 m/s which was determined by weighting the shear wave velocity for each layer based on cross-hole seismic site investigations ("best estimate").

The resolution for the impulse response result for shaft 4 was 1.2. This is a function of the L/D ratio of 23.3 and the shear wave velocity of the soil layers surrounding the shaft, including the sand fill, clay and glacial till. From FIGURE 6.17, the v_s/v_c ratio for shaft 4 was determined to be 0.035, which corresponds to an effective soil shear wave velocity, v_s, of 139 m/s for v_c equal to 3960 m/s.

This value is less than the effective shear wave velocity, 165 m/s, determined by the "best fit" weighted average, and is substantially less than the effective shear wave velocity, 213 m/s, determined by the site investigation weighted average. These weighted averages represent differences in v_s/v_c ratios of 19% and 53%, respectively, between the chart-derived values.

The resolution of the mobility signal for shaft 5 was equal to 1.05. Shaft 5 had the largest L/D ratio of 30 and passed through the sand fill, soft clay and glacial till layers and was seated on Dolomite bedrock. The experimental mobility response for shaft 5 exhibited the highest signal attenuation. This agrees with the trends in the theoretical resolution chart where the L/D and P/Q ratio for shaft 5 yielded the highest v_s/v_c ratio equal to 0.047 which corresponds to an effective soil shear wave velocity, v_s, of 185 m/s for v_c equal to 3940 m/s. This value is less than both the effective shear wave velocity, 210 m/s, determined by the "best fit" weighted average, and the effective shear wave velocity, 260 m/s, determined by the "best estimate" weighted average. These weighted averages represent differences in v_s/v_c ratios of 14% and 41%, respectively, between the chart-derived values.

For shafts 1 and 2, both with planned defects, the resolution of the experimental mobility was dominated by the resonances from the defect. In both cases, the resolution of the defect was larger than the resolution of the resonances from the shaft toe. This is a result of the lower L/D ratios of 7.2 and 4.9 for the planned defects in shafts 1 and 2, respectively, compared to the L/D ratios for the toe of the shaft. As seen in the resolution chart, lower L/D ratios correspond to higher resolutions for a given v_s/v_c ratio. Thus, the higher resolution of the defect governs the interpretation of the shaft integrity.

For shafts 3, 4, and 5, average v_s values found from the resolution chart are within 19% of the weighted averages of v_s found from the "best fit" simulations, which implies that the ideal resolution chart can be used for layered systems, albeit with some discrepancies arising from the assumption of uniform soil conditions. The closer agreement of these values with the "best fit" averages, as compared to v_s found from the cross-hole seismic tests, again emphasizes the need to consider effects of construction on the soil damping parameters.

6.3.2 Layered Subsurface Conditions

Resolution charts for more realistic stratigraphy for deep foundations, e.g. where there is a softer soil overlying a stiffer soil, were developed based on axisymmetric simulations of wave propagation through a drilled shaft surrounded by soil. For a multi-layer system, the important factors determining the resolution are the L/D ratio, the shear wave velocities of the soil layers, and the relative depth of the softer layer. As the soil shear wave velocity increases, the damping due to the concrete to soil interaction increases, and less energy is returned to the top of the shaft where it can be sensed by a transducer. Layered subsurface resolution charts were developed from results of parametric studies using the simulation program previously discussed in SECTION 2.3.1.4. The case of a concrete shaft embedded in a two layered soil system is specifically considered herein.

6.3.2.1 Shaft Parameters

The two-layer resolution charts were generated for shaft length-to-diameter (L/D) ratios of 10, 15, 20, 25, and 30. The wave propagation velocity and density of concrete were held constant for all cases at 4000 m/s (13124 ft/s) and 2400 kg/m^3 (150 pcf), respectively, typical of the concrete quality used at the NGES test section. Variation of the concrete density, as shown in FIGURE 6.18 for L/D ratios of 15, 20, 25, and 30 has a minimal effect on the P/Q resolution, especially for soil shear wave velocities equal to 150 m/s and greater. At lower shear wave velocities, v_s=100 m/s, the ratio of v_s to v_c becomes small, and variations in concrete density have a larger impact on the resolution because the shaft begins to behave more like a free, unconfined rod, where upon the concrete properties have a larger effect on the solution.

6.3.2.2 Soil Parameters

The soil stratigraphy consisted of a surficial soil layer, layer 1, and an embedment soil layer, layer 2. Four soil layer distributions were considered: (1) uniform soil, (2) 50% surficial, 50% embedment, (3) 66% surficial, 33% embedment and (4) 75% surficial, 25% embedment. The soil shear wave velocity, v_s, of the surficial layer was varied from 100 m/s, 150 m/s and 200 m/s, typical of a sand or a soft to medium clay. The ratio of the shear wave velocity of the embedment layer to the shear wave velocity of the surficial soil layer ($v_{s\,(2)}/v_{s\,(1)}$) was increased for each simulation until the resolution, P/Q, became 1.0. The density of the soil was held constant at 1920 kg/m^3 (120 pcf). The effect of variation in the soil density is illustrated in FIGURE 6.19 for L/D ratios of 15, 20, 25 and 30. For soil shear wave velocities 150 m/s and above, variation in soil density has a minimal effect on the resolution, more so for L/D ratios equal to 20 and higher. For lower shear wave velocities, v_s = 100 m/s, and smaller L/D ratios, the ratio of soil to concrete density has a larger effect on the resolution.

6.3.2.3 Selection of Resolution Parameters P and Q

For a perfectly cylindrical drilled shaft in a homogeneous soil layer considered in SECTION 6.3.1, P and Q can be selected as any of the maxima (P_i) and minima (Q_i) from the mobility plot due to the constant amplitude of the curve in the desired frequency range. When considering a drilled shaft embedded in a two-layer soil system, the P and Q values corresponded to the maximum and minimum values that yielded the lowest P/Q ratio. This ratio was the ratio limiting the resolution used to select peaks for D*f* to determine shaft length, L, or concrete propagation velocity, v_c, depending on which is the unknown. To illustrate this for a two-layer soil system, FIGURE 6.20 shows successive simulations where the soil shear wave velocity of the embedment layer was increased from 150 to 550 m/s while keeping the soil shear wave velocity of the surface layer constant at 150 m/s. The example shown is for an ideally cylindrical shaft with an L/D ratio of 20. The soil profile consisted of two layers: 66% surficial and 33% embedment.

As the embedment layer became more stiff relative to the surface layer, the amplitude of the second (P2) and third (P3) peaks decreased at a faster rate than the other peaks, (P1) and (P4), thus creating a limiting P/Q ratio for determining the resolution. Furthermore, peaks P(2) and (P3) started to pair together when the $v_{s\,(2)}$ / $v_{s\,(1)}$ ratio approached 3.0 and eventually became one single peak when the $v_{s\,(2)}$ / $v_{s\,(1)}$ ratio was 3.7 ($v_{s(2)}$ = 550 m/s). At this point, as a result of a strong reflection from the soil interface, the resolution of those two peaks became 1.0, which limited the identification of all

peaks which identified the shaft toe. In contrast, peaks (P1) and (P4) remained at the same frequency for all $v_{s\,(2)} / v_{s\,(1)}$ ratios. These resonant frequency changes lead to errors in estimated lengths when one only considers Df from adjacent peaks. In this example, a 36% underestimation of the shaft length would occur if the reflection from the soil interface was not recognized. Similar effects were also seen for the other two soil profiles considered in this parametric study. In general, as the stiffness of the soil of the second layer increased, the P and Q amplitudes decreased and frequencies changed for several of the resonances making it more difficult to determine the shaft length.

6.3.2.4 Layered Resolution Charts

The resolution charts developed for a two layer soil stratigraphy are shown in FIGURES 6.21, 6.22, 6.23, 6.24, and 6.25. A chart was developed for length-to-diameter, L/D, ratios of 10, 15, 20, 25, and 30. For each L/D ratio, the charts show the relationship between the resolution, P/Q, of the mobility response and the ratio of the shear wave velocities of the embedment layer to the surficial soil layer ($v_{s\,(2)} / v_{s\,(1)}$). In all cases, the resolution of the signal decreases from a given P/Q ratio for the homogeneous soil condition, $v_{s\,(2)} / v_{s\,(1)}$ equals 1.0, to a limiting $v_{s\,(2)} / v_{s\,(1)}$ ratio where the resolution is 1.0, and resonances from a shaft toe are no longer identified by constant frequency intervals. In FIGURE 6.20, this occurs when $v_{s\,(2)} / v_{s\,(1)}$ equals 3.7. As the L/D ratio increases, the limiting $v_{s\,(2)} / v_{s\,(1)}$ ratio becomes smaller .

These charts are useful for determining whether the impulse response method will provide meaningful results for a given shaft and surrounding soil conditions using conventional data reduction techniques. To predict the resolution for a given shaft using the two-layer resolution charts, the length and diameter of the shaft must be known, as well as the ratio of the shear wave velocity of the embedment soil layer to the surficial soil layer. At most sites, shear wave velocity measurements, such as cross-hole seismic, are not often conducted. Therefore, correlations from more common laboratory and field investigations are useful for determining the shear wave velocity of soils at a given site.

Hardin and Drnevich (1972) suggested that for many undisturbed cohesive soils and sands, the shear modulus may be estimated from the following relationship:

$$G = \frac{1230\,(2.973 - e)^2}{1 + e}\,(OCR)^K(\sigma'_0)^{0.5} \qquad (lb/in^2) \qquad (6.2)$$

where e is the void ratio, s_o', is the mean normal effective stress (lb/in^2), and K is an empirical constant that is a function of the plasticity index (PI) given in TABLE 6.6. The shear wave velocity is then computed using EQUATION 2.3.

For sands and gravels, Seed and Idriss (1970) developed the following relationship:

$$G = 1000\ K_2\ (\sigma'_0)^{0.5} \qquad (lb/ft^2) \qquad (6.3)$$

where K_2 is a constant which is related to the void ratio, e, or the relative density, D_r, and shown in TABLE 6.7.

Correlations from common in situ field tests, such as SPT and CPT, are also useful. One such correlation between SPT blow counts and shear modulus (kips/ft^2) is given by the following relationship developed by Imai and Tonouchi (1982):

$$G = 325\ N_{60}^{0.68} \qquad (kips/ft^2) \qquad (6.4)$$

where N_{60} is the blowcount corrected for overburden. A relationship between CPT tip resistance, q_c, and shear modulus (kPa) was developed by Rix and Stokoe (1991) for quartz sand:

$$G = 1634\ (q_c)^{0.25}\ (\sigma'_v)^{0.375} \qquad (kPa) \qquad (6.5)$$

where s_v' is the effective overburden pressure. Other such correlations from field investigations, including PMT and DMT as well, were compiled by Kramer (1996). Kramer suggests that these relationships should be used only as an estimate due to the scatter in the data on which they were based and from the variability of the results obtained by different investigators. The use of measured shear wave velocities with appropriate consideration of construction effects are more reliable than these empirical correlations.

6.3.2.5 Resolution of NGES Test Section Shafts

Resolution charts for layered subsurface conditions, rather than that for a uniform site, more appropriately address the issue of resolution for impulse response testing. From the two-layer resolution charts, the resolutions of shafts 3, 4 and 5 were predicted using both the "best estimate" and the "best fit" soil shear wave velocities. The soil profile for each case was simplified into a two-layer system, surficial and embedment, based on the relative soil shear wave velocities of each layer. This resulted in an "effective" shear wave velocity for each of the two layers determined by weighting the shear wave velocity for each layer to the length of the shaft through that layer.

For shaft 3, the resolution was predicted based on the two layer resolution chart developed for L/D equal to 20 shown in FIGURE 6.23. The subsurface profile was divided into two layers: layer 1 was the sand fill and layer 2 was the soft to medium clay, thus the two layer profile consisted of approximately 75% surficial and 25% embedment layers. For the "best estimate" case, $v_{s(1)}$ was

equal to 177 m/s, and the ratio $v_{s(2)} / v_{s(1)}$ was equal to 1.25; whereas $v_{s(1)}$ was equal to 110 m/s, and the ratio $v_{s(2)} / v_{s(1)}$ was equal to 1.55 for the "best fit" case. The predicted resolution values for each case are summarized in TABLE 6.8. As noted in FIGURE 6.23, the resolution was predicted to be 1.23 and 1.87 for the "best estimate" and "best fit" cases, respectively. The "best fit" resolution prediction is essentially equal to the resolution of 1.9 determined from the experimental impulse response result for shaft 3 in the accessible-head condition.

Since shaft 4 has an L/D ratio of 28, the predicted resolution was determined by interpolating between values found in the two layer resolution charts for L/D equal to 25 and 30, FIGURES 6.24 and 6.25, respectively. For the "best estimate" case, the subsurface profile was divided into two layers: layer 1 included the sand fill and soft clay, 17.4 m (57 ft), and layer 2 included the gravel, medium clay, and glacial till, 3.96 m (13 ft), thus the two layer profile consisted of approximately 75% surficial and 25% embedment layers. The shear wave velocity of the surficial layer, $v_{s(1)}$ was determined to be 194 m/s, based on a weighted average, and the ratio $v_{s(2)} / v_{s(1)}$ was equal to 1.5. Thus, the resolution was determined to be 1.03 for the "best estimate" case. For the "best fit" case, the soil profile was modified based on the simulation study presented in section 6.2.1.2. The subsurface profile was divided into two layers: layer 1 included the loose sand backfill to the depth of the temporary casing, 10.7 m (35 ft), and layer 2 included the soft clay, gravel, medium clay, and glacial till, 10.7 m (35 ft), thus the two layer profile consisted of approximately 50% surficial and 50% embedment layers. The shear wave velocity of the sand fill layer, $v_{s(1)}$ was determined to be 107 m/s, and the ratio $v_{s(2)} / v_{s(1)}$ was equal to 2.08. For these parameters, the resolution was determined to be 1.12 for the "best fit" case. This is less than the resolution of 1.2 determined for the experimental impulse response tests performed on shaft 4 in the accessible-head condition. However, it is a better estimate than predicted for the "best estimate" case.

The resolution for shaft 5 was predicted based on the two-layer resolution charts for an L/D ratio equal to 30 shown in FIGURE 6.25. For the "best estimate" case, layer 1 included the sand fill, soft clay, gravel, and medium clay, 20.7 m (68 ft), and layer 2 included the hard glacial till, 6.76 m (22.2 ft), thus the two layer profile consisted of approximately 75% surficial and 25% embedment layers. The shear wave velocity of the surficial layer, $v_{s(1)}$ had a weighted average equal to 204 m/s, and the ratio $v_{s(2)} / v_{s(1)}$ was equal to 2.13. Thus, as noted in FIGURE 6.25, the resolution was determined to be essentially 1.0 for the "best estimate" case. Similar to shaft 4, the soil profile was modified for the "best fit" case to account for the "loose" backfill surrounding the permanently-cased length of the shaft. The surficial layer included the loose sand backfill to the depth of the temporary casing, 11.9 m (39 ft), and the embedment layer included the soft clay, gravel, medium clay and glacial till, 15.6 m (51.2 ft), thus the two layer profile consisted of approximately 50% surficial and 50% embedment layers. The shear wave velocity of the sand fill layer, $v_{s(1)}$ was equal to 115 m/s, and the ratio $v_{s(2)} / v_{s(1)}$ was equal to 2.47, and as noted on FIGURE 6.25 for these parameters, the resolution was determined to be 1.03 for the "best fit" case. This is slightly less than the resolution of 1.05 determined for the experimental impulse response tests performed on shaft 5, however, it is a better estimate than the predicted resolution of 1.0 for the "best estimate" case, which suggested that no resonances from the shaft toe would be produced.

By comparing the experimental values of P/Q with the P/Q values based on the best-fit parameters in

TABLE 6.8, one can see that the charts based on the two-layer simulations can be used to evaluate the applicability of the impulse response method in field situations. However, accurate estimates are made only when appropriate soil parameters are used, i.e. those which have been adjusted to account for the effects of construction.

6.4 Frequency Ranges for Inaccessible Head Conditions

Analysis of shafts in accessible head conditions are based on the assumption of one-dimensional wave propagation wherein the wavelength of the longitudinal stress wave is greater than or equal to the diameter of the pile. For a 0.61 to 0.91 m shaft diameter and v_c equal to 4000 m/s, the frequencies which can be used and still maintain one-dimensional conditions vary from 4400 to 6560 Hz. Because the impulse hammer used herein imparts frequencies no higher than 2000 Hz, one dimensional conditions are maintained for the accessible head tests.

However, the larger areas created by the pile caps in the inaccessible head tests will limit the frequencies at which information can be extracted concerning an underlying drilled shaft. This "cutoff" frequency can be identified by comparing the experimental and "best-fit" mobility curves for shafts 1 through 5 (FIGURES 6.11, 6.12, 6.13, 6.14, and 6.15). It is postulated that this frequency can be identified as the frequency where the trends of an experimental mobility curve diverge from the corresponding "best-fit" simulated curve, since the simulation is based on one-dimensional wave propagation while the shaft - pile cap system is three dimensional. Just a simple separation of the two curves is believed to be insufficient to define the cutoff frequency since other factors may be responsible for the differences in behavior. For example in FIGURE 6.11 the cutoff frequency can be identified as about 460 Hz, the point when the mobility in the experimental curve has a local minima while that of the "best-fit" experimental curve continues to decrease. The cutoff frequencies identified in this way for all shafts are summarized in TABLE 6.9.

The data in TABLE 6.9 was evaluated to develop a relation which can be used to identify the approximate cutoff frequency, f_c, based on geometric relations and the idea that one-dimensional conditions are satisfied when the wavelength is greater than or equal to the diameter of the shaft. The following relation is proposed:

$$f_c = \frac{v_c}{\lambda_c} \approx \frac{v_c}{D_{eff}} = \frac{v_c}{D(\alpha_s + \alpha)} \qquad (6.6)$$

where l_c is the wavelength where wave propagation in a cylindrical rod is no longer one-dimensional, D_{eff} is the effective diameter of the pile cap - shaft system, D is the diameter of the shaft, a_s is a factor to account for the plan area of the pile cap relative to the area of the shaft, and is defined as:

$$\alpha_s = \frac{A_{eff}}{(\frac{\pi D^2}{4})} \qquad (6.7)$$

where A_{eff} is the effective area of the pile cap as defined in FIGURE 6.16, and, a_t is a factor to account for the relative thickness of the pile cap and is defined as:

$$\alpha_t = (1 + \frac{B}{D}) \qquad (6.8)$$

where B is the thickness of the pile cap.

In the limit, as the cap thickness goes to zero, the cap thickness factor goes to 1. As the tributary area of the shaft approaches that of the shaft, a_s goes to 1. As the tributary area gets large relative the area of the shaft, a_s gets large which makes the effective diameter of the shaft becomes large, and thus makes the cutoff frequency approach 0. As the cutoff frequency gets small, resonances from the shaft toe will be masked by three-dimensional effects.

The values for these parameters for each of the five shafts are found in TABLE 6.10. The values of v_c shown in TABLE 6.10 are those computed from the "best-fit" analysis of the accessible head tests (TABLE 6.2). A comparison of the frequencies found by the empirical equation and those determined by comparing the mobilities of the "best-fit" simulations and the experimental curves are shown in FIGURE 6.26. The agreement is reasonably good, and most importantly, the trend in the empirically-predicted data agrees with that of the experimentally-derived data. The relationship given in EQUATION 6.6 can be used to estimate the possible effectiveness of the impulse response test to identify resonances from the toe of a deep foundation for a given geometry of pile and pile cap system. This relationship is valid for concrete piles and shafts connected with a concrete pile cap.

6.5 Summary

Results from a numerical study on experimental impulse response signals have been presented. The numerical simulation study compared observed results, simulation results using the as-built shaft dimensions and "best estimate" concrete and soil properties, and simulation results using the shaft and soil properties required to achieve "best fit" simulations for the five NGES drilled shafts in the accessible-head condition. The "best fit" simulations were achieved for the five NGES shafts by altering the wave propagation velocity to align the peaks, locally increasing the cross-sectional area to account for construction techniques to match the observed mobility, and reducing the attenuating properties of the soils to match the resolution and low-strain stiffness. These effects are summarized in TABLE 6.11.

It was shown that construction procedures create variations in the as-built dimensions and surrounding soil conditions which have a substantial effect upon impulse response results. Results at the NGES site indicated that disturbance caused by loosely placing backfill in the annulus between the temporary casing and the permanent liner resulted in a 35 to 44% reduction in v_s, and disturbance from drilling in the soft to medium clay resulted in a 10 to 23% reduction in v_s. Overdrilling in soft to medium clays created an increase in diameter from 9.9 to13.2%, and using a corrugated permanent liner in the upper portion of the shafts increased the effective diameter by 4.9 to 6.6%.

For inaccessible-head analyses, the pile caps were simulated by translating the rectangular cap geometry to an "equivalent" cylinder to determine the "effective" diameter for each cap. A relationship between the tributary area of the pile cap and the "effective" diameter required for an axisymmetric simulation was developed. A method to determine the cutoff frequency at which information can be obtained concerning a shaft beneath a pile cap was proposed. Frequencies found by the empirical equation agreed with those determined by comparing the mobilities of the "best fit" simulations and the experimental curves.

Resolution charts were developed for both homogeneous subsurface conditions and two layer soil systems. The two layer resolution charts predicted a good match between the "best fit" shaft and soil parameters and the experimental impulse response tests performed on the NGES drilled shafts. Thus, the two layer resolution charts can be used to predict the applicability of the impulse response method to a given drilled shaft and subsurface conditions.

Table of Contents

Chapter 7. Parallel Seismic Testing

- 7.1 Introduction
- 7.2 Field testing program
  - 7.2.1 Test procedure
- 7.3 Results
  - 7.3.1 Depth of foundation
  - 7.3.2 Propagation velocities in drilled shafts
- 7.4 Compressive wave velocities in soil
  - 7.4.1 Parallel seismic results
  - 7.4.2 Effect of travel path on first arrival
- 7.5 Summary

7.1 Introduction

Parallel seismic tests were conducted by impacting the pile caps above each of the five drilled shafts, and measuring the travel times down the shaft, through the soil, to a receiver located in an adjacent water-filled borehole. The purposes of these experiments were to evaluate the accuracy of the method in determining the length of each of the five drilled shafts, to evaluate the capabilities of the method to define the type of material which comprises a deep foundation, and to define the distance the compression wave can travel through the adjacent soil before the signal attenuates beyond recognition.

7.2 Field Testing Program

Prior to the start of the field testing program, five cased boreholes, PS1 through PS5, were installed at the locations shown on FIGURE 3.4. These boreholes served as access holes for the parallel seismic testing. Three of the holes, PS1, PS2 and PS5, also were used in conjunction with the cross-hole seismic tests to determine the shear and compression wave velocities of the in situ soils. The remaining two holes were strategically placed to obtain a wide range of distances between the five in-place drilled shafts and the access holes, so that one could evaluate the signals over a wide range of stress wave travel distances. The distances between shafts and receiver holes ranged from a minimum of 0.8 m (2.8 ft) to a maximum of 12.5 m (41 ft).

Each of the five drilled shafts were tested using the parallel seismic test method. Five series of tests

were conducted for each shaft. For each test series, the hydrophone (receiver) was placed in the bottom of each access hole and raised in increments of 0.3 m (1 ft) after each impact, to create a profile of received signals, resulting in a total of 25 tests. A summary of the distances between the centers of the shafts and the access holes are given in TABLE 7.1.

The equipment utilized for the parallel seismic tests conducted was manufactured by STS Consultants of Northbrook, IL. The equipment has been described in SECTION 2.4.1.2, and included a four pound sledge hammer with an impact triggering mechanism, a portable field computer with appropriate controlling software, an amplifier unit, and an omni-directional receiver probe (transducer).

7.2.1 Test Procedure

With the access holes installed, the following test procedure was followed for each of the 25 possible configurations of drilled shafts and access holes:

1. The approximate location of the center of the shaft to be tested was located based on construction records, and marked on the pile cap.
2. The depth of the access hole was measured and recorded.
3. The access hole was completely filled with water.
4. The amplifier unit, hammer trigger cable and receiver probe cable were properly connected to the field computer.
5. The controlling computer software was initialized.
6. The operator name, location, structure number, test number, depth to be tested, and testing depth increment, 0.3 m (1 ft) was input.
7. The receiver probe was connected to the receiver cable, and lowered to the bottom of the access hole.
8. The pile cap was struck with the 4-pound sledge hammer at the predetermined location.
9. The signal quality was reviewed on the computer screen, and as necessary the signal gain control was adjusted. (Once set, the signal gain control was not changed again during the duration of the test).
10. The signal was then accepted, rejected and a new hit taken, or the multiple hit option was selected whereby additional hits could be made at the same elevation and the signals added to more clearly define the first arrival. A signal was accepted when a clear indication of the first arrival time could be observed, i.e., when the background noise level was small enough so as to not mask the first arrival.
11. Once the signal was accepted, the receiver probe was raised 0.3 m (1 ft).
12. Repeated steps 8 through 11 until the complete profile of signals was built up from the bottom to the top of the access hole.
13. The complete profile was saved to the hard drive for later analysis.

7.3 Results

The results of the parallel seismic method are commonly used to define the depth of a deep foundation, and to determine its material type as a function of the apparent propagation velocity in the foundation element. The results of the extensive testing program presented herein also were used to evaluate the compression wave velocities in the adjacent soil, as will be discussed in SECTION

7.4. A complete set of results of the testing program is presented in this chapter and APPENDIX B, and consists of compiled profiles of signals received over the entire depth of each access hole.

7.3.1 Depth of Foundation

7.3.1.1 Access Holes within 3 m of Shaft

The depth of a deep foundation conventionally is estimated from the compiled profile of signals, usually from an access hole located within 2 m (6.5 ft) of the structure. For a given depth herein, little difference was observed in the results from access holes within 3 m (9.8 ft) of a shaft, and thus this distance is used to represent conventional practice. The most common method to interpret the data is to identify either the bottom of a deep foundation or the location of a defect as the depth in the compiled profile where there is a change in slope of the lines of first arrival times. Another indication of the depth of a deep foundation is the depth where the amplitude of the first arrival significantly decreases when the data are plotted at the same scale for all tests. The following sections separately discuss the results of the parallel seismic tests for each of the three lengths of shafts because the variation of the compressive wave velocity of the soil adjacent to the shafts affects the interpretation of the observed signals.

Shaft with lengths of twelve meters

Shafts 1 and 3 were nominally 12 m long. Tests on access holes within 3 m (9.8 ft) of a shaft included shaft 1 - access hole 1 (referred to hereafter as sh 1-1) and sh 3-3. Refer to FIGURE 3.4 for the locations of the access holes relative to the shafts. The compiled profile for sh 3-3 with all signals plotted at the same scale is presented in FIGURE 7.1. Based on detailed construction records (FIGURE 3.14), the bottom of the shaft in the inaccessible head condition is 12.91 m (42.3 ft) below the top of the pile cap. As suggested on FIGURE 7.1, the bottom of the shaft is marked as 13.5 m (44.3) based on the change in slope of the first arrivals. Therefore this conventional interpretation method works well for the conditions associated with shaft 3 and access hole 3.

By examining the magnitude of the first arrivals and selecting the bottom of the shaft as the point where a significant reduction occurs in the amplitude of the first arrival, the length of the pile cap and shaft can be estimated to be about 13.75 m (45.1 ft), again in reasonable agreement with the actual bottom of the shaft. Note that this approach would be more accurate if a constant source of energy was applied at the top of the shaft, rather than an inevitably-variable impact produced by manually swinging a four pound hammer. The bottom of a shaft interpreted in this way can be in error if the input energy was not maintained to be at least approximately constant.

As indicated in FIGURE 7.2, a compiled profile for sh 1-1 with all signals plotted at the same scale, the signals from sh 1-1 were not as strong as those of sh 3-3 because of the refections from the soil-filled joint at a depth of 4.86 m (15.9 ft), which reduce the amount of energy which passes below this depth. However one can see the change in slope of first arrivals which suggests that the depth of shaft 1 is 13.5 m (44.3 ft), as compared to the actual depth of 12.68 m (41.6 ft). While the data are not as clear as the sh 3-3 in FIGURE 7.1, the length of the pile can be estimated to be 13.0 m (42.7 ft) based on the reduction of amplitude of the first arrival.

Shaft 3 - access hole 3 data represent almost ideal conditions to interpret results of parallel seismic tests in that the access holes are close to the shaft and are well below its bottom, and the shaft is tipped in a thick layer of soil with almost constant compressive wave velocity. No complications arise from having soils with different stiffnesses, and hence different shear and compression wave velocities, near the bottom of the shaft. Also no planned defects exist in shaft 3 to attenuate the signal as it travels down the shaft.

Shafts with lengths of twenty-one meters

Shafts 2 and 4 were nominally 21 m (69 ft) long. Tests for shafts of this length with access holes closer than 3 m (9.8 ft) include sh 2-1, sh 2-3, sh 4-1, sh 4-2, and sh 4-4. Refer to FIGURE 3.4 for the locations of the access holes relative to the shafts. The compiled profiles of the signals plotted to the same scale for sh 4-2 is presented in FIGURE 7.3. This test is representative of these shafts; the other profiles are presented in APPENDIX B. Based on detailed construction records (see CHAPTER 3), the bottom of the shaft in the inaccessible head condition is 21.95 m (72.0 ft) below grade. The slope of the first arrival times decreases after the hard silt layer is encountered, as a result of the increase in compression wave velocity in this stiffer layer. Because the shaft is tipped very close to this interface, the expected increase in slope due to encountering the bottom of the shaft is masked by the presence of the hard silt, and thus is not identifiable in this case. The presence of a stiffer layer near the bottom of the shaft is a common situation for many deep foundations. This stratigraphy causes a situation where no increase in slope of first arrival times is apparent because the increased distance between a shaft and the receiver probe below the bottom of the shaft is offset by the increased compression wave velocity of the underlying stiffer layer. In these cases, the bottom of the shaft cannot be identified. This was true for all parallel seismic tests within 3 m of the 22 m (72.2 ft) long shafts.

The bottom of shaft 4 can be identified by examining the amplitudes of the first arrivals (FIGURE 7.3). While not as clear as sh 3-3, one can still observe a noticeable drop in the amplitude around 22 m (72.2 ft), thus signaling the bottom of the shaft.

Similar responses were observed in sh 4-1. Interpretation of parallel seismic tests sh 2-1, sh 2-3 and sh 4-4 were hampered by the fact that the access hole extended only 1 to 2 m below the bottom the shaft. Compiled profiles for these four tests are given in APPENDIX B.

Shaft with length of twenty-eight meters

The compiled profile of sh 5-2 is shown on FIGURE 7.4. Interpretation of this test by evaluating changes of slope of the first arrivals is hampered by having the access hole only 1.5 m (4.9 ft) below the bottom of the shaft, and thus the bottom of the shaft cannot be identified with this approach.

The first arrival times at greater depths are somewhat difficult to identify because all data has been plotted at the same scale. A striking feature of this plot is the attenuation of the signal as depth increases beyond 16 m (52.5 ft). Because of this signal attenuation, identifying the bottom of this shaft is more difficult than for the shorter shafts. The bottom of this shaft can be estimated to be 27.75 m (91.0 ft) based on the changes in the magnitude of the first arrivals. For this longer shaft, if more energy had been applied to the top of the pile cap, then the changes in the amplitude of the first

arrivals near the bottom of the shaft would have been evaluated as easily as for the shorter shafts.

Summary of Results of Parallel Seismic Tests on Access Holes within 3 m

The results of all parallel seismic tests conducted in access holes located within 3 m (9.8 ft) of a test shaft are summarized in TABLE 7.2. The bottom of the 12 m (40 ft) long shafts were clearly identified within 0.8 m (2.6 ft) using the conventional approach of associating changes in the slope of first arrival times plotted versus depth with the bottom of a shaft.

The bottom of the longer shafts could not be identified using this method of interpretation. The existence of the hard silt with its higher compressive wave velocity, compared to that in the overlying softer clays, close to the bottom of the 21 m (70 ft) shaft masked the expected changes of slopes of the first arrival times at the shaft bottom. One could not identify the slope change because the travel times in the soils actually decreased as a result of the higher propagation velocities in the stiffer soil. Similar problems were encountered for sh 5-2 which was seated on the underlying dolomite, which is stiffer than the hard silt. Interpretation of this shaft was further complicated by the fact that the access hole extended only 2 m (6 ft) below the bottom of the shaft.

In all cases, estimates of the bottom of the shaft could be made based on the reduction of amplitude of the first arrival below the depths of the bottom of the shafts. The depths obtained using this latter approach, and given in TABLE 7.2, have estimated precisions between ±0.25 to 0.5 m (0.8 to 1.6 ft) and were accurate to within 1.1 m (3.6 ft) for all tests. Determination of depths using this method was progressively more subjective as the length of a shaft increased. It should be noted that these depth determinations were made with the knowledge of the actual bottom depths of the shafts. While this approach appears promising, the method would be much better if constant energy was input for each depth of the test, rather than the manual operation of a sledge hammer.

7.3.1.2 All Access Holes

First arrival times have been selected from each individual hammer impact, and plots of depth versus first arrival time have been constructed for all shafts. To aid in the selection of the first arrival time, different scales were used at different depths. To more clearly show the trends of the data as a function of access hole distance from the shaft, summary plots which show all access holes for each shaft on one figure are presented in FIGURES 7.5, 7.6, 7.7, 7.8, and 7.9.

Two trends are apparent in these plots. At some depth intervals, especially in the upper 5 to 10 m (16.4 to 32.8 ft), signal noise did not allow a clear determination of the first arrival. This is most likely attributable to a combination of the presence of the permanent casing in the upper 10 m (33 ft) and the improper backfilling around the top of the access hole and the upper casing of the drilled shaft which resulted in zones of very loose sand adjacent to the casing. The data in FIGURES 7.8 and 7.9 for shafts 4 and 5, which shared a common pile cap, suggest that the signals received in the upper 10 m (33 ft) came from either the top of the pile cap, or the bottom of the permanent casing, and that very little signal was transmitted through the temporary liner and the very loose sand. The temporary liner apparently acted as a wave guide such that the first signals received in the top 5 m (16.5 ft) came from energy emanating from the pile cap, and the first signals received in the lower 5 m (16.5 ft) came from energy emanating from the end of the permanent casing. These travel paths would account for the increase and subsequent decrease in first arrival times in the upper 10 m (33

ft) of the compiled profile. For shafts 1 through 3, first arrivals were only clearly observed starting from a depth of about 5 m (16.5 ft), and consequently only the decrease in arrival times were observed. Thereafter the arrival times began to increase, as is usually observed in parallel seismic tests where the hydrophone is adjacent to a deep foundation, because the signals were no longer constrained by the presence of the liner. Perhaps the soil beneath the bottom of pile caps 1 and 2 settled, resulting in no acoustic coupling between these caps and shafts 1, 2 and 3, and preventing any signal from traveling directly from the pile cap to the hydrophone.

The second trend in the data is that clear changes of slopes are not visible in most of the data. This lack of easily identifiable foundation bottoms can be attributed to the fact that most of the access holes were more than 3 m (9.8 ft) from a drilled shaft. In some cases, the access holes did not extend a sufficient distance below the bottom of the drilled shafts. As discussed in SECTION 7.3.1.1, the effects of the hard silt layer further complicated interpretation of data.

7.3.2 Propagation Velocities in Drilled Shafts

As a means to identify the type of material which comprises a deep foundation, the propagation velocity of the concrete (or pile material) can be estimated as the slope of the depth versus first arrival time line in the soil adjacent to the pile. The slopes of these lines represents the propagation velocity in the shaft because for vertical shafts and vertical access holes, the only increase in arrival times should be caused by longer travel times in the concrete. For example, in the case of sh 4-2 (FIGURE 7.2) the slope of this line resulted in a value of 4510 m/s (14,800 ft/sec) which corresponds reasonable well with the propagation velocity of 4100 m/s as determined two months after shaft construction (SECTION 5.2.1).

The propagation velocities computed from the results of the parallel seismic test results are summarized in TABLE 7.3. These values were determined from the slope of the first arrival times at the depths adjacent to the shafts, but only at depths below the location of the permanent casing and above the bottom of the shaft. Consequently, only about 2 m (6.5 ft) of compiled signals could be used to determine the velocities in shorter shafts 1 and 3, and for the most distant access holes for these shafts, no straight line could be fit through the data at these elevations. Because of the relative paucity of data for shafts 1 and 3, the variations in computed velocities are greater for these two shafts than for the other three deeper shafts which had more data in the depths of interest. With these exceptions, the velocities correspond reasonably well with the range of velocities representative of the concrete after 2 months of aging, 3800 to 4100 m/s (12,500 to 13,500 ft/s) as described in SECTION 5.2.1.

7.4 Compressive Wave Velocities in Soil

7.4.1 Parallel Seismic Results

The presence of five access holes near each shaft allows one to evaluate the compression wave velocities in the soils adjacent to the shaft. Calculations of the compressive wave velocities were made in a manner similar to that which is used to analyze seismic refraction data. Herein, the time of first arrival of the stress wave was plotted versus the distance from the shaft to the receiver hole. The time versus distance plots for a number of depths adjacent to the shafts are shown in FIGURES 7.10,

7.11, 7.12, 7.13, and 7.14. The inverse slopes of these lines yield the compression wave velocity at a particular depth. The selected depths were adjacent to the drilled shafts so that the stress waves would follow horizontal travel paths from the shaft to the receiver.

A summary of the compression velocities determined from the slope of the best fit line as compared to the results of the cross hole seismic testing are summarized in TABLE 7.4, and are graphically shown on FIGURE 7.15. Also given in the table are the correlation coefficients for each best fit line. As shown, the correlation coefficients for most of the data are close to 1, indicating a good fit of the data which shows that the waves emanating from the hammer blow on the pile cap propagate as far as 12.5 m, well beyond the distance between the foundation and where access holes are usually installed. These data suggest that one can determine compressive wave velocity in soils if two access holes are installed adjacent to the foundation and parallel seismic tests are conducted in each. By fitting a line to these data, one can find a reasonable average compression wave velocity which compared well to the "known" compression wave velocities determined by previous cross hole seismic testing at the test site. Therefore access holes do not need to be located within 2 m of a foundation for parallel seismic testing for the signals generated by the impact to be received by the hydrophone. The addition of a second access hole allows one to obtain variations in compressive wave velocity with depth in the soil, so that compiled profiles can be more accurately interpreted.

7.4.2 Effect of Travel Path on First Arrival

Variations in compression wave velocities of soil and the fact that the path of a stress wave from the impact point to the receiver in a parallel seismic test can be complex depending upon the subsurface profile and the properties of the various layers are the main reasons why access holes must be close to the structure for parallel seismic testing. In general, if the soil profile is uniform with a constant compression wave velocity within the area being tested, the stress path would be as that shown in FIGURE 7.16. This is termed the direct wave.

Another possible path which can occur is that of the refracted wave as shown in FIGURE 7.17. If an upper soil stratum has compressive wave velocities smaller than that of an underlying stratum, then the first arrival time may be caused by a wave which travels from the pile through the underlying stratum and up to the receiver. The refracted P-wave generated by the critically incident P-wave will travel along the interface in the lower stratum as shown in FIGURE 7.16. By elastic theory, it has been shown that the refracted wave causes a disturbance along the interface and that this disturbance generates a wave in the upper medium. This new wave is called the head wave and travels at a velocity v_{p1} in a direction inclined at (90° - i_c) to the interface, where i_c is the critical angle of incidence.

At receivers close to the source, the direct wave will arrive before the head wave, but there is some receiver distance at which the head wave will arrive before the direct wave because it travels for a significant time in the higher-velocity lower stratum. This wave composed of the initial P-wave, and the head wave is referred to as the refracted wave.

Travel time equations can be written for the direct wave and the refracted wave. The travel time t_d for the direct wave is given by:

$$t_d = \frac{d}{v_{conc}} + \frac{\Delta x}{v_p} \qquad (7.1)$$

where d is the travel distance in the pile, v_{conc} is the propagation velocity in concrete, Dx is the distance between the shaft and the access hole, and v_p is the compression wave velocity in the soil. The travel time for the refracted wave, t_h, can be expressed by equation:

$$t_h = \frac{H}{v_{conc}} + \frac{\Delta x - (H-d)(\tan i_c)}{v_R} + \frac{H-d}{v_R \cos i_c} \qquad (7.2)$$

using the relationships:

$$\sin i_c = \frac{v_R}{v_R} \qquad (7.3)$$

and

$$\cos i_c = \sqrt{1 - \frac{v_R^2}{v_R^2}} \qquad (7.4)$$

one can simplify EQUATION 7.2 to:

$$t_h = \frac{H}{v_{conc}} + \frac{\Delta x}{v_R} + \left[\frac{1}{v_R \cos i_c} - \frac{\tan i}{v_R}\right](H-d) \qquad (7.5)$$

EQUATIONS 7.1 and 7.5 suggest that if one has a stiffer stratum near a pile tip, the shortest time for a wave to travel from the pile to a receiver will not necessarily be that of the direct path, but will depend on the relative velocities in each stratum and the distance between the pile and the access hole. While the possibility of a direct path is maximized if the access hole is as close as possible to the foundation, there is still the problem of interpreting the slope changes when a stiff layer is located near the bottom of a shaft, as was discussed in SECTION 7.3.1.1.

7.4 Summary

The parallel seismic testing program has been described and its results presented in this chapter. Parallel seismic tests, as conventionally practiced, i.e. with short distances between a structure and an access hole, can be used to define the bottom of the 12 m (40 ft) drilled shafts at the NGES test section, as well as to identify the material type from the computed propagation velocity in the structural material. The bottoms of all shafts were correlated with decreases in amplitudes of the first arrival when all records for an access hole were plotted to the same scale, albeit with some degree of subjectivity. A constant energy impact source, which induces more energy than was input by the manual operation of the four pound sledge hammer, would have made this approach more accurate and less subjective.

The conventional approach of using changes of slope of the plot of depth versus first arrival to identify the bottom of a deep foundation works best when the tip of the pile is in a soil with uniform stiffness, as was the case for the 12 m (40 ft) shafts. Supplementing this approach of interpretation by examining the amplitudes of the first arrivals on a plot with the same scale for all records allows one to better interpret signals in more common situations encountered in practice, e.g. a stiffer layer near the bottom of a deep foundation.

Compression waves from the impact can be observed at much greater distances (at least 12.5 m) from the structure than are currently used (<2 m), as noted by the agreement between the compressive wave velocity in the soil from the parallel seismic and cross hole seismic testing. However, due to variations of compression wave velocity with depth and the uncertainty in the travel paths, the interpretation of the compiled first arrival profiles becomes more difficult, especially in conditions where subsurface conditions are unknown.

Table of Contents

Chapter 8. Summary and Conclusions

Several low-strain non-destructive techniques used for evaluation of deep foundations have been reviewed. The sonic echo and impulse response methods are surface reflection techniques which are used primarily as a quality control tool for drilled shafts and driven concrete piles. In these techniques, stress waves generated at the surface of a structure reflect off the bottom of a foundation or anomaly located within the foundation, and are recorded with a transducer also attached to the surface of the structure. The parallel seismic method is a direct transmission method that relies on measuring the first arrival of stress waves generated at the surface of a structure with a receiver lowered down an access borehole installed adjacent to the structure. This method currently is used to evaluate the continuity of existing deep foundations, and in some cases, to identify unknown foundation types.

A test section was constructed at the National Geotechnical Experimentation Site at Northwestern University to evaluate application of these non-destructive testing methods to inaccessible deep foundations. The test section consists of five drilled shafts constructed in three groups. The drilled shafts were constructed with diameters ranging from 610 to 914 mm (2 to 3 ft) and lengths varying from 12.2 to 27.4 m (40 to 90 ft). Pile caps vary in thickness from 610 to 1524 mm (2 to 5 ft). Two of the shafts were constructed with defects, one with a reduced cross-section and another with a thin, soil-filled joint. Impulse response and sonic echo data were obtained in both the accessible and inaccessible head conditions. Parallel seismic tests were conducted for the inaccessible-head condition. The soils at the location of the NDE test section site have been well characterized by laboratory and field investigations, including cross-hole seismic tests, nine CPT tests and two soil borings. Construction of the test section was controlled, and careful observations were made of the shaft dimensions, as-built depths and drilling procedures. At this test section, one can currently conduct parallel seismic, sonic logging, sonic echo and impulse response tests on five drilled shafts constructed with pile caps.

The results of sonic echo, impulse response, and parallel seismic investigations at the NDE test section have been presented. The conventional impulse response method was evaluated to assess the effect of concrete age on the propagation velocity and the effect of geophone coupling. Numerical simulations of impulse response signals for accessible and inaccessible shafts were performed to assist the interpretation of field-obtained signals. Shaft and soil parameters were examined to achieve the best fit between the experimental and simulated mobility curves. To quantify the effect of the foundation-soil interaction on the impulse response results, resolution charts were developed for both homogeneous subsurface conditions and layered soil systems.

Sonic echo and impulse response tests were conducted on the five drilled shafts before and after the pile caps were constructed such that both the accessible- and inaccessible-head conditions were evaluated with the two methods. Based on the results of the sonic echo and impulse response tests

performed on the five NGES drilled shafts and the numerical simulations of the impulse response tests, the following conclusions can be drawn:

Accessible-Head Shafts:

- The toe was identified for all five NGES drilled shafts, having L/D ratios from 20 to 30.
- Both planned defects, the soil-filled joint and the neck with a 25% reduction in cross-sectional area were identified.
- An unplanned anomaly was identified in shaft 4, which was verified by numerical simulations to be a bulge which had an increased cross-sectional area of 140% located at the depth of the temporary casing.
- The use of impulse response tests to identify lengths of shafts are limited primarily by the L/D ratio of the shaft and the ratio of the shear wave velocity of the soil to the propagation velocity of the concrete.
- For uniform soil conditions, the accuracy of determining the length of a deep foundation is ±5% which is based on errors in assumed propagation velocities.
- When soil strata with significantly different shear wave velocities are present, numerical simulations help interpret the results because of the strong reflection from the interface of the two soil strata.

Construction Effects:

- The loosely placed backfill in the annulus between the temporary casing and the permanent liner resulted in a 35 to 44% reduction in the apparent shear wave velocity of the soil.
- Disturbance from drilling in the soft to medium clay resulted in a 10 to 23% reduction in v_s.
- Overdrilling in soft to medium clays created an increase in diameter from 9.9 to 13.2%, consistent with the values reported in drilled shaft literature.
- Using a corrugated permanent liner in the upper portion of the shafts increased the effective diameter by 4.9 to 6.6%.

Inaccessible-Head Shafts:

- The presence of the increased mass of the pile cap atop the five drilled shafts caused the average mobility and the signal resolution to decrease.
- The interface between the pile cap and the drilled shaft created an impedance change which caused reflections from the incident wave and resulted in less energy being transmitted down the shaft.
- The ability to determine shaft integrity for inaccessible shafts depends on the thickness of the pile caps and the length-to-diameter ratio of the shafts, as well as the soil conditions adjacent to a shaft.
- The toe of the shaft could be identified for inaccessible shafts with L/D ratios as high as 23 with a B/D ratio of 0.67 and with L/D ratios as high as 20 with a B/D ratio of 2.5.

Evaluation of Existing Deep Foundations:

- In inaccessible-head conditions, the toe of a shaft may be identified using mobility data at "cutoff" frequencies which are a function of the propagation velocity and diameter of the

shaft, the tributary area of the intervening structure above the shaft, and the thickness of the intervening structure. For the shafts at the test section, these cutoff frequencies varied between 400 and 600 Hz.
- The interface between the drilled shaft and pile cap can be identified with higher frequencies in velocity spectrum.
- Site-specific construction procedures must be considered when interpreting the results of impulse response tests, especially because the soil immediately adjacent to a shaft has such a large effect on the resolution of the signals in a mobility plot.

Parallel seismic tests were conducted in five boreholes located at distances varying from 0.8 to 12.5 m to the five drilled shafts. The results of these tests were used to verify the depth of the shafts, to determine its material types as a function of the apparent propagation velocity (these two purposes are common applications of the method), and to evaluate the compression wave velocities in the soil adjacent to the shafts. The latter application is possible because of the five access holes located at different distances from a shaft allowed one to interpret the first arrival times in a manner similar to seismic refraction tests, thus computing the compression wave velocity in the soil.

Based on the parallel seismic testing performed at the NGES at Northwestern University, the following conclusions can be drawn:

- The bottoms of the shafts could be identified using conventional data reduction methods when the access hole was within two meters of the shaft. However, it was necessary to consider the bottom as defined by two different methods: the change of slope of first arrival times versus depth and the depth where the amplitude of the first arrival significantly decreases.
- The approach of defining the bottom of a foundation by examining amplitudes of first arrivals requires a constant energy source to be used to generate all signals in a parallel seismic profile.
- The standard approach of defining the bottom of foundation by examining the slopes of the first arrival times plotted versus depth works well when there is a soil of uniform stiffness near the bottom of the foundation. The bottom of the foundation can easily be masked by changes in compression wave velocities at soil strata boundaries.
- The apparent propagation velocity of the shafts determined from the slope of the first arrival time versus depth adjacent to a shaft agreed well with the propagation velocity through concrete.
- Compression waves from impact of the structure can be observed at much greater distances, at least 12.5 m, from the structure than is currently used (<2 m), as noted by the agreement between the compression wave velocities found by the cross-hole seismic and parallel seismic testing. However, due to variations of compression wave in soil with depth, and the uncertainty in travel paths, the interpretation of the complied first arrival profiles becomes more difficult as the distance between the access hole and the shaft increases, especially in cases were the subsurface conditions are unknown.

Table of Contents

References

Achenbach, J.D. (1975). Wave Propagation in Elastic Solids. North-Holland Publishing Co.; New York, American Elsevier Publishing Co.

ASTM, (1983). "Test Method for Pulse Velocity through Concrete," Standard C-597, Annual Book of ASTM Standards: Concrete and Aggregates, Philadelphia, Pa.

ASTM, (1986). "Test Method for Compressive Strength of Cylindrical Concrete Specimens," Standard C-39, Annual Book of ASTM Standards: Concrete and Aggregates, Philadelphia, Pa.

ASTM, (1987). "Practice for Making and Curing Concrete Test Specimens in the Field," Standard C-31, Annual Book of ASTM Standards: Concrete and Aggregates, Philadelphia, Pa.

Baker, C.N., Parikh, G., Briaud, J.L., Drumright, E.E. and Mensah, F. (1993). "Drilled Shafts for Bridge Foundations," FHWA Publication No. FHWA-RD-92-004, Federal Highway Administration, McLean, Virginia, August.

Bray, D.E. and McBride, D. Eds. (1992). Non-Destructive Testing Techniques. John Wiley and Sons, Inc., New York, p. 261, 364.

Cannon, J.G.K. (1990). "Integrity Testing of Piled Foundations," The Institution of Engineers Australia Structural Engineering Conference, Aidelaide, October 3-5, pp. 450-455.

Caputo, V. (1974). "Low-Strain Dynamic Testing on Piles," A Workshop in Pile Foundations: Experimental Investigations, Analysis and Design, Napoli, December 12-15, pp.165-198.

Davis, A.G. (1994). "Impedance Log for the Length and Shape Measurements of Drilled Shafts from Mobility (TDR) Tests," Unpublished computer program, STS Consultants, Inc. March.

Davis, A.G. and Dunn C.S. (1974). "From Theory to Field Experience with Non-Destructive Vibration Testing of Piles," Proceedings of the Institution of Civil Engineers, Part 2, No. 57, December, pp. 571-593.

Davis, A.G. and Hertlein, B.H. (1991). "The Development of Non-Destructive Small-Strain Methods for Testing Deep Foundations: A Review," Transportation Research Board, 70th Annual Meeting, January 13-17, Washington, D.C.

Davis, A.G. and Hertlein, B.H. (1993). "Evaluation of the Integrity of Some Large Concrete Structures Using NDT," American Concrete Institute Spring Convention, Vancouver, March.

Davis, A.G. and Robertson, S.A. (1975). "Economic Pile Testing," Ground Engineering, May, pp. 40-43.

Dowding, C.H. (1996). Construction Vibrations. Prentice Hall, Inc., Englewood Cliffs, New Jersey.

Finno, R.J. editor (1989). Predicted and Observed Axial Behavior of Piles. Geotechnical Special Publication No. 23., American Society of Civil Engineers, New York, New York.

Graff, K.F. (1975). Wave Motion in Elastic Solids. Dover Publications, Inc., New York.

Halmshaw, R. (1991). Non-Destructive Testing. Edward Arnold, London, pp. 158-161.

Hardin, B.O. and Drnevich, V.P. (1972). "Shear Modulus and Damping in Soils: Design Equations and Curves," Journal of the Soil Mechanics and Foundations Division, ASCE, Vol. 98, No. SM7, July, pp. 667-692.

Hearne, T.M., Stokoe, K.H. and Reese, L.C. (1981). "Drilled-Shaft Integrity by Wave Propagation Method," Journal of Geotechnical Engineering, American Society of Civil Engineers, Volume 107, No. 10, October, pp. 1327-1344.

Hertlein, B.H. (1995). Portable PC-Based Field Test Equipment Service Use and Calibration Guide. STS Consultants, Inc. Northbrook, Illinois.

Higgs, J.S. and Robertson, S.A. (1979). "Integrity Testing of Concrete Piles by Shock Method," Concrete, October, pp. 31-33.

Imai, T. and Tonouchi, K. (1982). "Correlation of N-Value with S-Wave Velocity and Shear Modulus," Proceedings, 2nd European Symposium on Penetration Testing, Amsterdam, pp. 57-72.

Mor, G. (1991). "Fault Detecting in Foundation Piles and Sheet Pile Walls with Ultrasonic Investigations," 4th International Conference on Piling and Deep Foundations, Balkema of Rotterdam, Volume 1, Stresa, April 7-12, pp. 625-626.

Kramer, S.L. (1996). Geotechnical Earthquake Engineering. Prentice-Hall, Inc. New Jersey.

Olson, L.D., Jalinoos, F, and Aouad, M.F. (1995). "Determination of Unknown Subsurface Bridge Foundations," A Final Report prepared for NCHRP, August.

Paquet, J. (1968). "Etude Vibratoire des Pieux en Beton: Response Harmonique," Annales Inst. Tech. Batim., 21st year, No. 245, May, pp. 789-803.

Peck, R.B., Hansen, W.E., and Thornburn, T.H. (1974). Foundation Engineering. John Wiley &

Sons, Inc. New York.

Popovics, J. (1994). "A Survey of Developments in Ultrasonic NDE of Concrete," IEEE Transactions of Ultrasonics, Ferroelectrics, and Frequency Control. Vol. 41, No. 1, January.

Richart, F.E., Hall, J.R. & Woods, R.D. (1970). Vibrations of Soils and Foundations. Prentice Hall, Inc., Englewood Cliffs, New Jersey.

Rix, G.J. and Stokoe, K.H. (1991). "Correlation of Initial Tangent Modulus and Cone Penetration Resistance," Calibration Chamber Testing, International Symposium on Calibration Chamber Testing, A.B. Huang, ed., Elsevier Publishing, New York, pp. 351-362.

Sansalone, M. and Carino, N.J. (1986). "Impact-Echo: A Method for Flaw Detection in Concrete Using Transient Stress Wave Analysis," NBSIR 86-3452, Maryland, September.

Seed, H.B. and Idriss, I.M. (1970). "Soil Moduli and Damping Factors for Dynmaic Response Analyses," Report No. EERC 70-10, Earthquake Engineering Research Center, University of California, Berkeley, California.

Stain, R.T. (1982). "Integrity Testing," Civil Engineering, April and May, pp. 55-59 and 71-73.

Stas, C. and Kulhawy, F.H. (1984). "Critical Evaluation of Design Methods for Foundations Under Axial Uplift and Compression Loading," Report No. EPRI EL-3771, Electric Power Research Institute, Palo Alto, CA, November.

Timoshenko, S.P. and Goodier, J.N. (1951, 1970). Theory of Elasticity. McGraw Hill, New York.

Table of Contents

Appendix A

- TABLE A-1 Accessible-head testing schedule for shaft 1
- TABLE A-2 Accessible-head testing schedule for shaft 2
- TABLE A-3 Accessible-head testing schedule for shaft 3
- TABLE A-4 Accessible-head testing schedule for shaft 4
- TABLE A-5 Accessible-head testing schedule for shaft 5

Table of Contents

Appendix B

- FIGURE B-1 Compiled parallel seismic profile: shaft 1 access hole 2
- FIGURE B-2 Compiled parallel seismic profile: shaft 1 access hole 3
- FIGURE B-3 Compiled parallel seismic profile: shaft 1 access hole4
- FIGURE B-4 Compiled parallel seismic profile: shaft 1access hole5
- FIGURE B-5 Compiled parallel seismic profile: shaft 2 access hole1
- FIGURE B-6 Compiled parallel seismic profile: shaft 2 access hole 2
- FIGURE B-7 Compiled parallel seismic profile: shaft 2 access hole 3
- FIGURE B-8 Compiled parallel seismic profile: shaft 2 access hole 4
- FIGURE B-9 Compiled parallel seismic profile: shaft 2 access hole 5
- FIGURE B-10 Compiled parallel seismic profile: shaft 3 access hole 1
- FIGURE B-11 Compiled parallel seismic profile: shaft 3 access hole 2
- FIGURE B-12 Compiled parallel seismic profile: shaft 3 access hole 4
- FIGURE B-13 Compiled parallel seismic profile: shaft 3 access hole 5
- FIGURE B-14 Compiled parallel seismic profile: shaft 4 access hole 1
- FIGURE B-15 Compiled parallel seismic profile: shaft 4 access hole 3
- FIGURE B-16 Compiled parallel seismic profile: shaft 4 access hole 4
- FIGURE B-17 Compiled parallel seismic profile: shaft 4 access hole 5
- FIGURE B-18 Compiled parallel seismic profile: shaft 5 access hole 1
- FIGURE B-19 Compiled parallel seismic profile: shaft 5 access hole 3
- FIGURE B-20 Compiled parallel seismic profile: shaft 5 access hole 4
- FIGURE B-21 Compiled parallel seismic profile: shaft 5 access hole 5

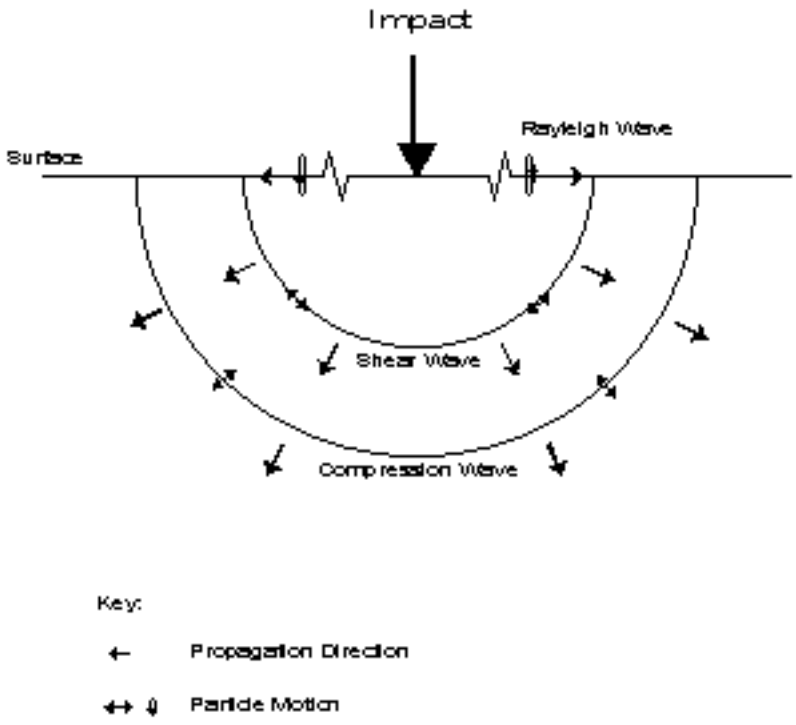

Figure 2.1 Wavefronts of Compression, Shear and Rayleigh Waves Produced by a Point Impact on a Surface

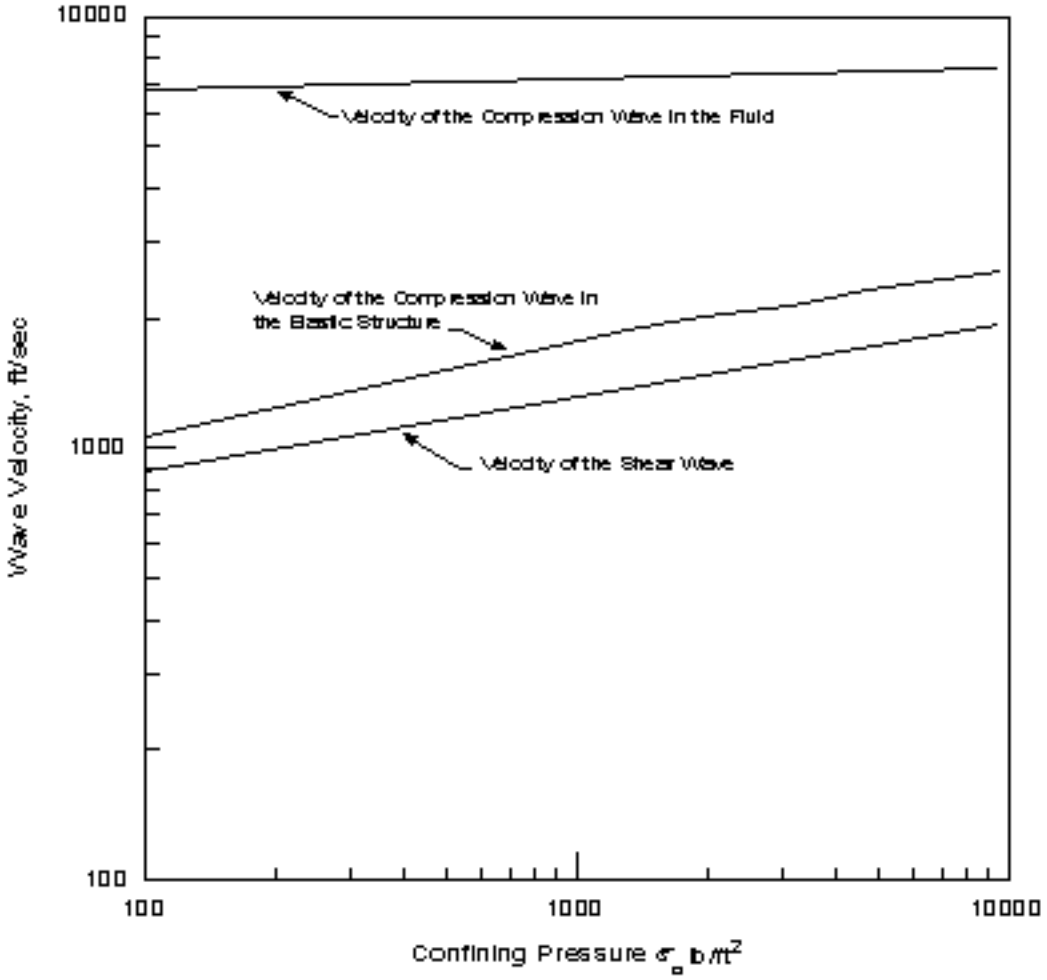

Figure 2.2 Theoretical Variation of the Two Compression-Wave Velocities and the Shear-Wave Velocity with Confining Pressure, as Calculated from the Biot (1956) Theory (from Hardin, 1961), (after Richart et. al., 1970)

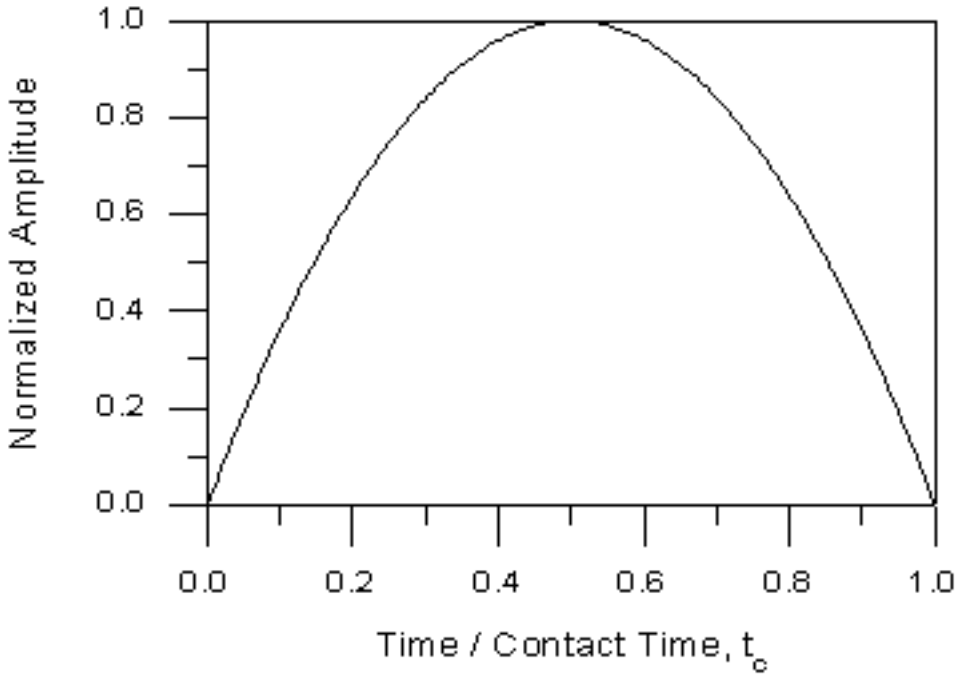

Figure 2.3 Force-Time Function of Elastic Impact of a Sphere on a Solid (after Sansalone and Carino, 1986)

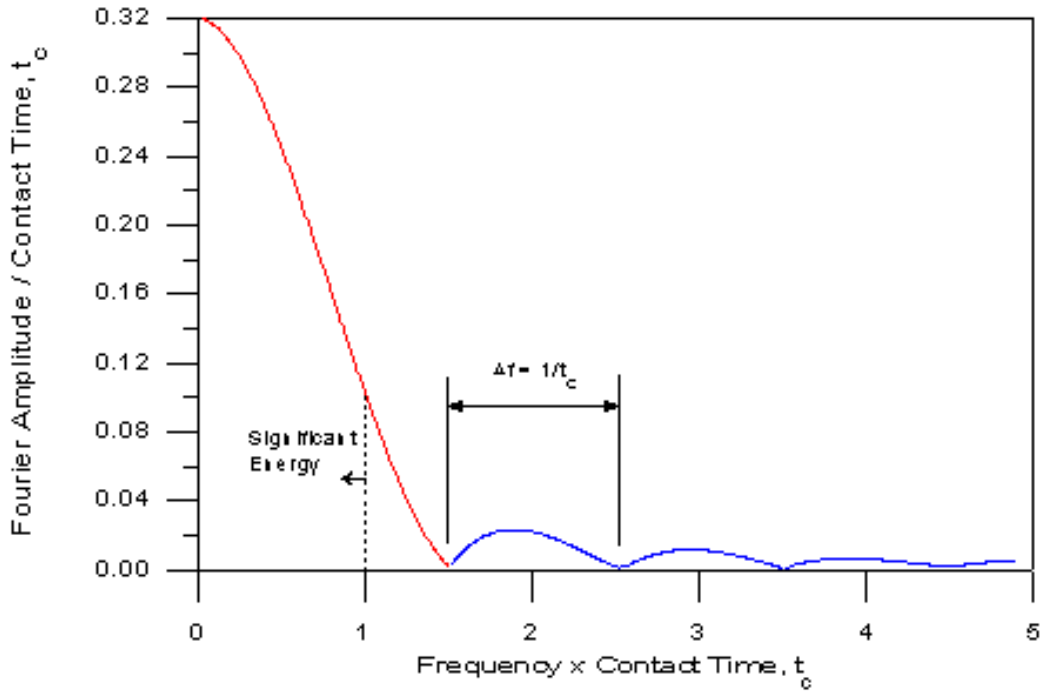

Figure 2.4 Frequency Spectrum of Force-Time Function (after Sansalone and Carino, 1986)

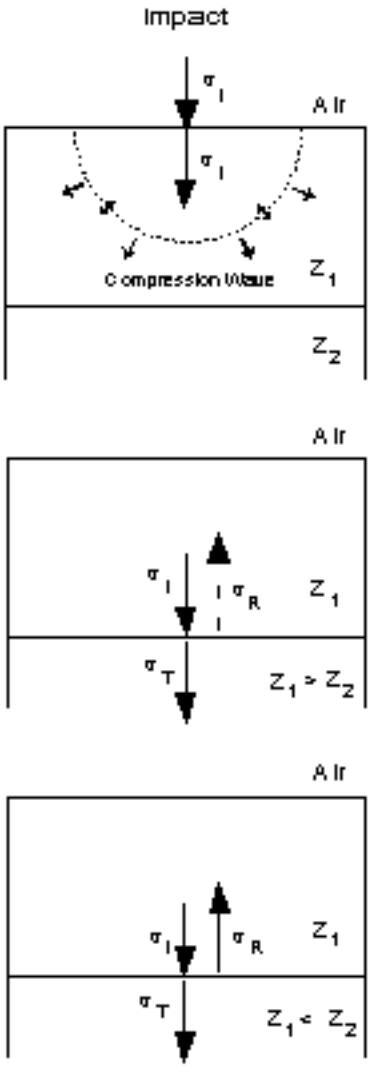

Figure 2.5 Reflection and Transmission of a Stress Wave at an Impedance Change

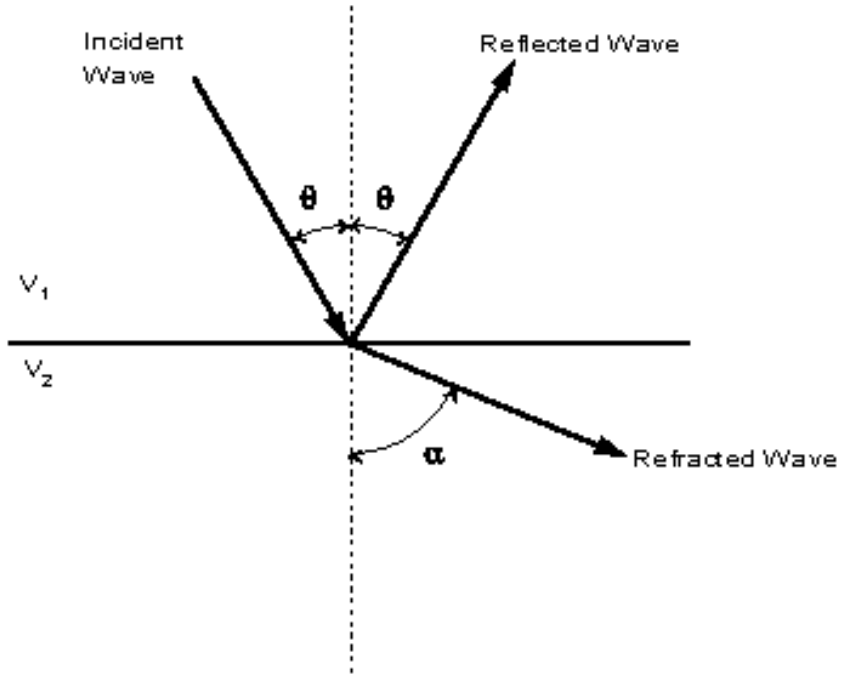

Figure 2.6 Reflection and Refraction of an Incident Compression Wave at an Interface

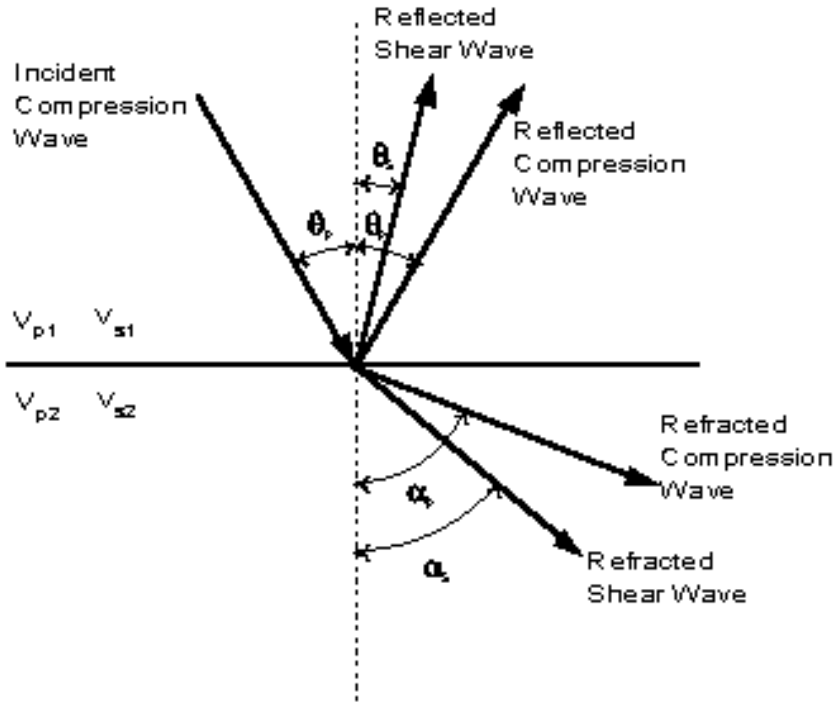

Figure 2.7 Mode Conversion of an Incident Compression Wave at an Interface

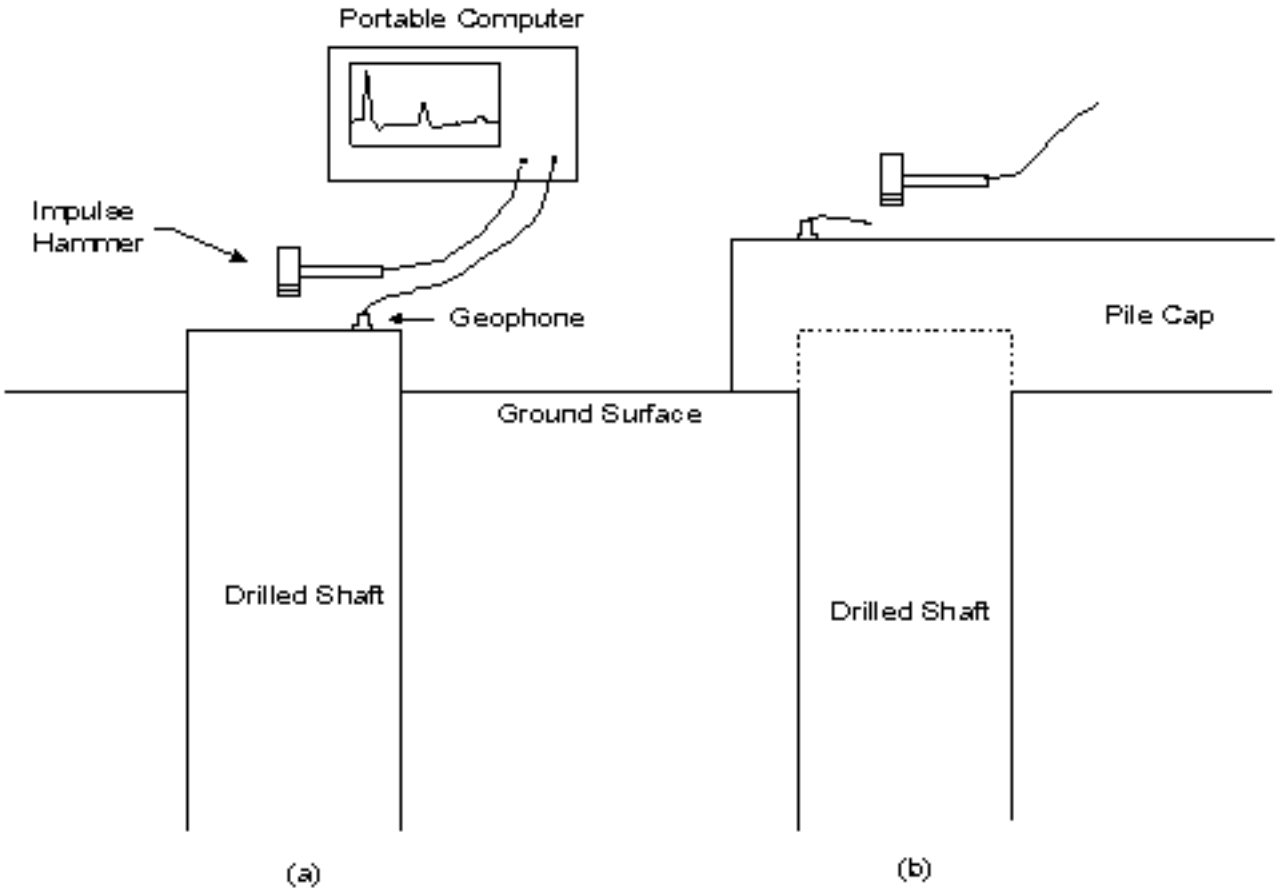

Figure 2.8 Testing Setup for Surface Reflection Techniques: (a) Accessible-Head and (b) Inaccessible-Head

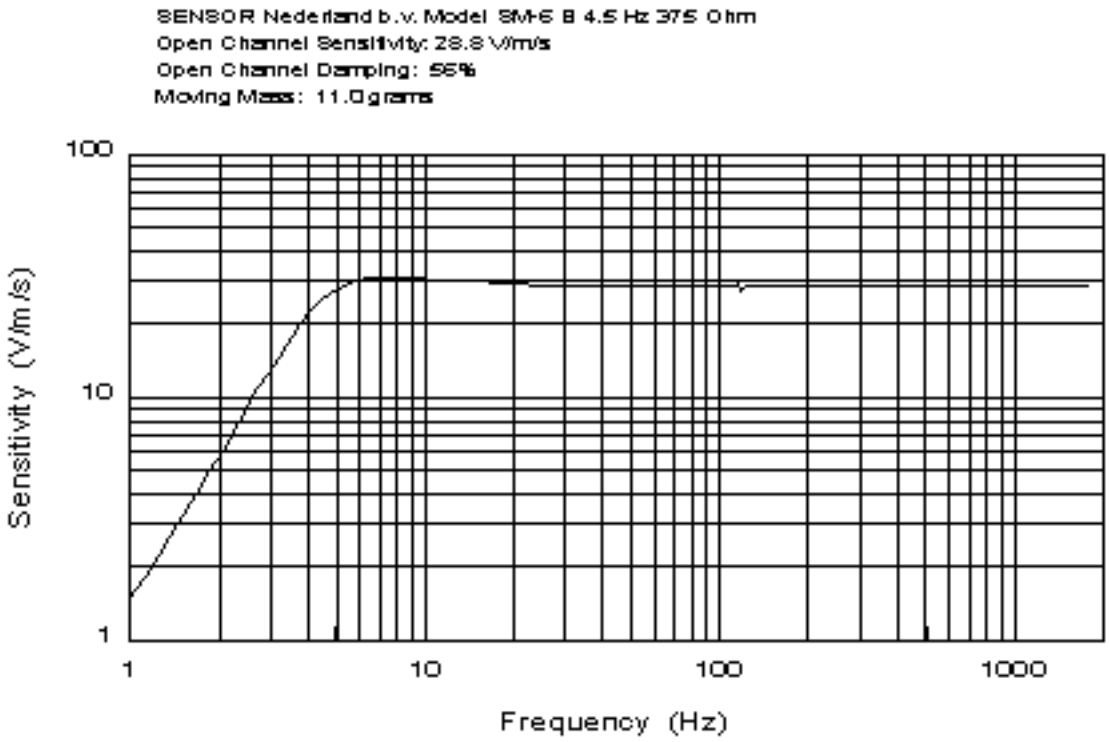

Figure 2.9 Response Curve for SM-6 Digital Grade Geophone
(adapted from Sensor Nederland b.v. Literature)

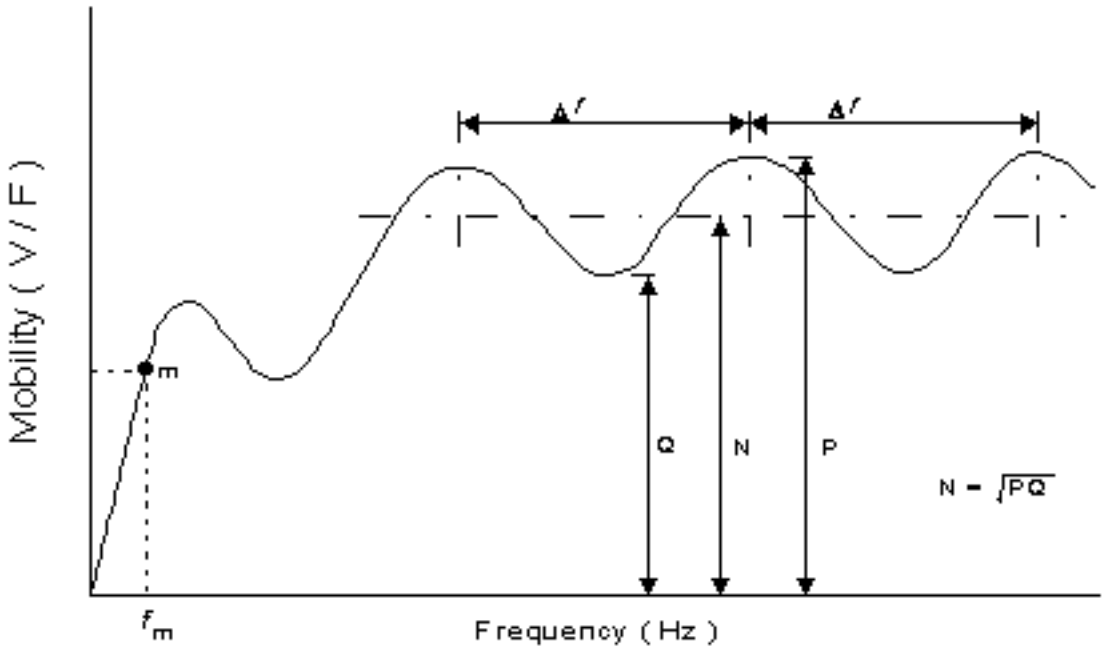

Figure 2.10 Ideal Impulse Response Result

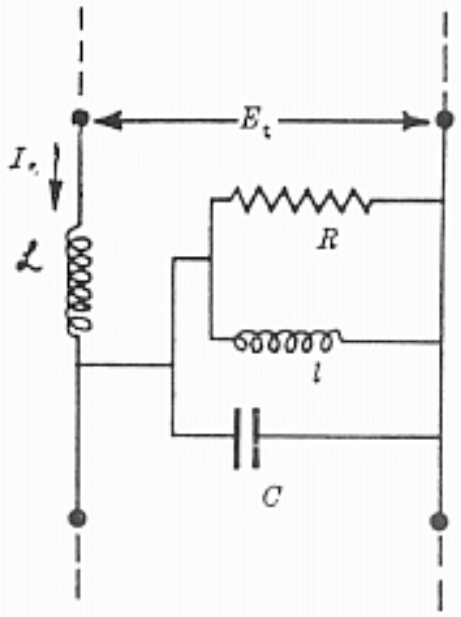

Figure 2.11 Electric Analogue of a Pile Segment (after Davis & Dunn, 1974)

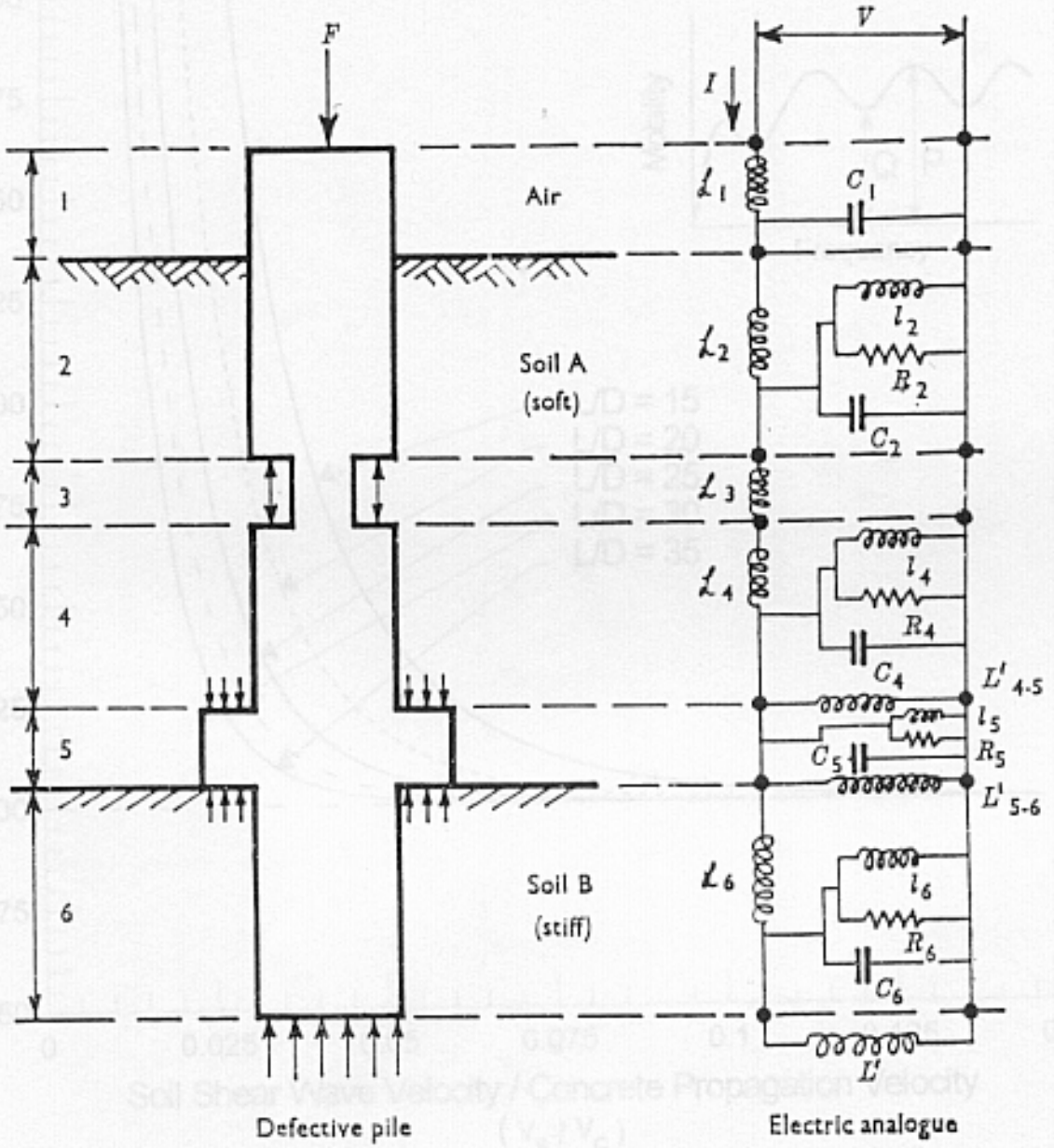

Figure 2.12 Electric Analogue for a Defective Pile (after Davis & Dunn, 1974)

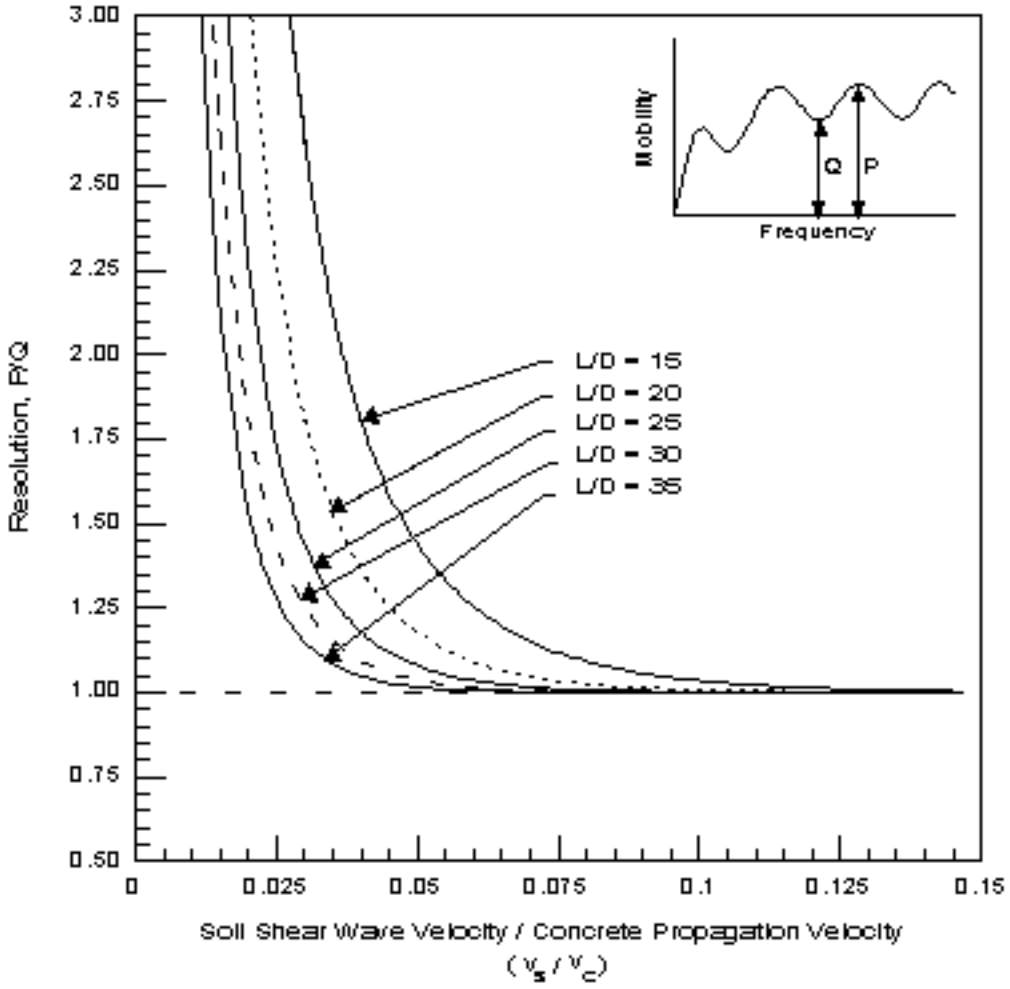

Figure 2.13 Ideal Resolution Chart

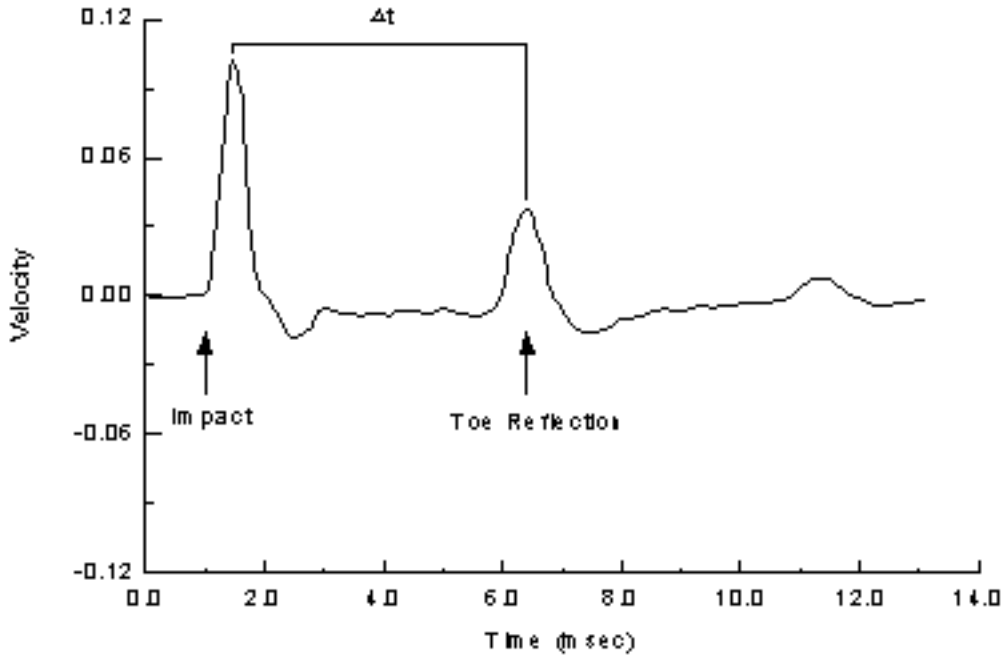

Figure 2.14 Typical Sonic Echo Result: Velocity versus Time

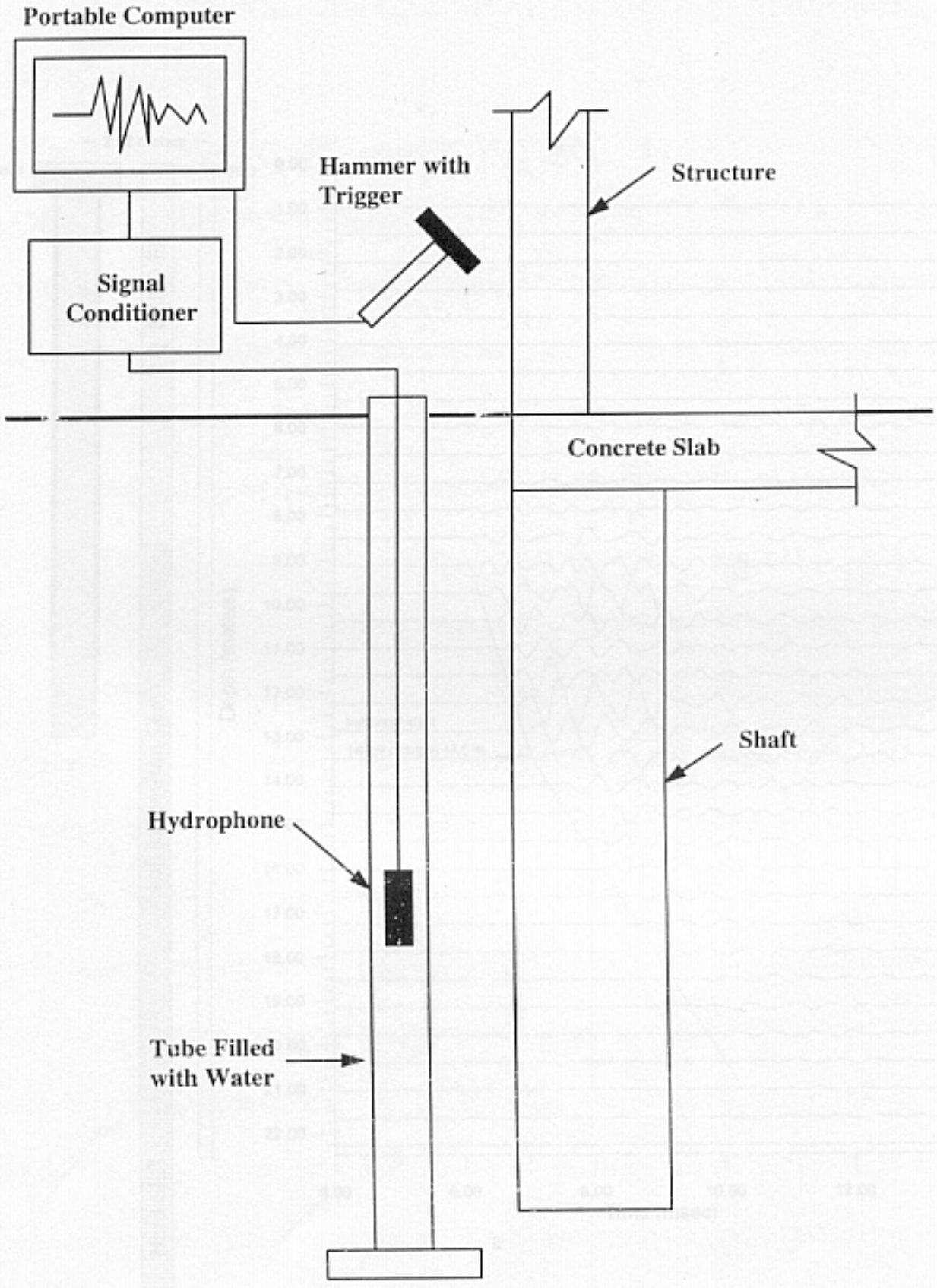

Figure 2.15 Typical Testing Arrangement for Parallel Seismic Testing (adapted from Stain, 1982)

Figure 2.13 Typical Testing Arrangement for Parallel Seismic Testing
(adapted from Stain, 1982)

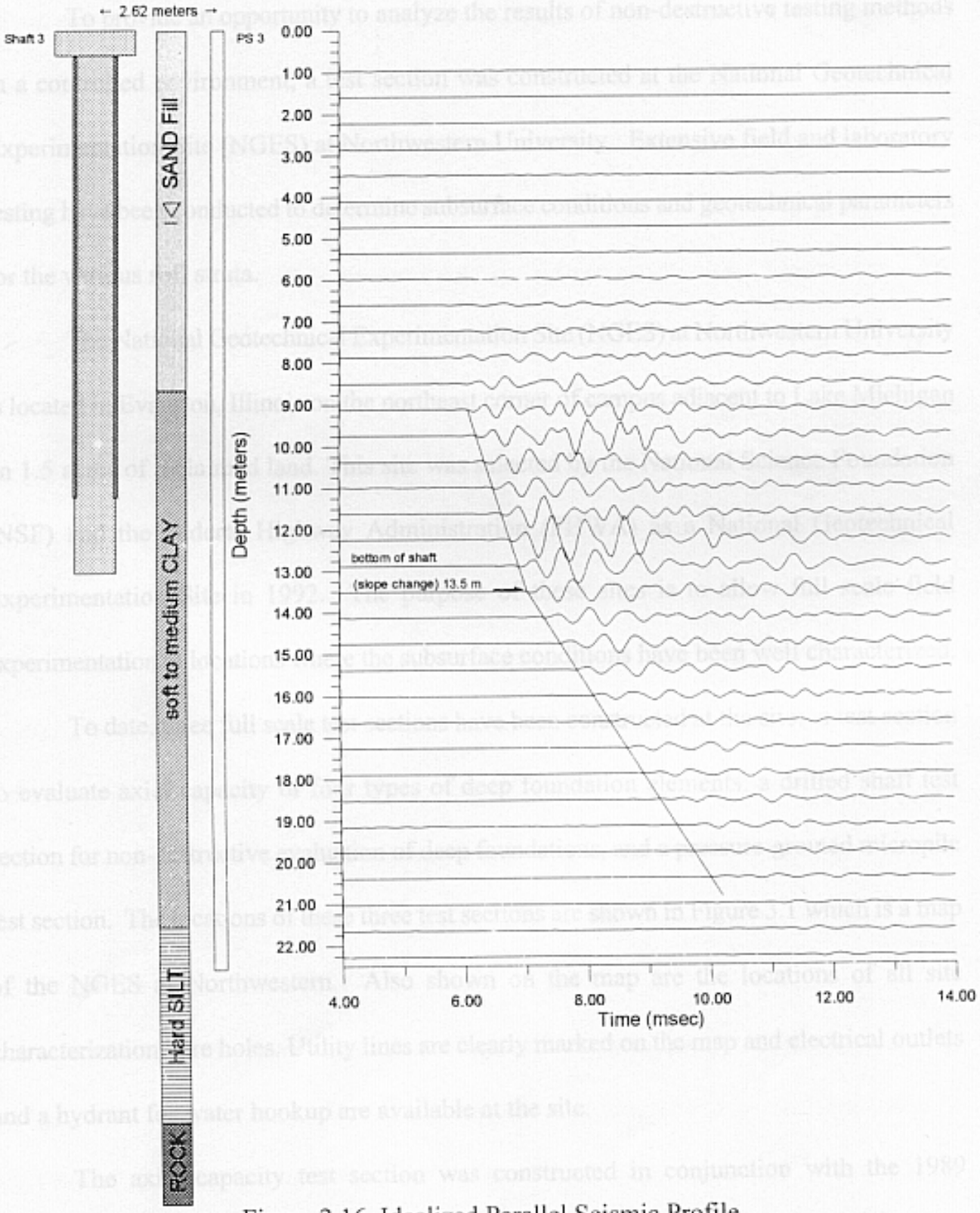

Figure 2.16 Idealized Parallel Seismic Profile

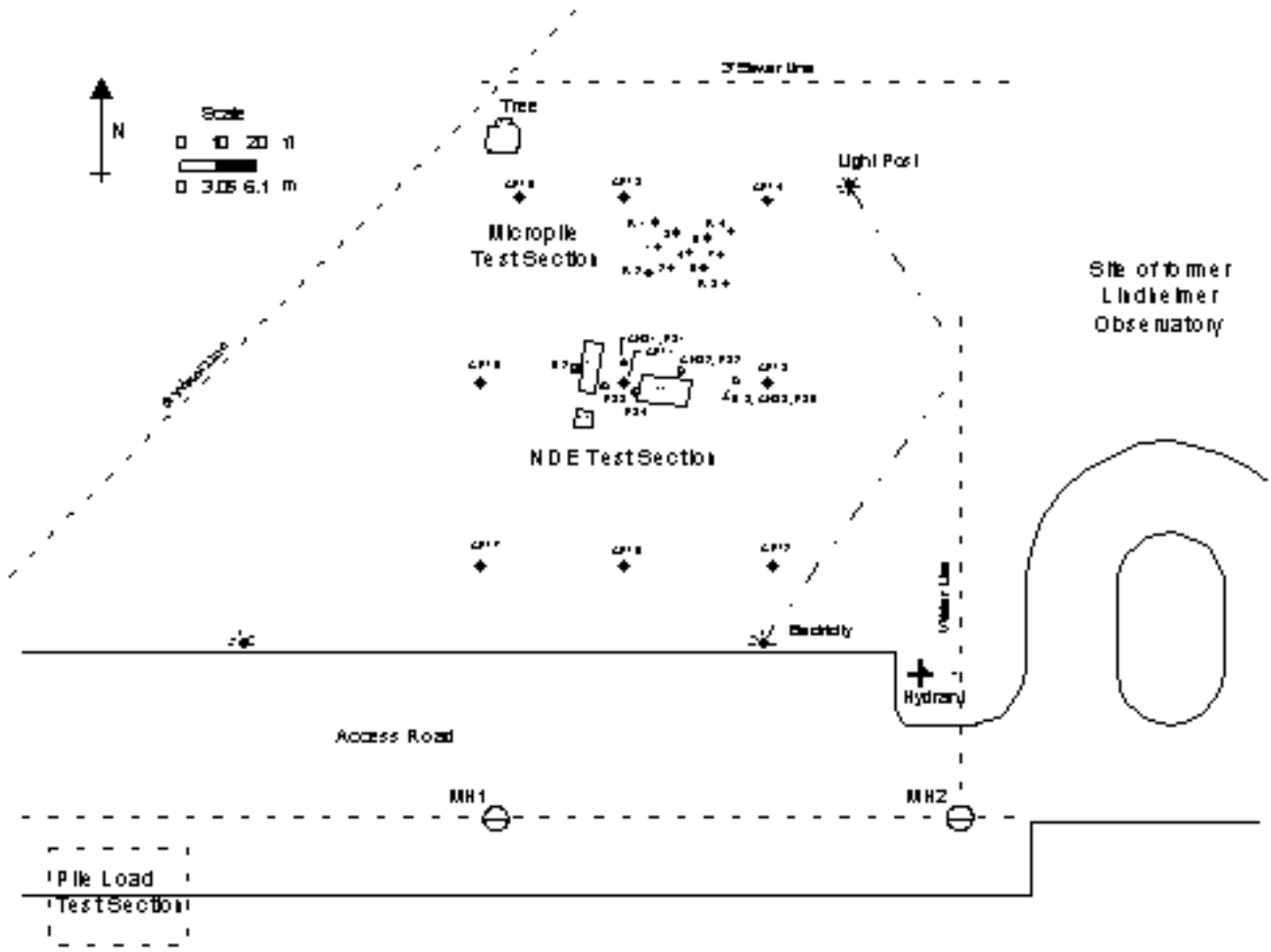

Figure 3.1 Plan of the National Geotechnical Experimentation Site (NGES) at Northwestern University

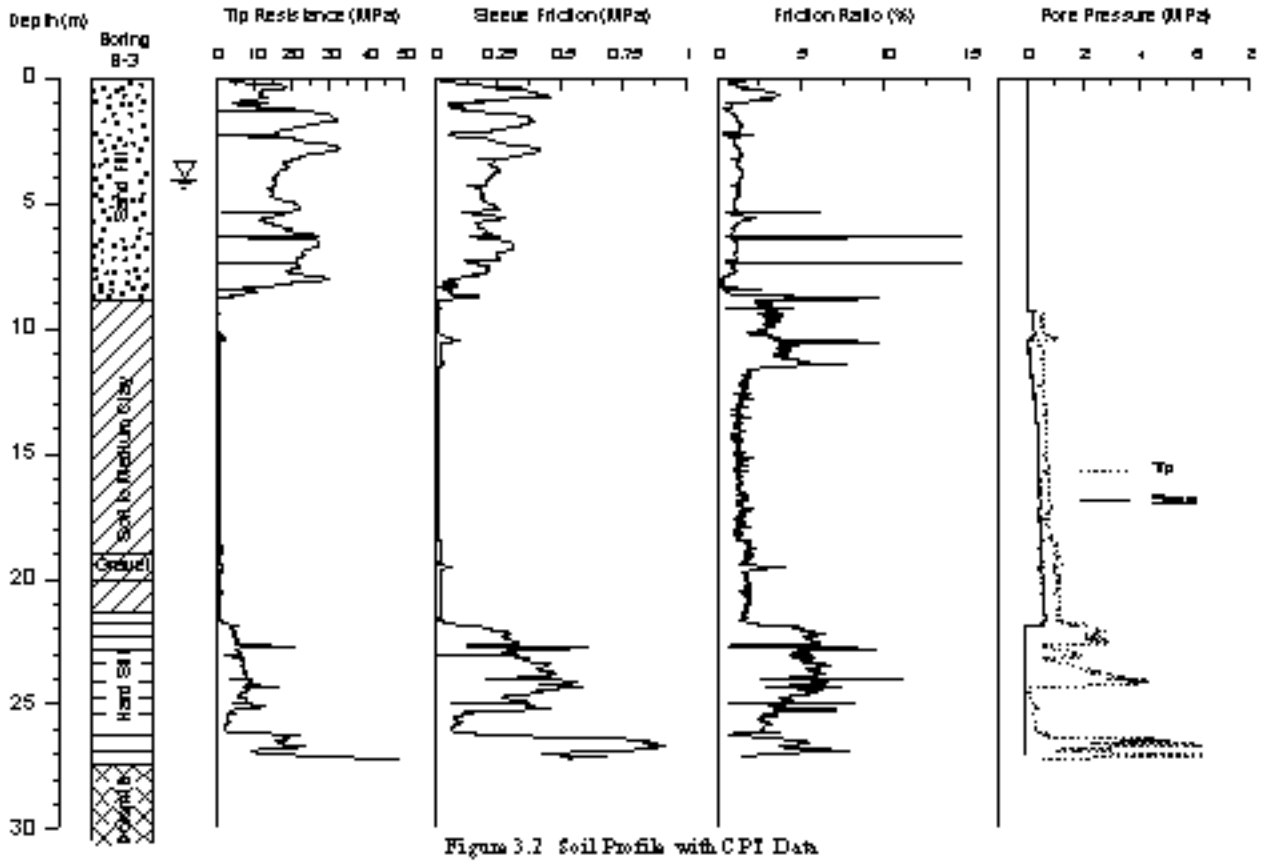

Figure 3.2 Soil Profile with CPT Data

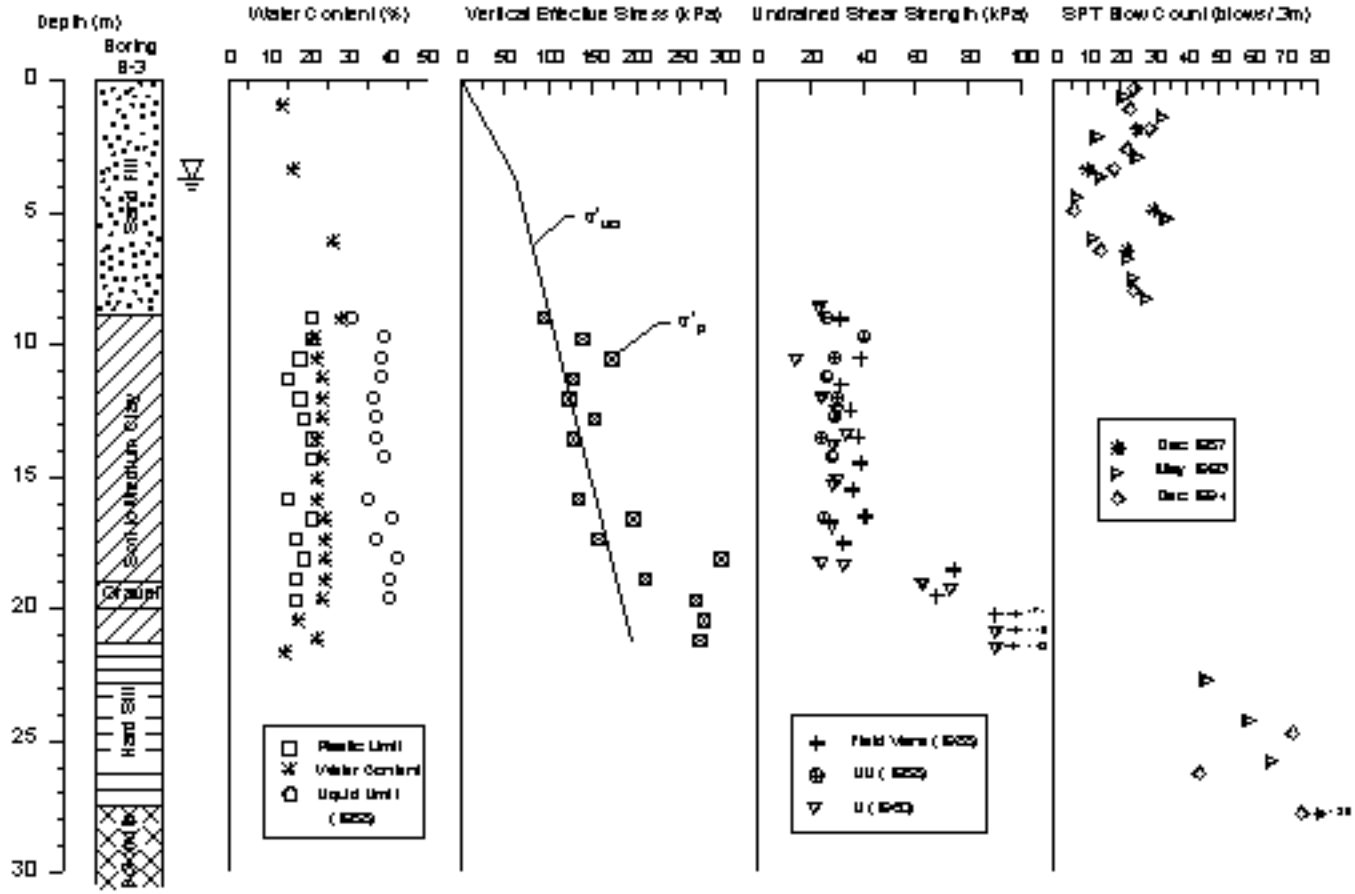

Figure 3.3 Geotechnical Characteristics of NGES Soils

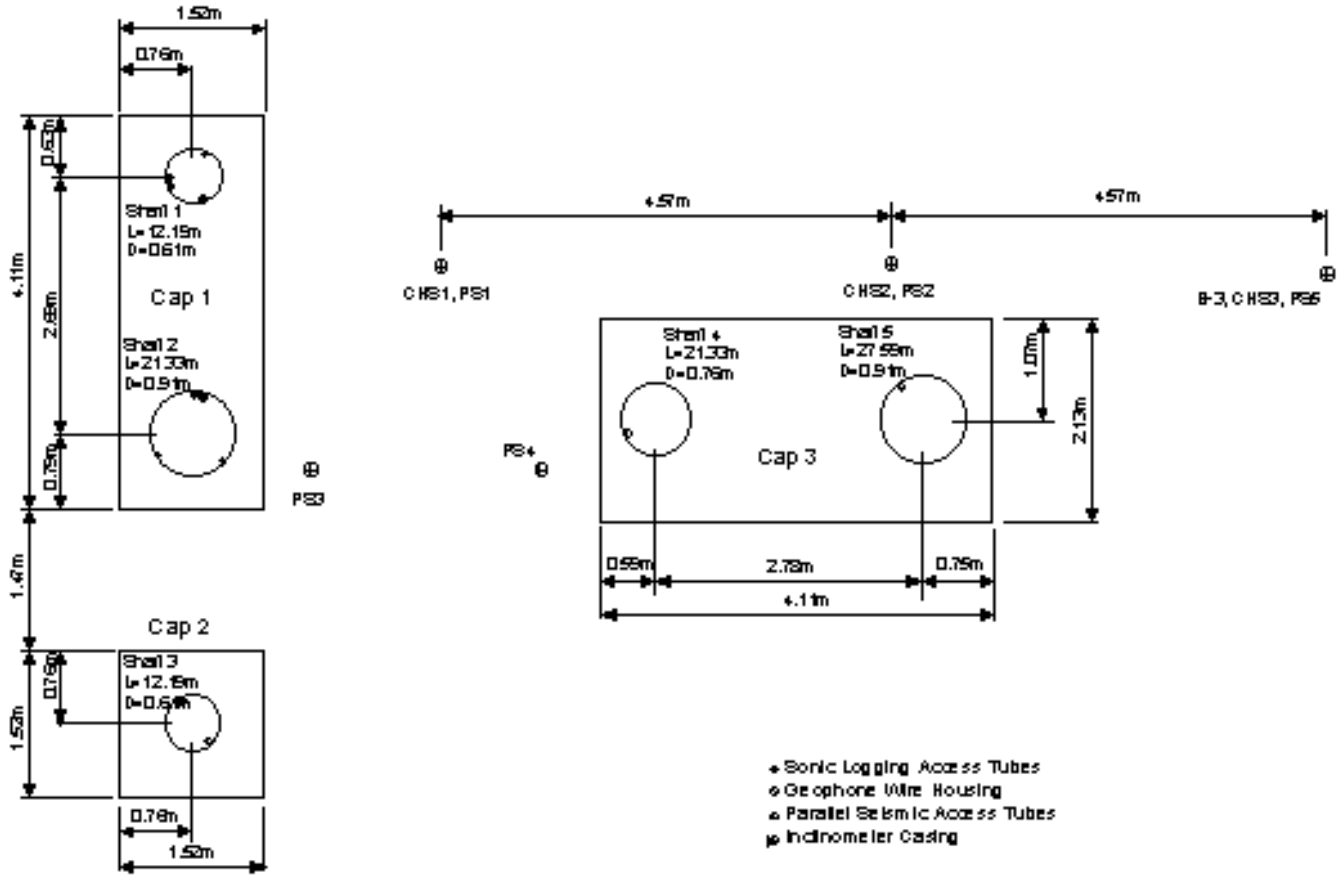

Figure 3.4 NDE Test Section, Plan View

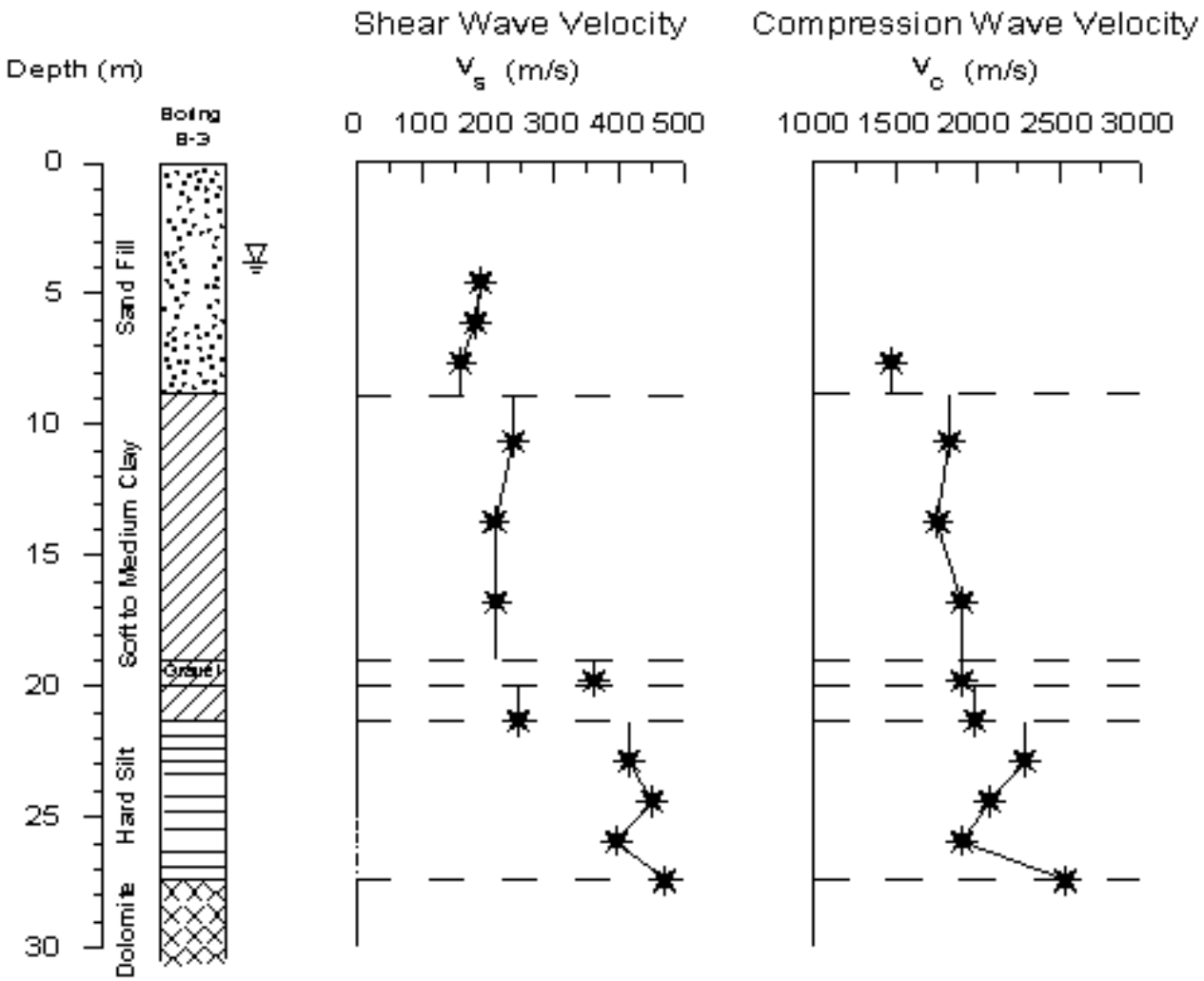

Figure 3.5 Shear and Compression Wave Velocities of NGES Soils

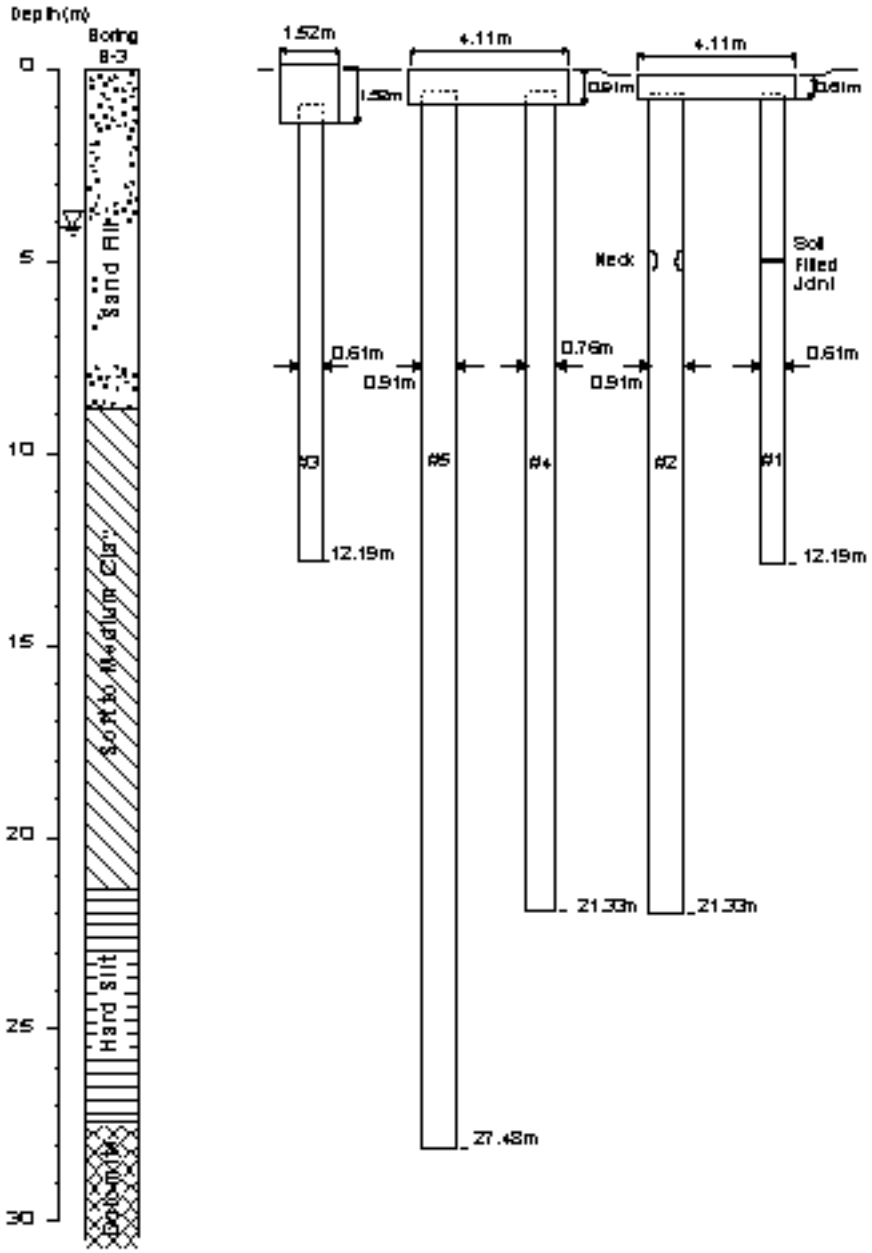

Figure 3.6 Profile View of NGES Test Section

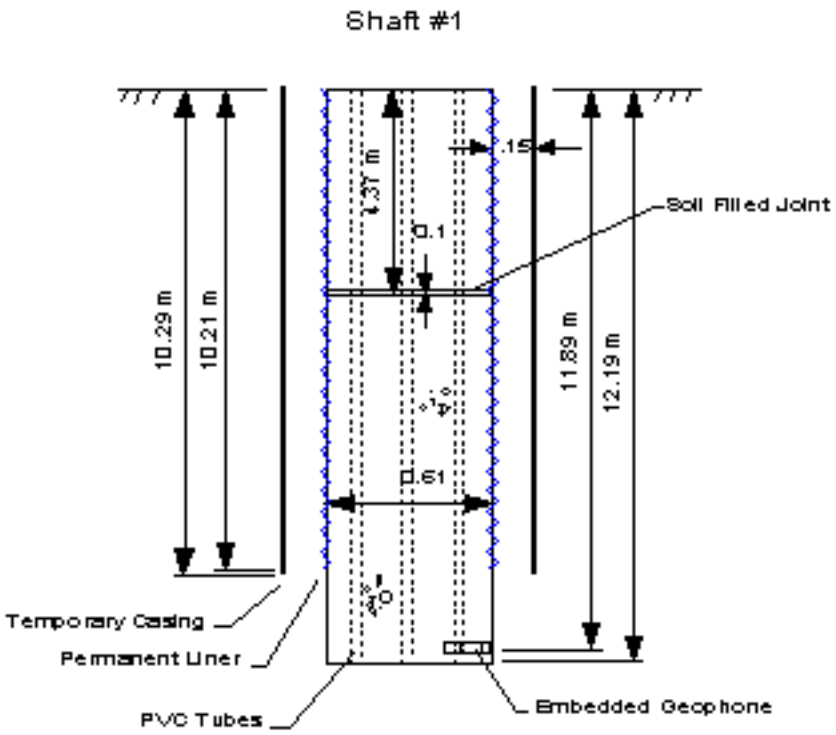

Figure 3.7 Detailed Schematic of Shaft 1 - Accessible-Head Condition

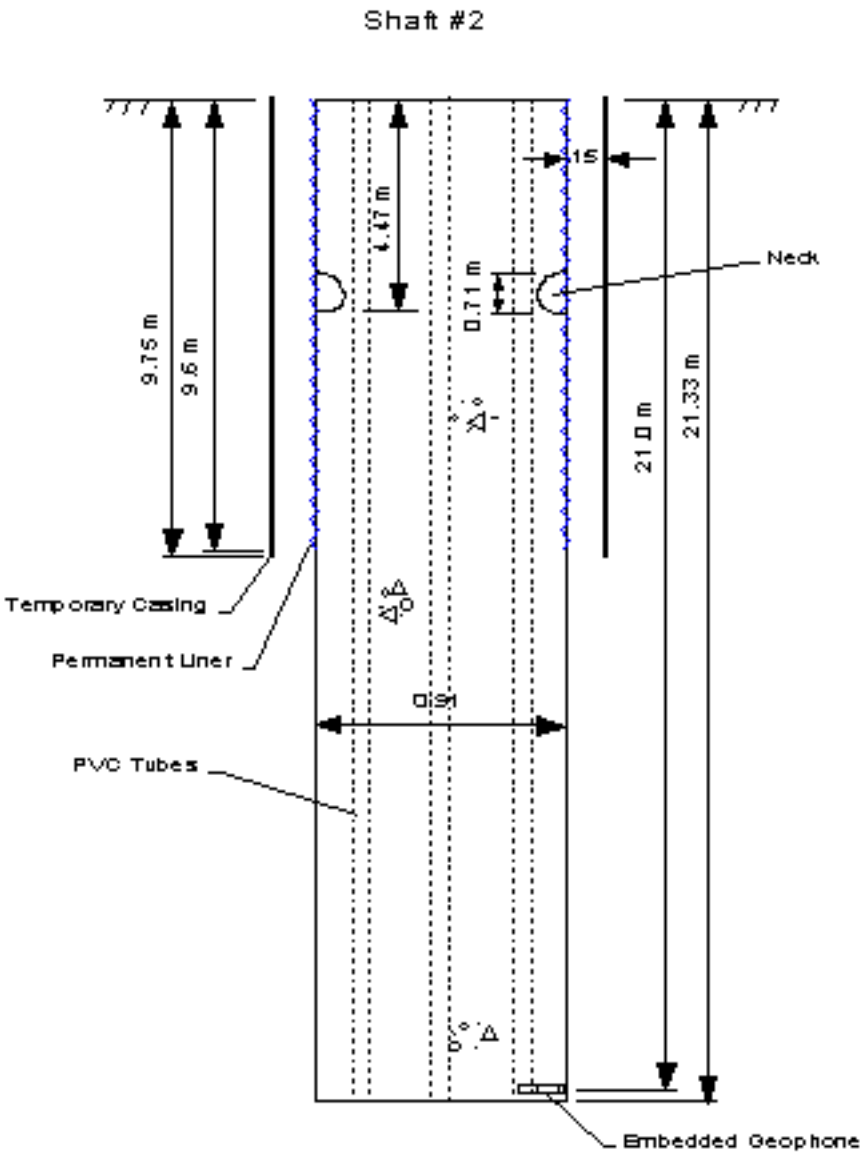

Figure 3.8 Detailed Schematic of Shaft 2 - Accessible-Head Condition

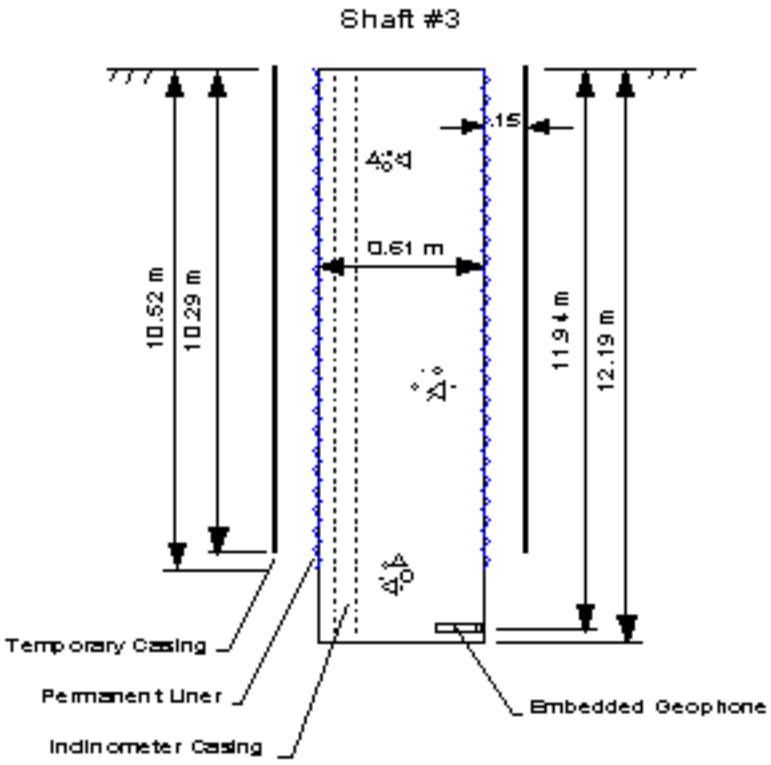

Figure 3.9 Detailed Schematic of Shaft 3 - Accessible-Head Condition

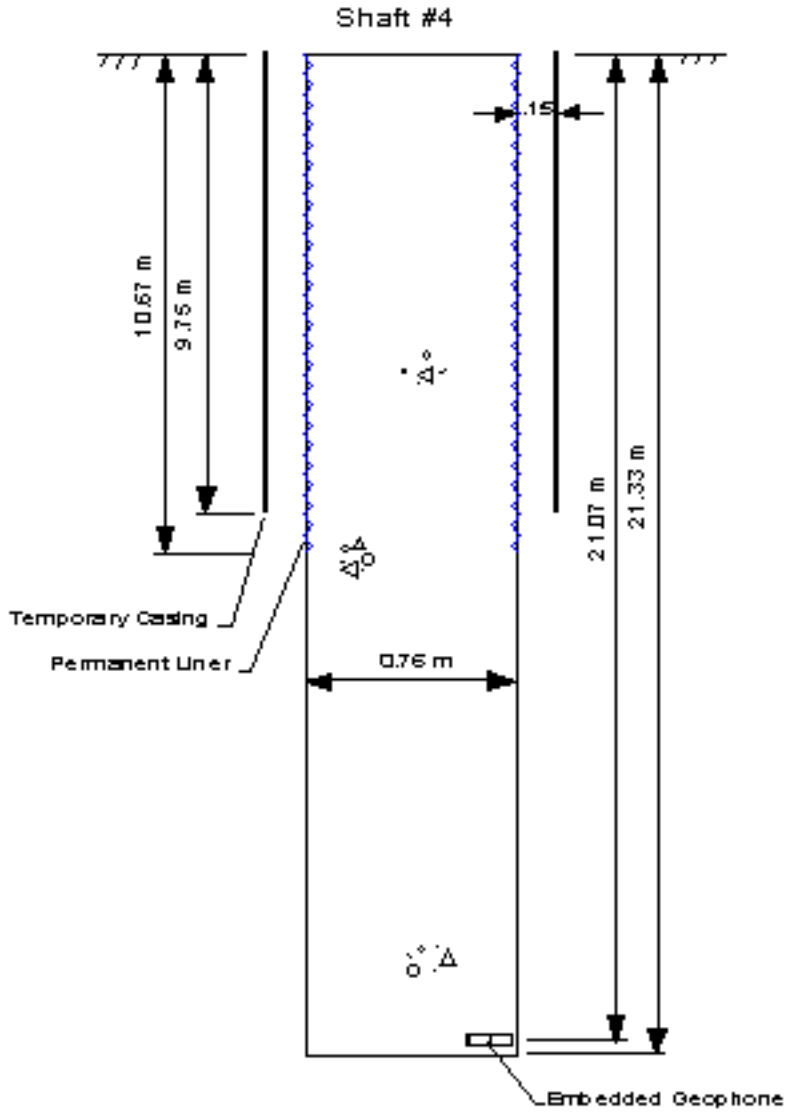

Figure 3.10 Detailed Schematic of Shaft 4 - Accessible-Head Condition

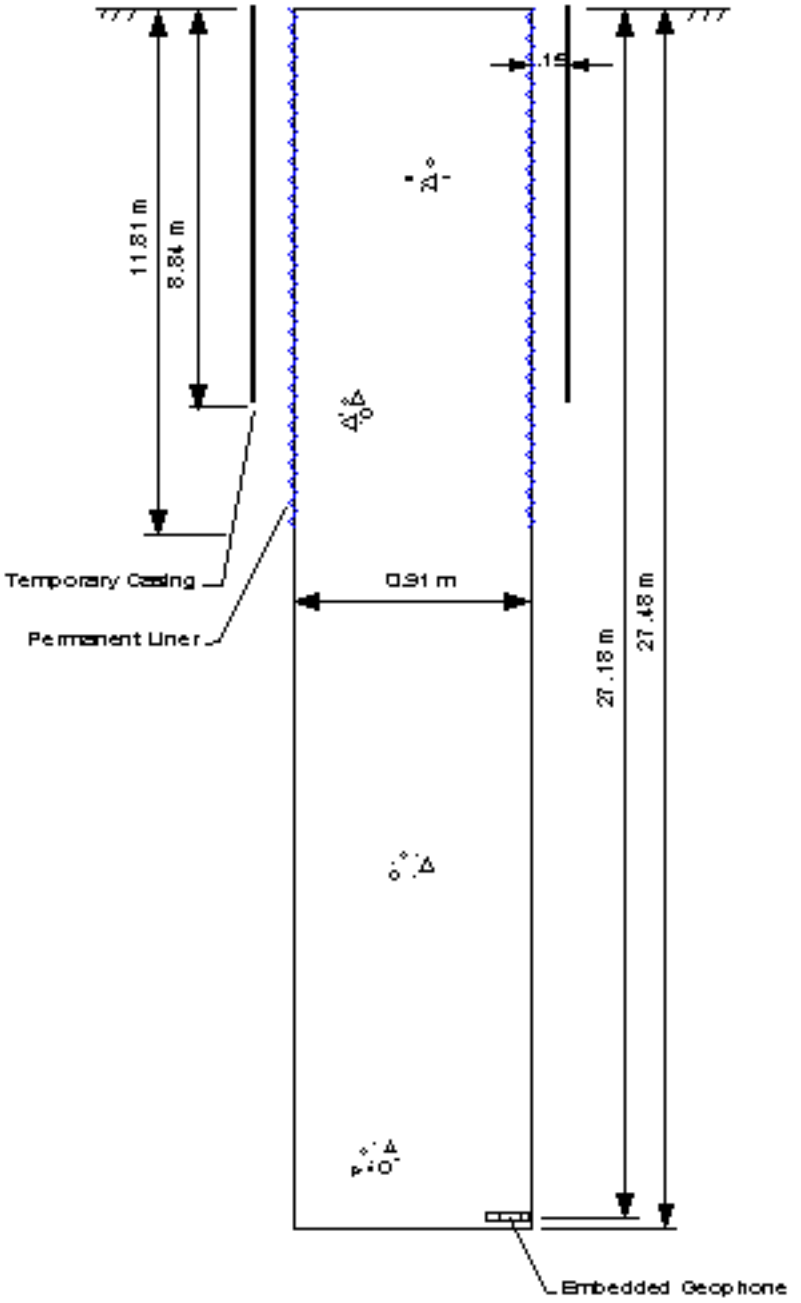

Figure 3.11 Detailed Schematic of Shaft 5 - Accessible-Head Condition

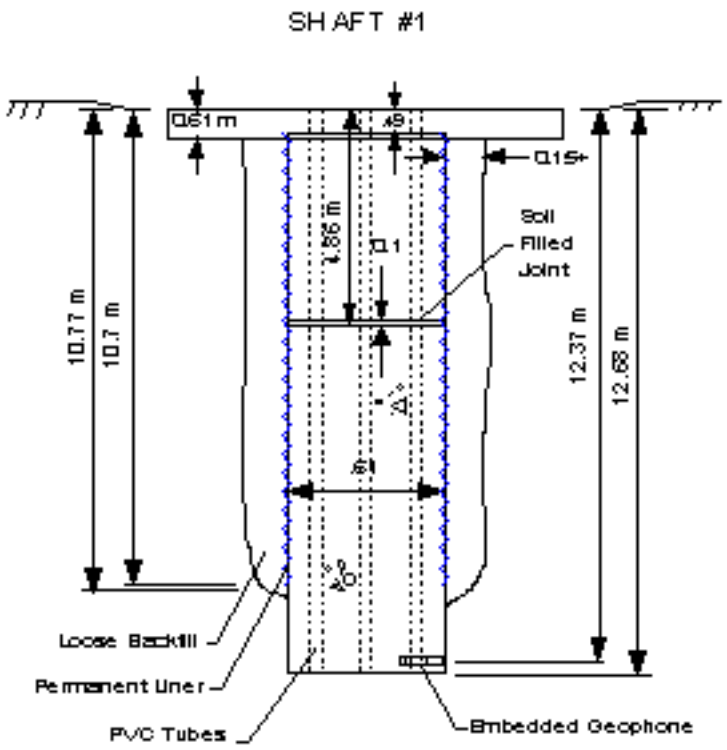

Figure 3.12 Detailed Schematic of Shaft 1 - Inaccessible-Head Condition

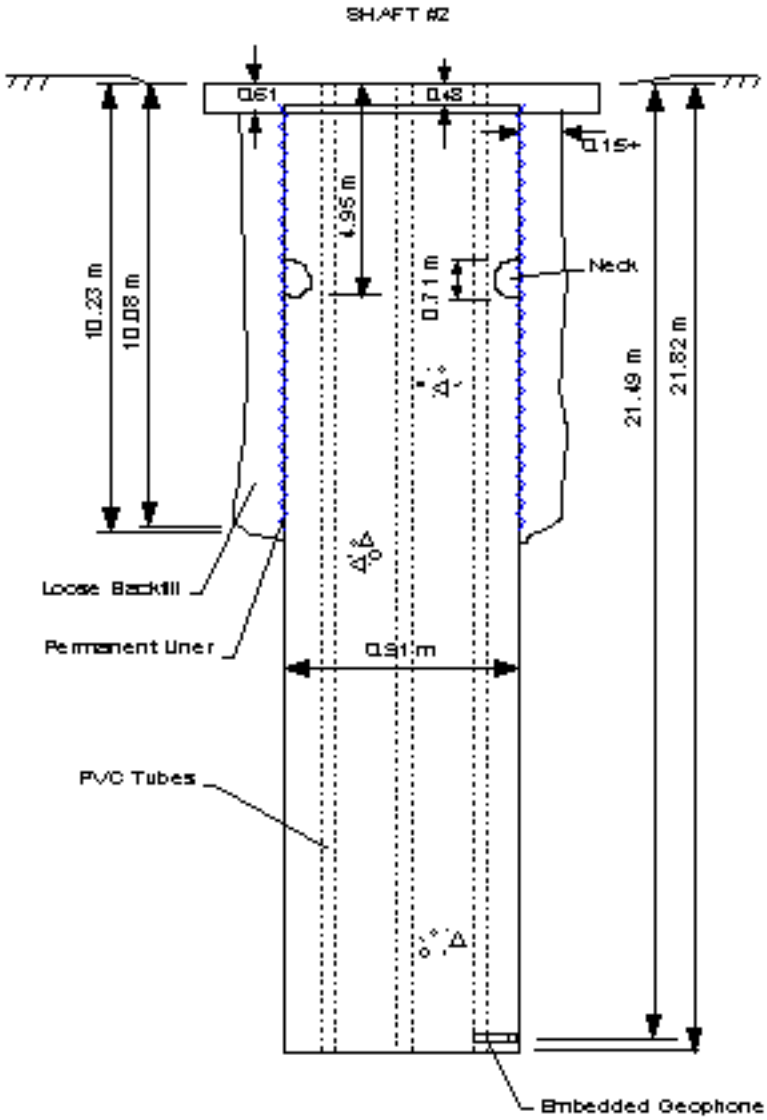

Figure 3.13 Detailed Schematic of Shaft 2 - Inaccessible-Head Condition

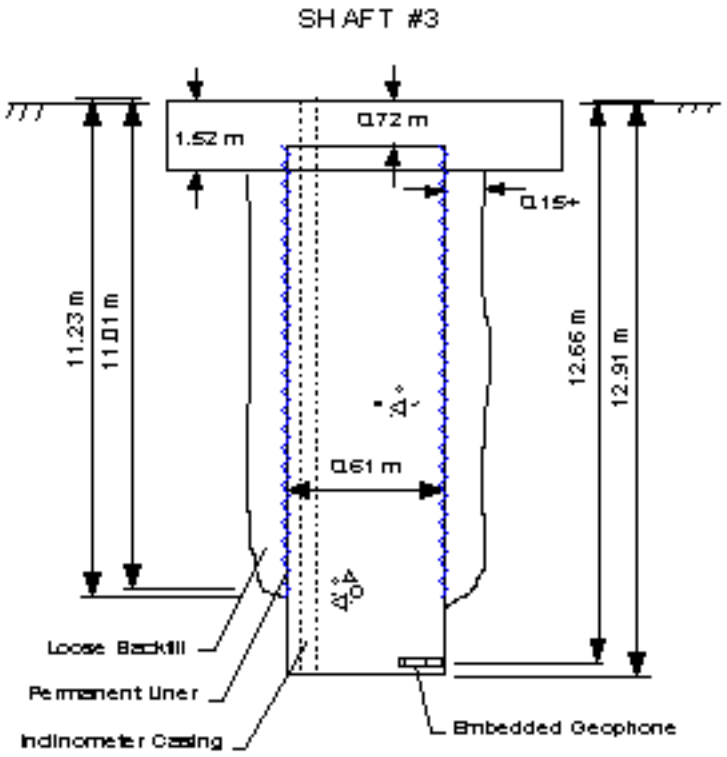

Figure 3.14 Detailed Schematic of Shaft 3 - Inaccessible-Head Condition

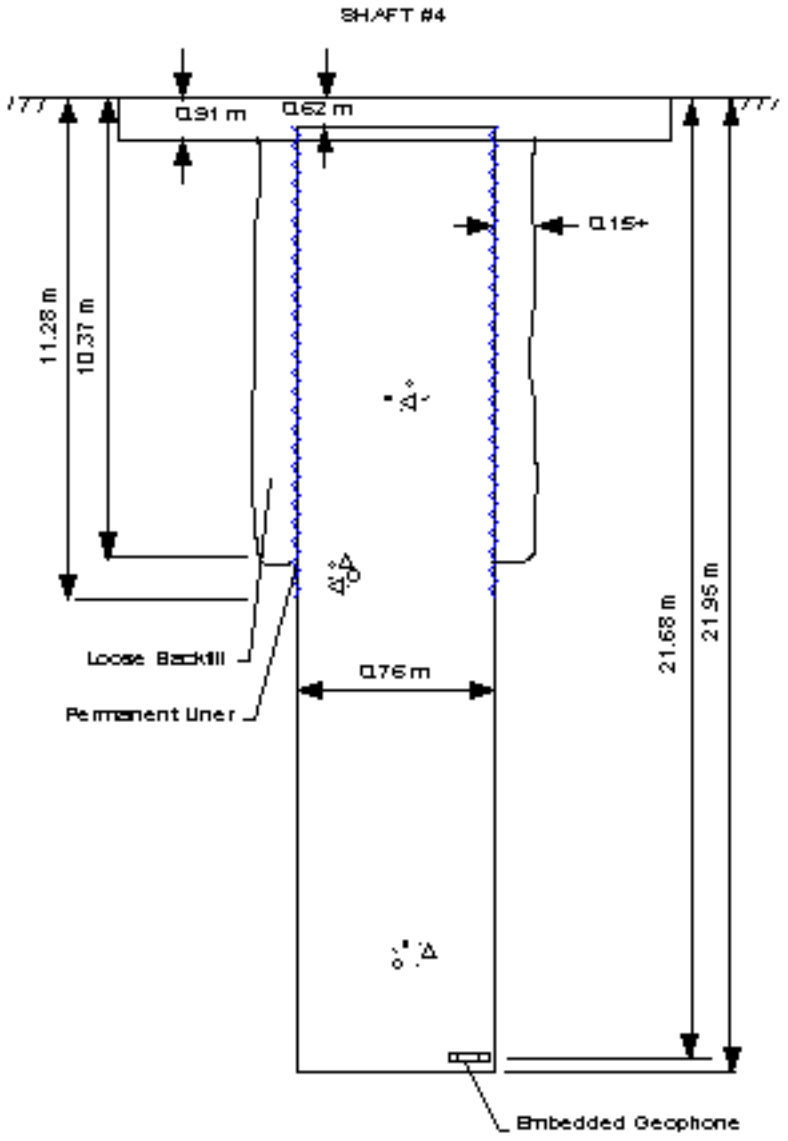

Figure 3.15 Detailed Schematic of Shaft 4 - Inaccessible-Head Condition

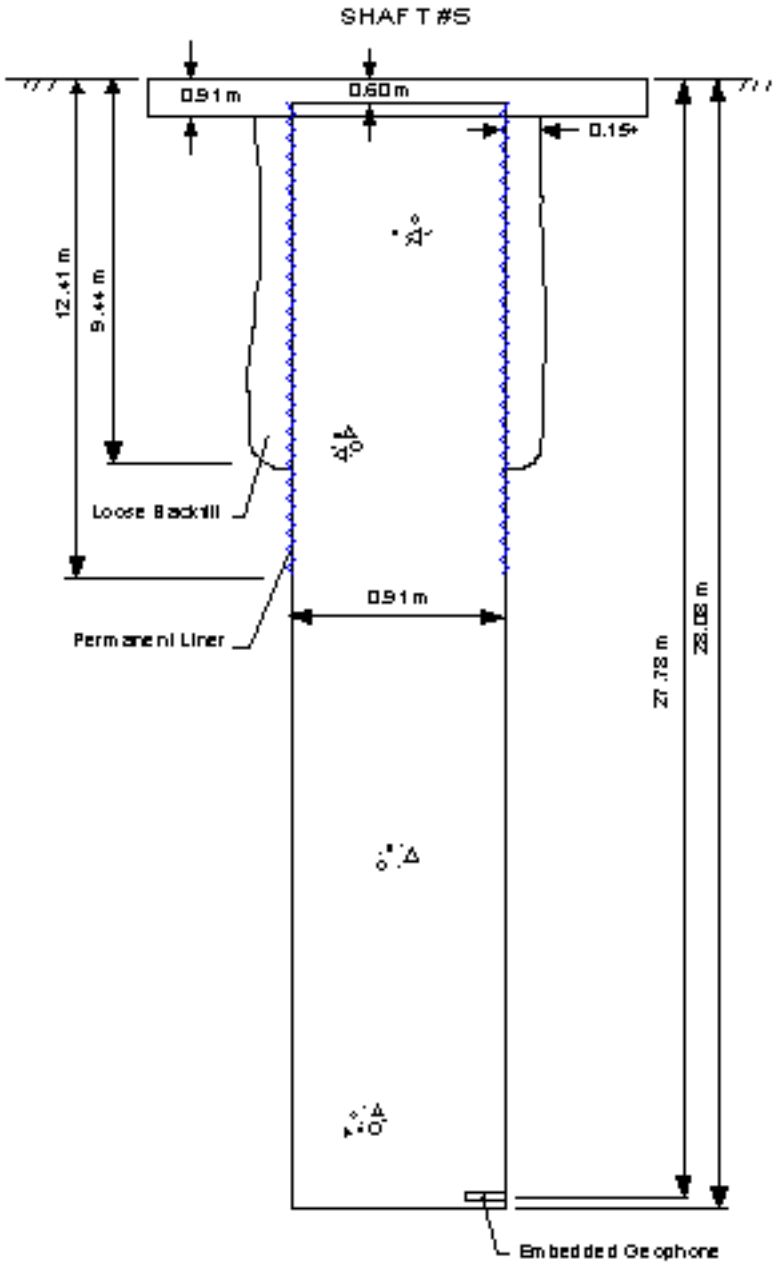

Figure 3.16 Detailed Schematic of Shaft 5 - Inaccessible-Head Condition

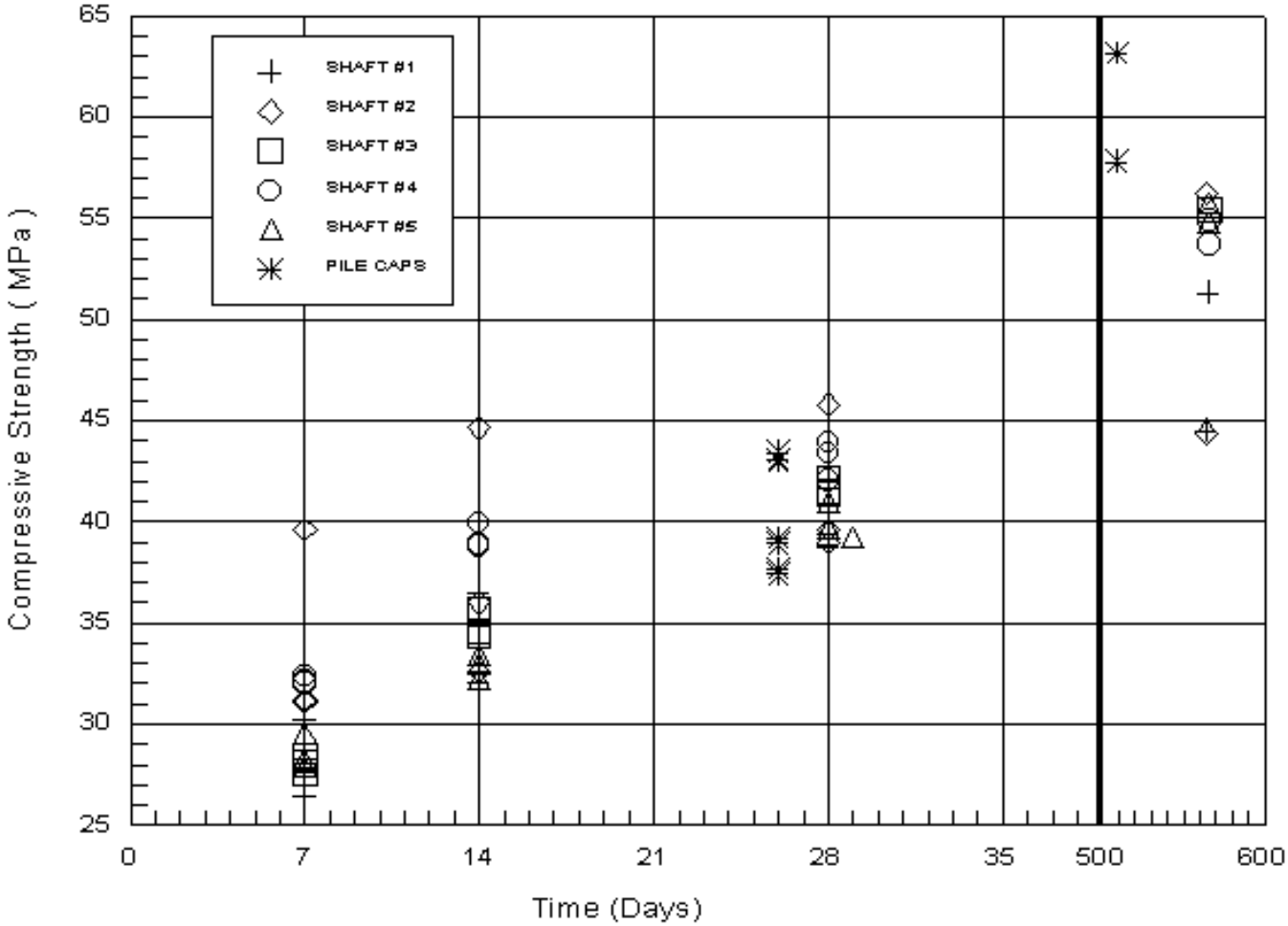

Figure 3.17 Unconfined Compression Test Results on Concrete Cylinders

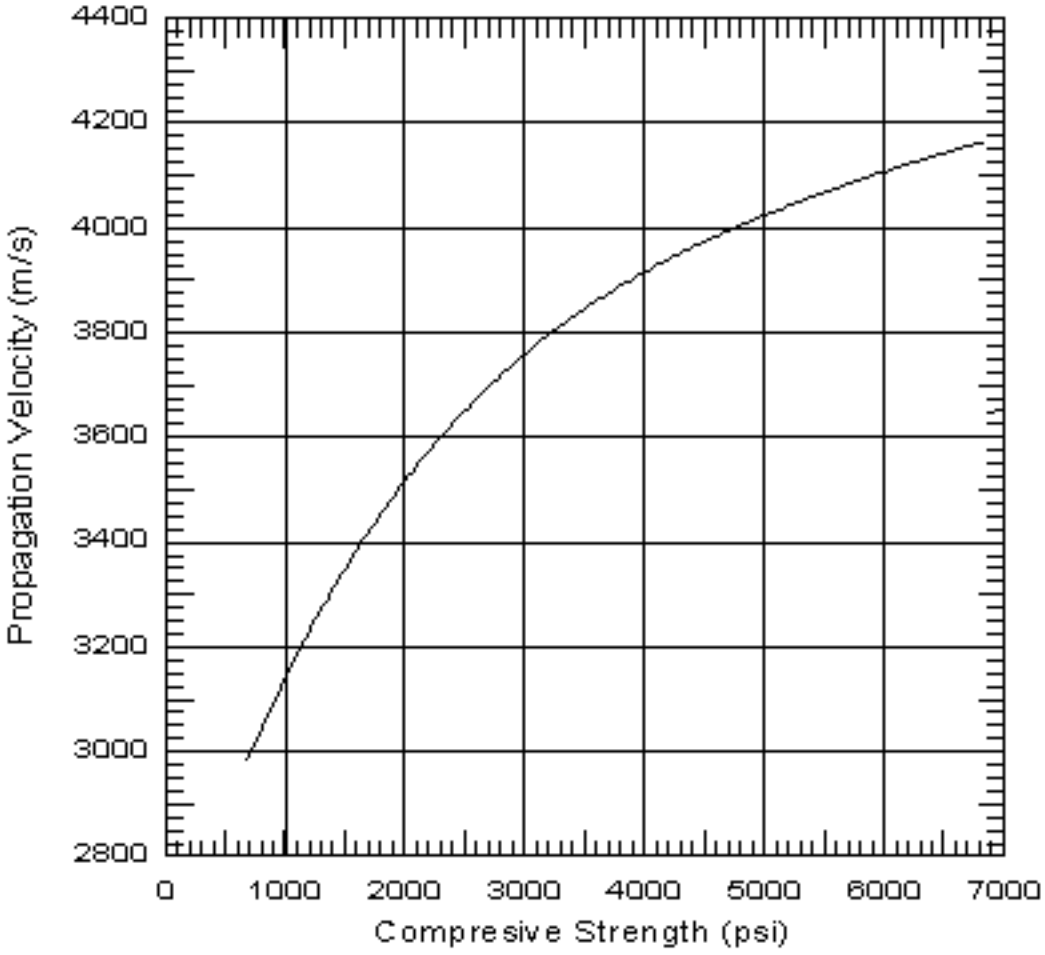

Figure 3.18 Correlation Between Propagation Velocity and Compresive Strength of Typical Concrete (after Davis and Robertson, 1975)

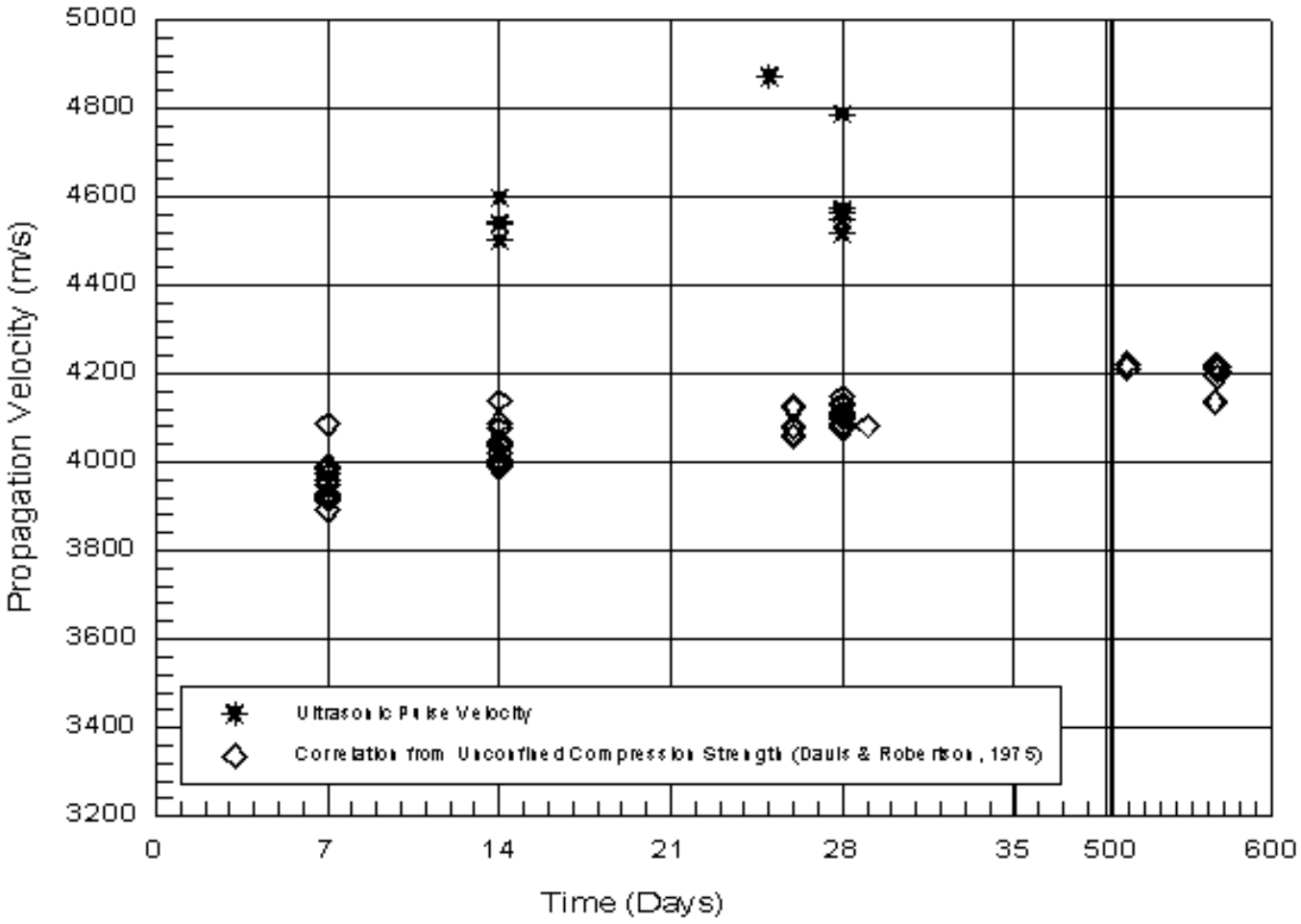

Figure 3.19 Change in Propagation Velocity with Concrete Age - Determined from UC and UPV Tests

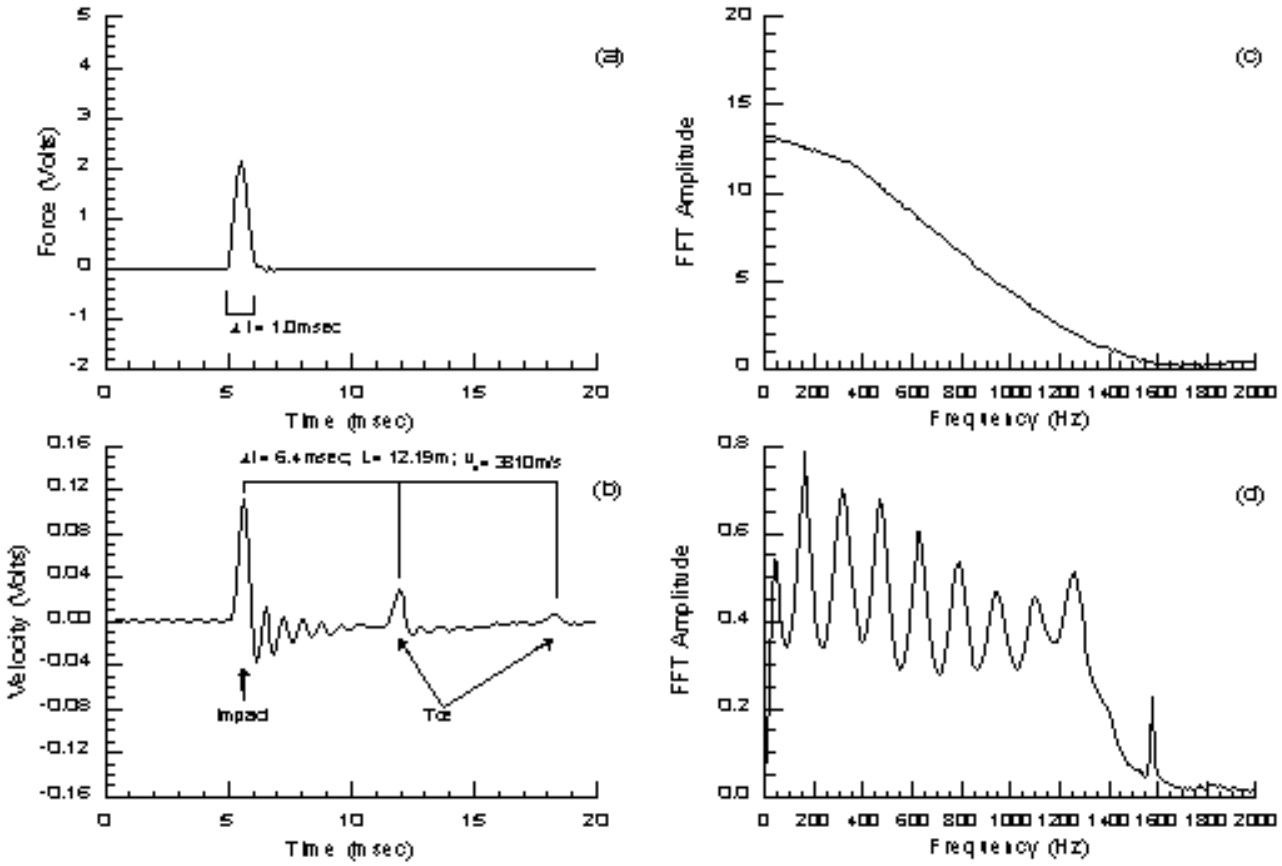

Figure 4.1 Impulse Response Result - Shaft 3: Time Domain and Frequency Spectrum

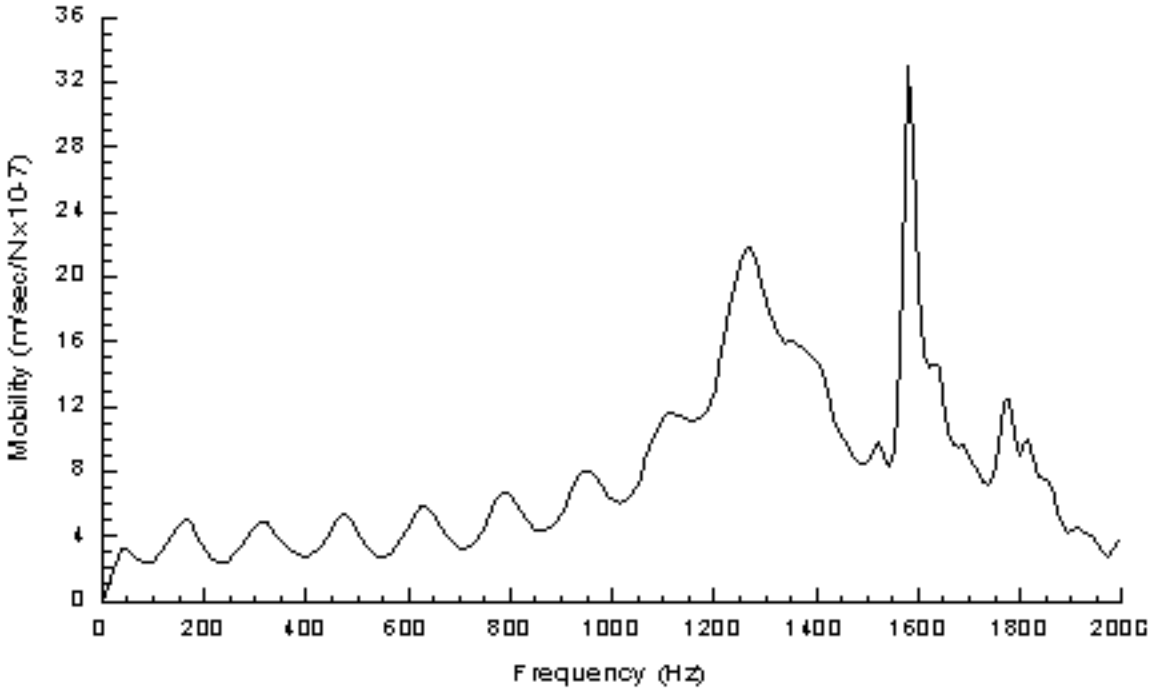

Figure 4.2 Impulse Response Result - Shaft 3: Mobility Plot up to 2000 Hz

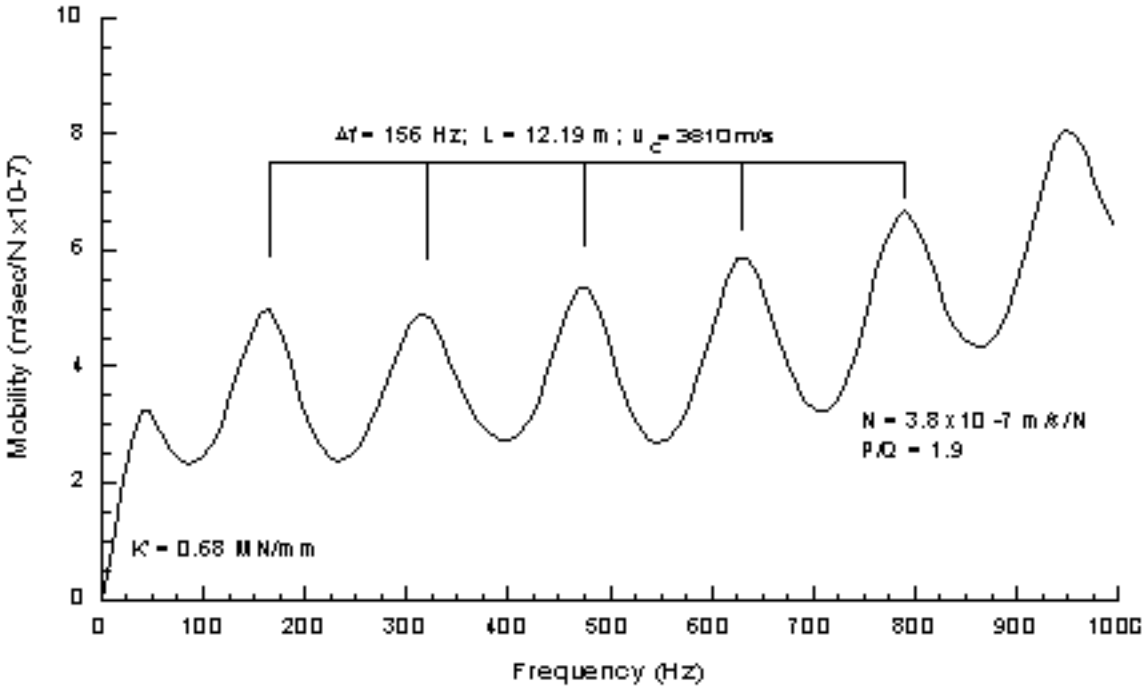

Figure 4.3 Impulse Response Result - Shaft 3: Mobility Plot up to 1000 Hz

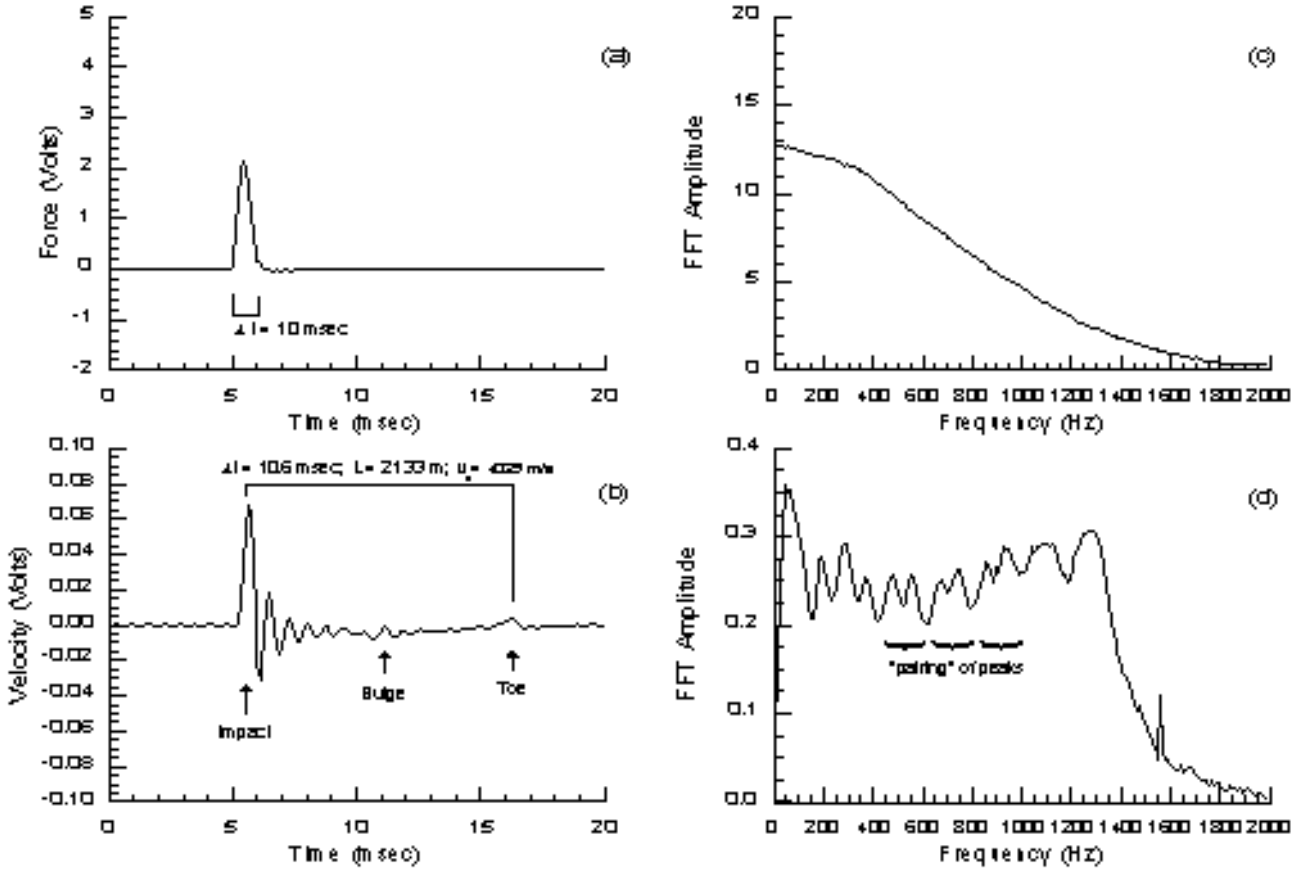

Figure 4.4 Impulse Response Result - Shaft 4: Time Domain and Frequency Spectrum

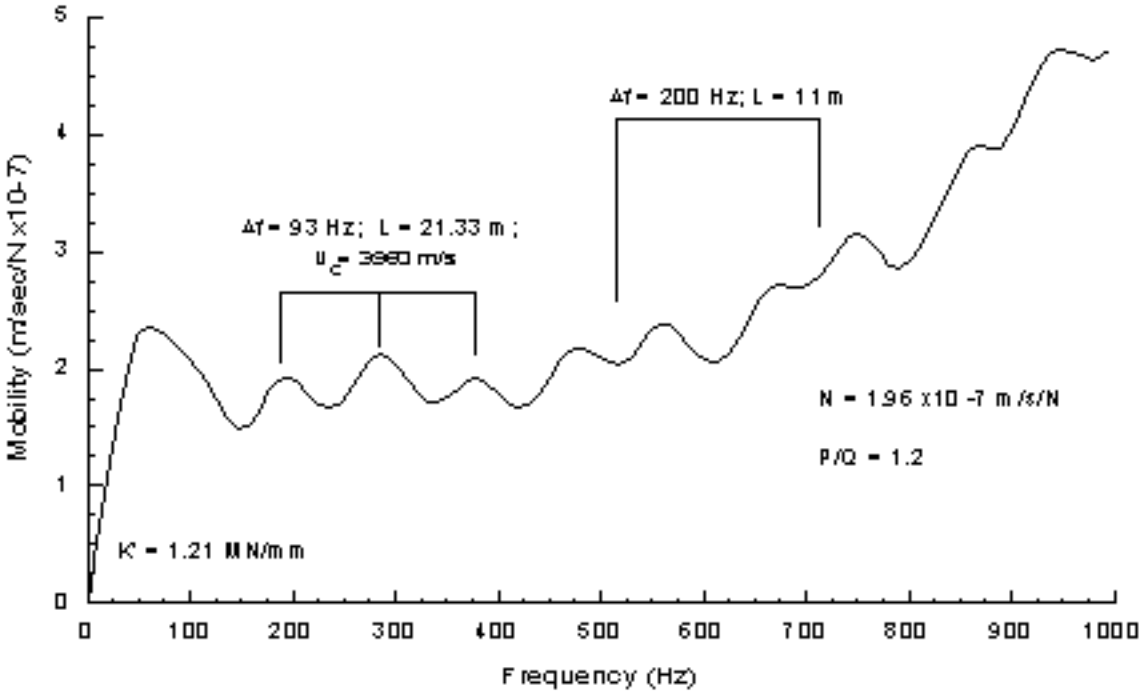

Figure 4.5 Impulse Response Result - Shaft 4: Mobility Plot

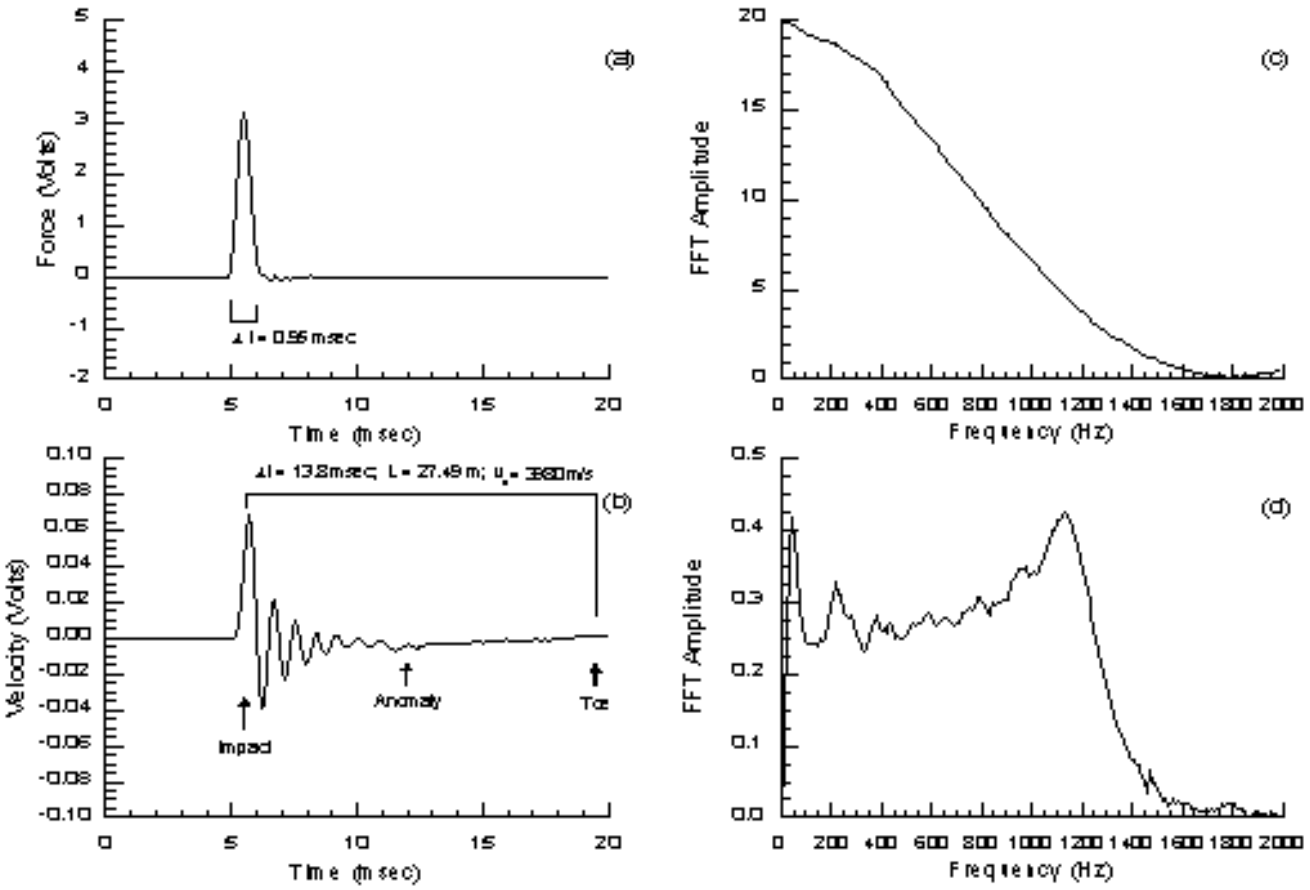

Figure 4.6 Impulse Response Result - Shaft 5: Time Domain and Frequency Spectrum

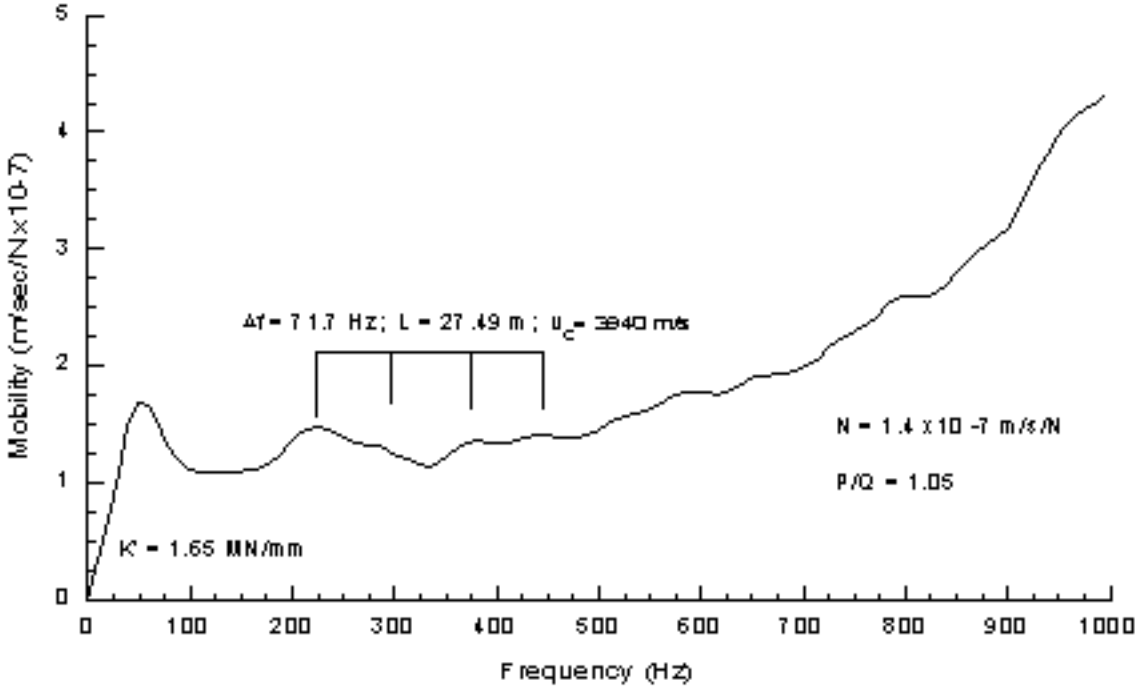

Figure 4.7 Impulse Response Result - Shaft 5: Mobility Plot

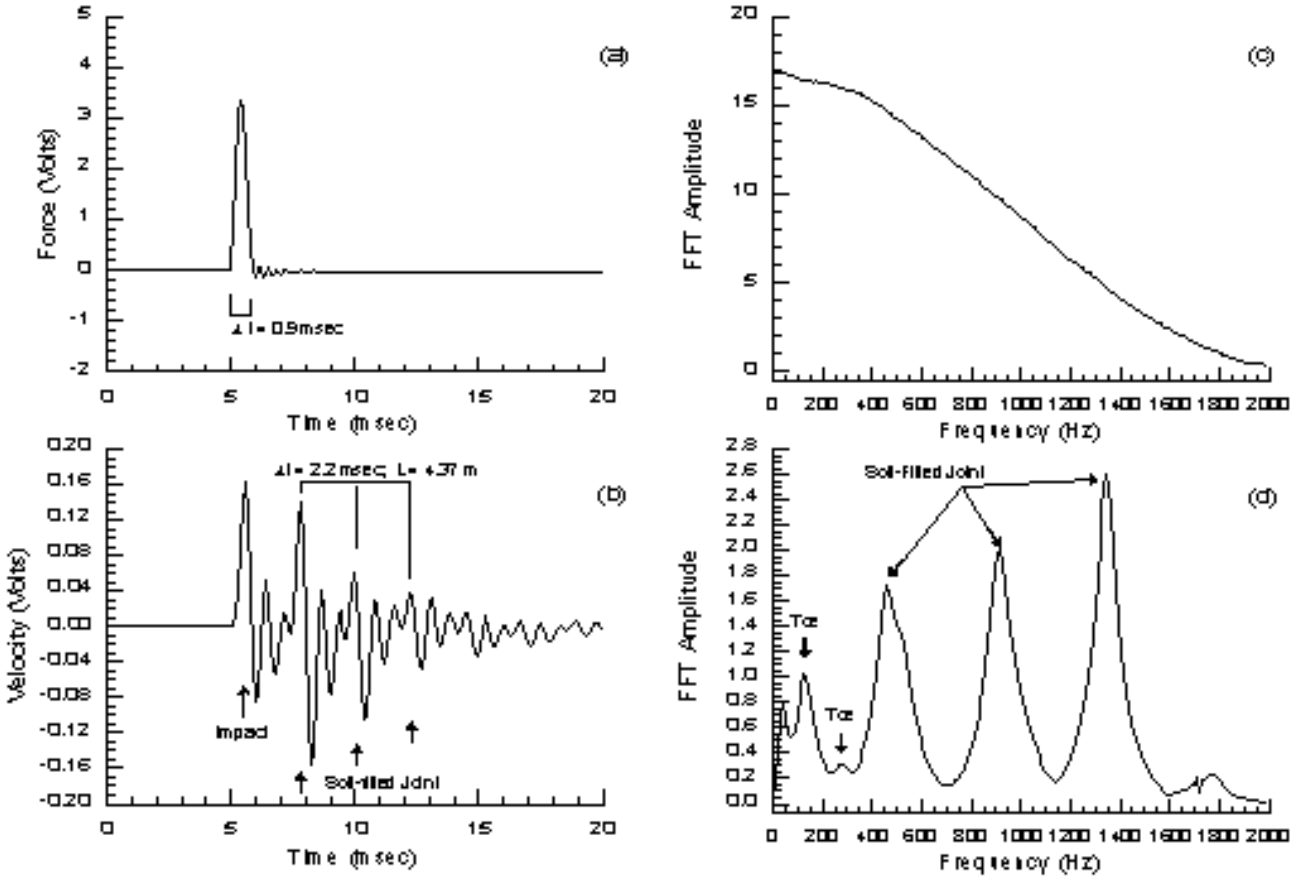

Figure 4.8 Impulse Response Result - Shaft 1: Time Domain and Frequency Spectrum

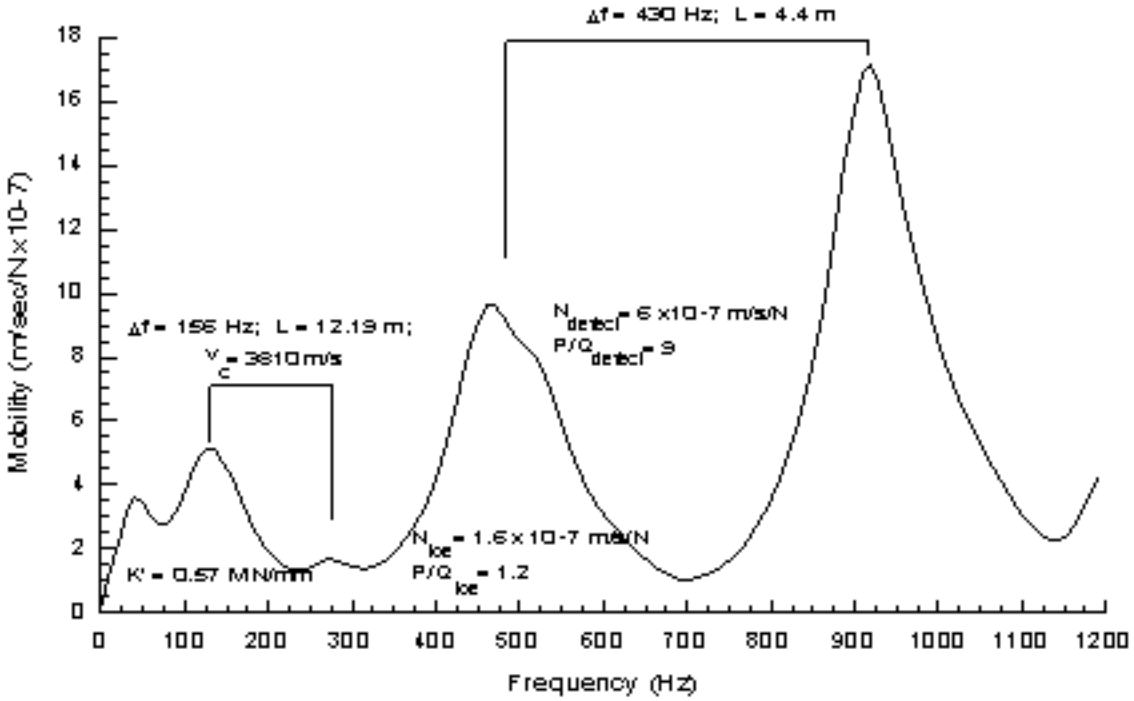

Figure 4.9 Impulse Response Result - Shaft 1: Mobility Plot

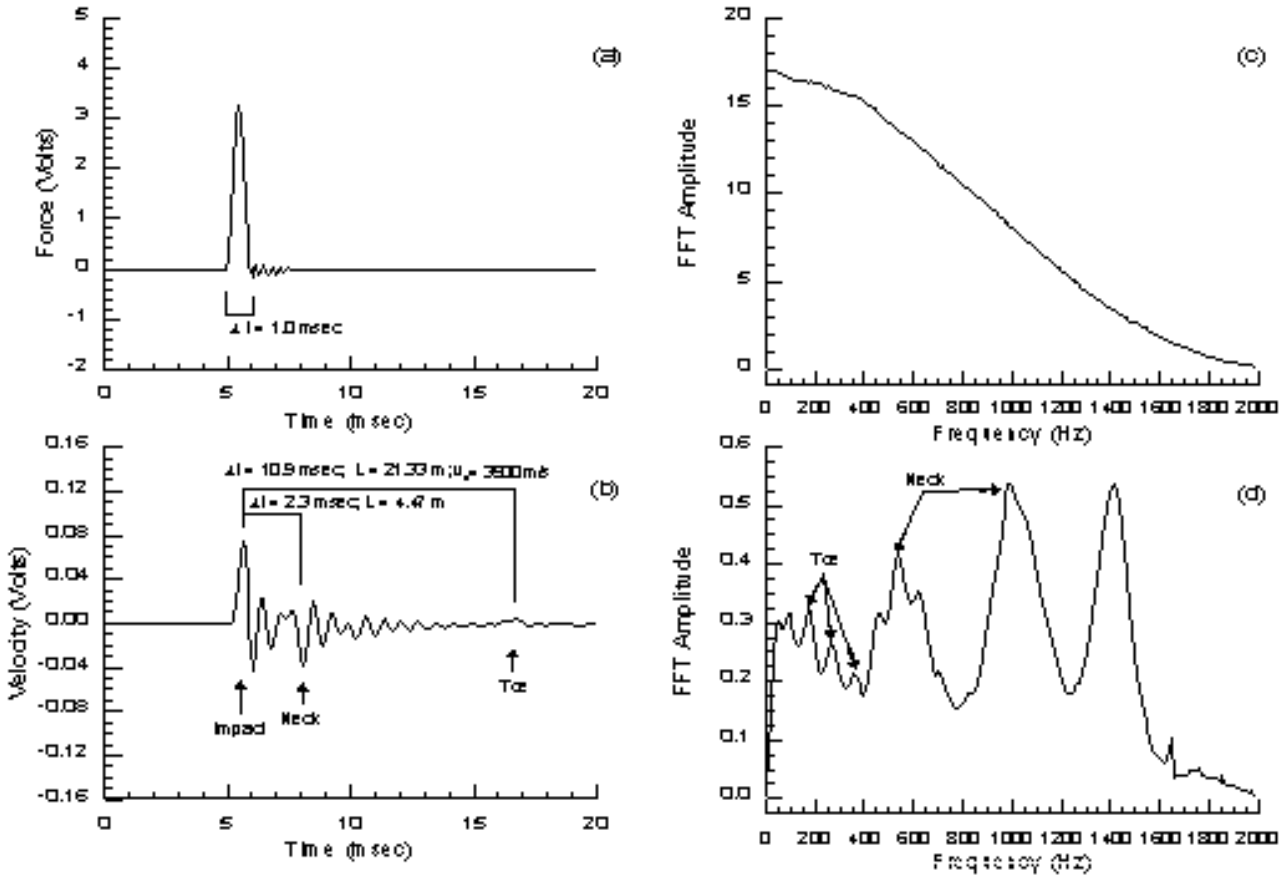

Figure 4.10 Impulse Response Result - Shaft 2: Time Domain and Frequency Spectrum

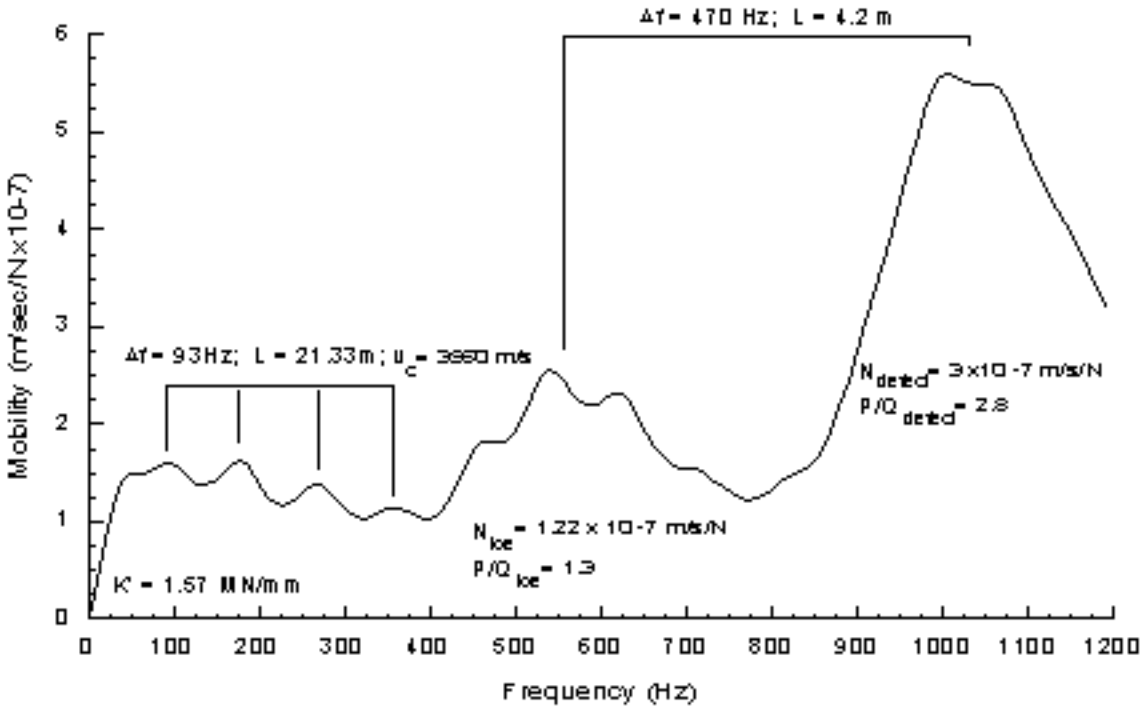

Figure 4.11 Impulse Response Result - Shaft 2: Mobility Plot

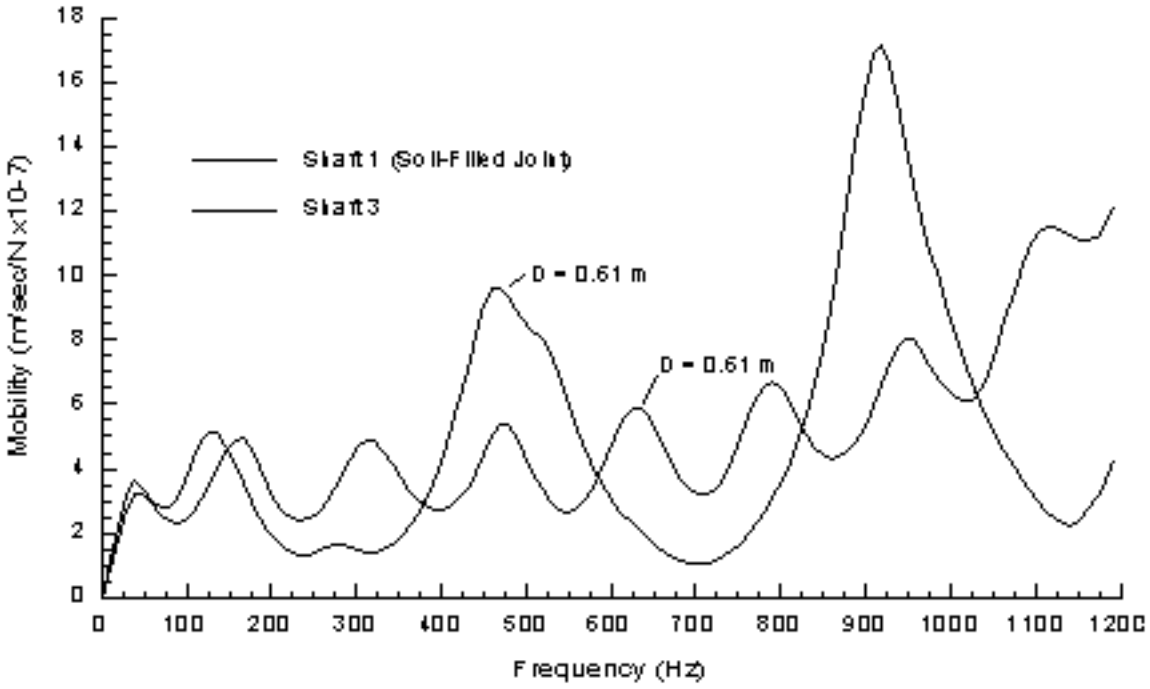

Figure 4.12 Effect of Soil-Filled Joint on Mobility Plot: Comparison of Shafts 1 & 3

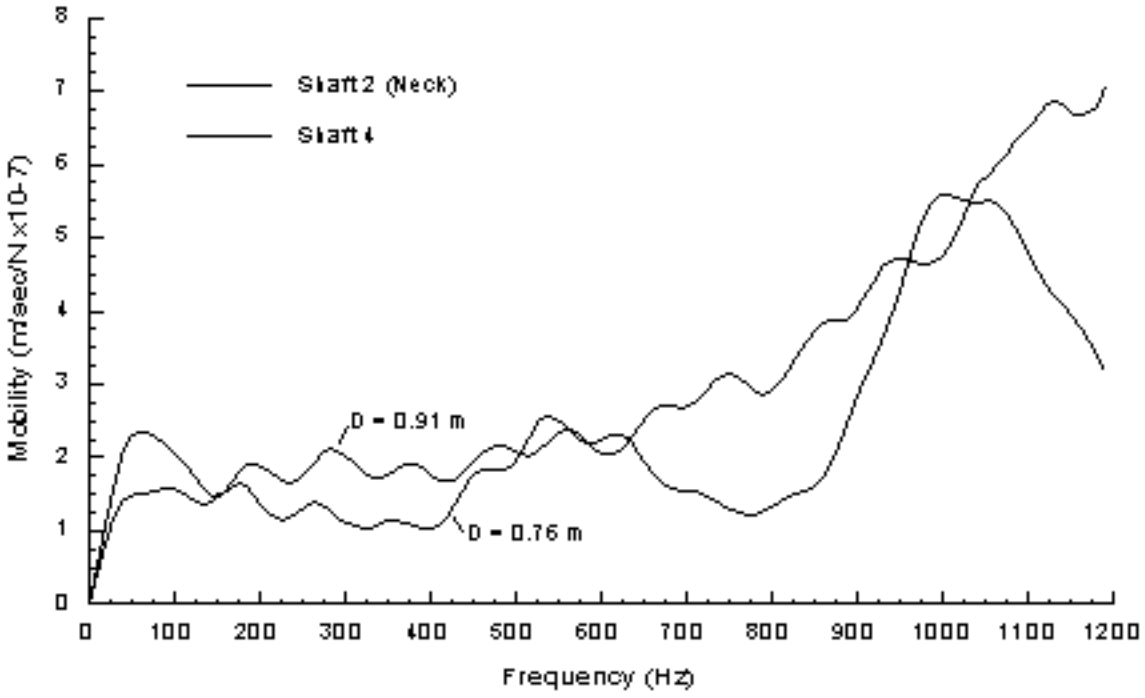

Figure 4.13 Effect of Neck Defect on Mobility Plot: Comparison of Shafts 2 & 4

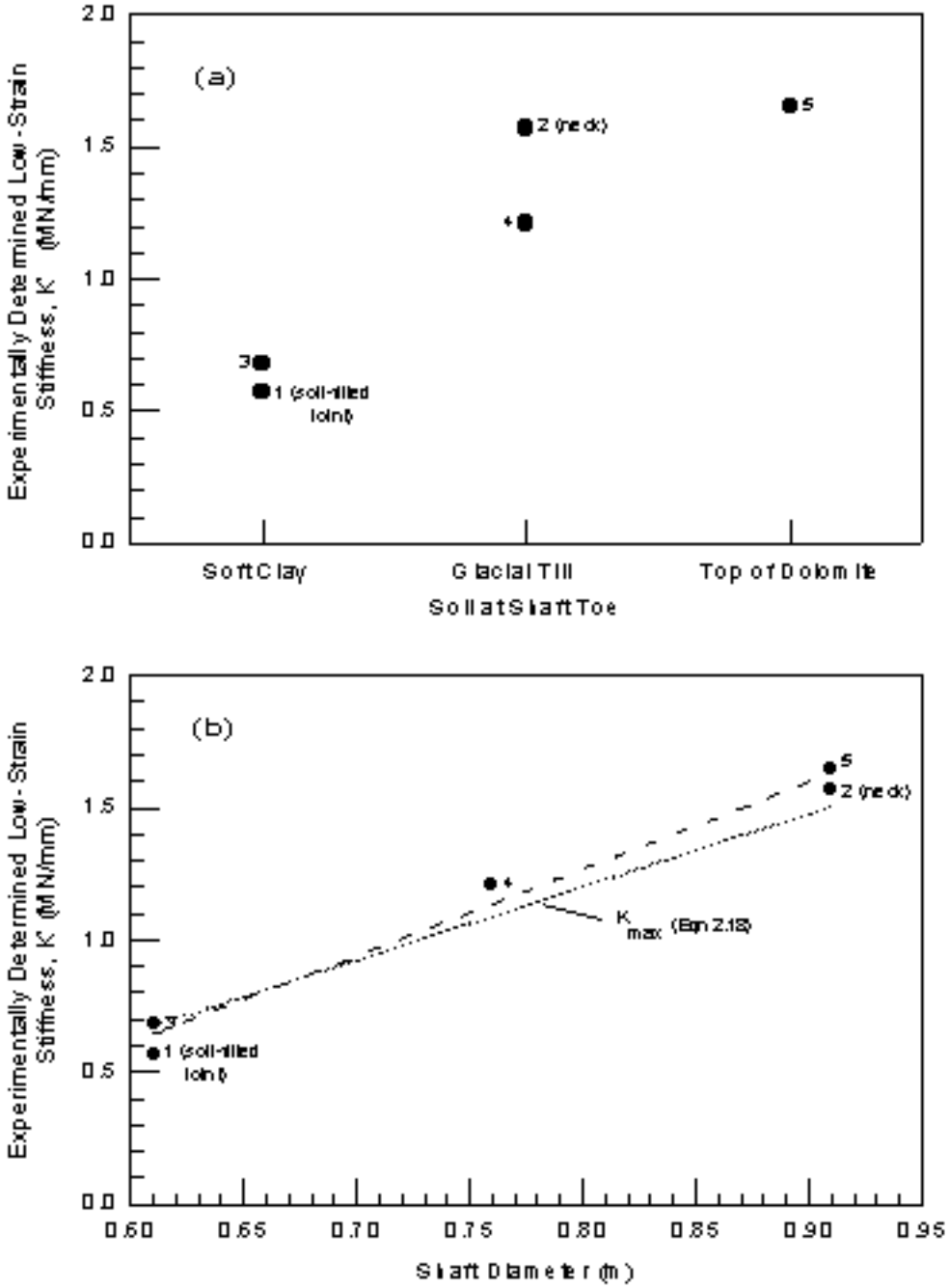

Figure 4.14 Experimentally Determined Low-Strain Stiffness, K' as a function of (a) Soil Conditions at Shaft Toe, and (b) Shaft Diameter.

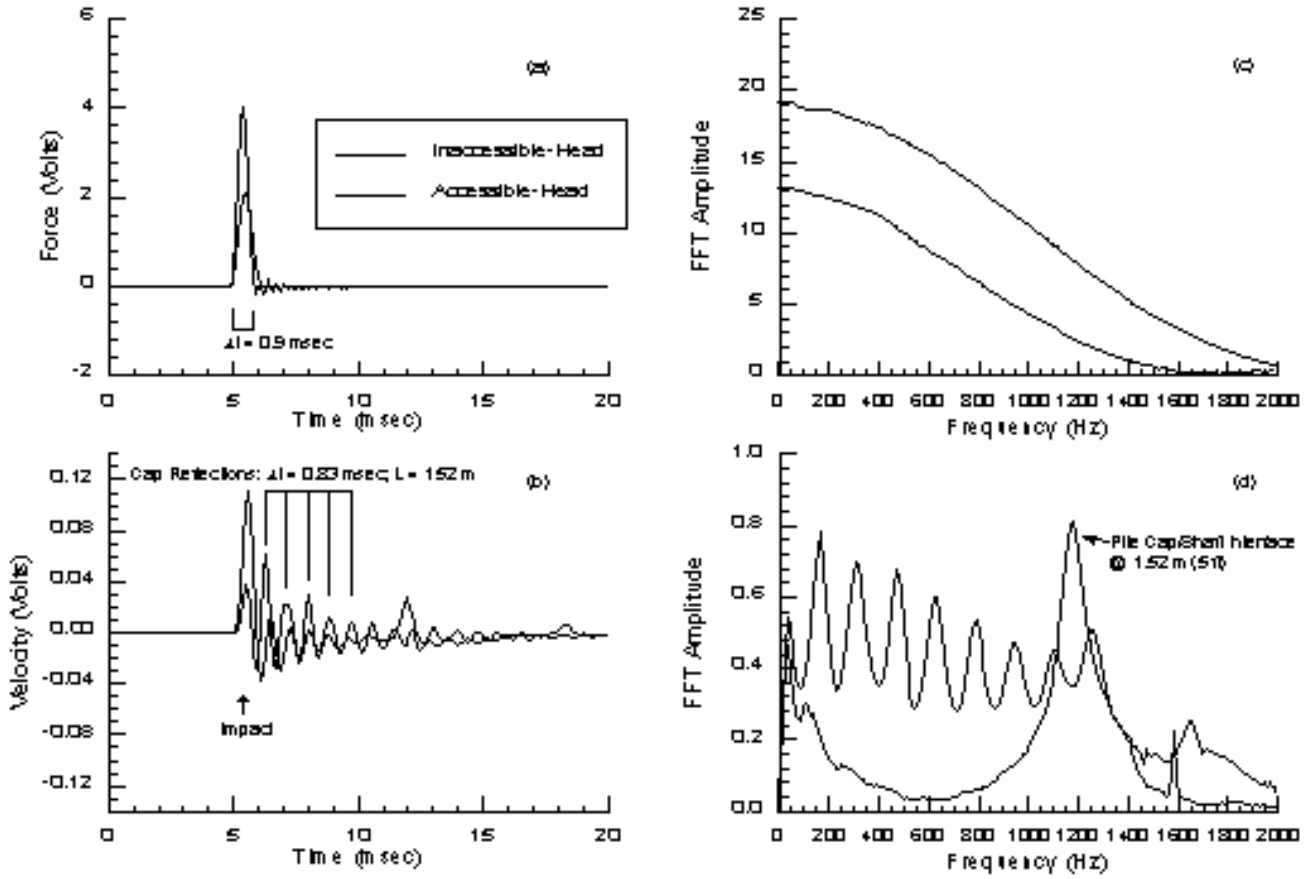

Figure 4.15 Impulse Response Result - Shaft 3 with Pile Cap: Time Domain and Frequency Spectrum

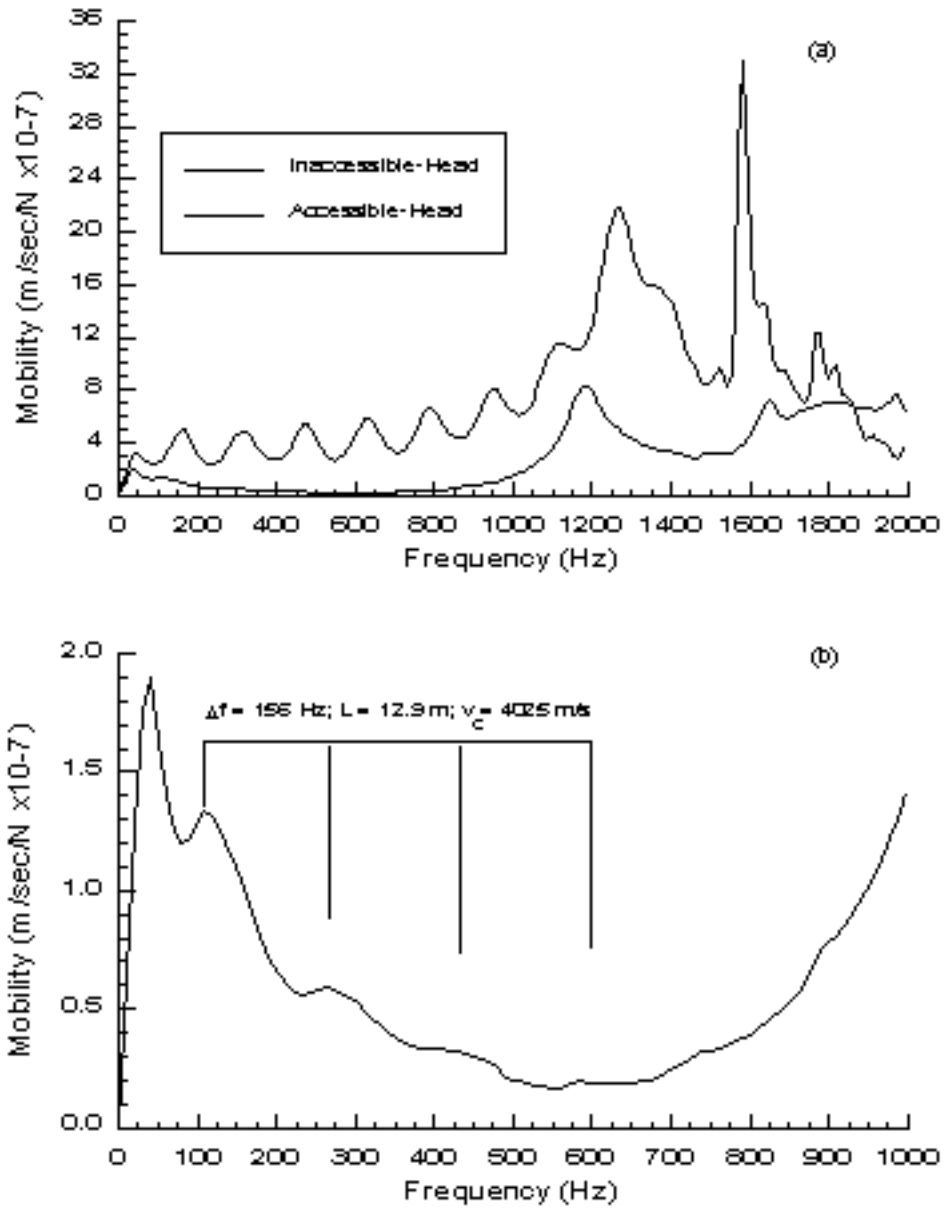

Figure 4.16 Impulse Response Result - Shaft3 with Pile Cap: Mobility Plot

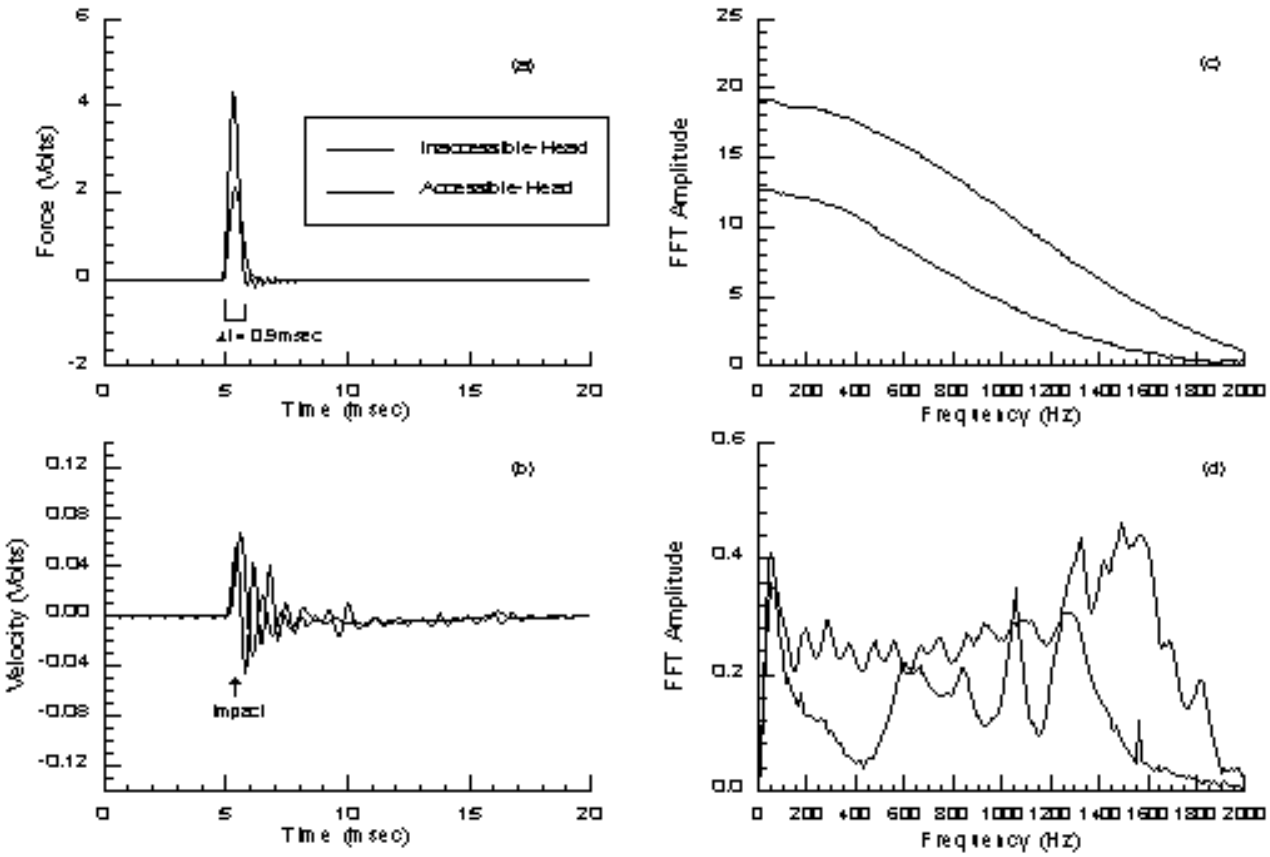

Figure 4.17 Impulse Response Result - Shaft 4 with Pile Cap: Time Domain and Frequency Spectrum

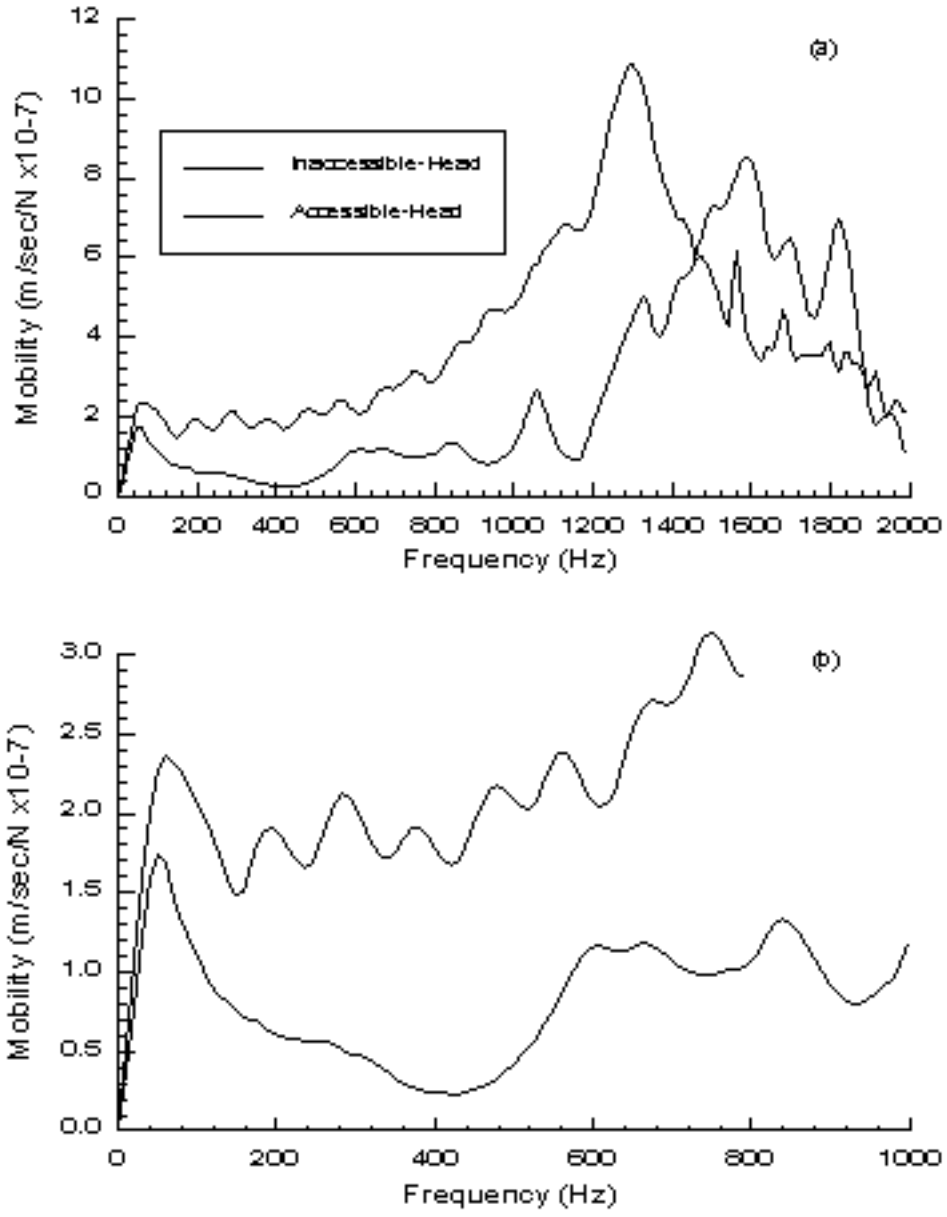

Figure 4.18 Impulse Response Result- Shaft4 with Pile Cap: Mobility Plot

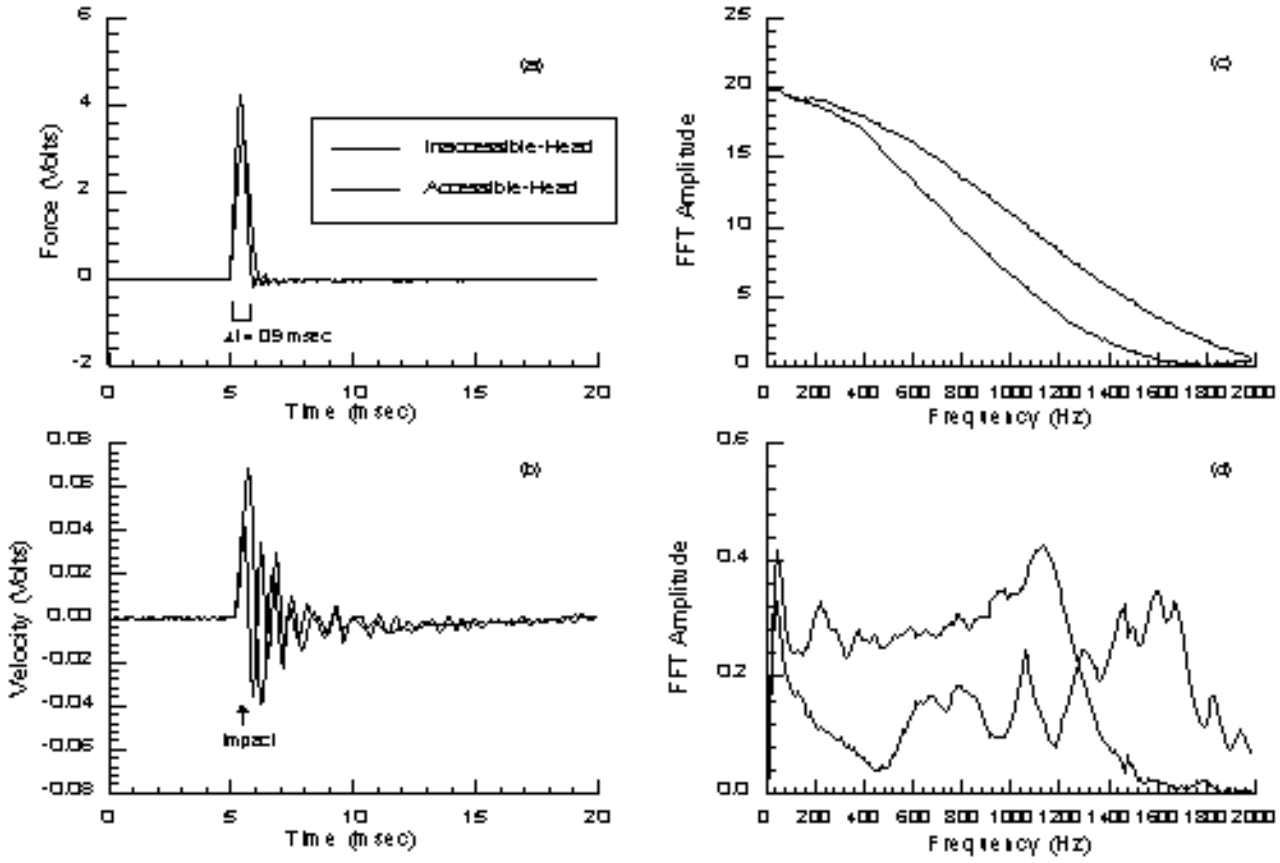

Figure 4.19 Impulse Response Result - Shaft 5 with Pile Cap: Time Domain and Frequency Spectrum

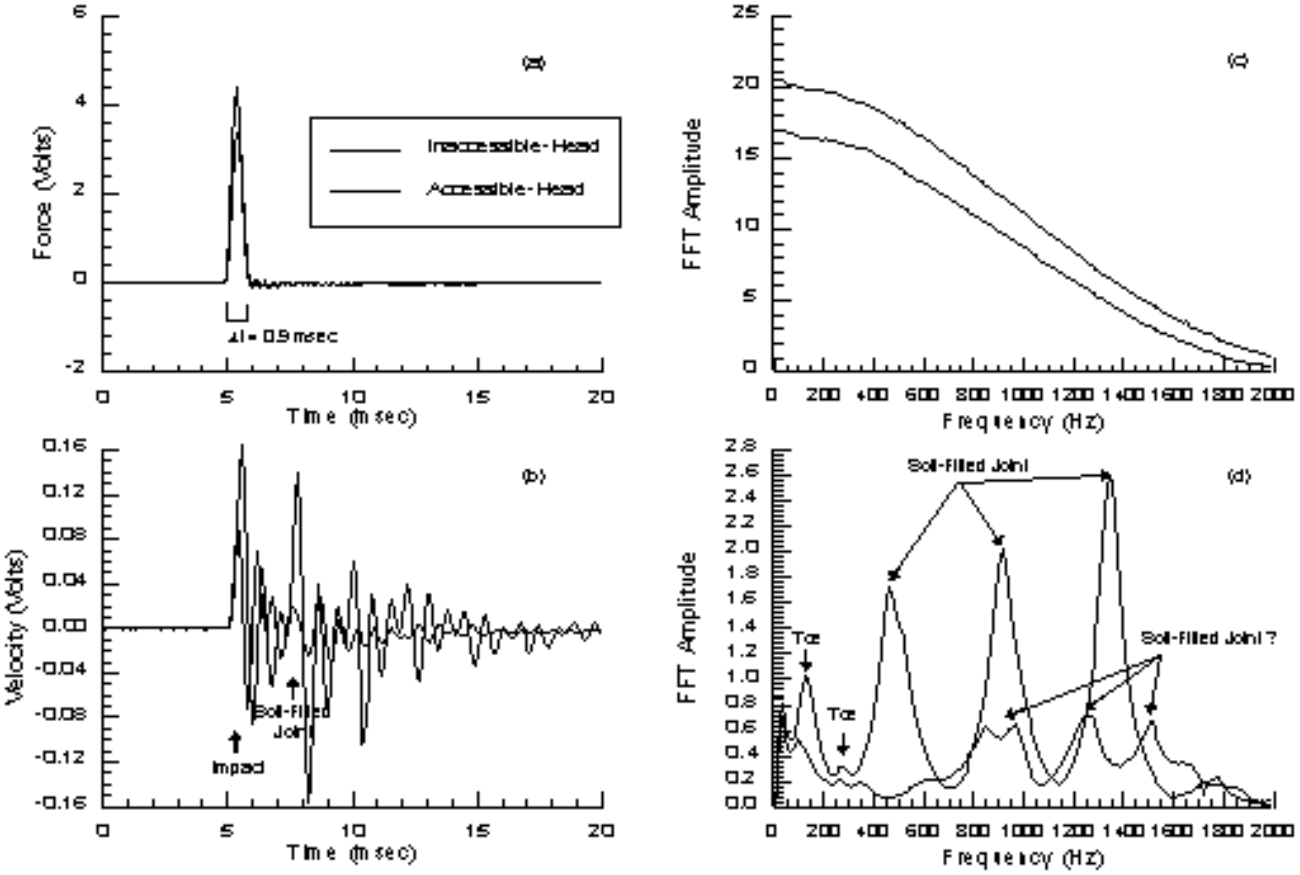

Figure 4.21 Impulse Response Result - Shaft 1 with Pile Cap: Time Domain and Frequency Spectrum

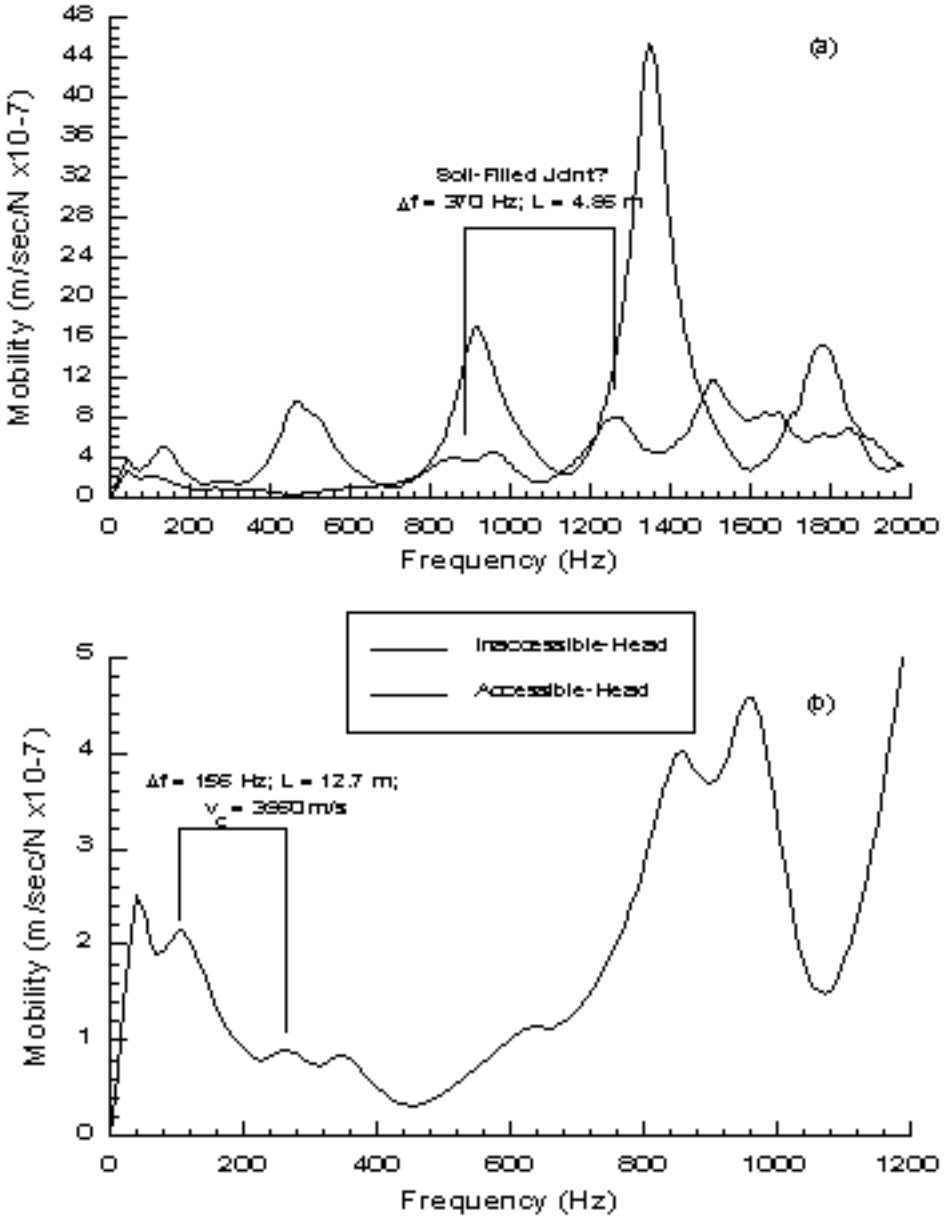

Figure 4.22 Impulse Response Result - Shaft 1 with Pile Cap: Mobility Plot

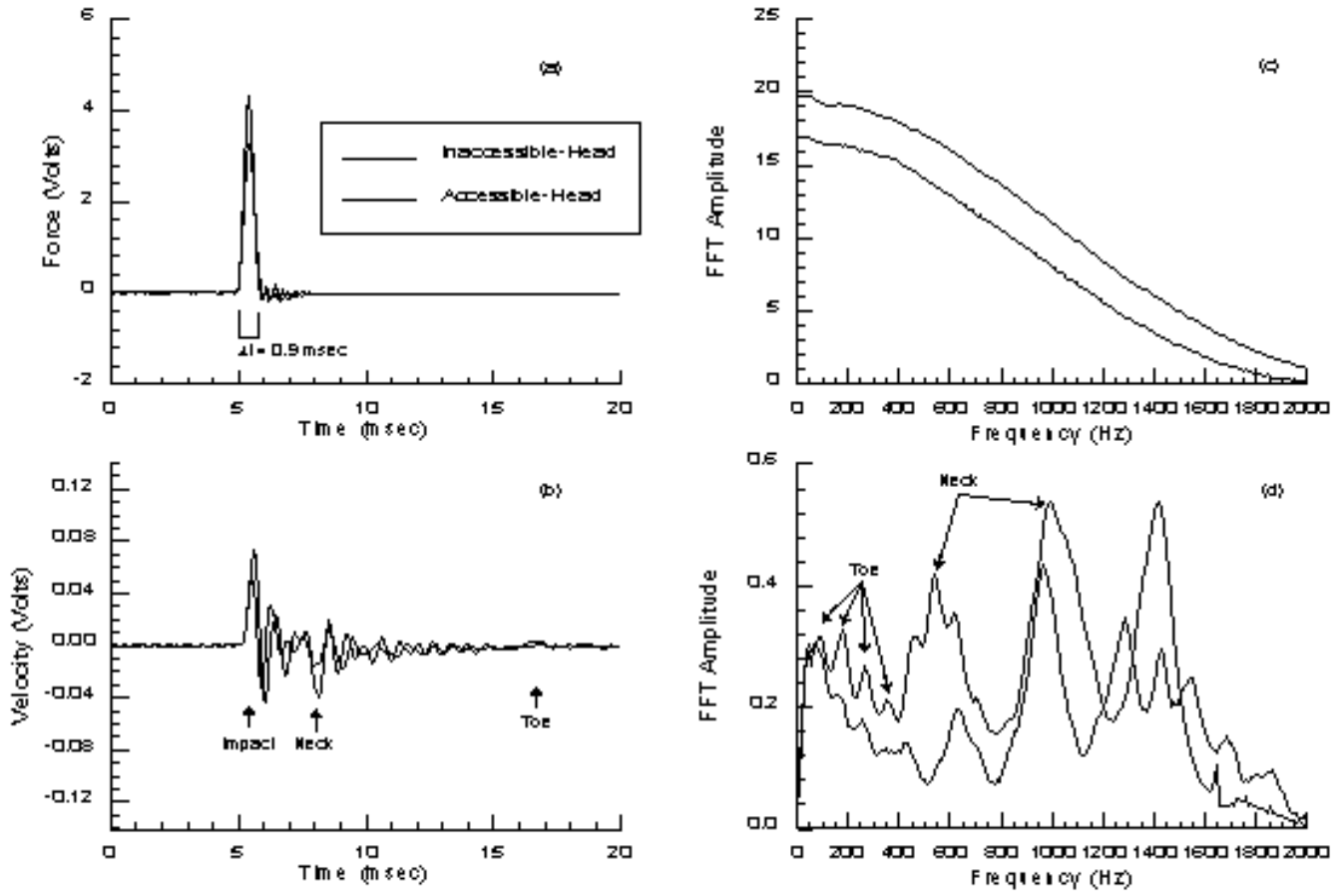

Figure 4.23 Impulse Response Result - Shaft 2 with Pile Cap: Time Domain and Frequency Spectrum

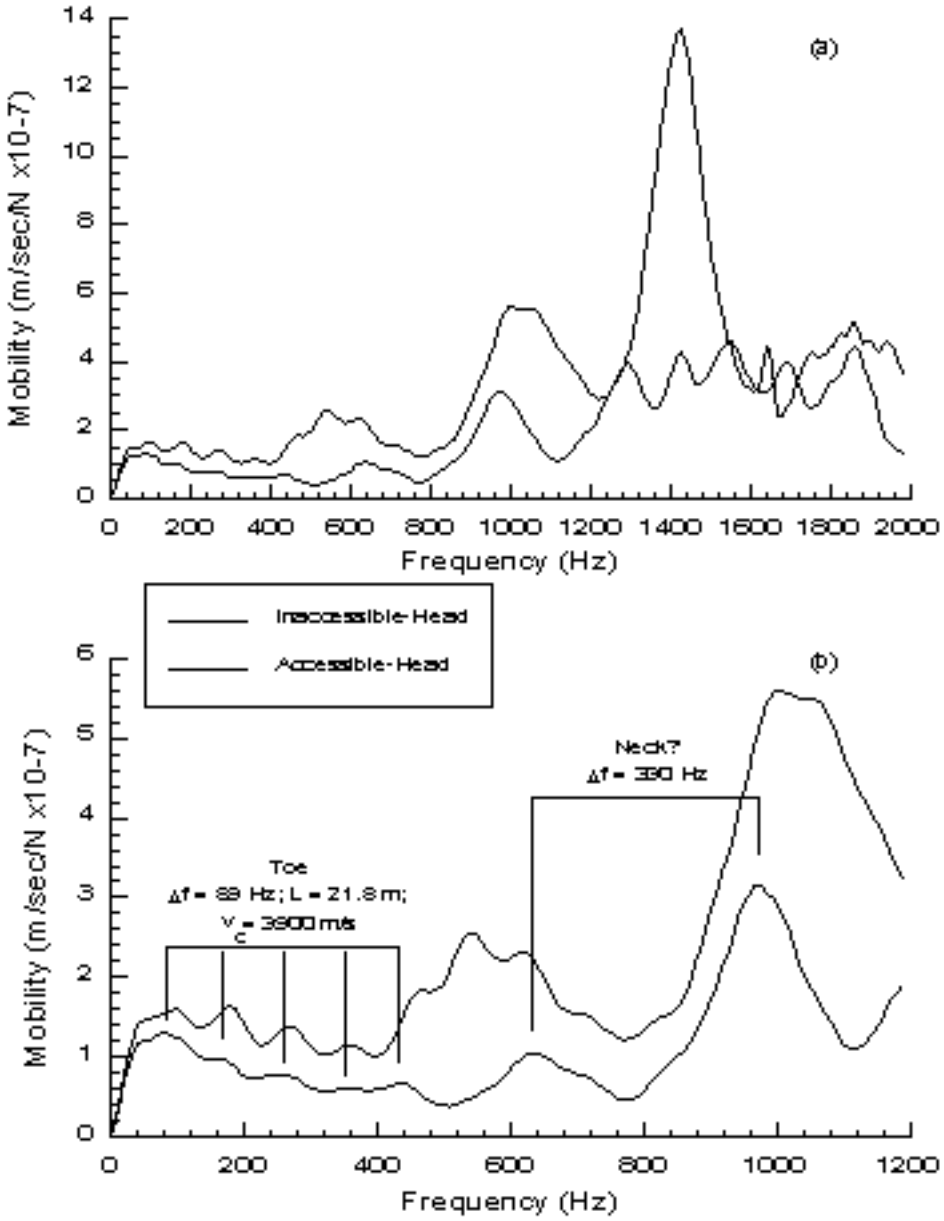

Figure 4.24 Impulse Response Result - Shaft 2 with Pile Cap: Mobility Plot

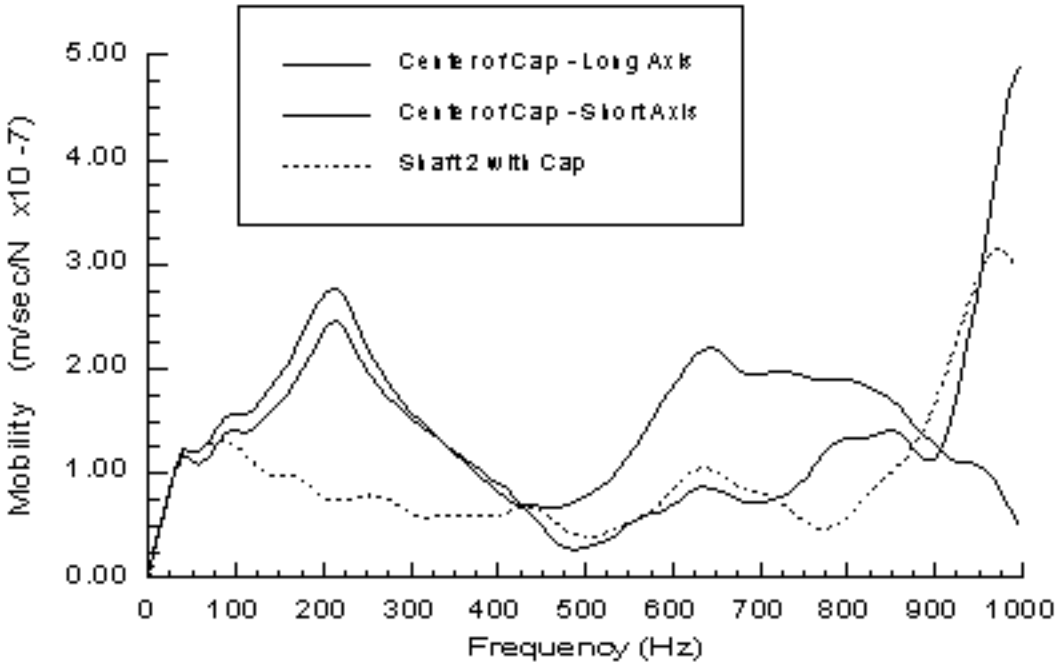

Figure 4.25 Center of Pile Cap Test - Pile Cap 1

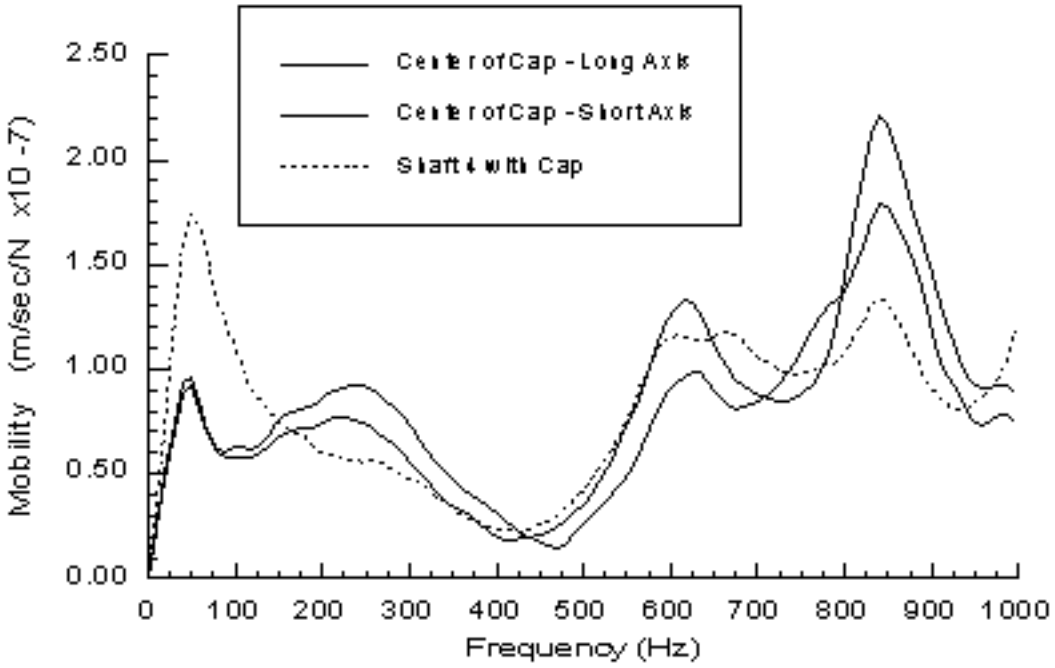

Figure 4.26 Center of Pile Cap Test - Pile Cap 3

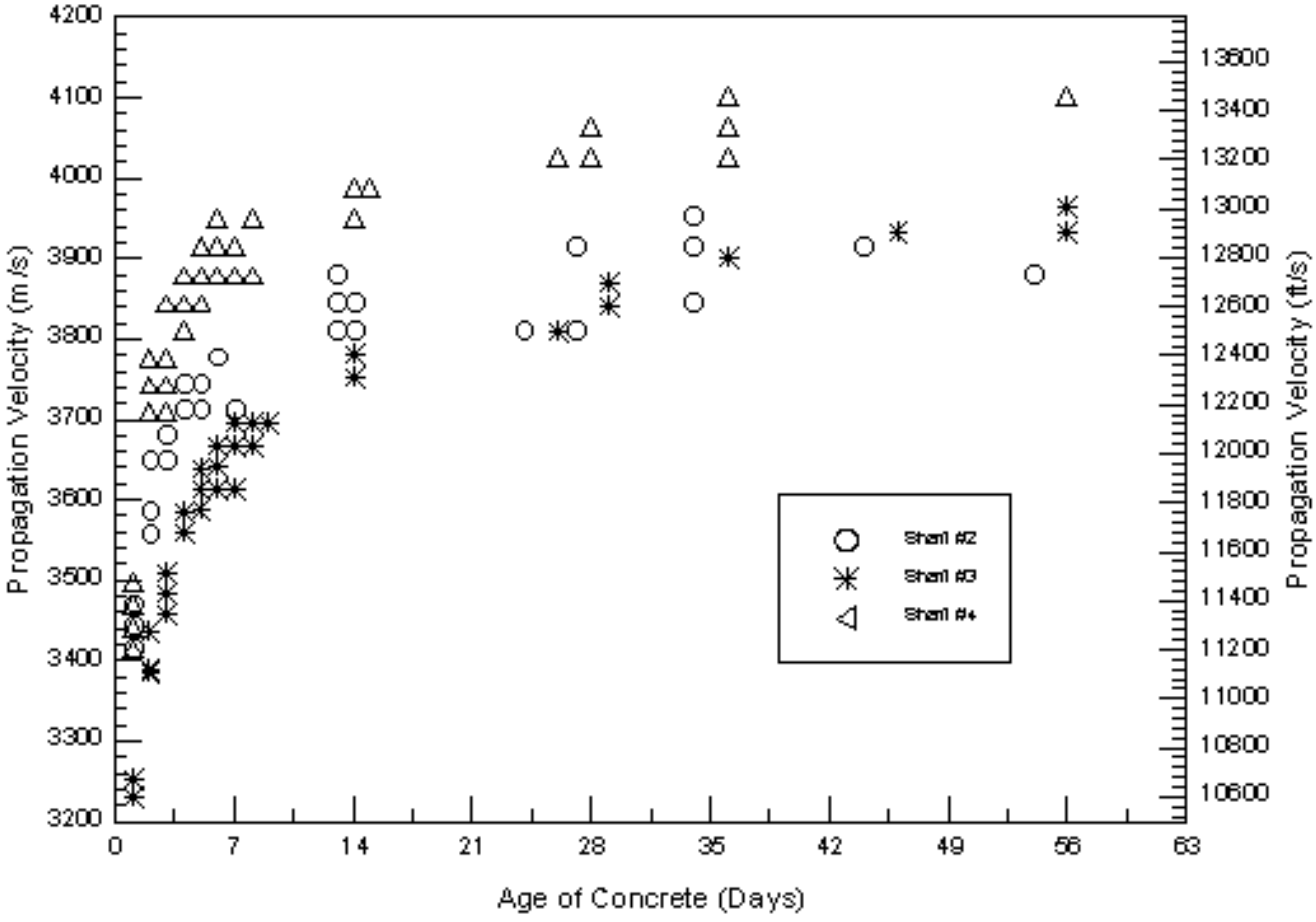

Figure 5.1 Propagation Velocity from Velocity-Time Plots versus Concrete Age

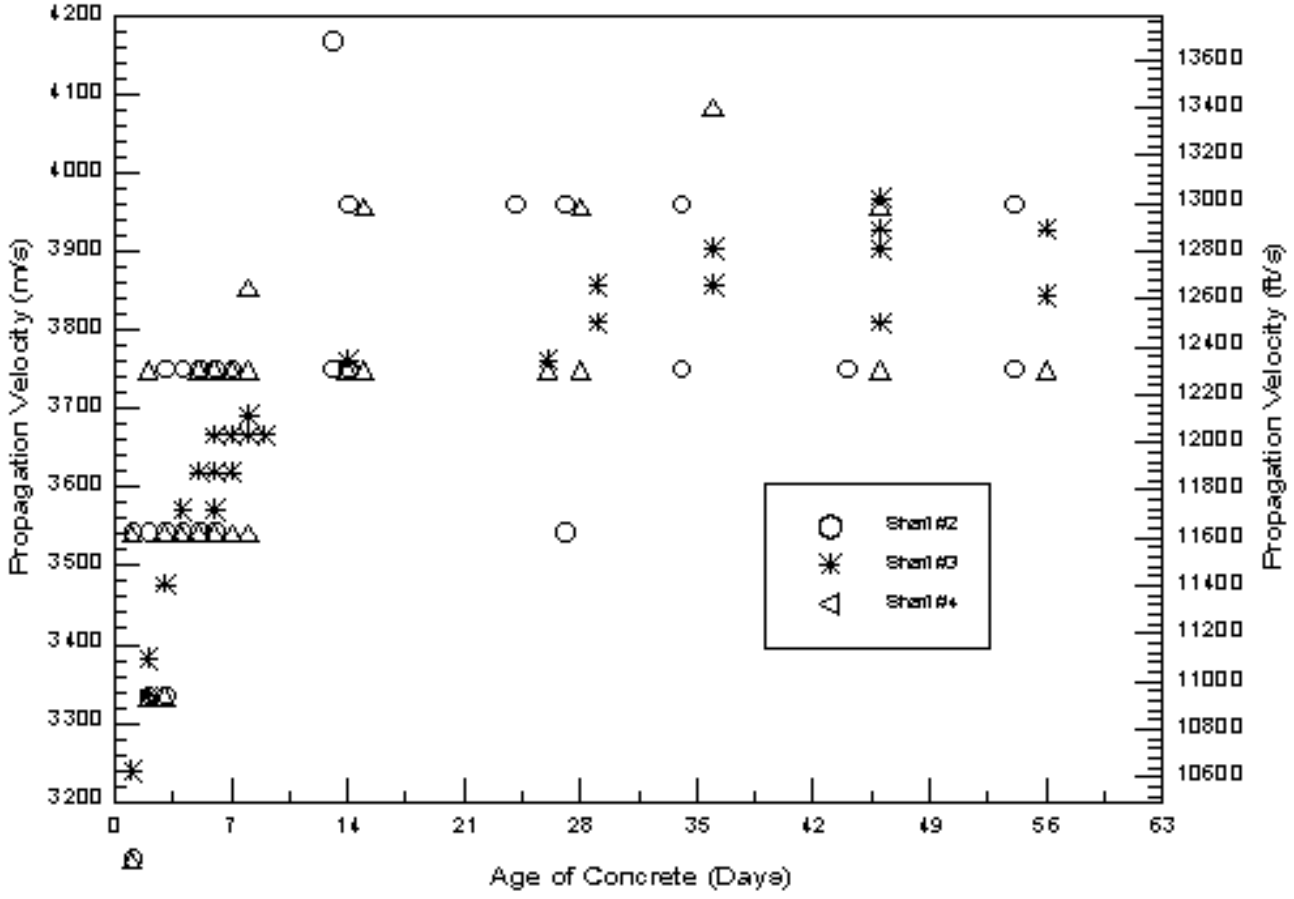

Figure 5.2 Propagation Velocity from Mobility Plots versus Concrete Age

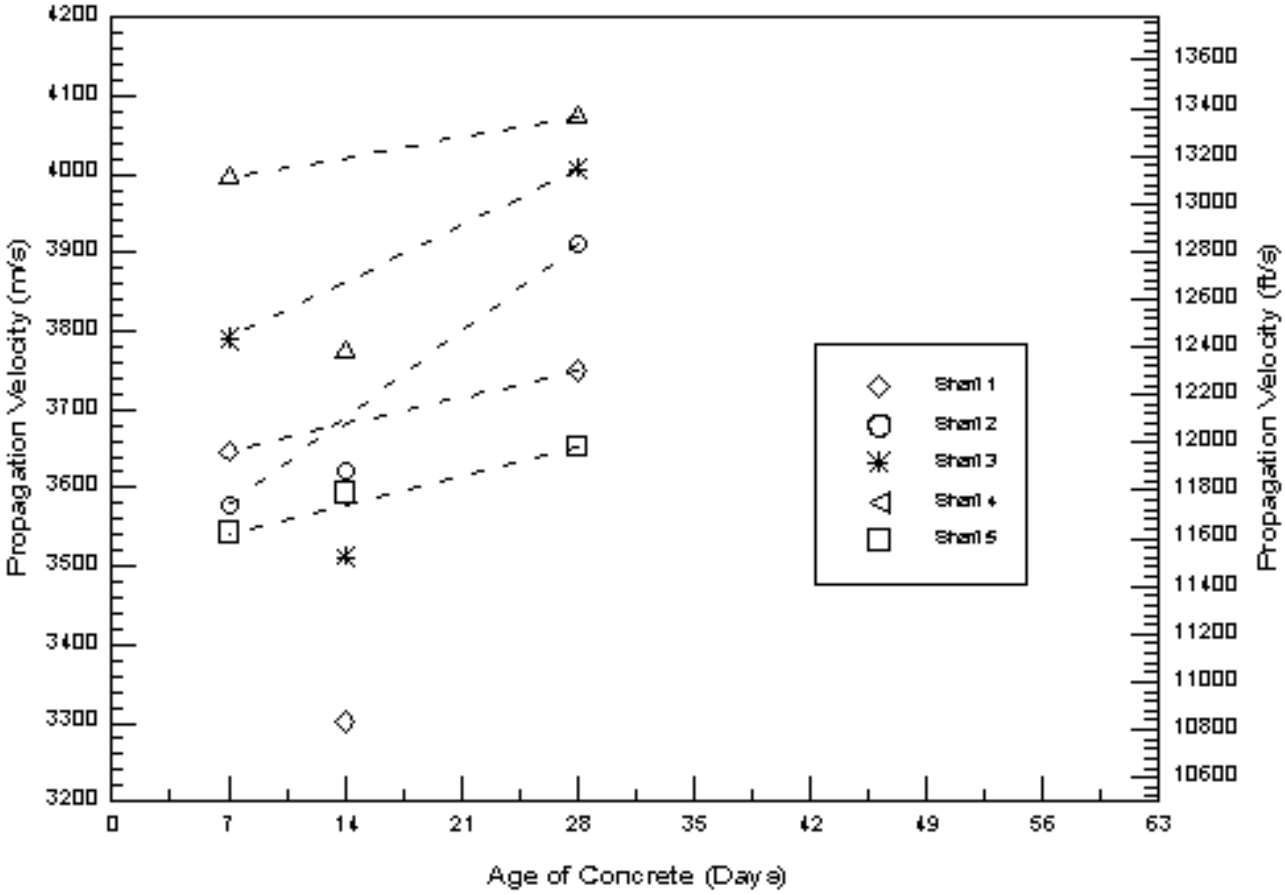

Figure 5.3 Propagation Velocity from Embedded Geophone versus Concrete Age

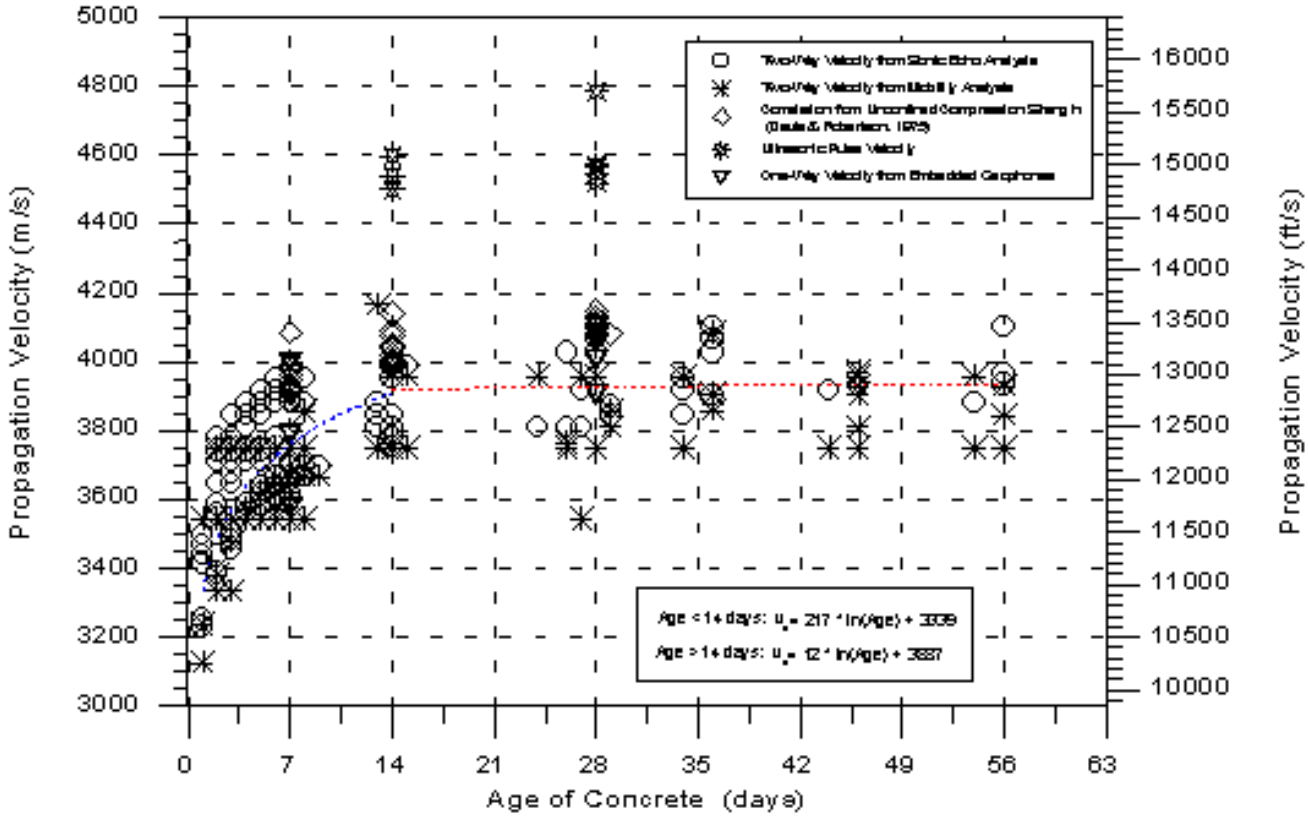

Figure 5.4 Propagation Velocity from All Field and Laboratory Tests as a Function of Concrete Age

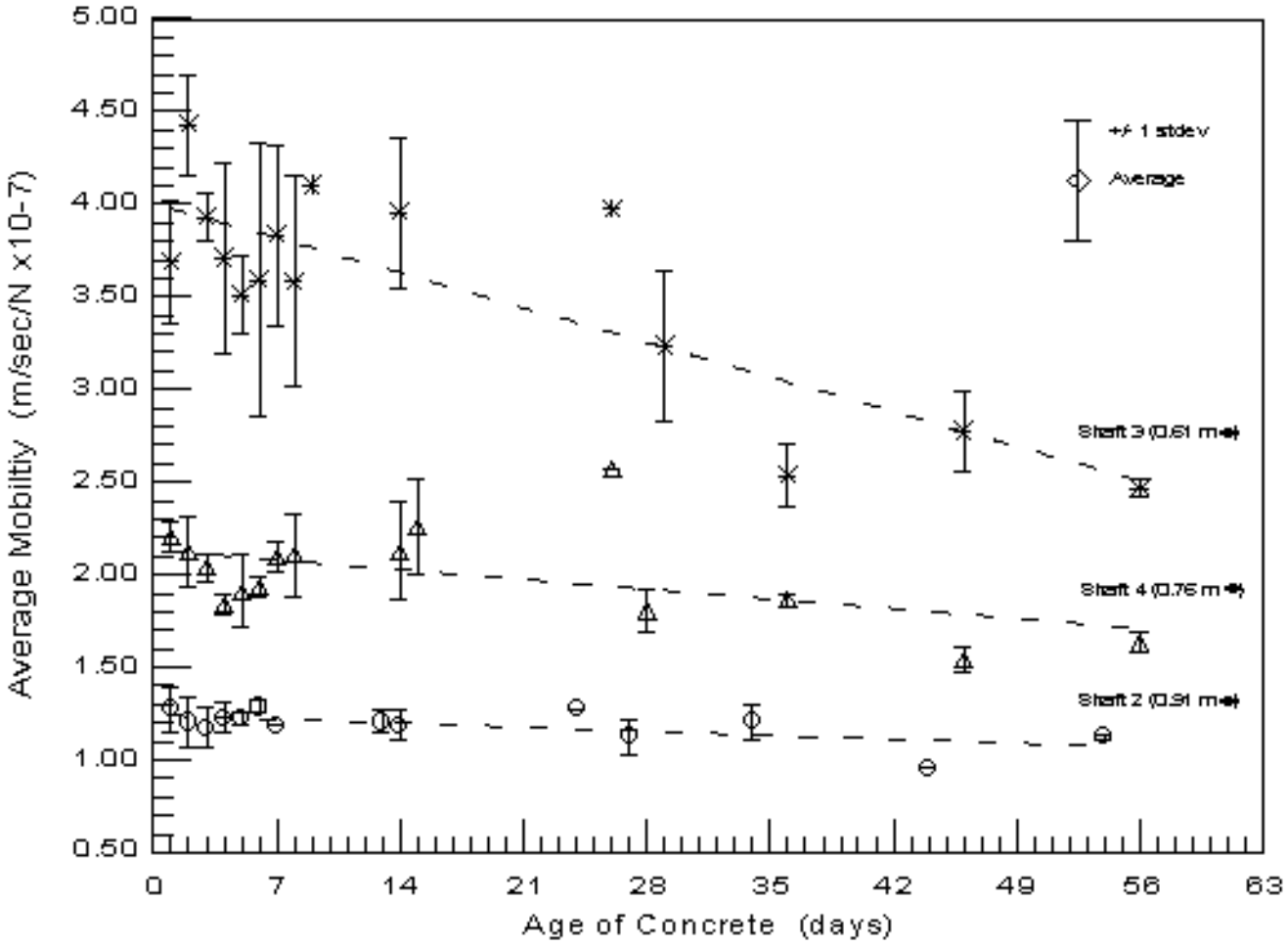

Figure 5.5 Average Shaft Mobility versus Concrete Age

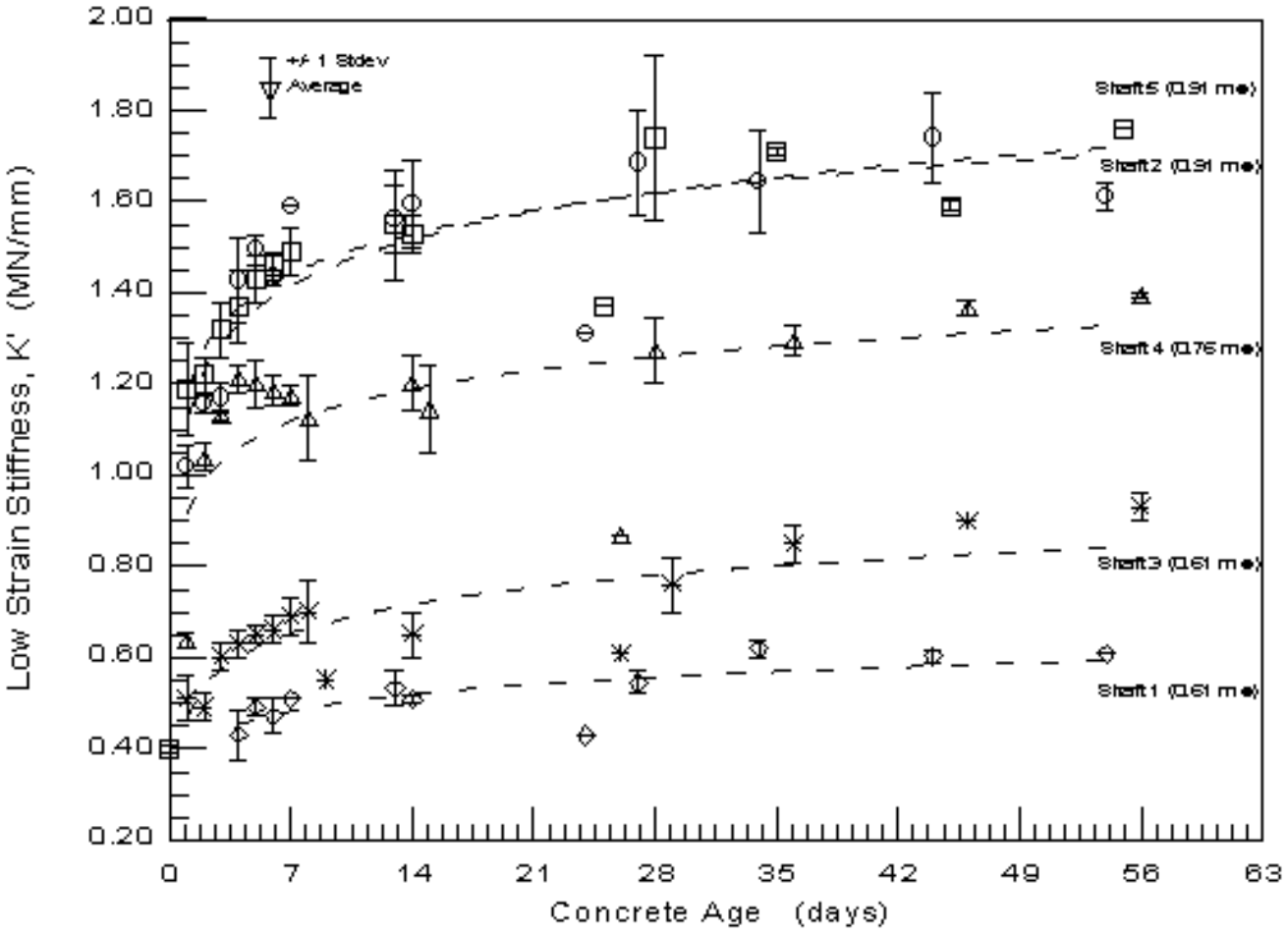

Figure 5.6 Low-Strain Stiffness versus Concrete Age

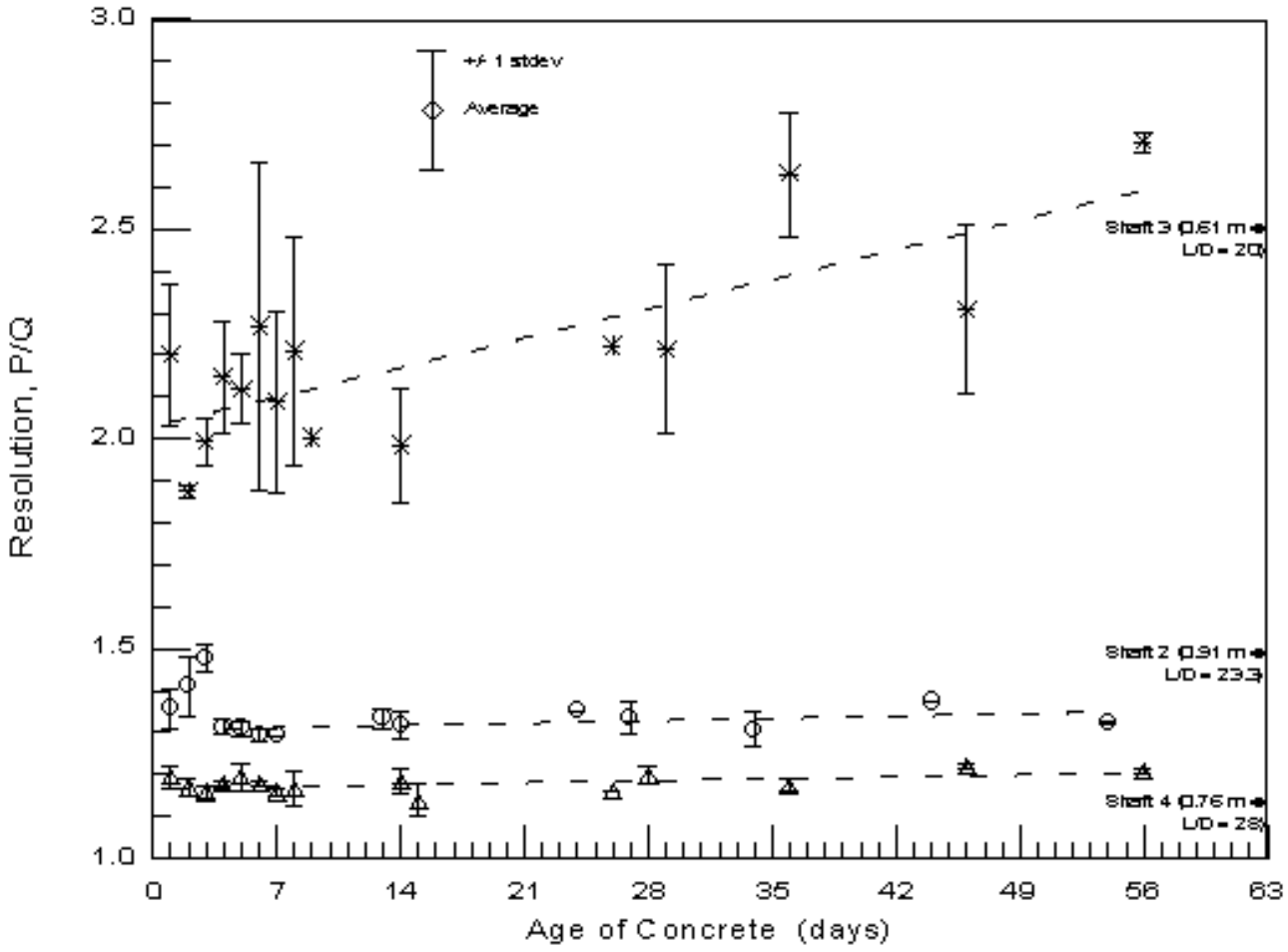

Figure 5.7 Resolution versus Concrete Age

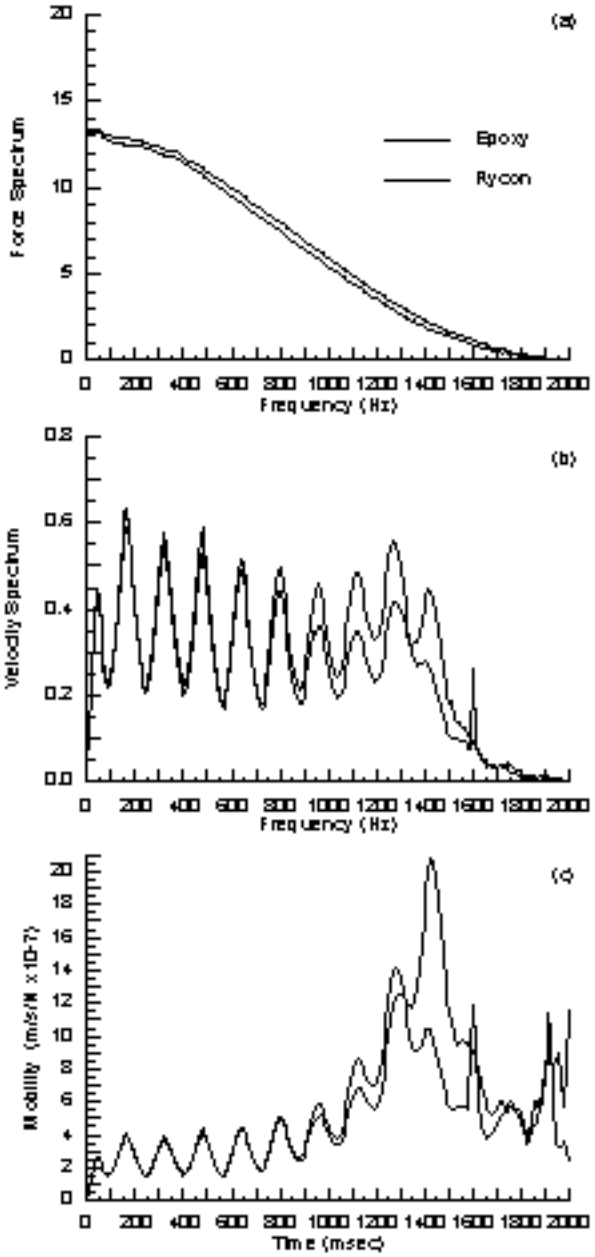

Figure 5.8 Comparison of Rycon and Epoxy Couplants - Shaft 3

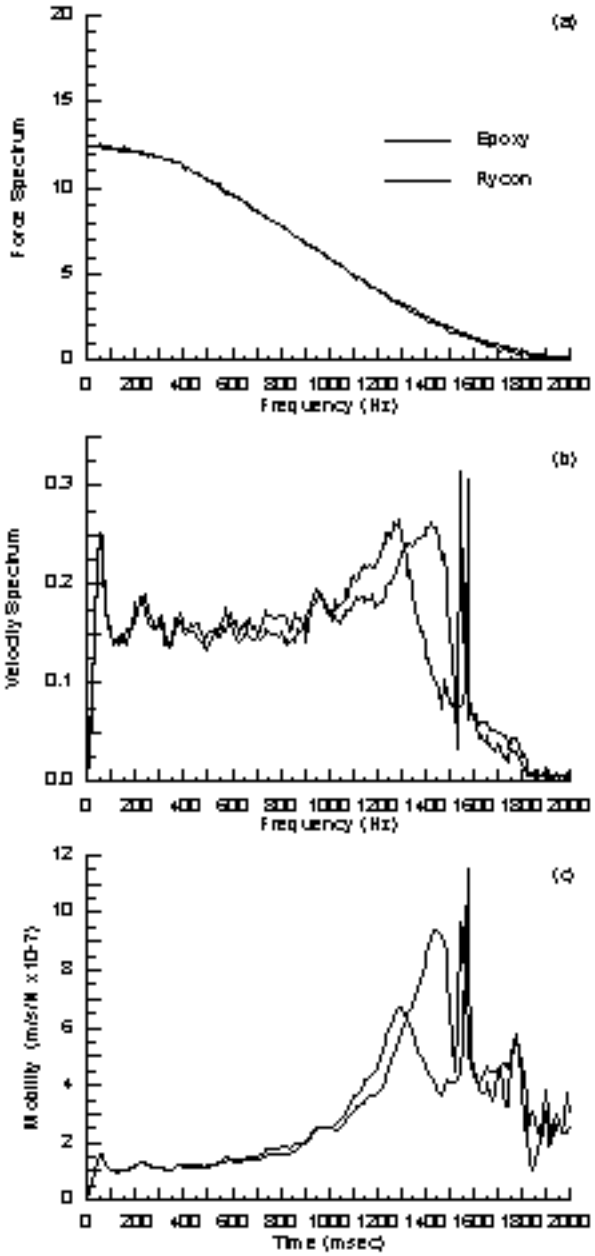

Figure 5.9 Comparison of Rycon and Epoxy Couplants - Shaft 5

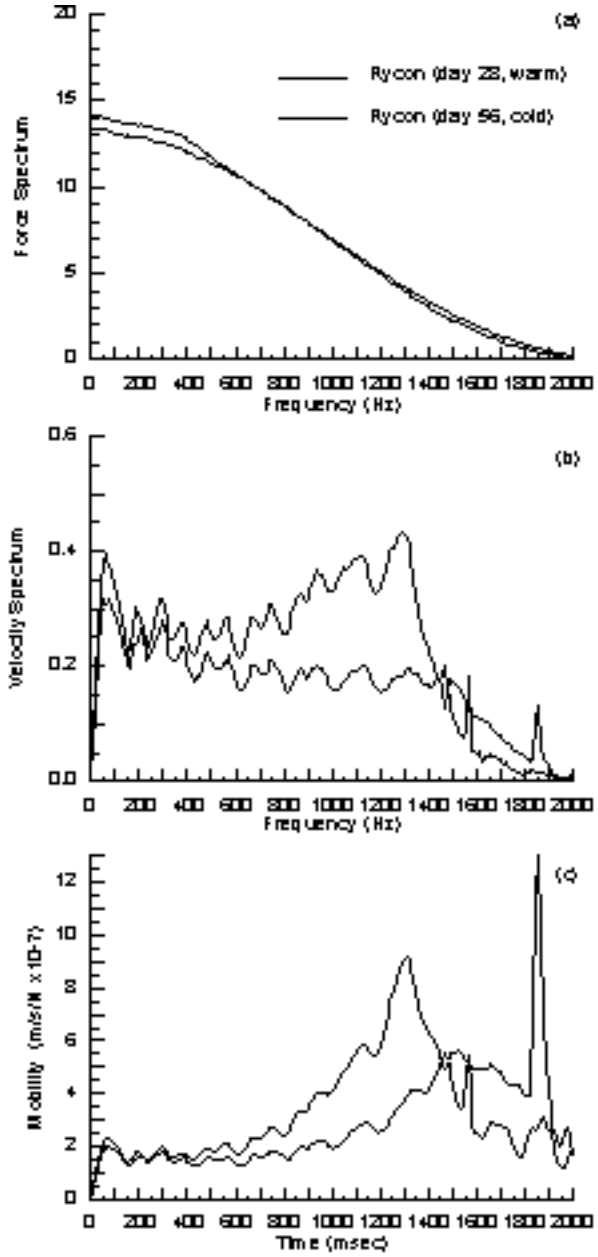

Figure 5.10 Temperature Effect on Rycon Grease - Shaft 4

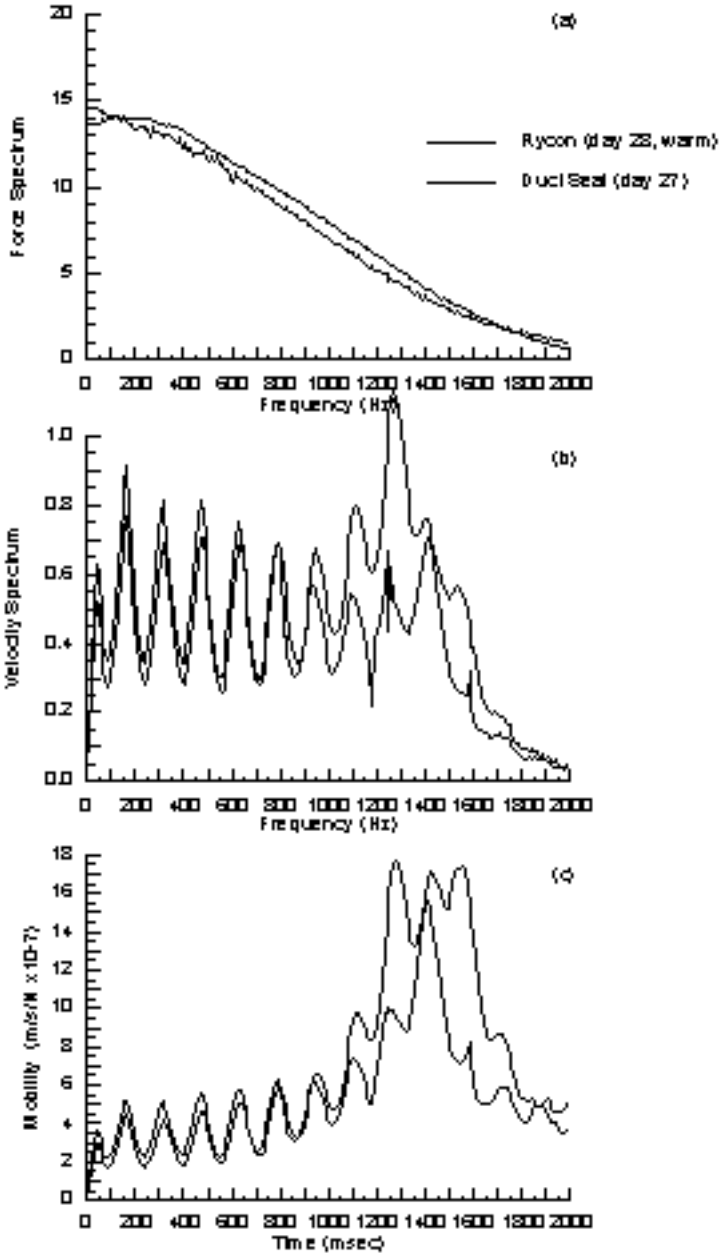

Figure 3.11 Comparison of Rycon and Duct Seal Coupons - Shaft 3

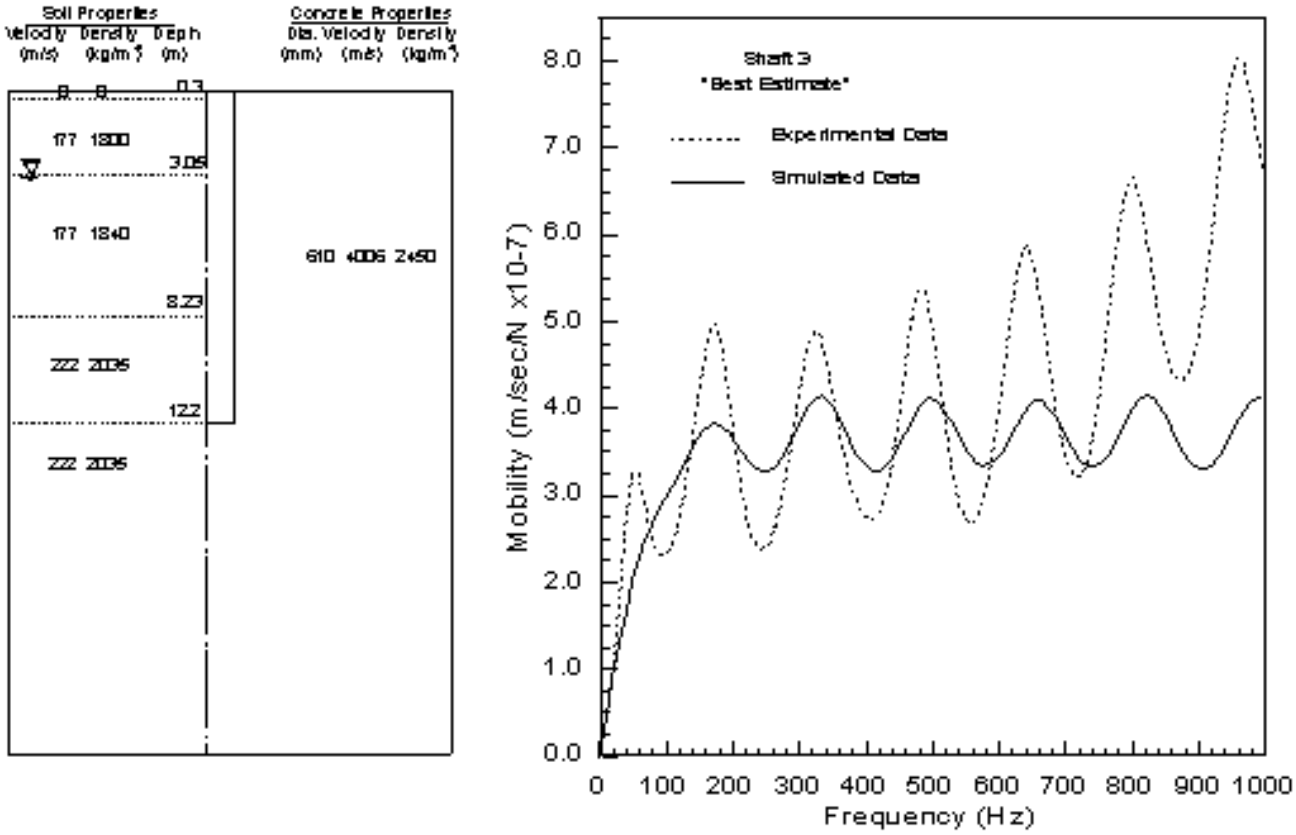

Figure 6.1 "Best Estimate" Numerically-Simulated and Experimental Mobilities: Shaft 3

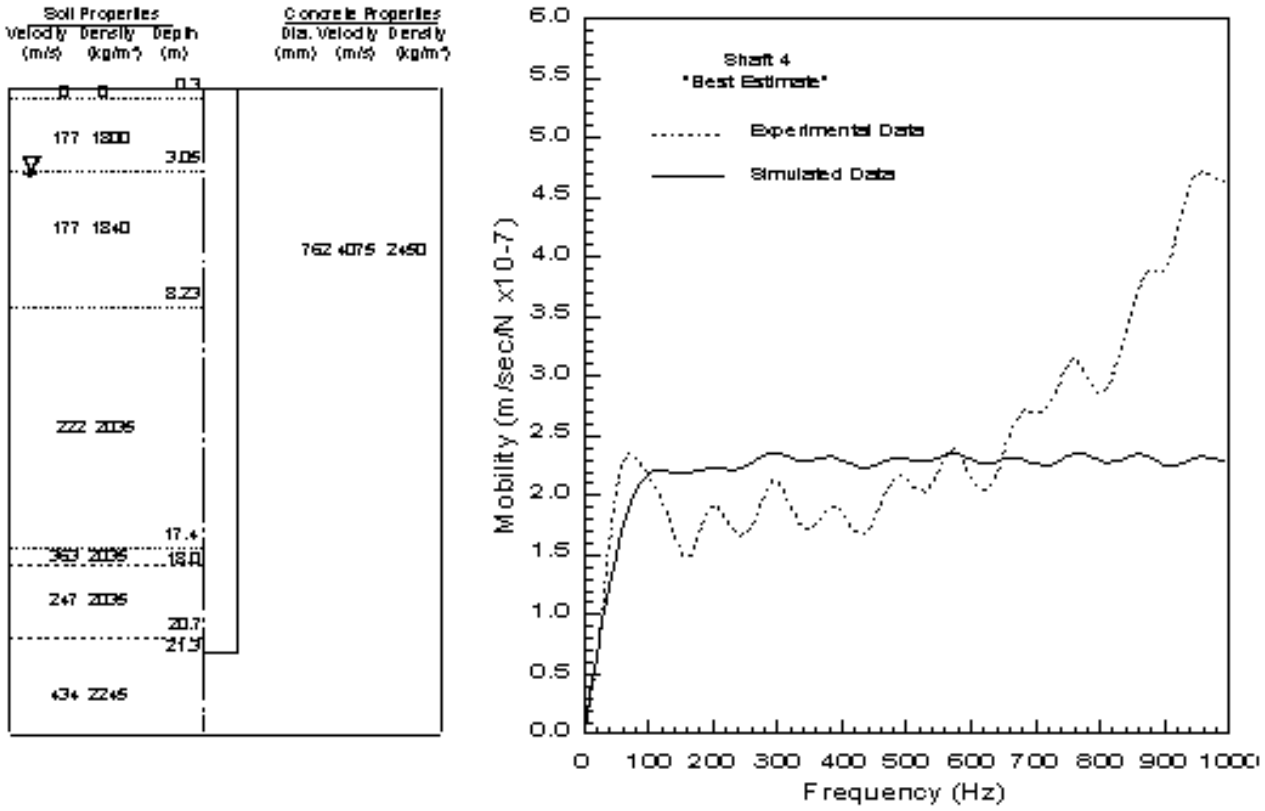

Figure 6.2 "Best Estimate" Numerically-Simulated and Experimental Mobilities: Shaft 4

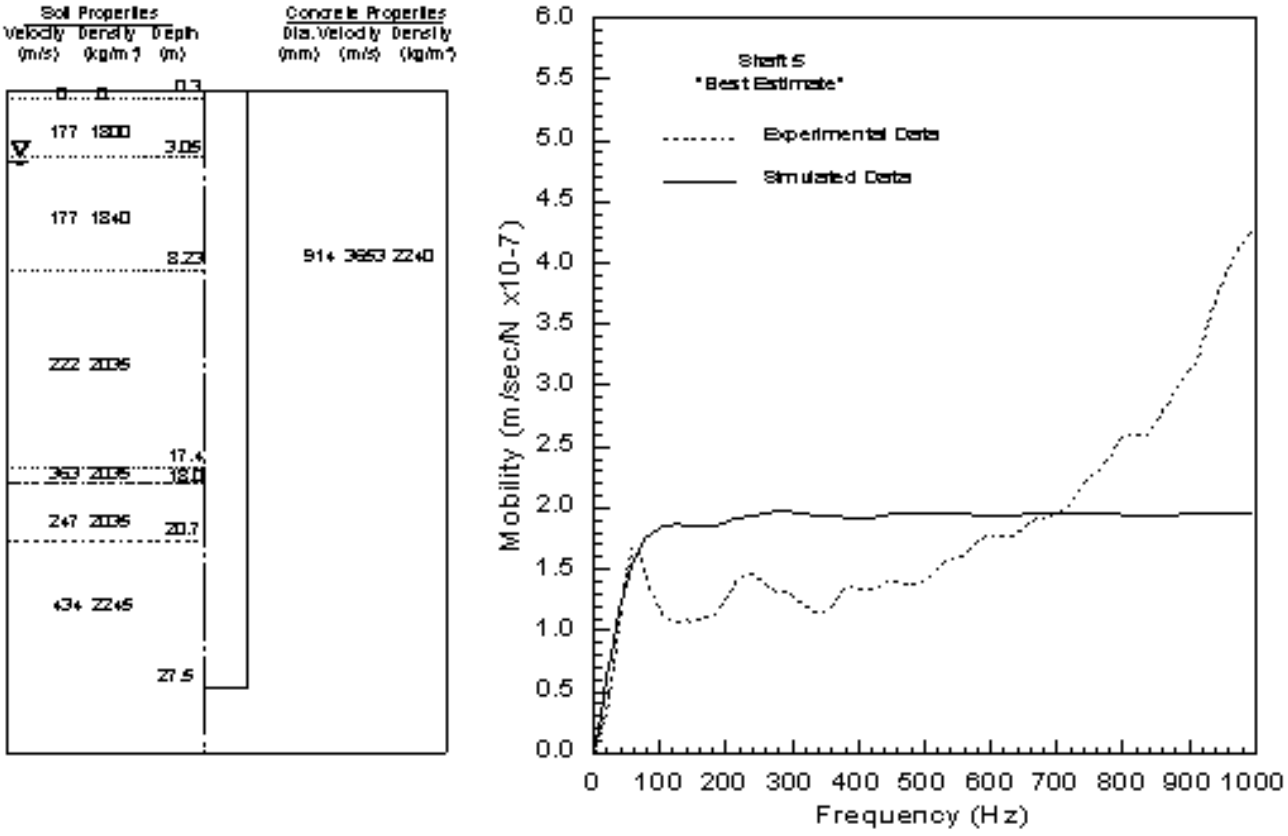

Figure 6.3 "Best Estimate" Numerically-Simulated and Experimental Mobilities: Shaft 5

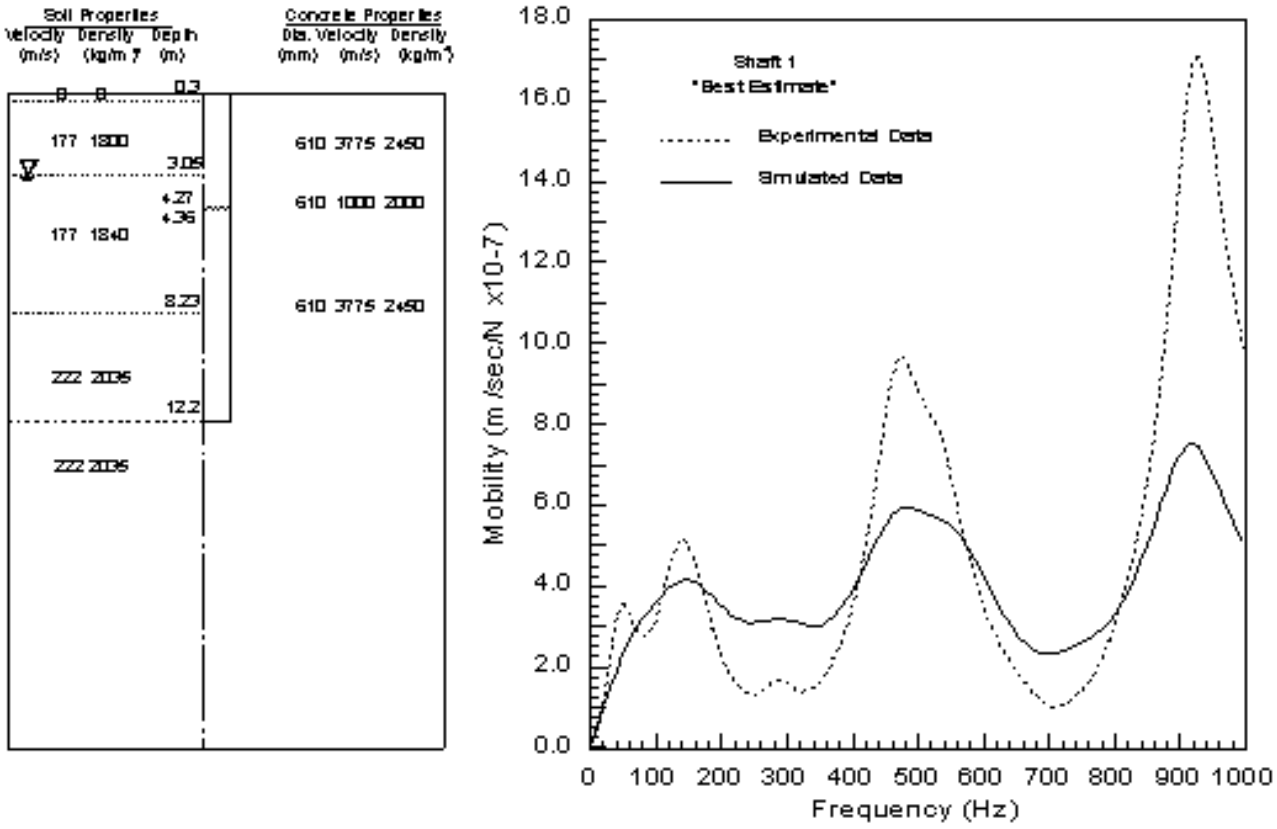

Figure 6.4 "Best Estimate" Numerically-Simulated and Experimental Mobilities: Shaft 1

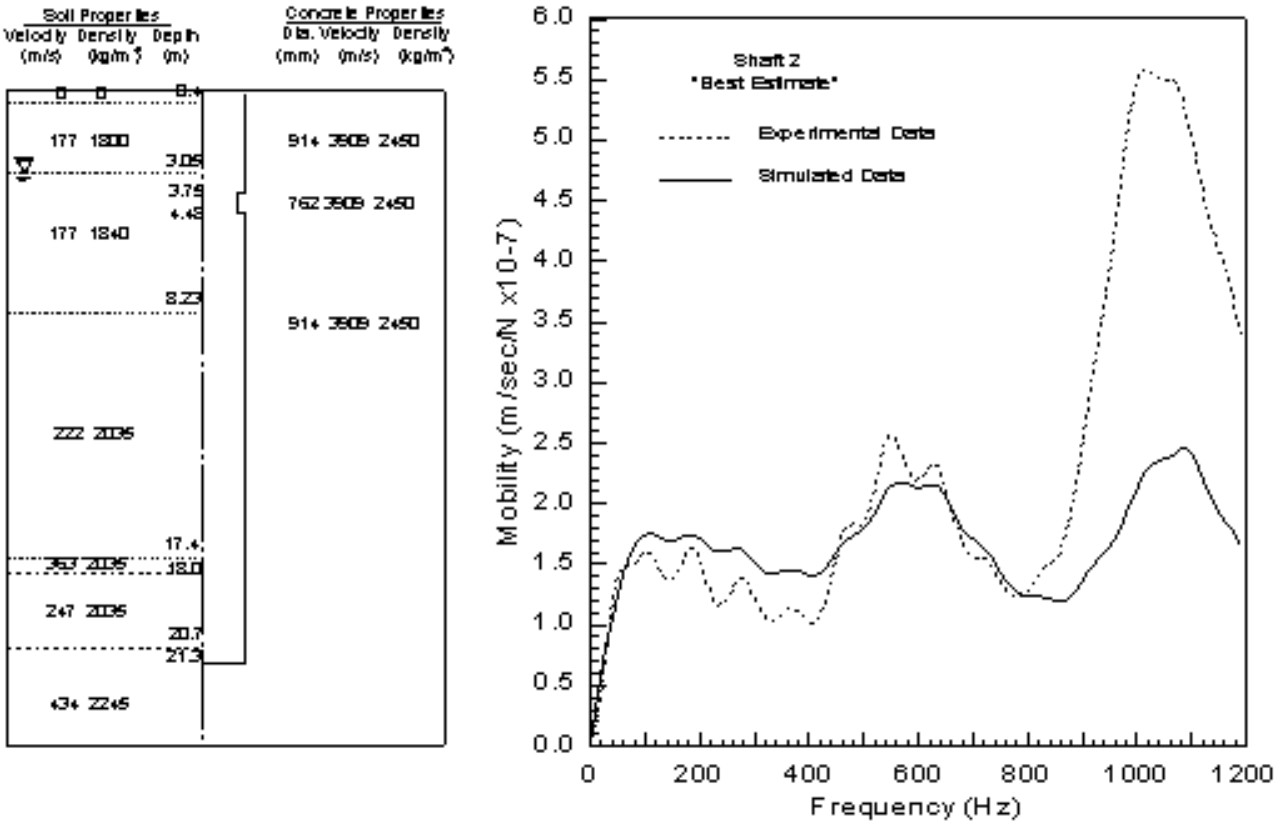

Figure 6.5 "Best Estimate" Numerically-Simulated and Experimental Mobilities: Shaft 2

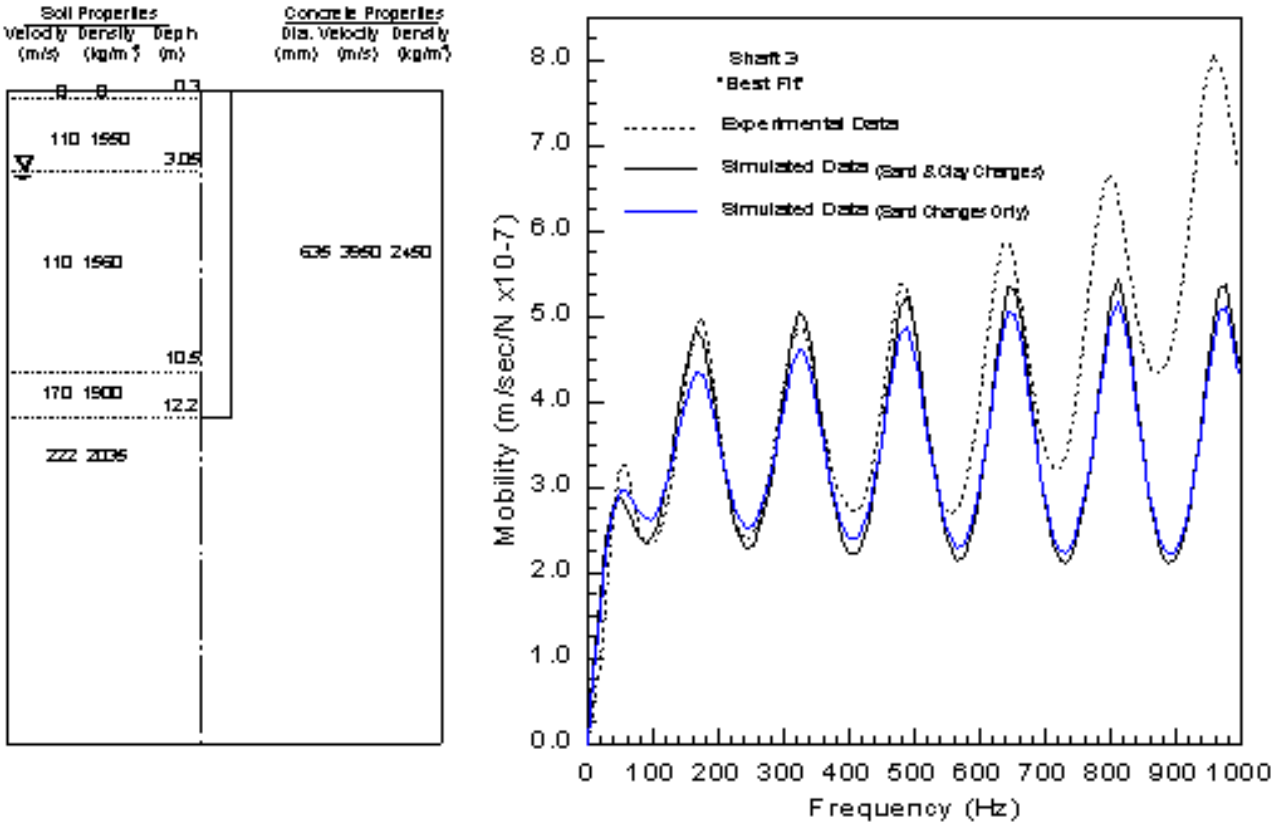

Figure 6.6 "Best Fit" Numerically-Simulated and Experimental Mobilities: Shaft 3

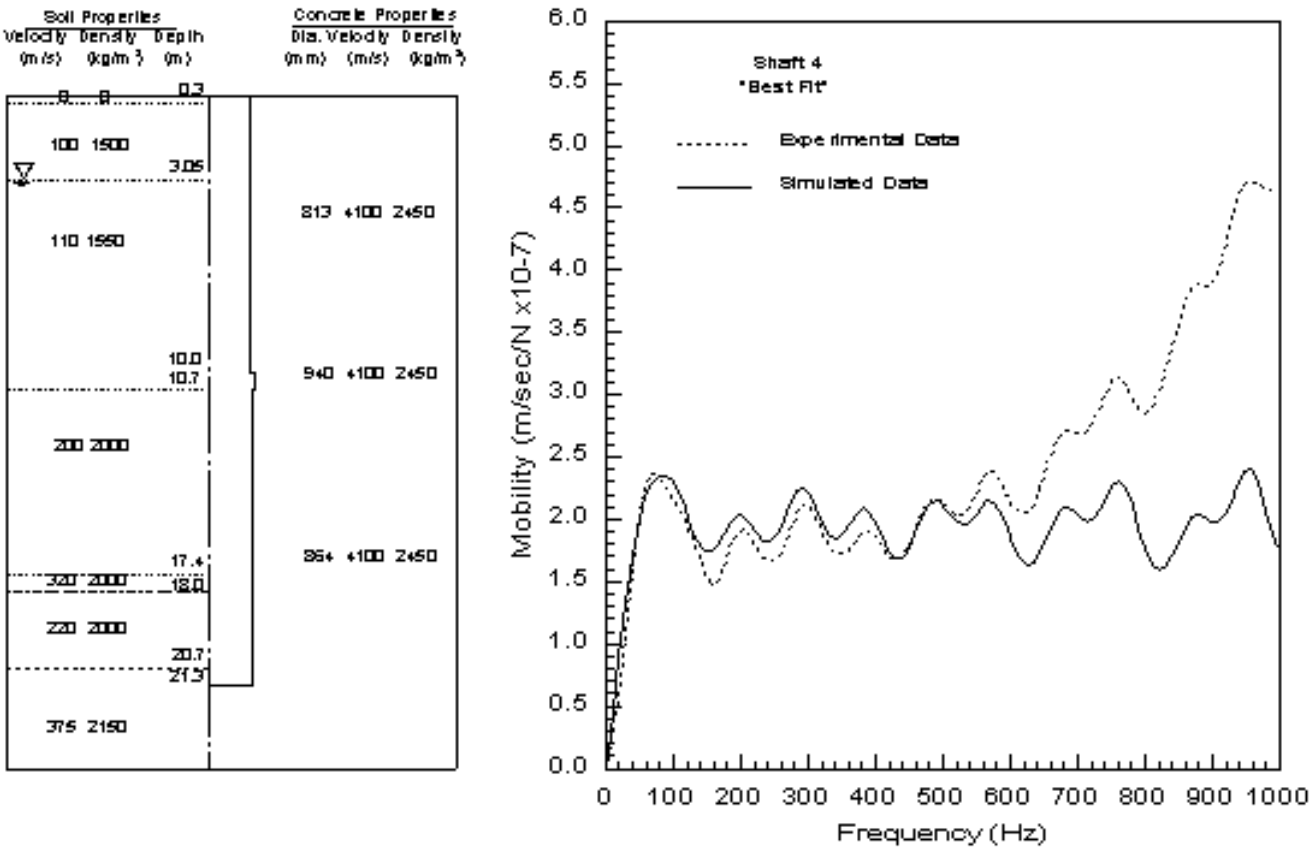

Figure 6.7 "Best Fit" Numerically-Simulated and Experimental Mobilities: Shaft 4

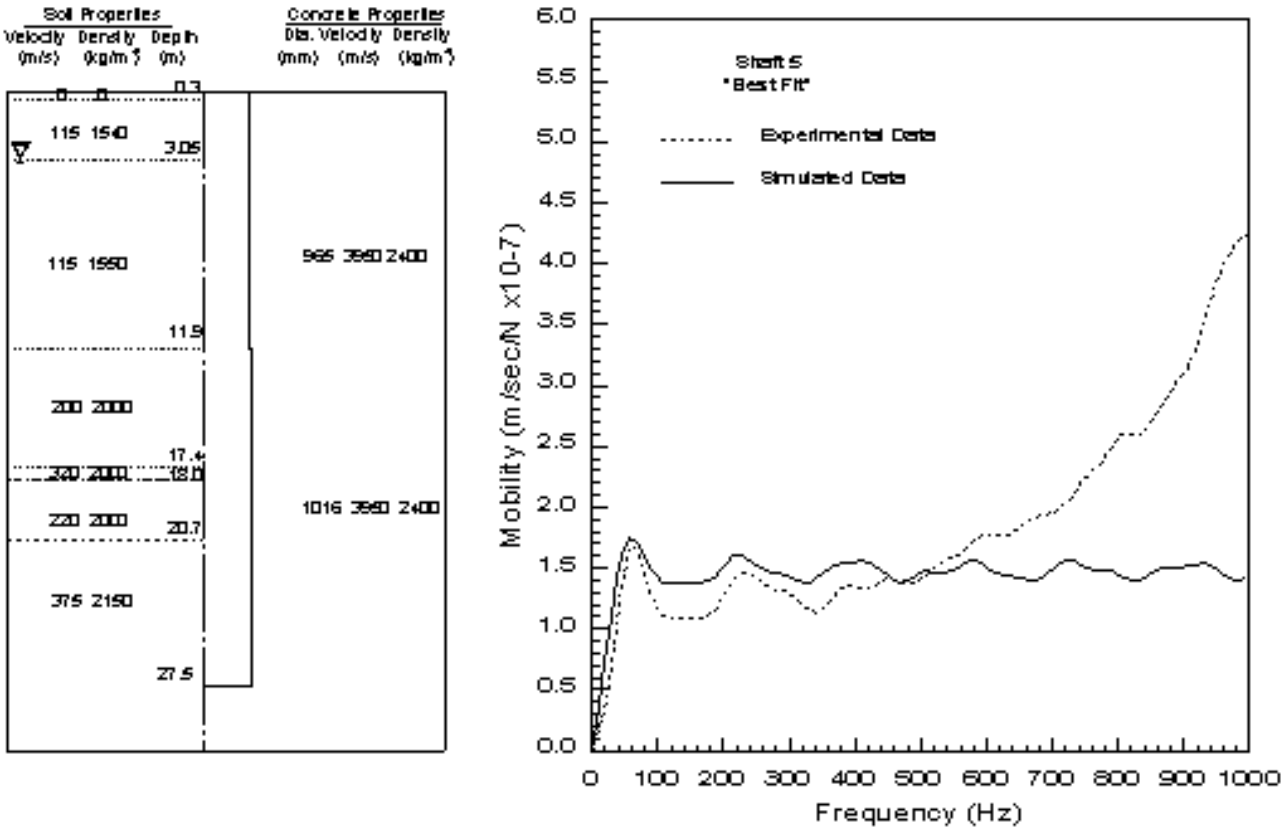

Figure 6.8 "Best Fit" Numerically-Simulated and Experimental Mobilities: Shaft 5

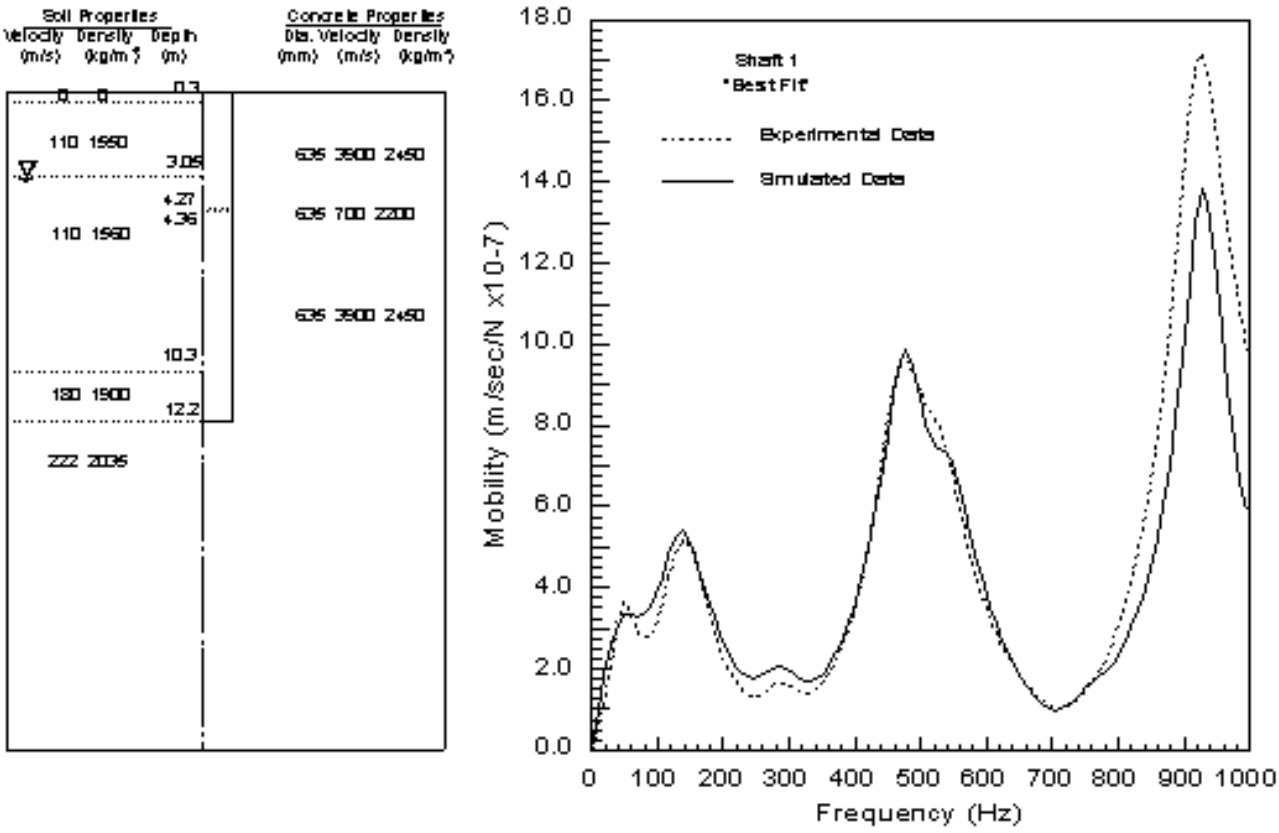

Figure 6.9 "Best Fit" Numerically-Simulated and Experimental Mobilities: Shaft 1

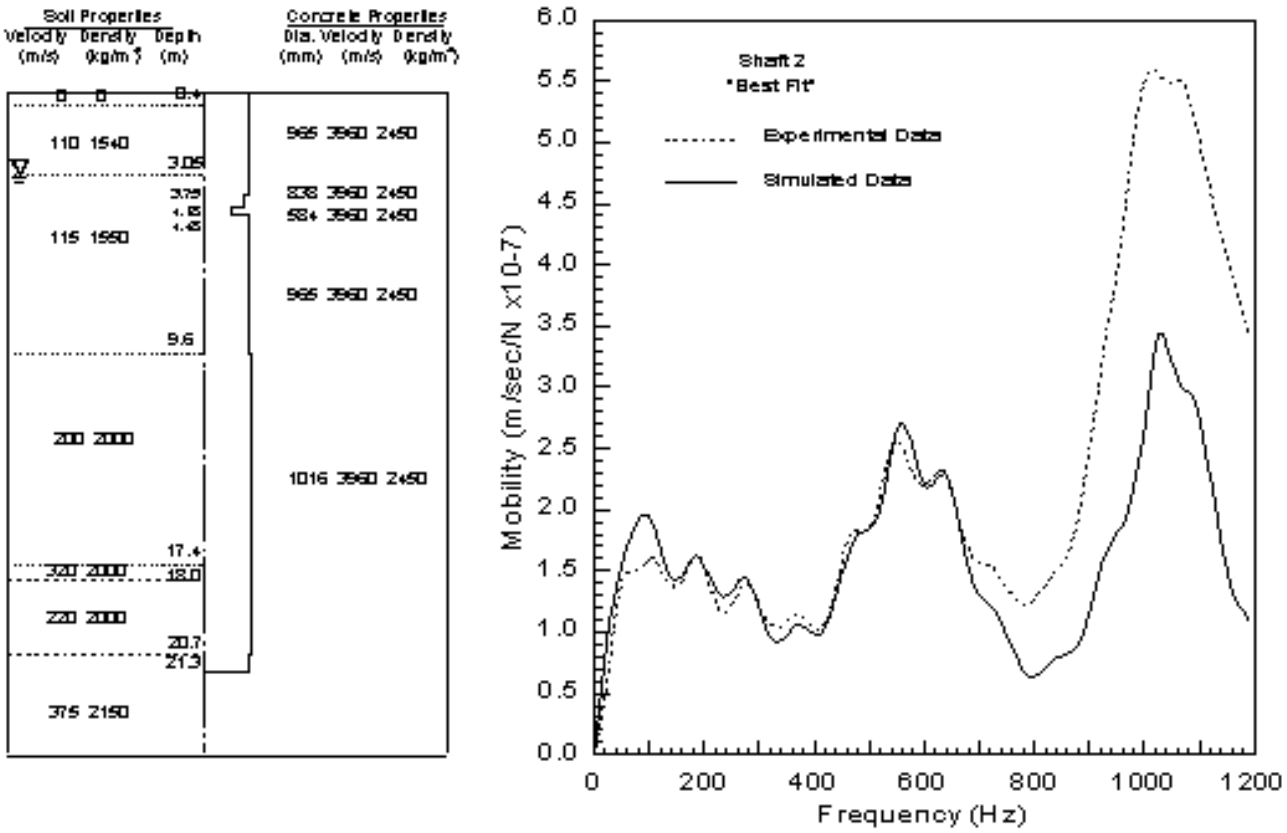

Figure 6.10 "Best Fit" Numerically-Simulated and Experimental Mobilities: Shaft 2

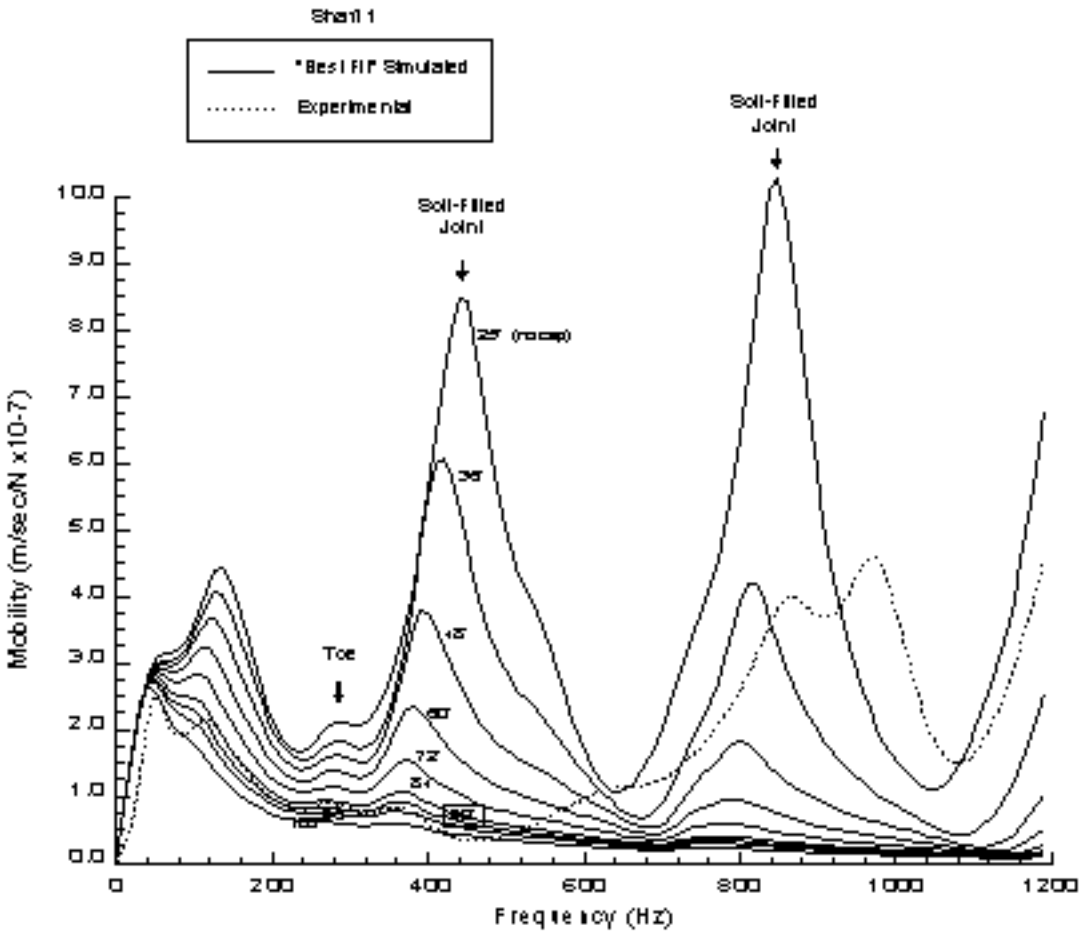

Figure 6.11 Numerical Simulation of Shaft 1 with Varying Pile Cap Diameter

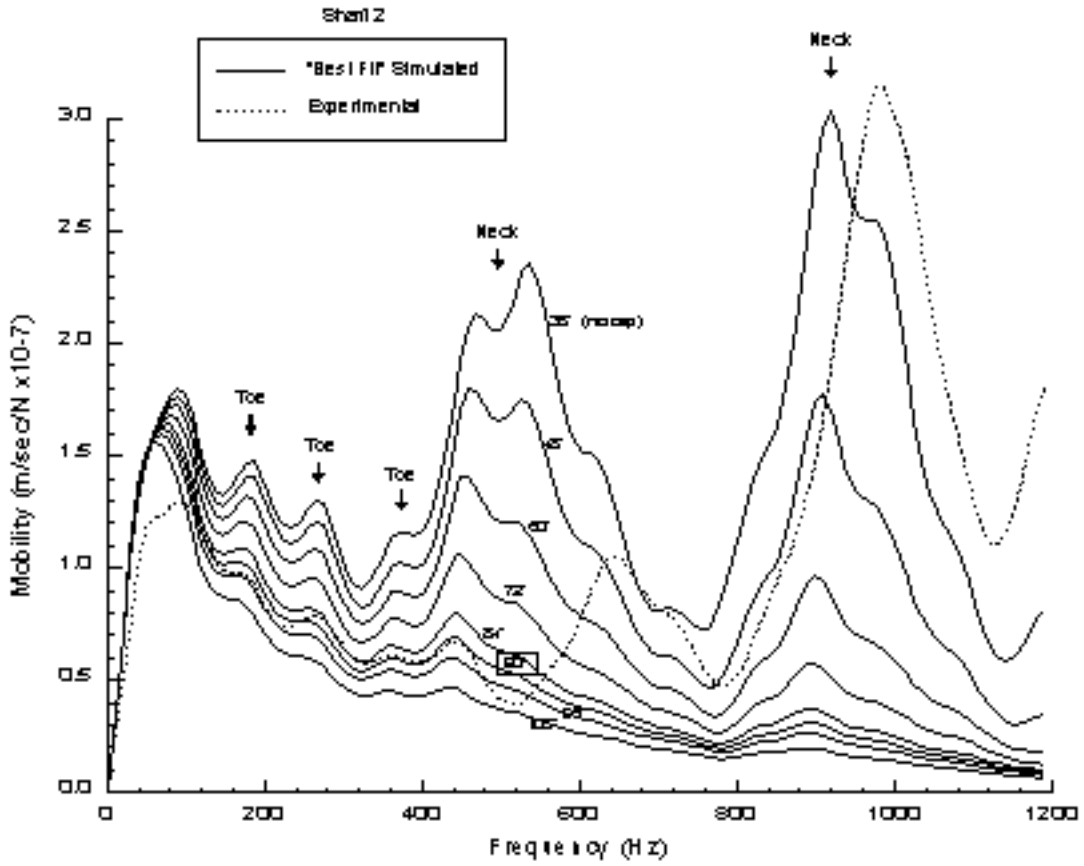

Figure 6.12 Numerical Simulation of Shaft 2 with Varying Pile Cap Diameter

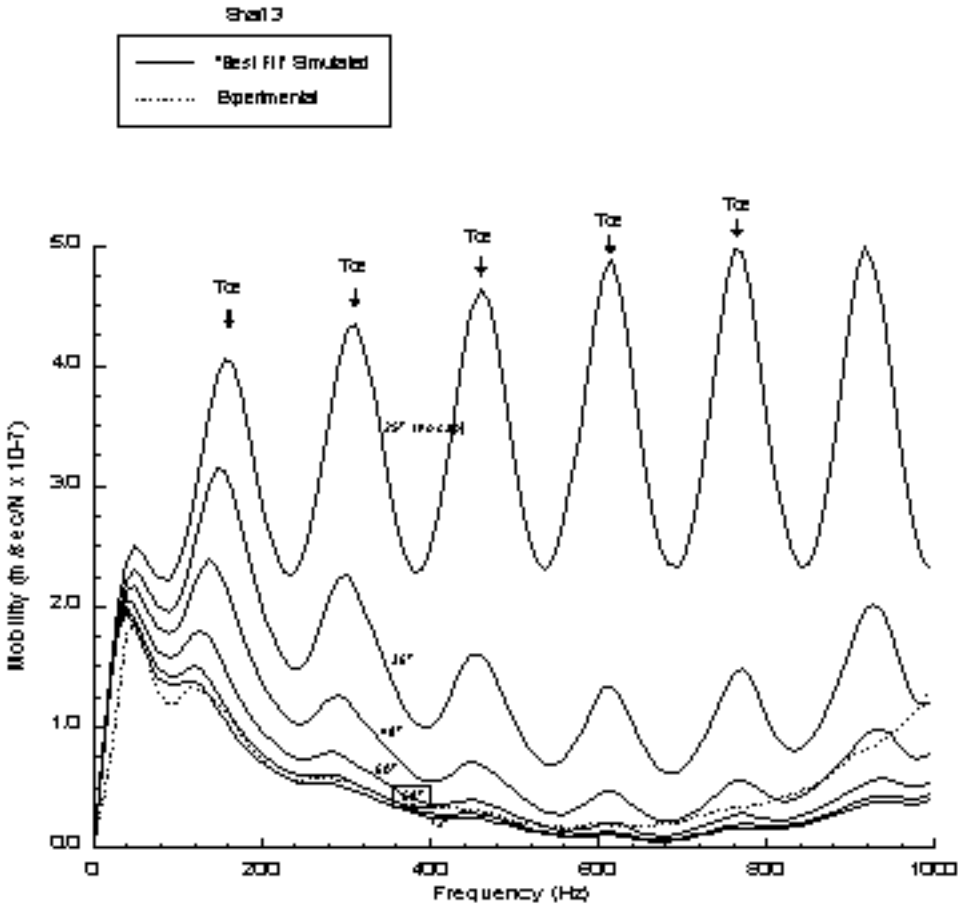

Figure 6.13 Numerical Simulation of Shaft 3 with Varying Pile Cap Diameter

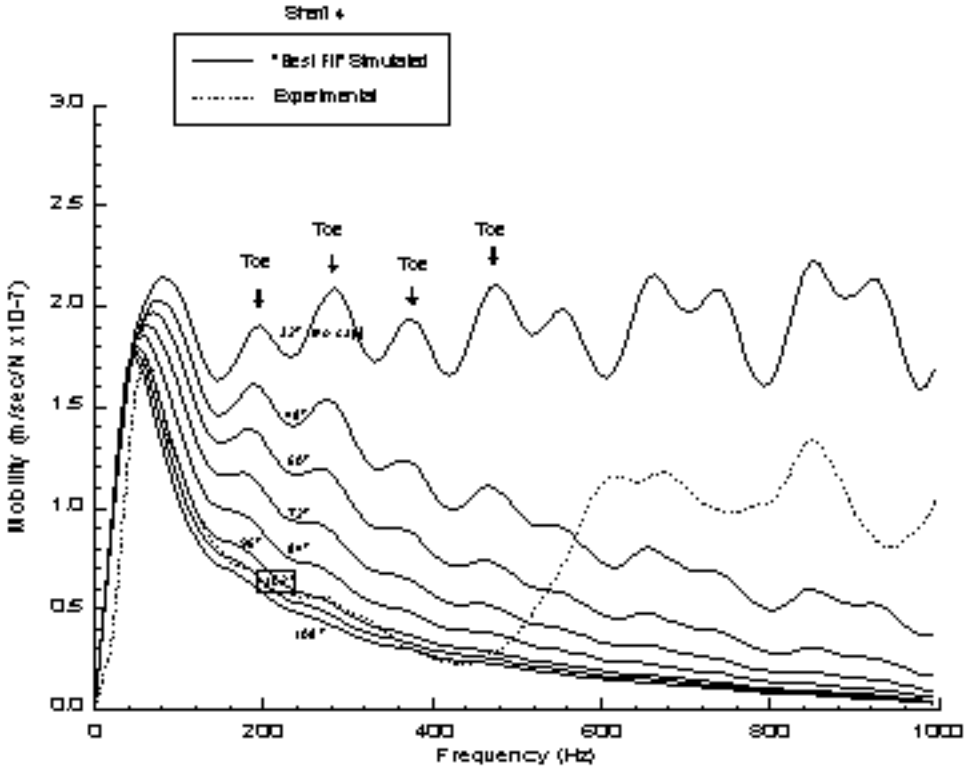

Figure 6.14 Numerical Simulation of Shaft 4 with Varying Pile Cap Diameter

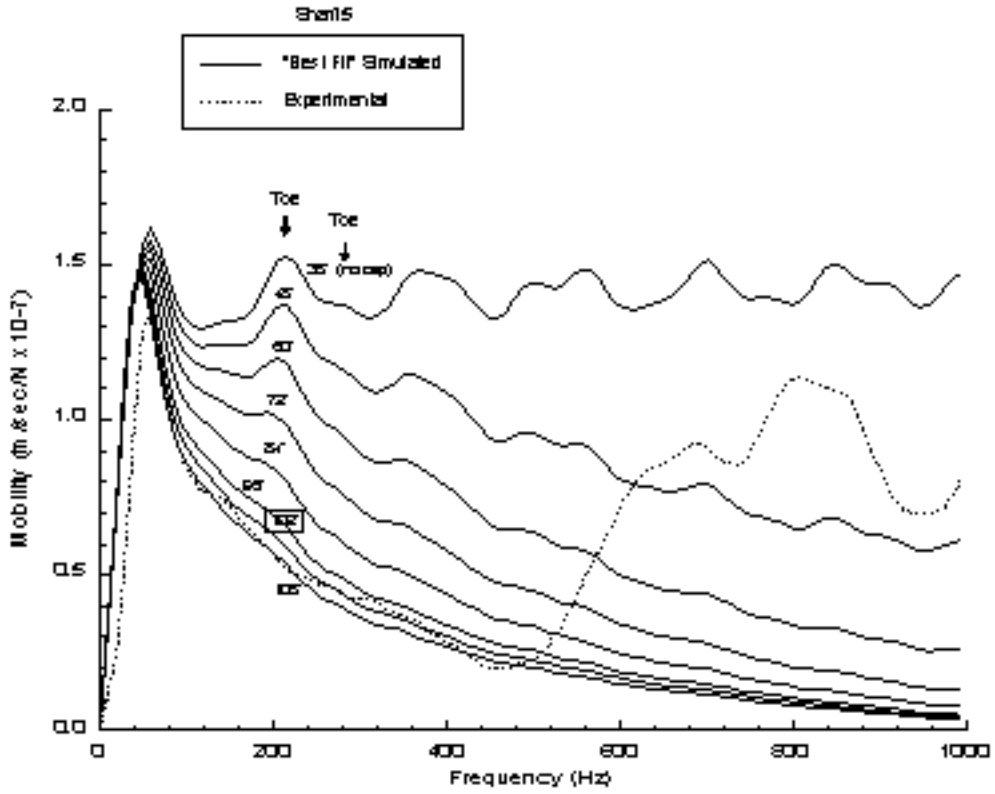

Figure 6.15 Numerical Simulation of Shaft 5 with Varying Pile Cap Diameter

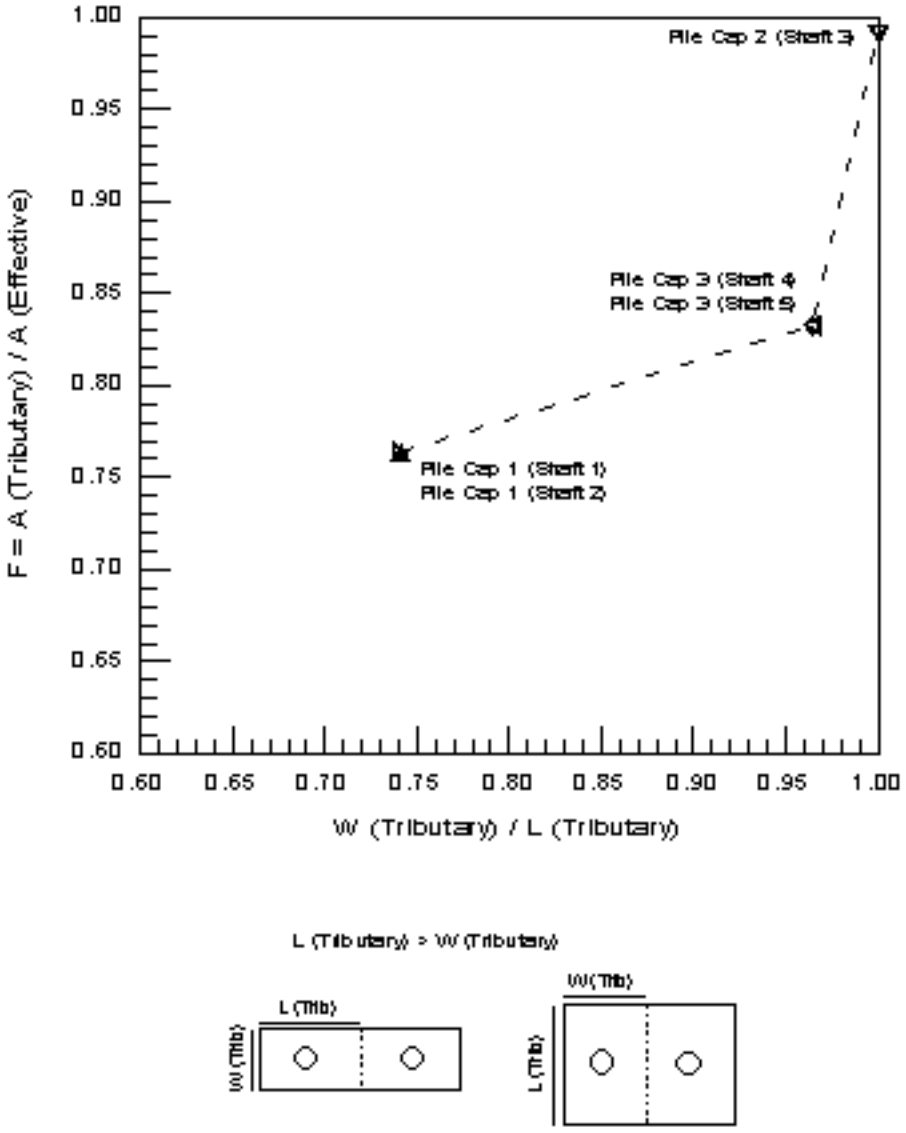

Figure 6.16 Factor to Determine "Effective" Area from Tributary Area of Pile Cap

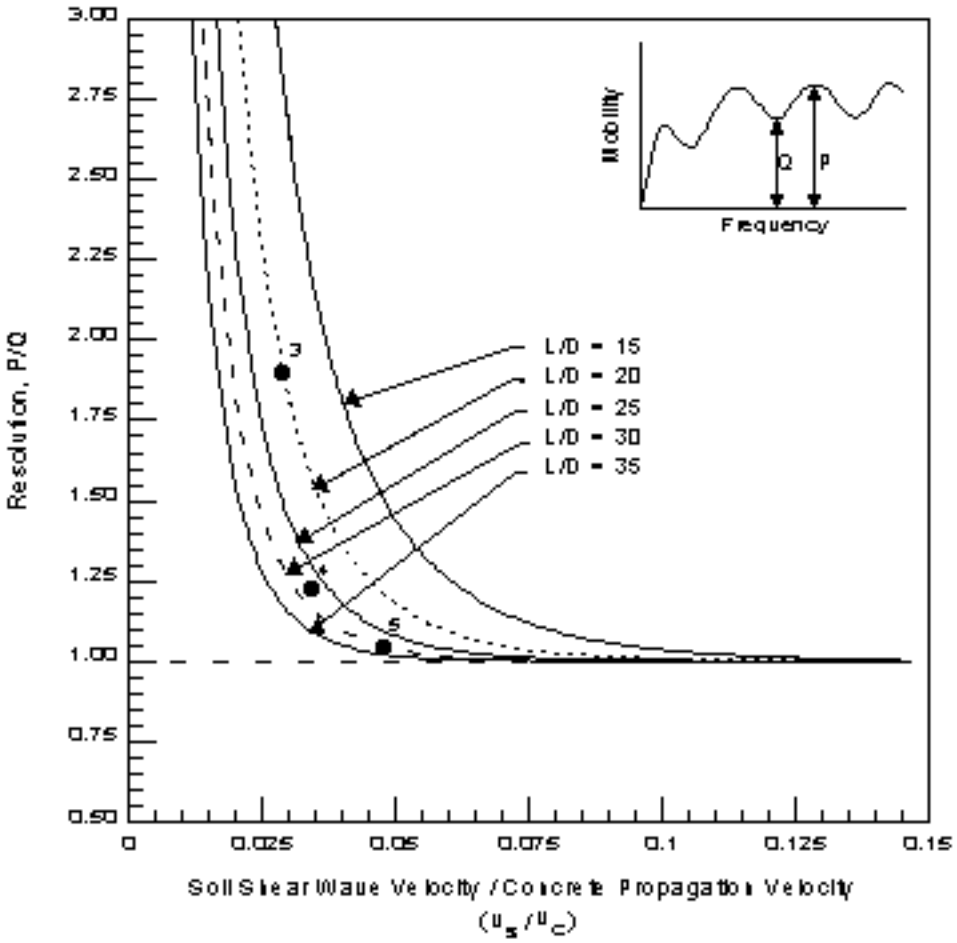

Figure 6.17 Resolution of NGES Shafts Compared to Ideal Resolution Chart

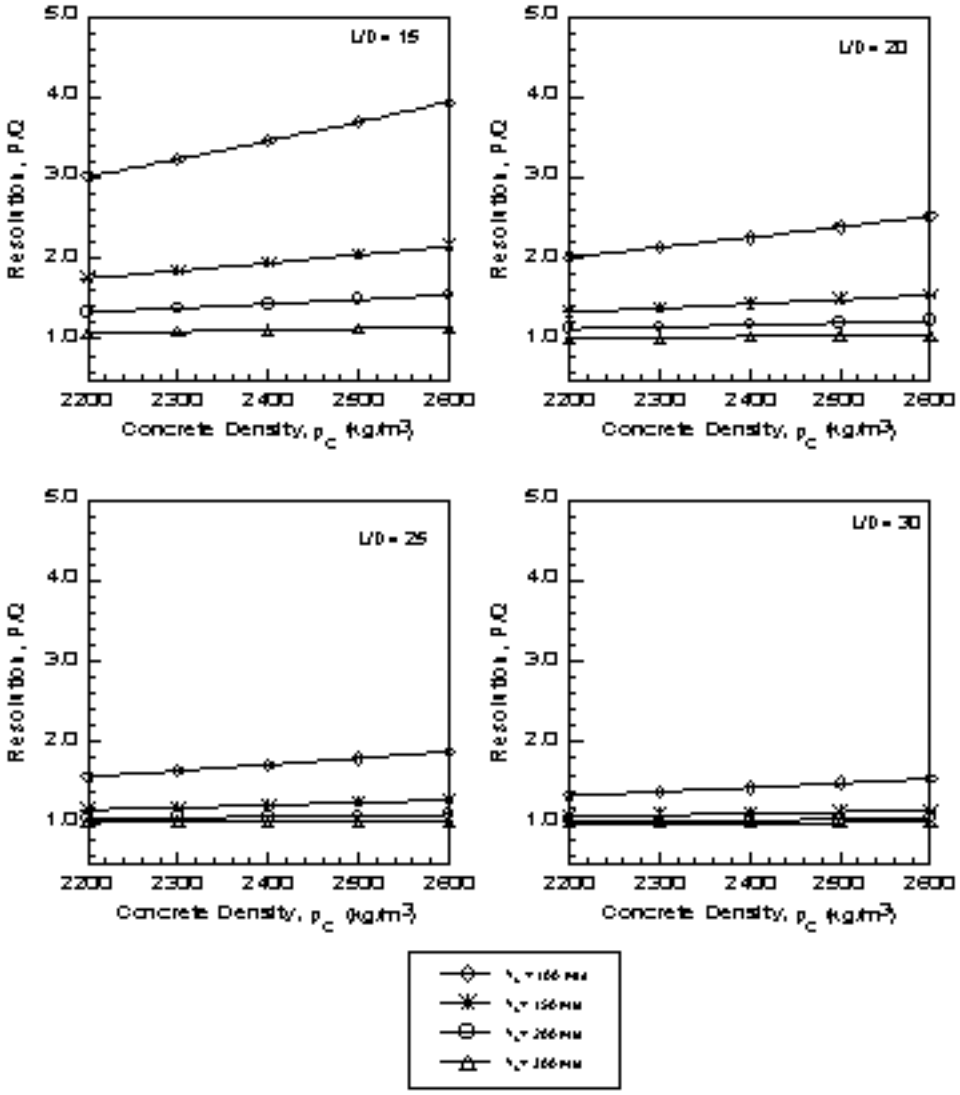

Figure 6.18 Effect of Concrete Density Variation on Resolution

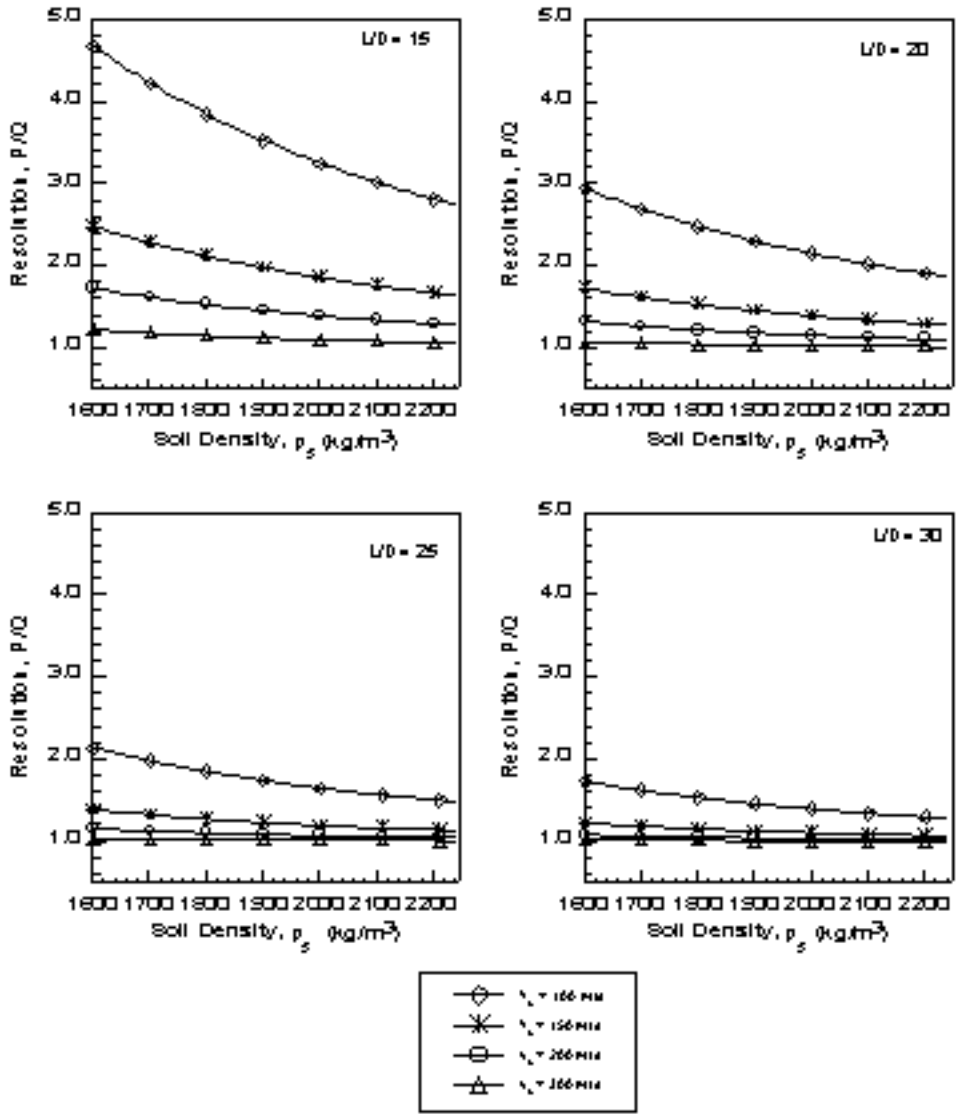

Figure 6.19 Effect of Soil Density Variation on Resolution

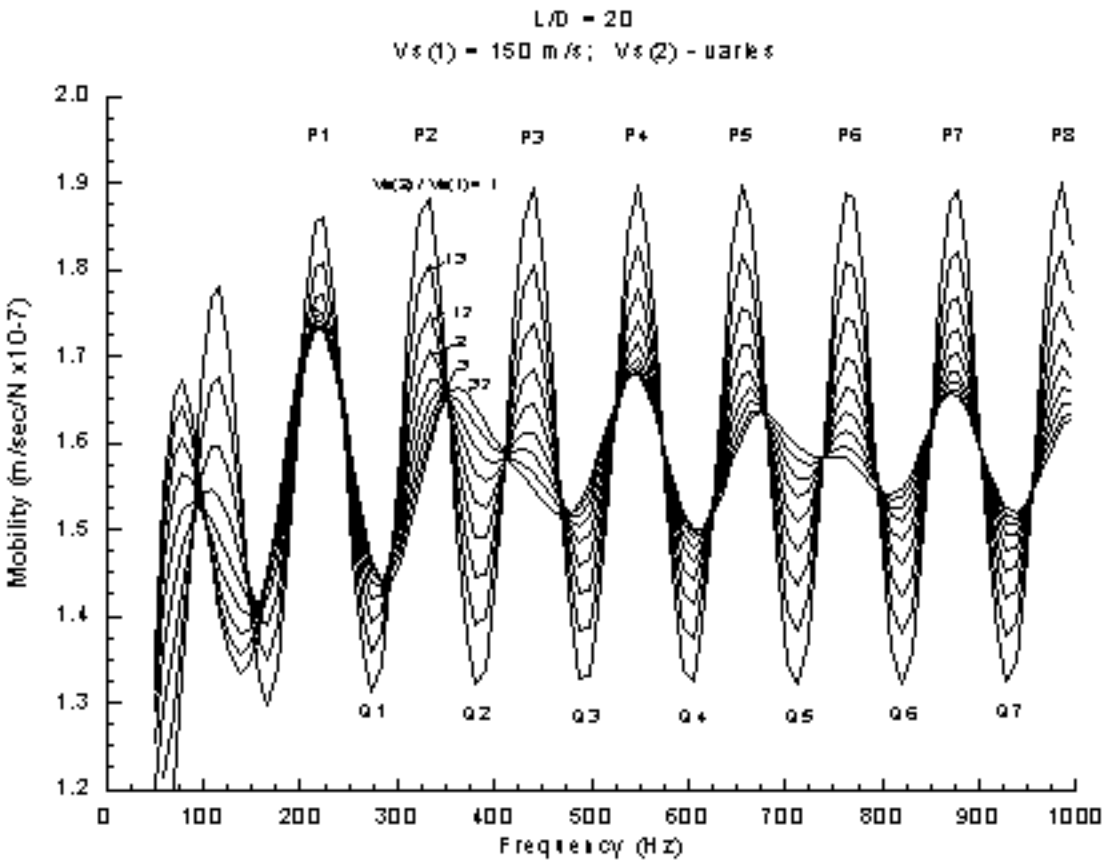

Figure 6.20 Effect of Embedment Layer Soil Stiffness of the Mobility Resolution

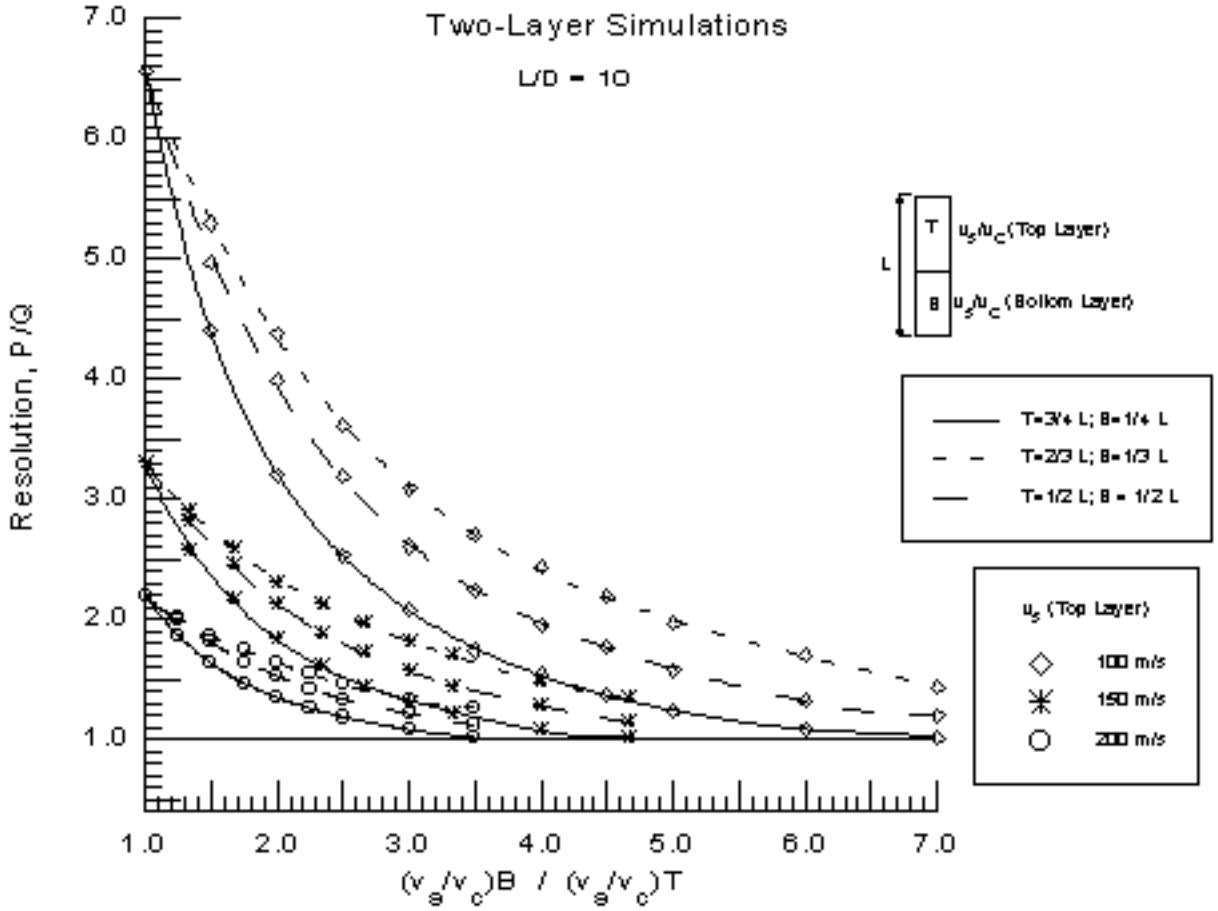

Figure 6.21 Resolution Chart for a Two-Layer Subsurface Profile, L/D = 10

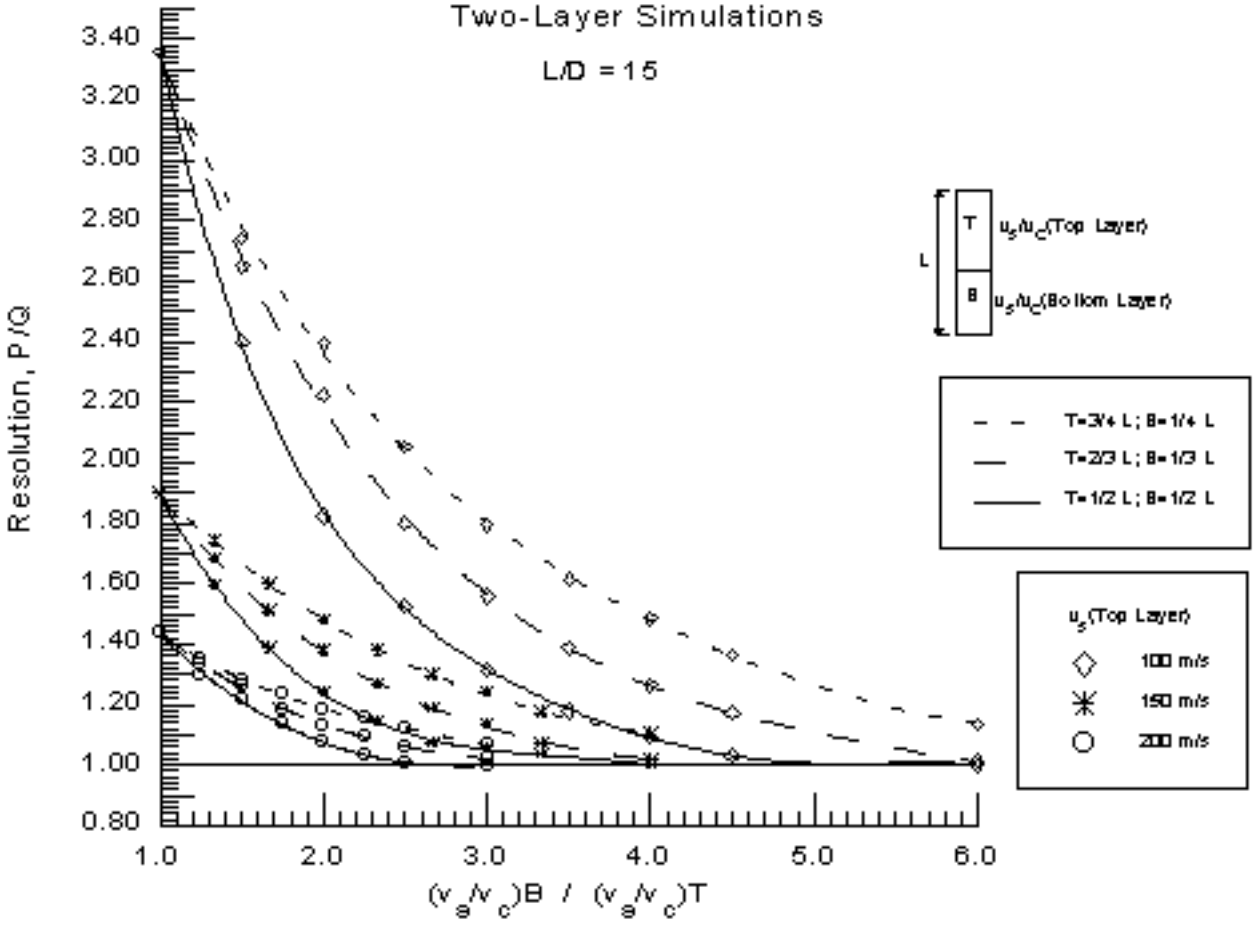

Figure 6.22 Resolution Chart for a Two-Layer Subsurface Profile, L/D = 15

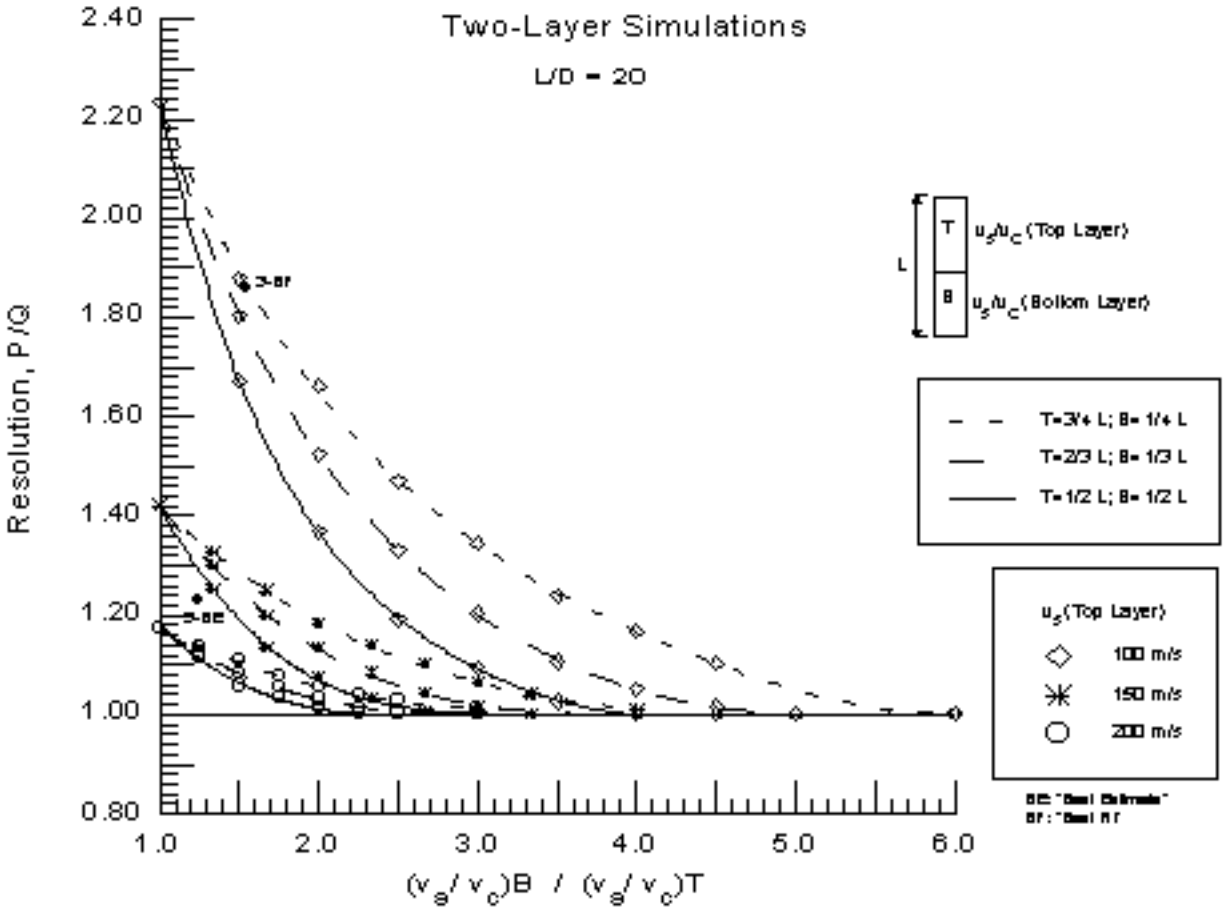

Figure 6.23 Resolution Chart for a Two-Layer Subsurface Profile, L/D = 20

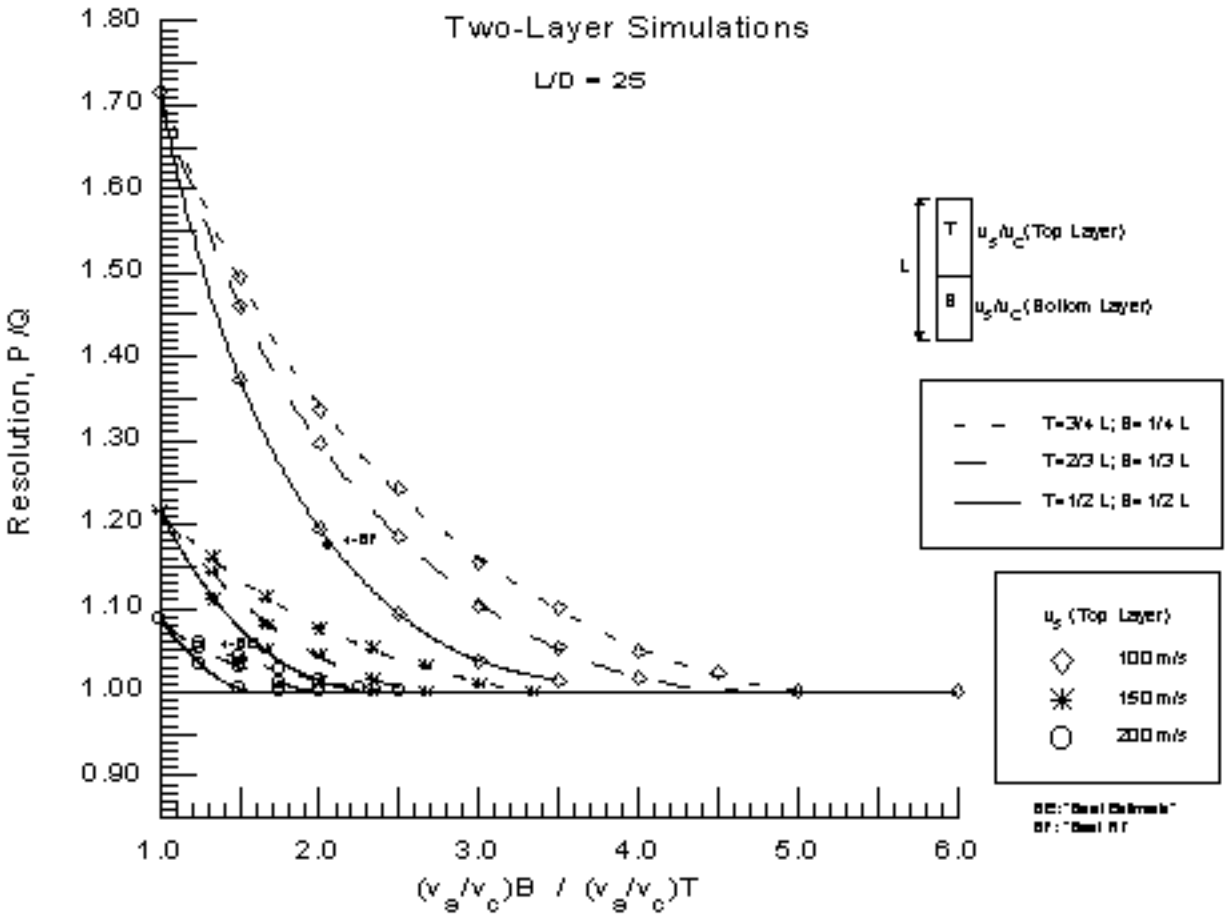

Figure 6.24 Resolution Chart for a Two-Layer Subsurface Profile, L/D = 25

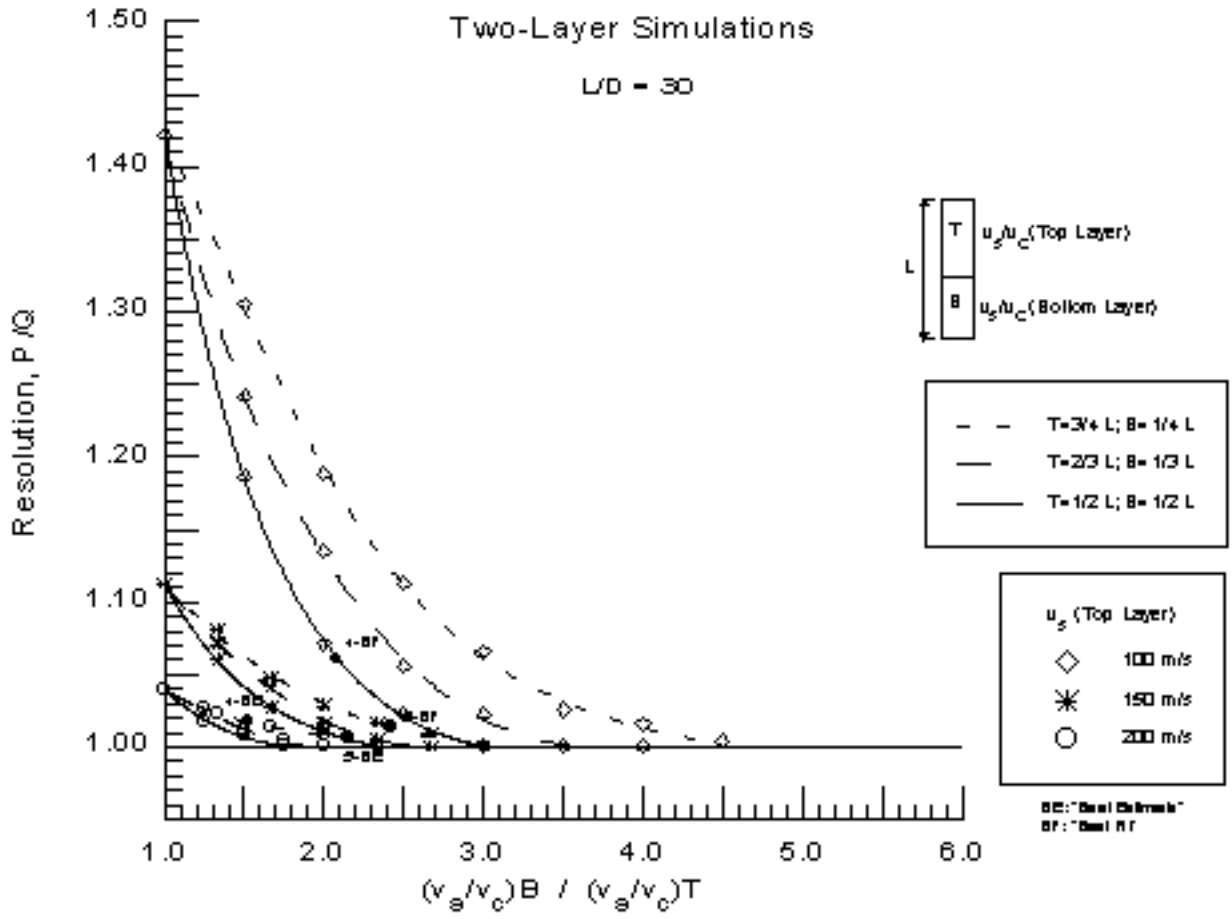

Figure 6.25 Resolution Chart for a Two-Layer Subsurface Profile, L/D = 30

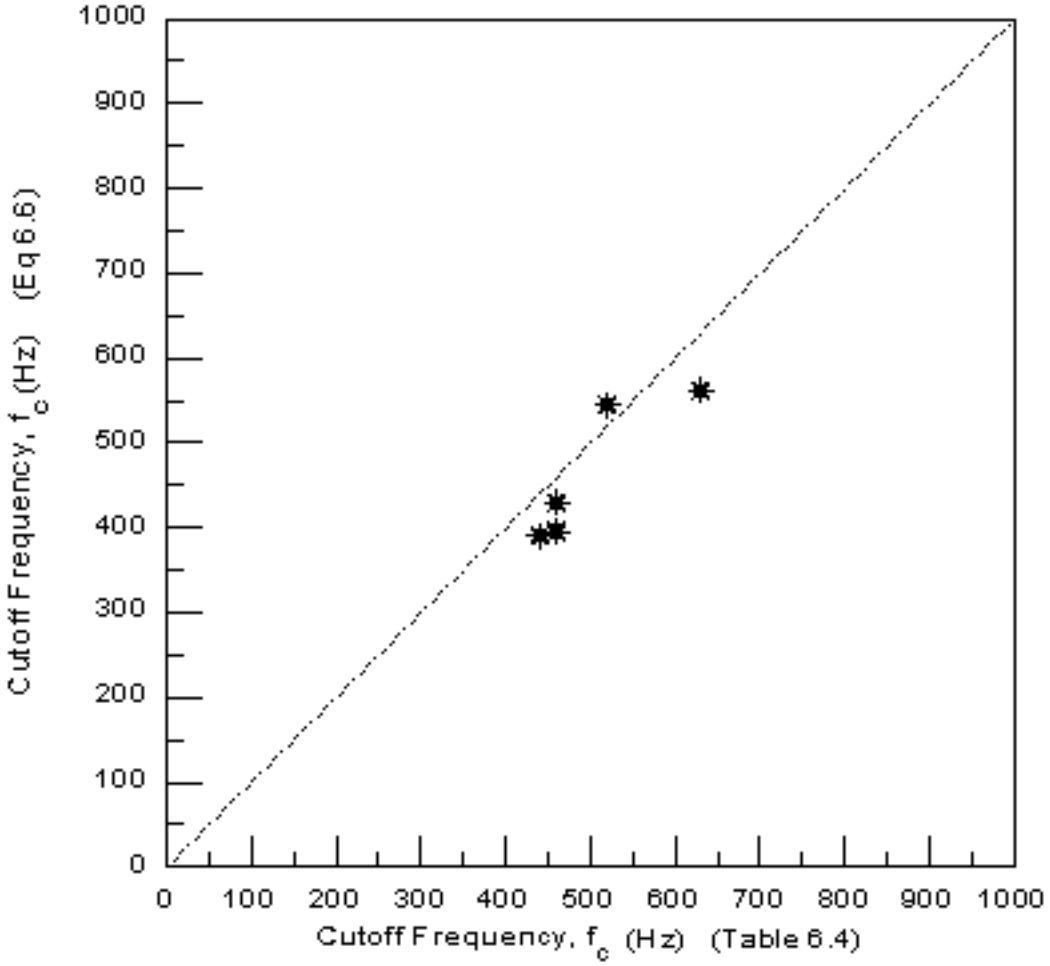

Figure 6.26 Comparison of Cutoff Frequencies

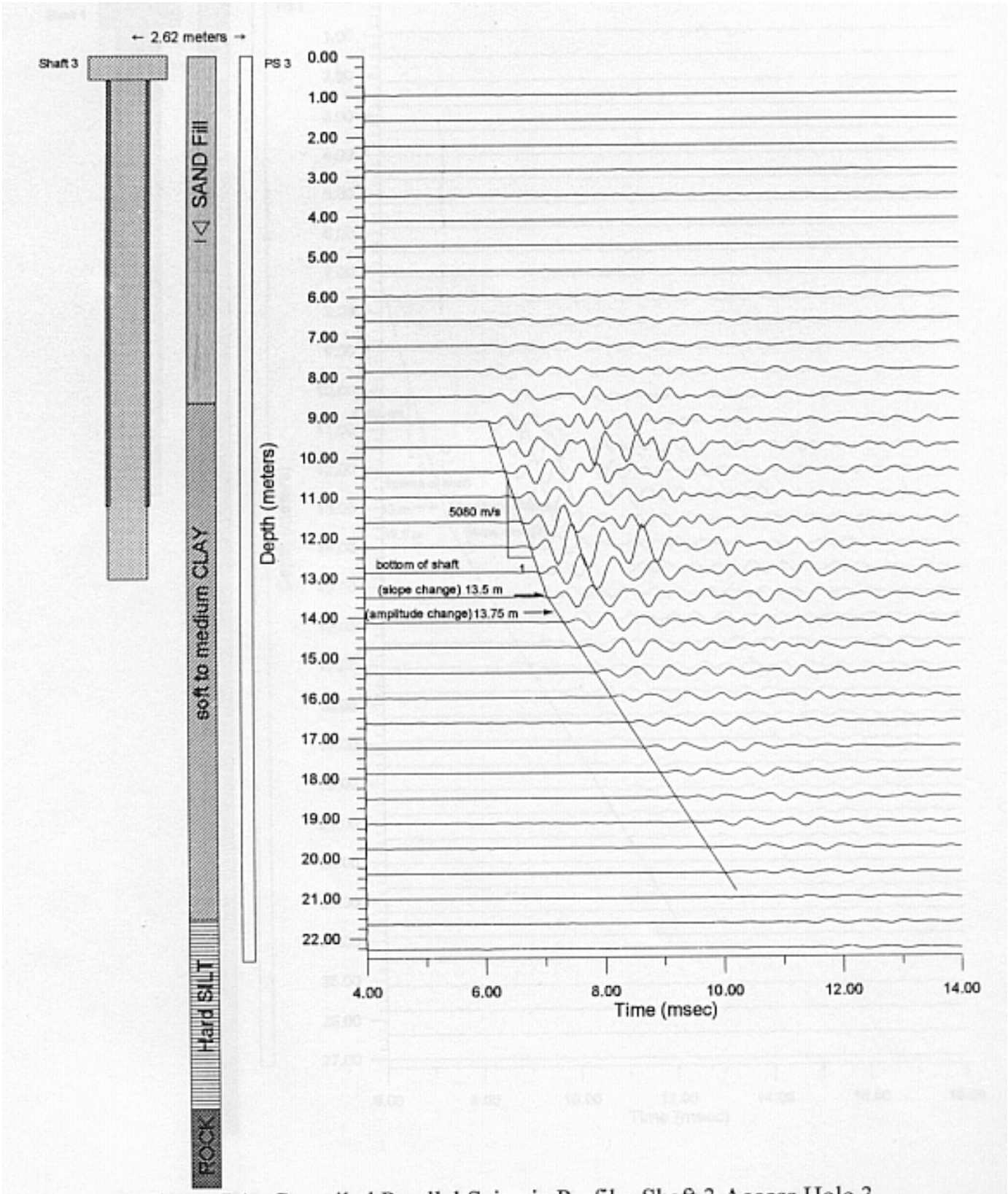

Figure 7.1. Compiled Parallel Seismic Profile: Shaft 3 Access Hole 3

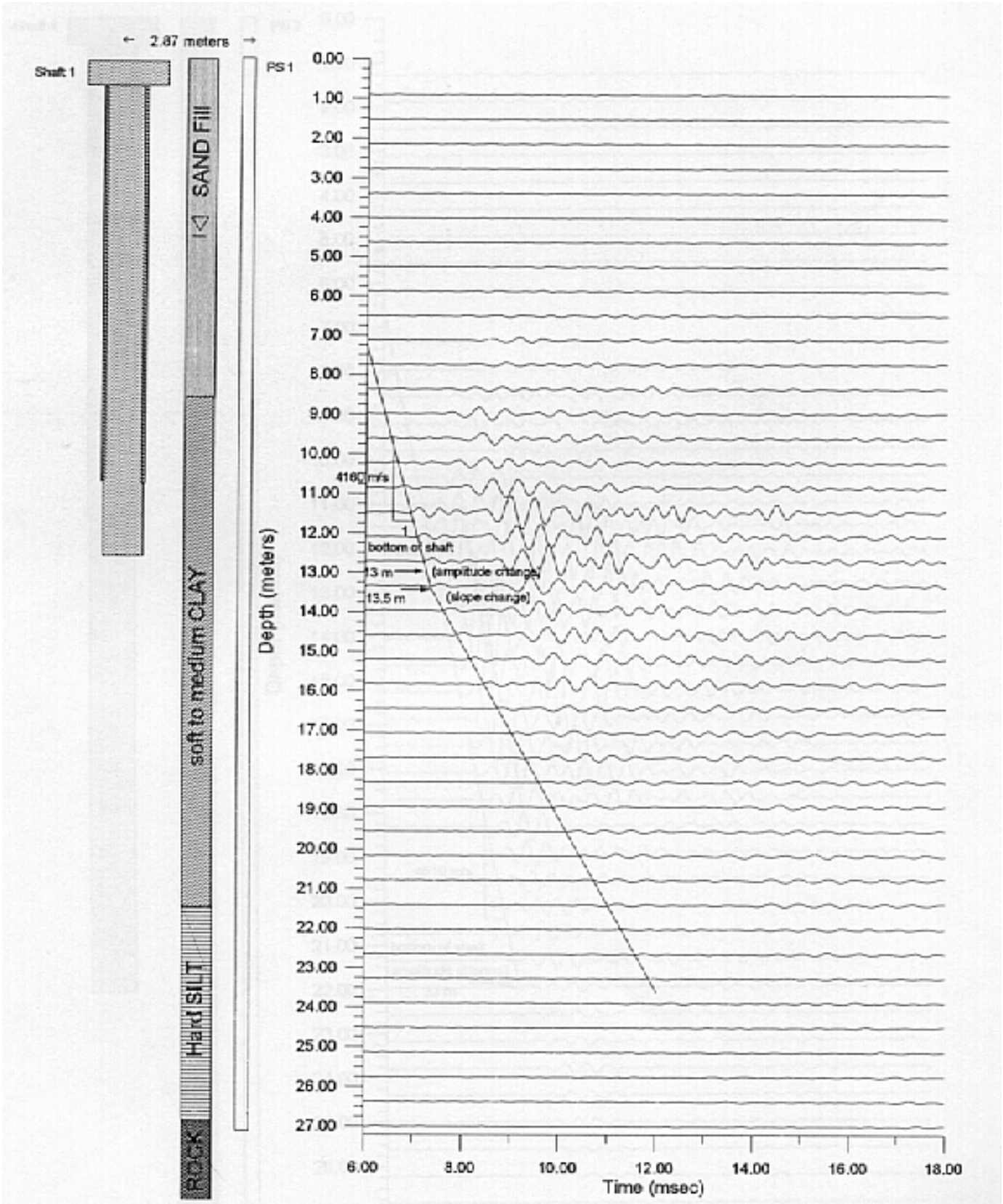

Figure 7.2 Compiled Parallel Seismic Profile: Shaft 1 Access Hole 1

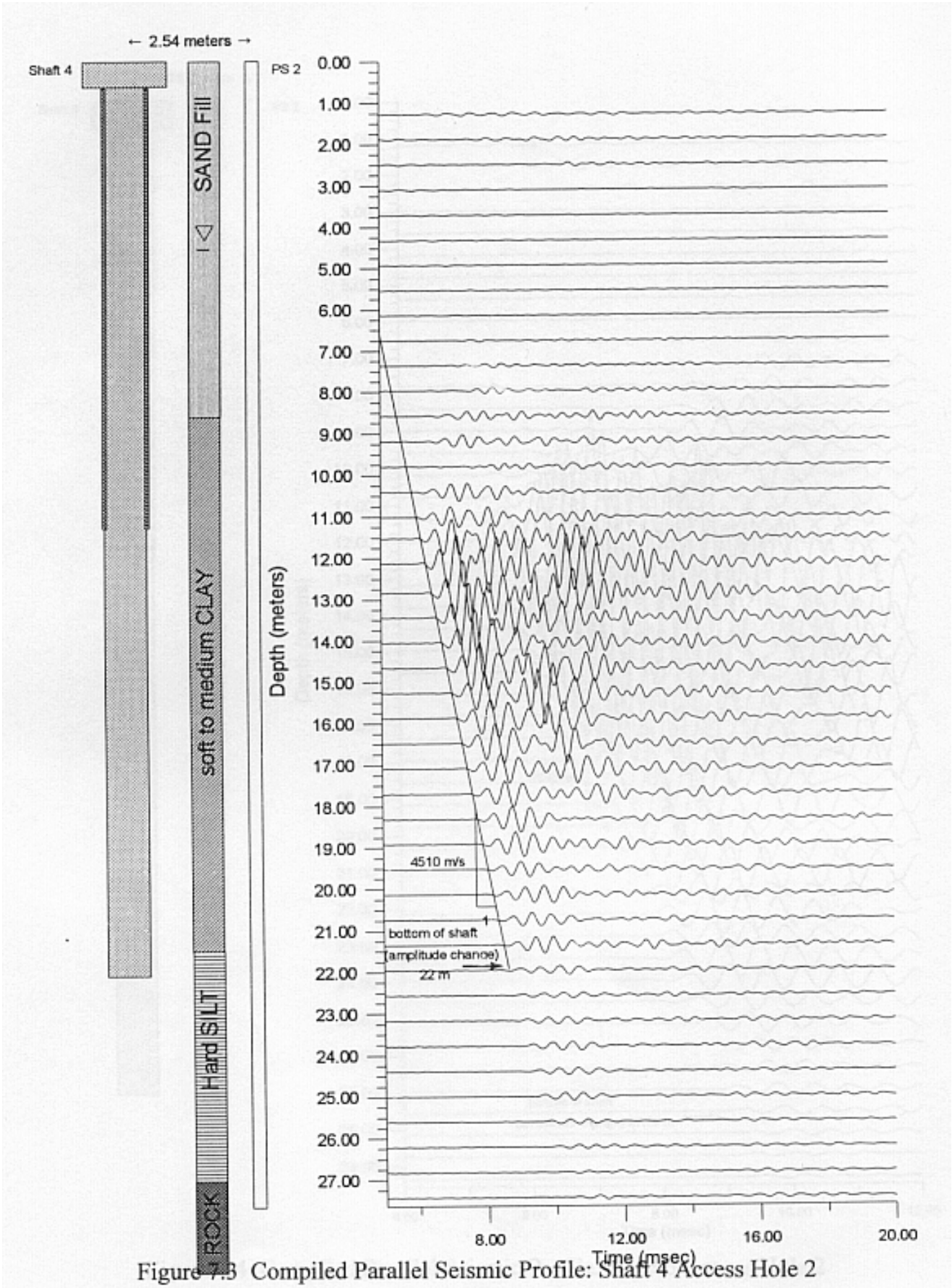

Figure 7.3 Compiled Parallel Seismic Profile: Shaft 4 Access Hole 2

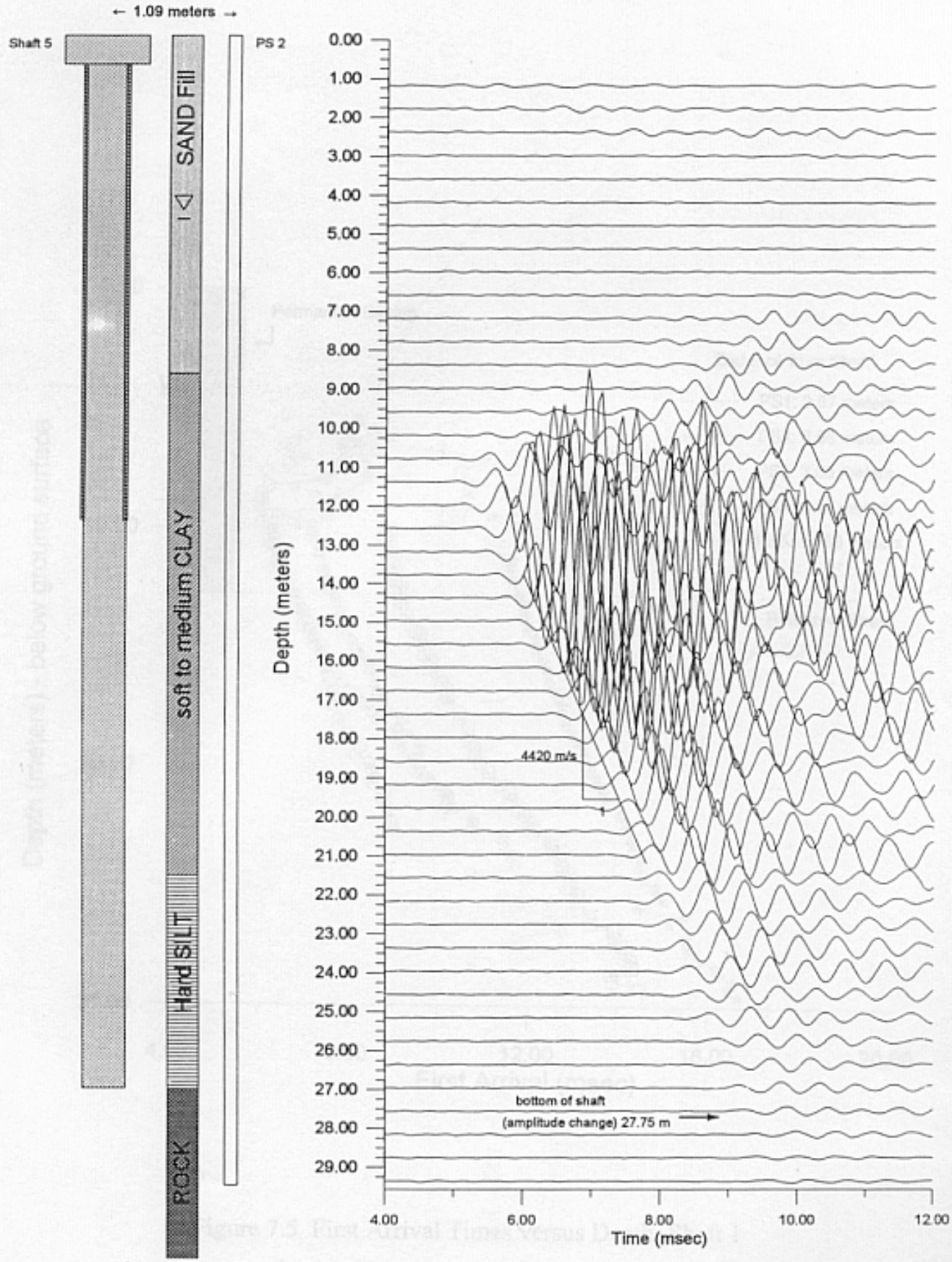

Figure 7.4 Compiled Parallel Seismic Profile: Shaft 5 Access Hole 2

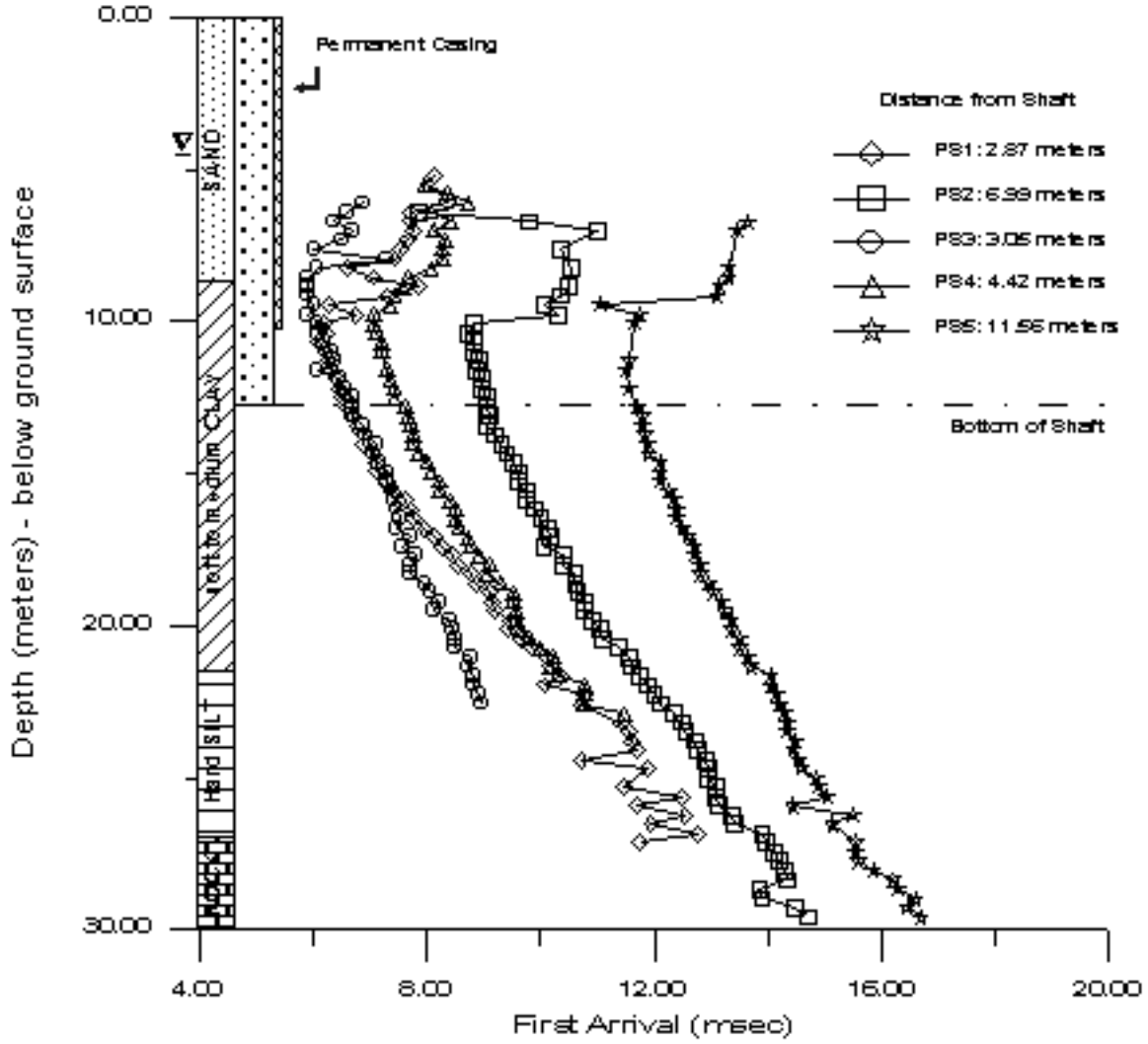

Figure 7.5 First Arrival Times versus Depth: Shaft 1

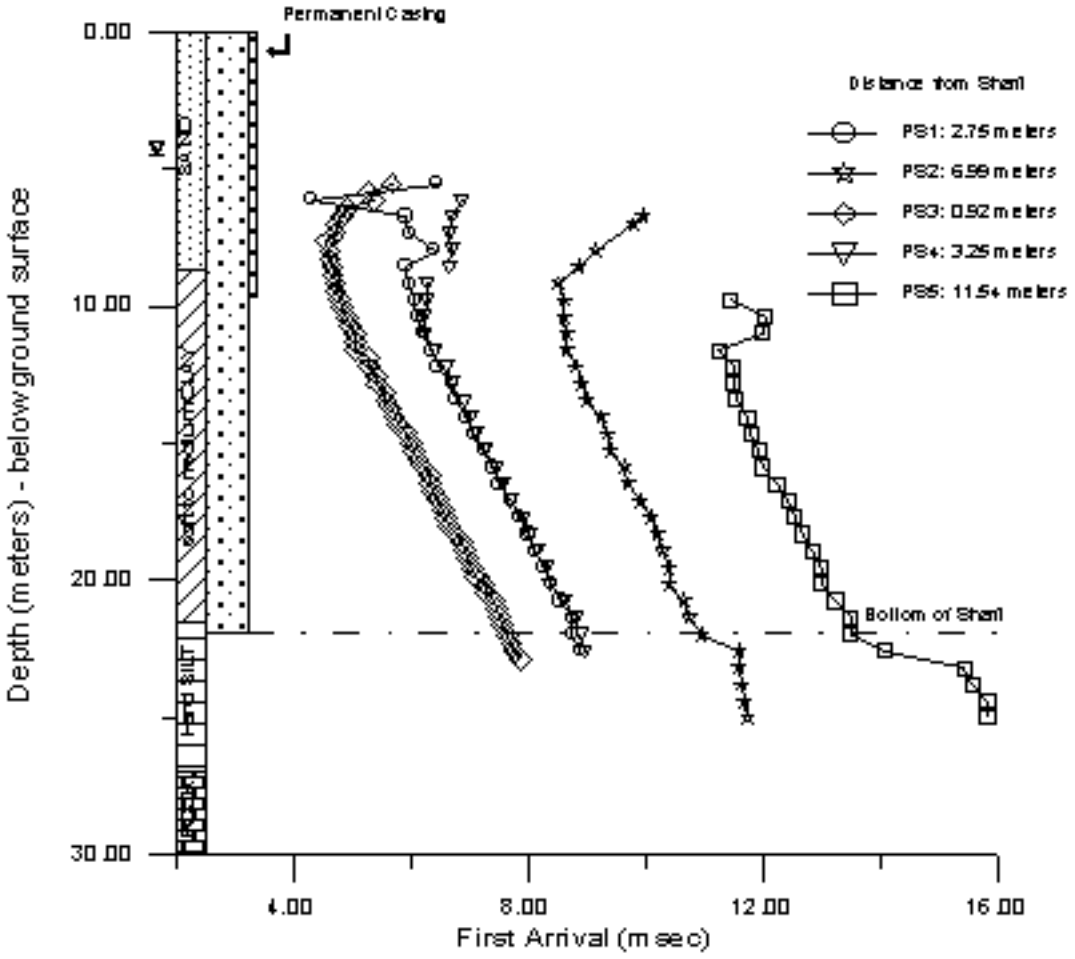

Figure 7.6 First Arrival Times versus Depth: Shaft 2

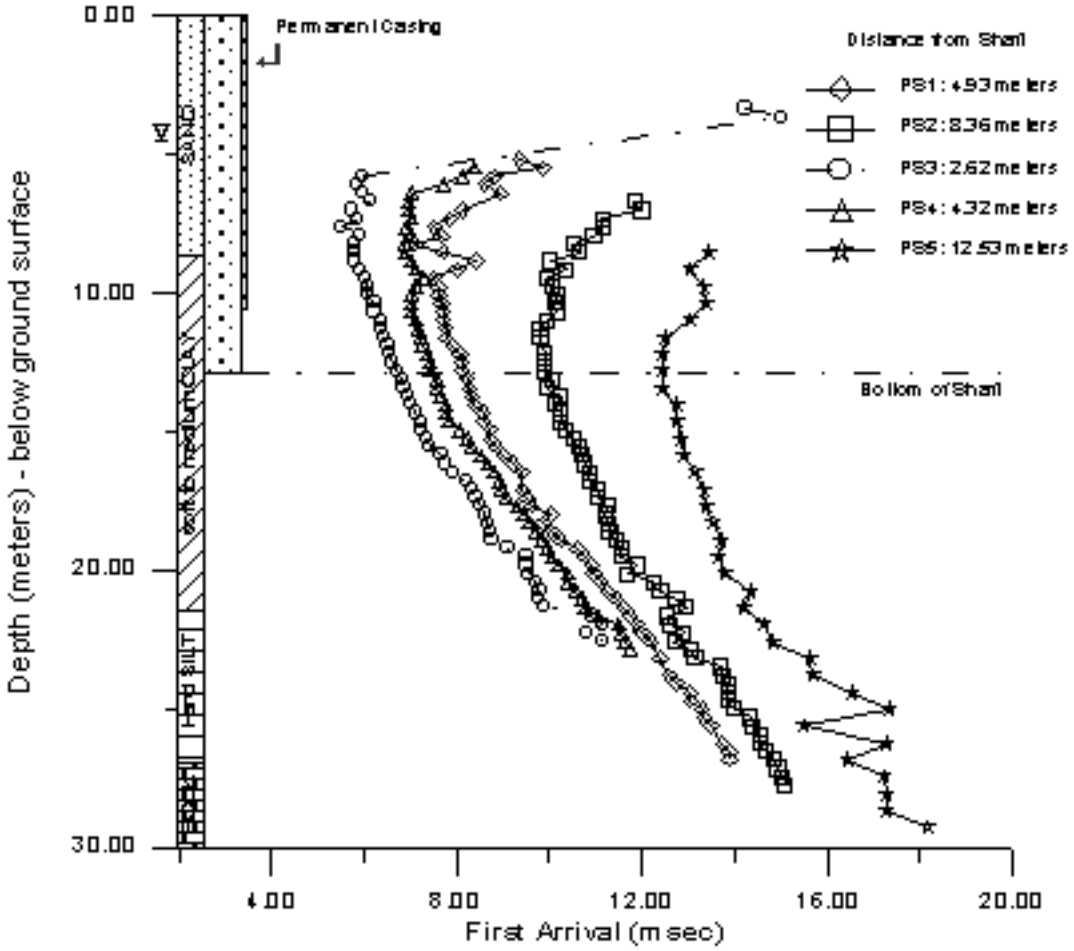

Figure 7.7 First Arrival Times versus Depth: Shaft 3

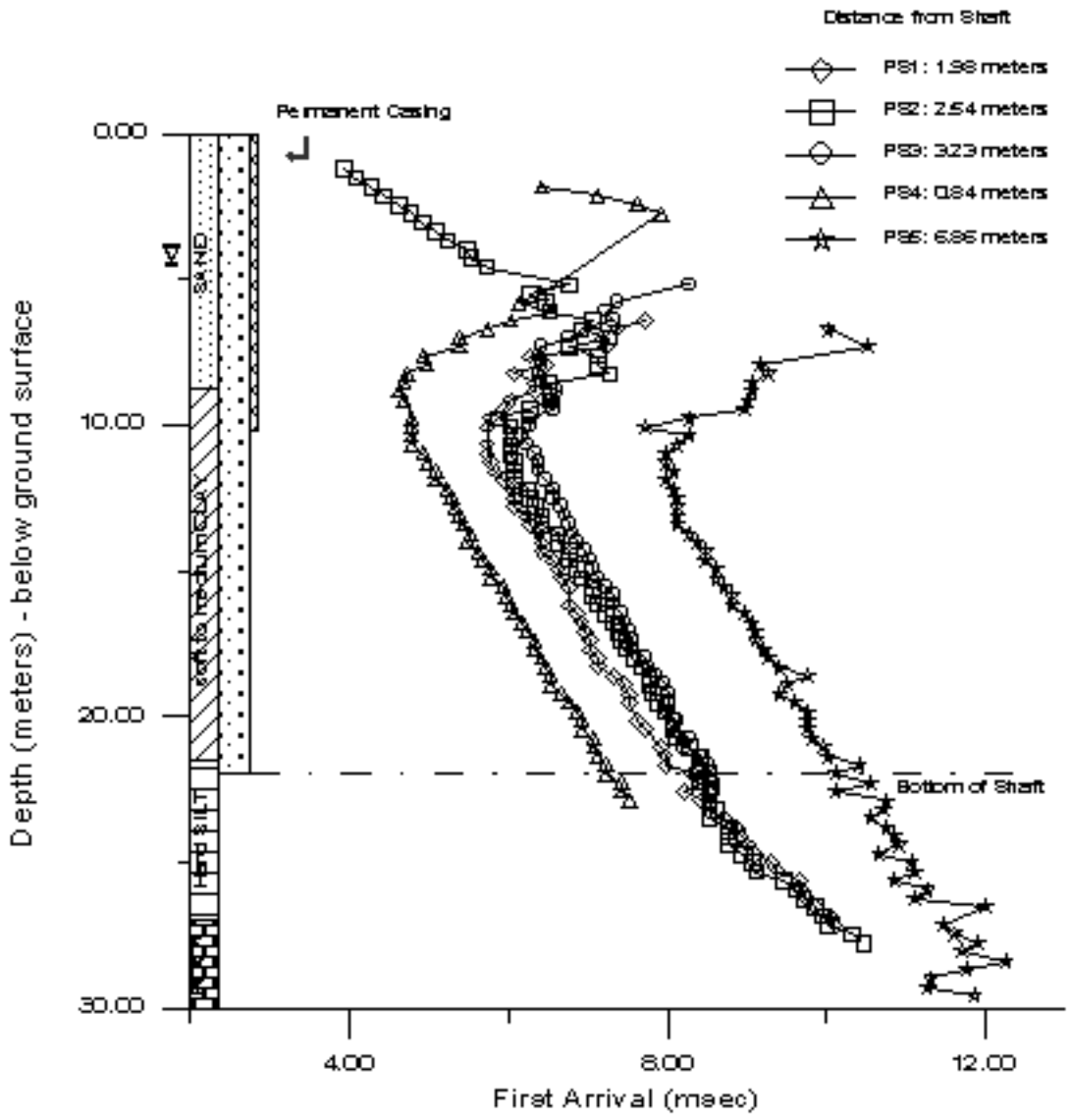

Figure 7.8 First Arrival Times versus Depth: Shaft 4

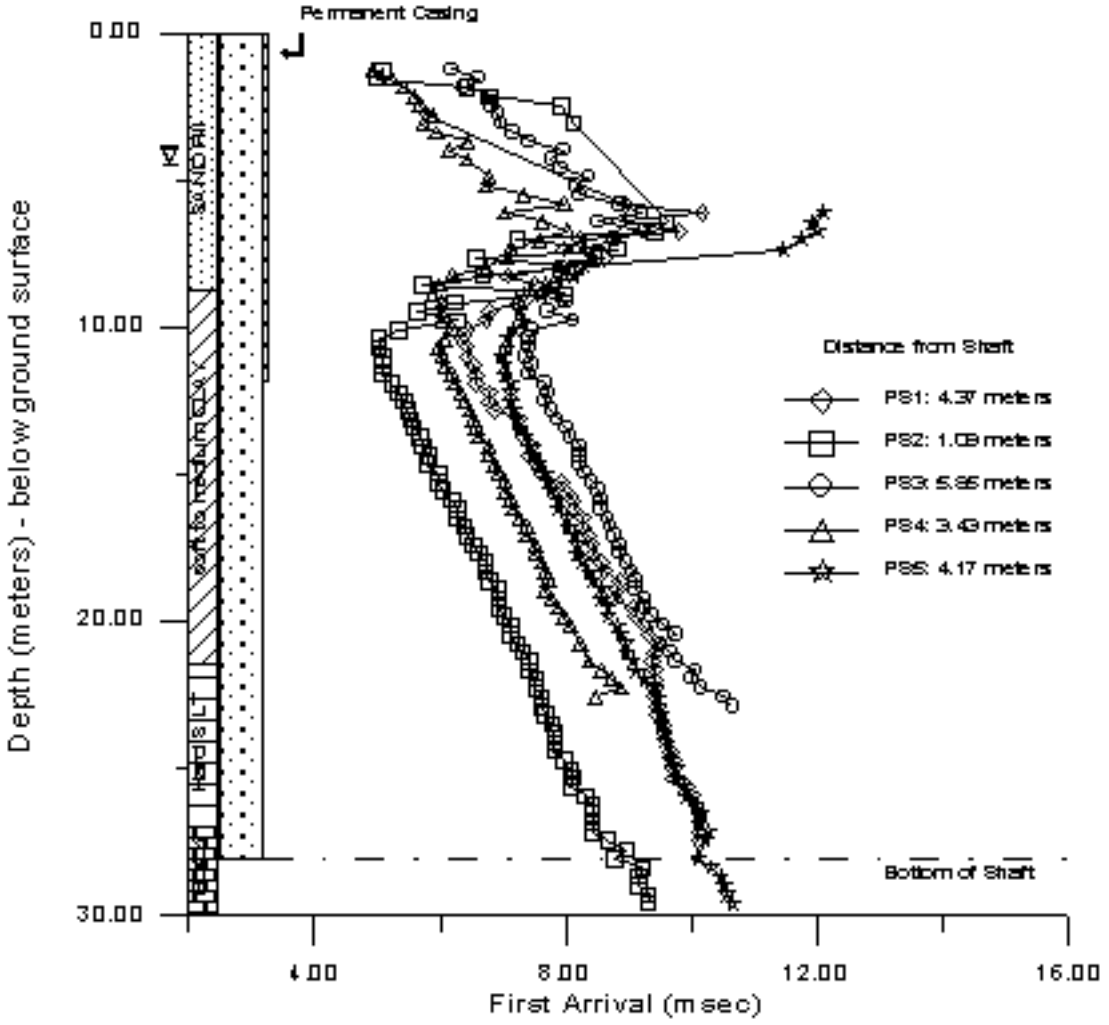

Figure 7.9 First Arrival Times versus Depth: Shaft 5

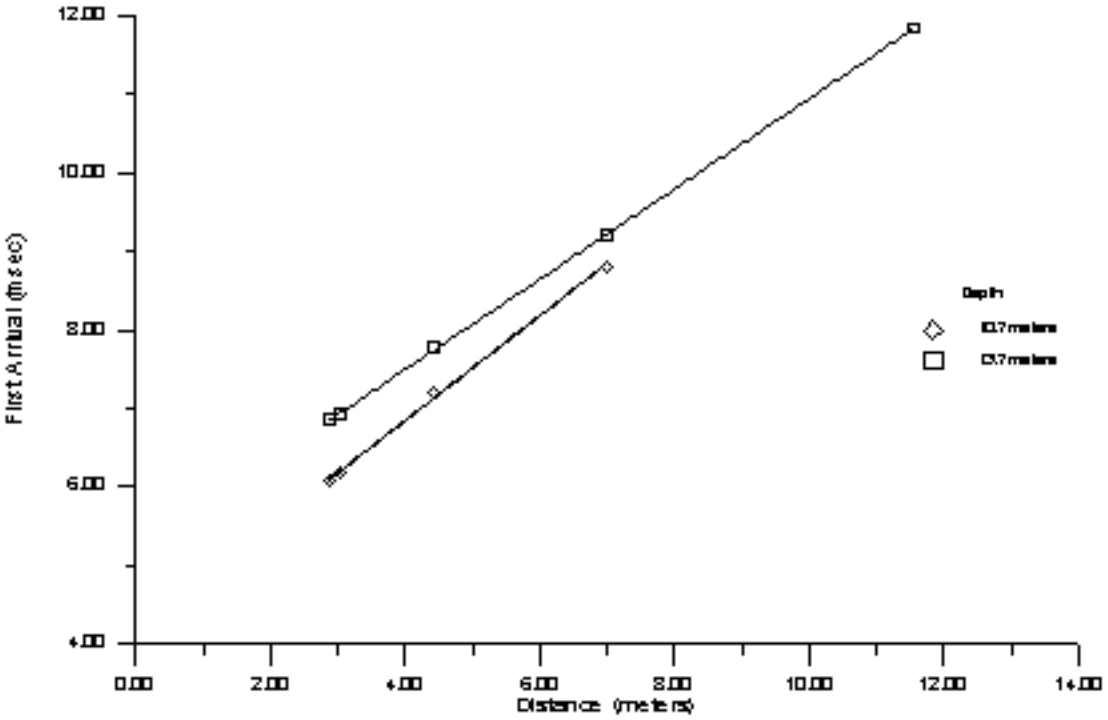

Figure 7.10 First Arrival Times versus Distance from Shaft: Shaft 1

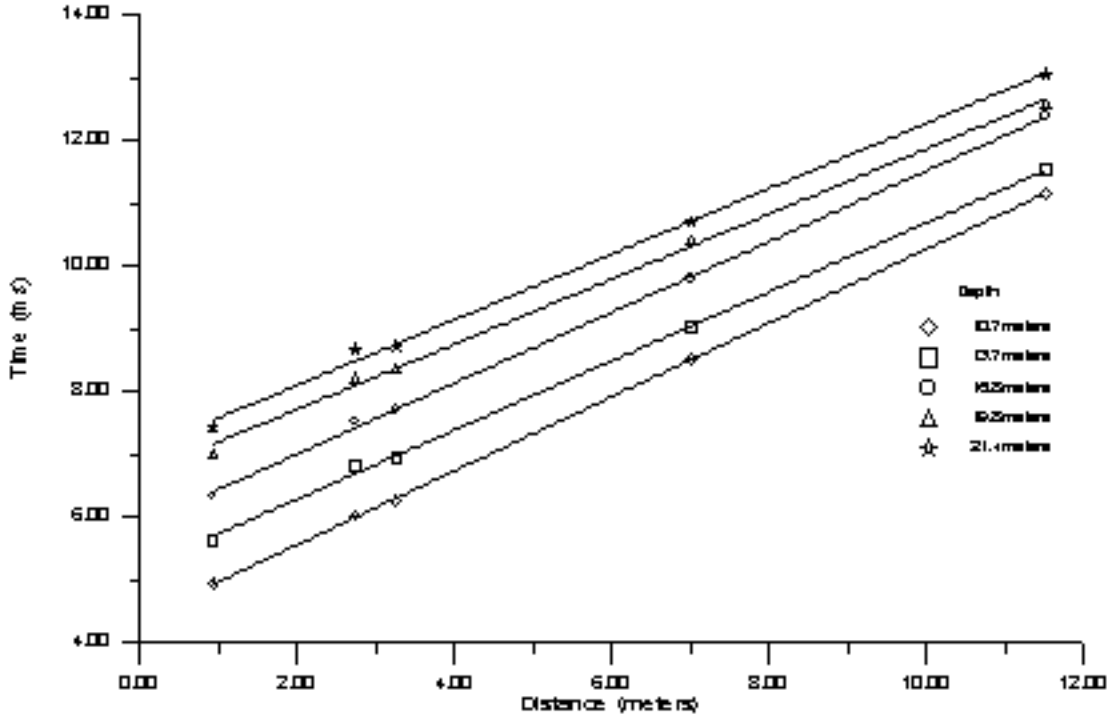

Figure 7.11 First Arrival Times versus Distance from Shaft: Shaft 2

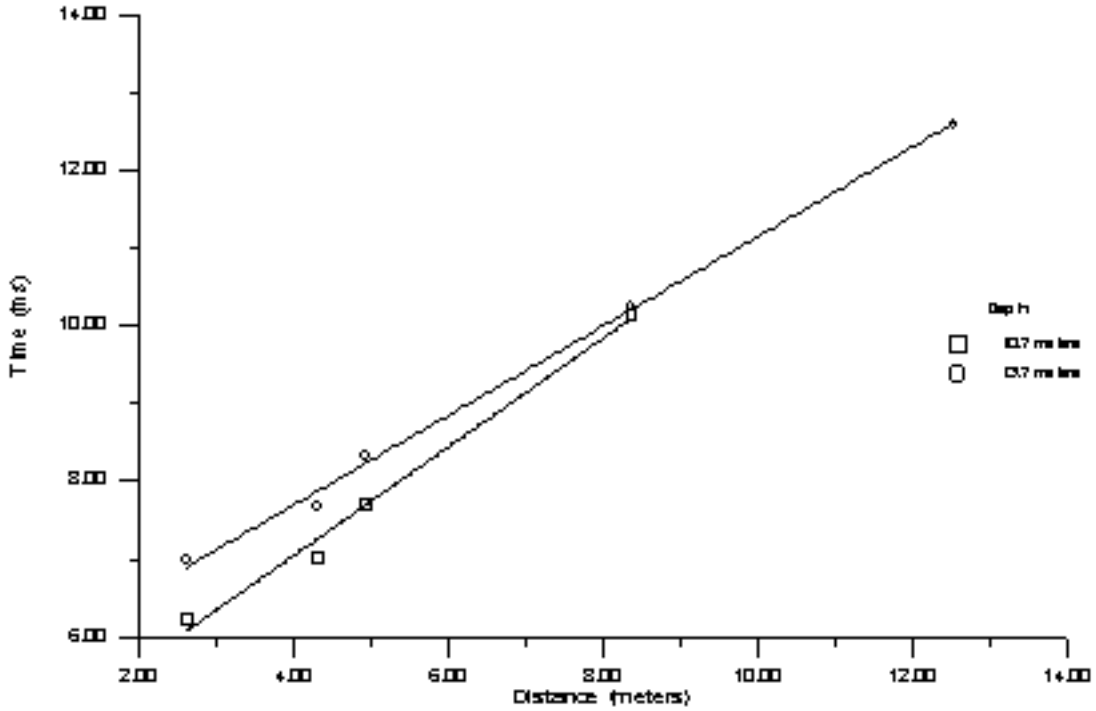

Figure 7.12 First Arrival Times versus Distance from Shaft: Shaft 3

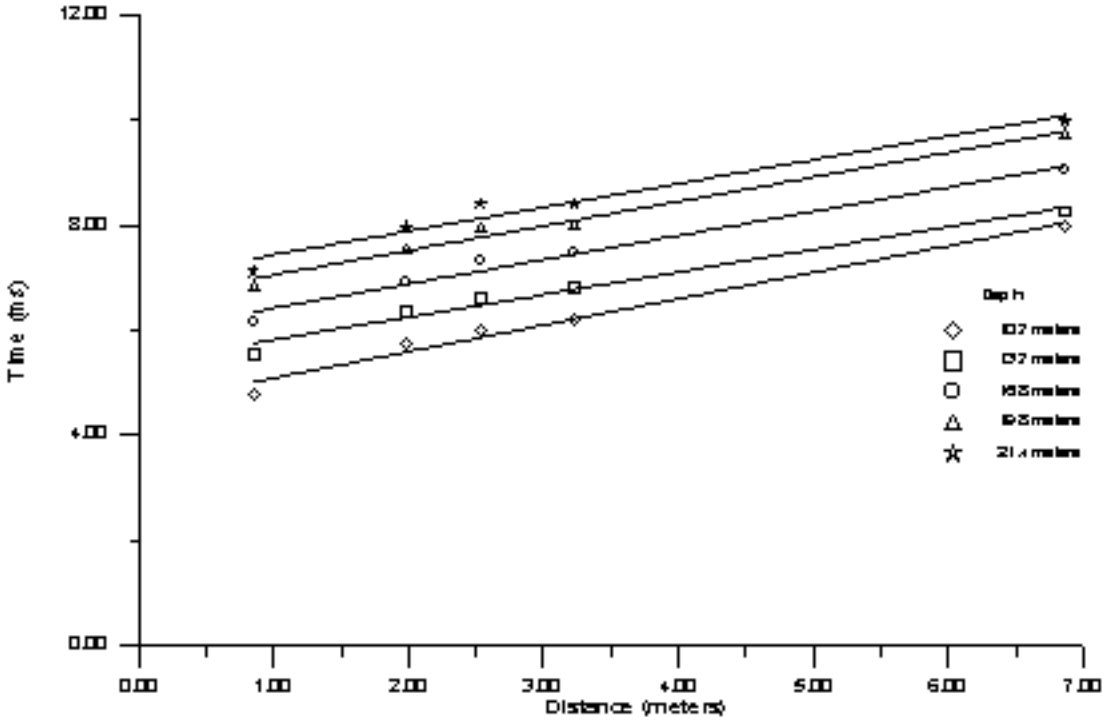

Figure 7.13 First Arrival Times versus Distance from Shaft: Shaft 4

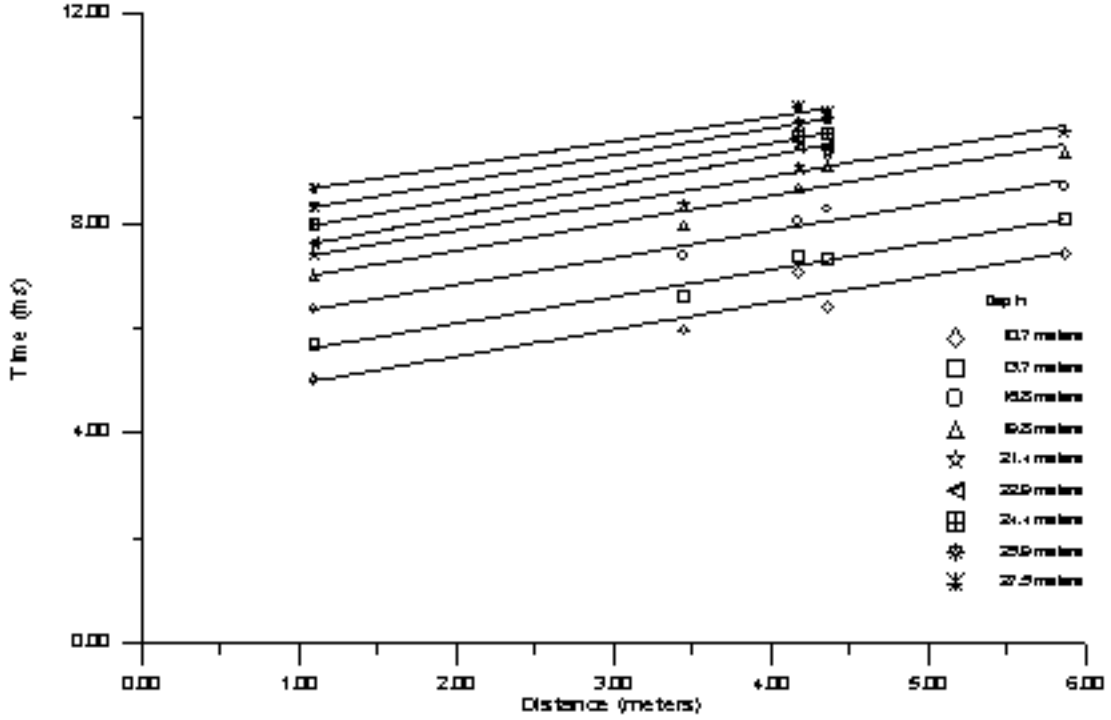

Figure 7.14 First Arrival Times versus Distance from Shaft: Shaft 5

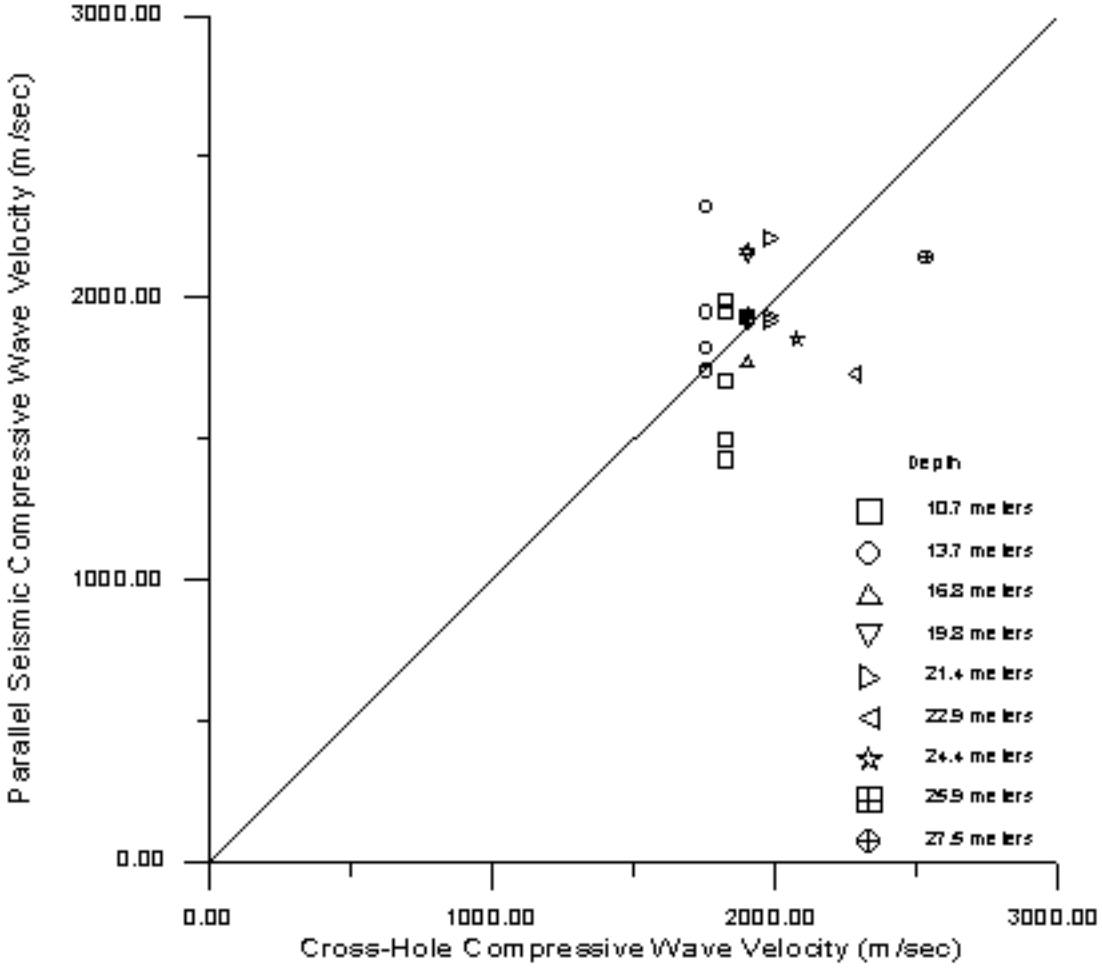

Figure 7.15 Comparison of Compression Wave Velocities from Results of Cross-hole and Parallel Seismic Tests

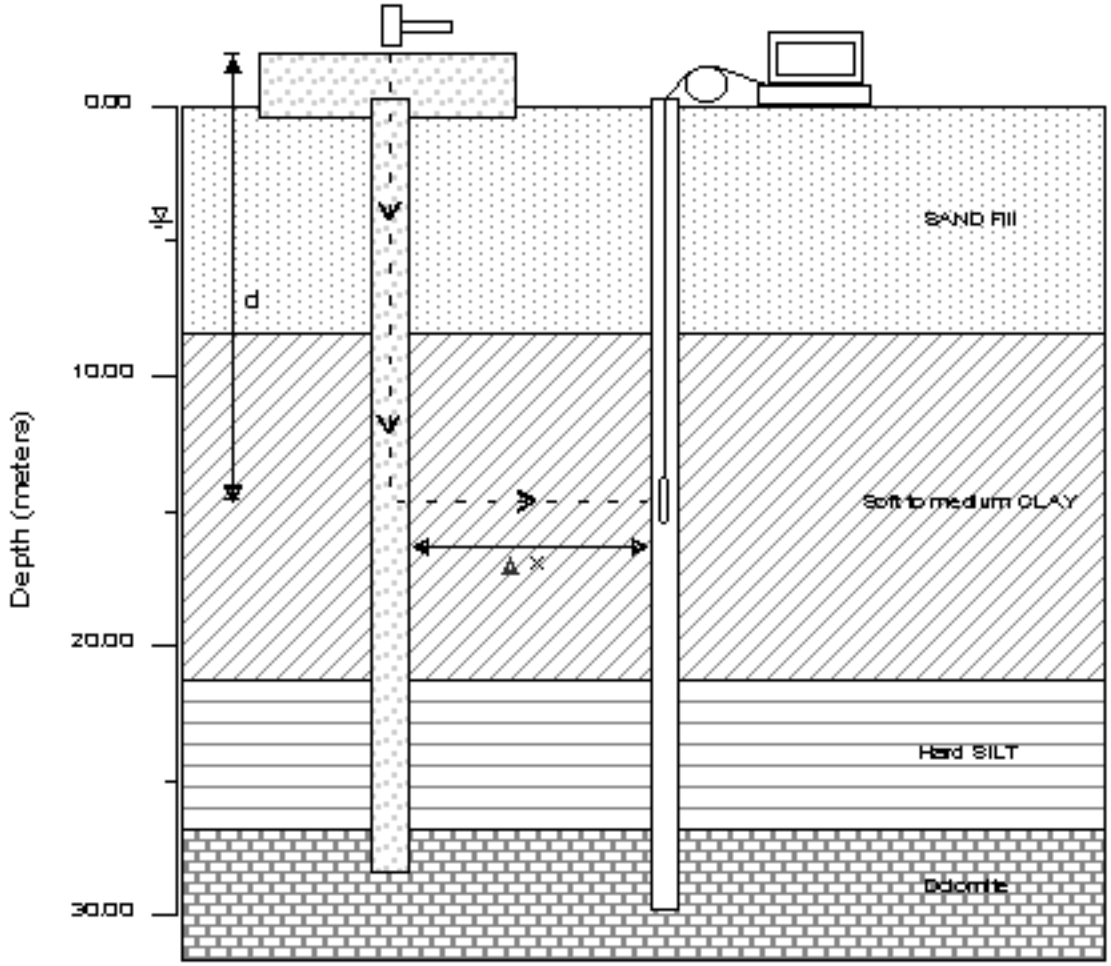

Figure 7.16 Travel Path for Direct Wave

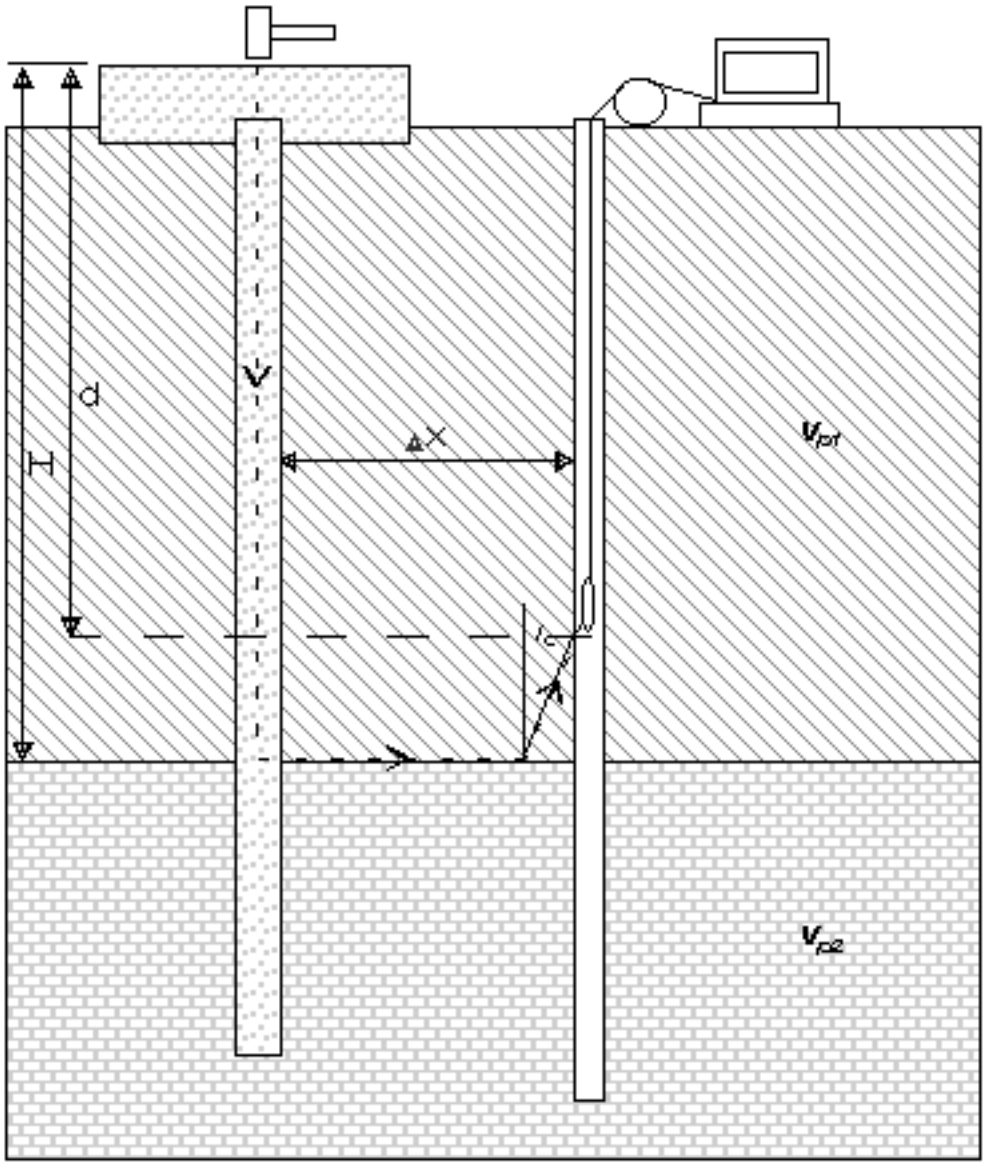

Figure 7.17 Travel Path for Refracted Wave

Table 2.1 Typical Propagation Velocities for Various Materials

Medium	Density, ρ (kg/m^3)	Compression Wave Velocity, V_c (m/s)	Shear Wave Velocity, V_s (m/s)
Air	1.2[a]	340[a]	-
Water	1000[a]	1480[a]	-
Steel	7800[a]	5900[a]	3200[a]
Concrete	2400	3500-4500	2500-3400
Sand	1500-2100[d]	500-2000[b]	100-850[b]
Clay	1700-2000[d]	400-1700[b]	100-800[b]
Limestone	2700	2000-5900[b,c]	1000-3100[b,c]
Granite	2750	2400-5000[b,c]	1200-2500[b,c]

[a]Achenbach, 1975
[b]Dowding, 1996
[c] heavily jointed to non-jointed
[d]Peck, *et. al.*, 1974

Table 2.2 Range of Input Frequencies for Impulse Hammer Tips

Hammer Tip		Range of Frequencies
Stiffness	Color	
Hard	Black	0 to 2000 Hz
Medium	Red	0 to 800 Hz
Soft	Brown	0 to 650 Hz
Very Soft	Grey	0 to 600 Hz

Table 2.3 Analogous Relationships between Mechanical and Electrical Systems (after Richart, *et. al.* (1970))

Mechanical	Electrical
Force = F	Current = I
Velocity = z' = v	Voltage = V
Displacement = z = u	$\int V\,dt$
Acceleration = z" = a	dV / dt
Damping	1/Resistance = 1/R
Spring = k	1/Inductance = 1/L
Mass = m	Capacitance = C

Table 3.1 Field Investigations at the Northwestern NGES

Date	Field Investigation
Pile Load Test Site	
Dec 11, 1987	Soil boring with continuous sampling SPT in sands and alternating 76 and 127 mm (3 and 5 in.) diameter tube samples in clay
Dec 12, 1987	Field vane boring
Mar 25, 1987	Four CPT soundings
Apr 19 & 20, 1988	Four pneumatic piezometers installed within clay stratum
Apr 30, 1988	Soil boring with Menard PMT and SPT tests
May 8, 1988	Piezocone sounding
May 15, 1988	DMT sounding
NDE Test Site	
May 5, 1993	Soil boring with continuous sampling SPT in sands and 76 mm (3 in.) diameter tube samples in clay
Dec 9, 1994	Soil boring with continuous sampling SPT in sands & till and alternating 76 and 127 mm (3 and 5 in.) diameter tube samples in clay
Dec 10, 1994	Cross-hole seismic tests
Aug 12-15, 1996	Nine CPT soundings

Table 3.2 NDE Test Section Details

Shaft	Length, L (m)	Diameter, D (cm)	Cap Height, B (cm)	L/D	B/D	Comments
1	12.2	61.0	61.0	20	1	Soil-filled joint
2	21.3	91.4	61.0	23.3	.67	Reduced cross-section
3	12.2	61.0	152.4	20	2.5	
4	21.3	76.2	91.4	28	1.2	
5	27.5	91.4	91.4	30	1	

Table 3.3 Summary of Casing and Liner Dimensions

Shaft #	Temporary Casing (TC)		Permanent Liner (PL)	
	Diameter[A], D_{TC} (cm)	Length, L_{TC} (m)	Diameter[A], D_{HL} (cm)	Length, L_{HL} (m)
1	91.4	10.29	61.0	10.21
2	121.9	9.75	91.4	9.6
3	91.4	10.29	61.0	10.52
4	106.7	9.75	76.2	10.67
5	121.9	8.84	91.4	11.81

[A]Inner diameter

Table 3.4 Length of Sonic Logging Access Tubes

Access Tube	Depth (m)[A]
Shaft 1	
1N	12.64
1S	12.69
1W	12.75
Shaft 2	
2N	21.74
2E	21.69
2W	21.74

[A]Depth measured from top of pile cap to bottom of tubing

Table 3.5 Spacing between Sonic Logging Access Tubes

Access Tubes	Spacing (m)[A]
Shaft 1	
1N-1S	0.34
1W-1N	0.38
1S-1W	0.25
Shaft 2	
2N-2E	0.61
2E-2W	0.65
2W-2N	0.57

[A]Spacing measured center to center of tubing

Table 3.6. Cased Borehole Dimensions

Borehole	Length (m)	Diameter (cm)
PS1	26.97	5.08
PS2	28.84	10.16
PS3	22.41	5.08
PS4	22.58	5.08
PS5	29.3	10.16

Table 3.7. Dimensions of Pile Caps

Pile Cap	Length (m)	Width (m)	Height (m)	Shafts in Group
1	4.11	1.52	0.61	1 & 2
2	1.52	1.52	1.52	3
3	4.11	2.13	0.91	4 & 5

Table 3.8 Average Density of Concrete Cylinders

Cylinders	Density (kg/m^3)	Std. Dev. (kg/m^3)
Shaft 1	2454	56
Shaft 2	2473	61
Shaft 3	2437	16
Shaft 4	2423	9
Shaft 5	2238	11
Shafts 1-5	2405	98
Shafts 1-4	2450	48
Pile Caps	2390	32

Table 4.1. Summary of Impulse Response Results - Accessible-Head (Day 28)

Shaft No.	L/D ratio	Average Mobility, N $\sqrt{(P_i^* Q_i)}$ (m/s/N E-7)	Theoretical Mobility Range[A] (m/s/N E-7)	Velocity, v_c (m/s)	Resolution P_i/Q_i	Low Strain Stiffness, K' (MN/mm)
1	20	6 (defect) 1.6 (toe)	3.6 - 4.1	3810	9 (defect) 1.2 (toe)	0.57
2	23.3	3 (defect) 1.2 (toe)	1.4 - 1.8	3960	2.8 (defect) 1.3 (toe)	1.57
3	20	3.8	3.6 - 4.1	3810	1.9	0.68
4	28	1.9	2.0 - 2.6	3960	1.2	1.21
5	30	1.4	1.4 - 1.8	3940	1.05	1.65

[A] v_c = 3500 to 4500 m/s ; ρ_c = 2400 kg/m^3

Table 4.2. Summary of Accessible- and Inaccessible-Head Impulse Response Results

Shaft No.	L/D ratio	B/D ratio	Average Mobility, N (m/s/N E-7)			Low Strain Stiffness, K' (MN/mm)	
			Accessible	Inaccessible	Theoretical[a]	Accessible	Inaccessible
1	20	1	6 (defect) 1.6 (toe)	1.0	3.6 - 4.1	0.57	0.9
2	23.3	0.67	3 (defect) 1.2 (toe)	0.7	1.4 - 1.8	1.57	1.83
3	20	2.5	3.8	0.5	3.6 - 4.1	0.68	1.32
4	28	1.2	1.9	0.6	2.0 - 2.63	1.21	1.54
5	30	1	1.4	0.5	1.4 - 1.8	1.65	1.93

[a] v_c = 3500 to 4500 m/s ; ρ_c = 2400 kg/m^3

Table 6.1 Average Soil Parameters for Simulation of NGES Drilled Shafts

Soil Layer		Density kg/m^3	Shear Wave Velocity (m/s)
Sand Fill	0 - 8.8 m	1840	177
Soft to Medium Clay	8.8 - 18 m	2035	222
Clay w/ Gravel	18 - 18.6 m	2035	363
Soft to Medium Clay	18.6 - 21.3 m	2035	247
Hard Till	21.3 - 27.4 m	2245	434

Table 6.2 Summary of Shaft Parameter Changes for "Best Estimate" to "Best Fit" Simulations

Shaft No.	Propagation Velocity, v_c (m/s)			Shaft Diameter, D (m)			Density, ρ_c (kg/m^3)		
	"Best Estimate" Simulation	"Best Fit" Simulation	% Change (+ / -)	"Best Estimate" Simulation	"Best Fit" Simulation	% Change (+ or -)	"Best Estimate" Simulation	"Best Fit" Simulation	% Change (+ / -)
1	3775	3900	3.3				2450	2450	0
liner				0.61	0.64	4.9			
joint	1000	700	-30				2000	2200	10
2	3909	3960	1.3				2450	2450	0
liner				0.91	0.97	6.6			
neck				0.76	0.84	10.5			
				0.76	0.58	-23.7			
overdrill				0.91	1.0	9.9			
3	4006	3950	-1.4				2450	2450	0
liner				0.61	0.64	4.9			
4	4075	4100	0.6				2450	2450	0
liner				0.76	0.81	6.6			
overdrill				0.76	0.86	13.2			
bulge				0.76	0.94	23.7			
5	3653	3950	8.1				2240	2400	7.1
liner				0.91	0.97	6.6			
overdrill				0.91	1.0	9.9			

Table 6.3 Summary of Soil Parameter Changes for "Best Estimate" to "Best Fit" Simulations

Soil Layer	Shear Wave Velocity, v_s (m/s)			Density, ρ_s (kg/m^3)		
	"Best Estimate" Simulation	"Best Fit" Simulation	% Change (+ / -)	"Best Estimate" Simulation	"Best Fit" Simulation	% Change (+ / -)
Sand	177	100 to 115	-44 to -35	1800	1500 to 1550	-17 to -14
Saturated Sand	177	110 to 115	-38 to -35	1840	1550 to 1560	-16 to -15
Soft-Med. Clay	222	170 to 200	-23 to -10	2035	1900 to 2000	-7 to -2
Clay w/ Gravel	363	320	-12	2035	2000	-2
Soft-Med. Clay	247	220	-11	2035	2000	-2
Glacial Till	434	375	-14	2245	2150	-4

Table 6.4 Summary of "Best Estimate" and "Best Fit" Simulated and Experimental Mobility Results

Shaft No.	Average Mobility, N √(PQ) (m/s/N E-7)			Resolution P/Q			Low-Strain Stiffness, K' (MN/mm)		
	Experimental	"Best Estimate" Simulation	"Best Fit" Simulation	Experimental	"Best Estimate" Simulation	"Best Fit" Simulation	Experimental	"Best Estimate" Simulation	"Best Fit" Simulation
1 toe	1.6	3.2	1.9	1.2	1.06	1.17	0.57	0.95	0.59
defect	6	4.6	6	9	2.5	8			
2 toe	1.2	1.6	1.2	1.3	1.08	1.26	1.57	1.73	1.35
defect	3	3	3	2.8	1.7	2.9			
3	3.8	3.7	3.7	1.9	1.24	1.9	0.68	1.09	0.66
4	1.9	2.3	2.1	1.2	1.04	1.2	1.21	1.64	1.21
5	1.4	1.9	1.5	1.05	1.0	1.05	1.65	1.77	1.46

Table 6.5 Summary of Resolution for Accessible-Head Impulse Response Tests

Shaft No.	L/D ratio	Resolution P_i/Q_i
1 toe	20	1.2
defect	7.2	9
2 toe	23.3	1.3
defect	4.9	2.8
3	20	1.9
4	28	1.2
5	30	1.05

Table 6.6 Overconsolidation Ratio Exponent, K
(after Hardin and Drnevich, 1972).

PlasticityIndex	K
0	0
20	0.18
40	0.30
60	0.41
80	0.48
≥100	0.50

Table 6.7 Constant K_2 as a Function of Void Ratio or Relative Density (after Seed and Idriss, 1970).

Void Ratio, e	K_2	Relative Density, D_r(%)	K_2
0.4	70	90	70
0.5	60	75	61
0.6	51	60	52
0.7	45	45	42
0.8	39	40	40
0.9	33	30	33

Table 6.8 Resolution Prediction from Two Layer Resolution Charts

Shaft No.	Experimental P/Q	Predicted P/Q from Two Layer Resolution Charts	
		"Best Estimate" Parameters	"Best Fit" Parameters
3	1.9	1.23	1.87
4	1.2	1.03	1.12
5	1.05	1.00	1.03

Table 6.9 "Cutoff" Frequencies for Inaccessible Head Tests

Shaft No.	Cutoff Frequency (Hz)
1	460
2	520
3	630
4	440
5	460

Table 6.10 Cutoff Frequencies from Experimental and Empirical Methods

Shaft	B/D	D (m)	A_{eff} (m^2)	α_s	α_t	v_c (m/s)	f_c (Hz)
1	1.0	0.61	4.11	14.05	2	3876	396
2	0.67	0.91	4.11	6.31	1.67	3960	545
3	2.5	0.61	2.34	8.01	3.5	3950	563
4	1.2	0.76	5.27	11.61	2.2	4100	391
5	1.0	0.91	5.27	8.1	2	3950	430

Table 6.11 Parameter Effects for Achieving "Best Fit" Simulations

Parameter	Effect
Propagation Velocity, v_c	Align Peaks, Match Mobility
Concrete Density, ρ_c	Match Mobility
Shaft Diameter, D	Match Mobility
Soil Shear Wave Velocity, v_s	Resolution, Low-Strain Stiffness
Soil Density, ρ_s	Resolution, Low-Strain Stiffness

Table 7.1 Distance between Drilled Shafts and Access Holes (m)

Shaft No.	Access Hole 1	Access Hole 2	Access Hole 3	Access Hole 4	Access Hole 5
1	2.87	6.99	3.05	4.42	11.56
2	2.75	6.99	0.92	3.25	11.54
3	4.93	8.36	2.62	4.32	12.53
4	1.98	2.54	3.23	0.84	6.86
5	4.37	1.09	5.85	3.43	4.17

Table 7.2 Summary of Results within 3 m of a Drilled Shaft

Test No.	Depth (m)	Depth: Slope Change (m)	Depth: Amplitude Change (m)	Access Hole Depth below Bottom of Shaft (m)
1-1	12.68	13.5	13 ± 0.25	14
2-1	21.82	n.i.	22 ± 0.25	2
2-3	21.82	n.i.	21.75 ± 0.25	0.5
3-3	12.91	13.5	13.75 ± 0.25	9.5
4-1	21.95	n.i.	22.5 ± 0.5	5.5
4-2	21.95	n.i.	22 ± 0.25	5.5
4-4	21.95	n.i.	21.75 ± 0.25	1
5-2	28.08	n.i.	27.75 ± 0.5	2

Note: n.i.: not identifiable with this method of analysis

Table 7.3 Summary of Propagation Velocities in Concrete (m/s)

Shaft No.	Access Hole 1	Access Hole 2	Access Hole 3	Access Hole 4	Access Hole 5
1	4160	6350	5080	5160	n/a
2	3990	4510	4140	4070	3890
3	4950	n/a	5080	4070	n/a
4	4770	4510	4770	4660	4300
5	4610	4420	4450	4450	4420

Note: n.a.: not applicable because first arrival times did not form a straight line in depths adjacent to drilled shaft below the bottom of the permanent casing.

Table 7.4 Compression Wave Velocities from Parallel Seismic and Cross-Hole Seismic Tests

Depth (m)	Cross-Hole Seismic P-Wave (m/s)	Shaft 1		Shaft 2		Shaft 3		Shaft 4		Shaft 5	
		Velocity (m/s)	r^2	Velocity (m/s)	r^2	Velocity (m/s)	r^2	Velocity (m/s)	r^2	Velocity (m/s)	r^2
10.7	1830	1500	.998	1700	.999	1430	.990	1980	.979	1950	.899
13.7	1760	1740	.999	1820	.999	1300	.997	2320	.975	1950	.977
16.8	1910	n.a.		1770	.999	n.a.		2170	.984	1950	.968
19.8	1910	n.a.		1930	.998	n.a.		2150	.986	1910	.931
21.3	1920	n.a.		1920	.997	n.a.		2210	.963	1930	.956
22.9	2290	n.a.		n.a.		n.a.		n.a.		1730	.998
24.4	2080	n.a.		n.a.		n.a.		n.a.		1850	.999
25.9	1910	n.a.		n.a.		n.a.		n.a.		1930	.999
27.4	2540	n.a.		n.a.		n.a.		n.a.		2140	.988

Note: n.a.: data not applicable since hydrophone is below bottom of shaft.

$$v_R = \frac{0.862 + 1.14\nu}{1 + \nu} v_s \qquad (2.5)$$

$$v_p = \sqrt{\frac{E(1-\nu)}{\rho(1+\nu)(1-2\nu)}} \qquad (2.2)$$

$$v_c = v_{bar} = \sqrt{\frac{E}{\rho}} \qquad (2.6)$$

$$\frac{A_R}{A_I} = \left[\frac{Z_2 - Z_1}{Z_2 + Z_1} \right] = \left[\frac{\rho_2 v_{p2} - \rho_1 v_{p1}}{\rho_2 v_{p2} + \rho_1 v_{p1}} \right] \qquad (2.11)$$

$$K' = \frac{2\pi f_m}{V/F_m} \qquad (2.17)$$

$$K_{max} = \frac{AE}{L}\sqrt{\frac{P}{Q}}\coth^{-1}\sqrt{\frac{P}{Q}} \quad ; \quad K_{min} = \frac{AE}{L}\sqrt{\frac{Q}{P}}\coth^{-1}\sqrt{\frac{P}{Q}} \qquad (2.18)$$

$$L = \frac{\nu_c}{2\Delta f} \qquad (2.16)$$

$$N = \frac{1}{\rho_c v_c A} \qquad (2.19)$$

$$\frac{P_i}{Q_i} = cth^2\left(\frac{2\pi \cdot r \cdot L\sqrt{G \cdot \rho_s}}{2\sqrt{\frac{E \cdot A}{L} \cdot \rho_c \cdot A \cdot L}}\right)$$

$$= cth^2\left(\pi \cdot r \cdot L\sqrt{\frac{G \cdot \rho_s}{E \cdot A^2 \cdot \rho_c}}\right) \qquad (2.29)$$

$$= cth^2\left(\frac{L}{r}\sqrt{\frac{\nu_s^2 \cdot \rho_s \cdot \rho_s}{\nu_c^2 \cdot \rho_c \cdot \rho_c}}\right)$$

$$= cth^2\left(\frac{L}{r} \cdot \frac{\nu_s}{\nu_c} \cdot \frac{\rho_s}{\rho_c}\right)$$

$$v_s = \sqrt{\frac{G}{\rho}} \qquad (2.3)$$

$$f_c = \frac{\nu_c}{\lambda_c} = \frac{\nu_c}{D_{dl}} = \frac{\nu_c}{D(\alpha_s + \alpha)} \qquad (6.6)$$

$$t_R = \frac{H}{v_{conc}} + \frac{\Delta x - (H-d)(\tan i_c)}{v_R} + \frac{H-d}{v_R \cos i_c} \qquad (7.2)$$

$$t_{\bar{d}} \frac{d}{v_{conc}} + \frac{\Delta x}{v_p} \qquad (7.1)$$

$$t_R = \frac{H}{v_{conc}} + \frac{\Delta x}{v_{EI}} + \left[\frac{1}{v_{EI}\cos i_c} - \frac{\tan i_c}{v_{EI}}\right](H-d) \qquad (7.5)$$

Table A-1 Accessible-Head Testing Schedule for Shaft 1

File Name	Test Date	Concrete Age (days)
LF1X1A	9/6/94	4
LF1X1B	9/6/94	4
LF1X1C	9/6/94	4
LF1Y1A	9/6/94	4
LF1Y1B	9/6/94	4
LF1Y1C	9/6/94	4
LF1X2A	9/7/94	5
LF1X2B	9/7/94	5
LF1Y2A	9/7/94	5
LF1Y2B	9/7/94	5
LF1Y2C	9/7/94	5
LF1X3A	9/8/94	6
LF1X3B	9/8/94	6
LF1Y3A	9/8/94	6
LF1Y3B	9/8/94	6
LF1X7A	9/9/94	7
LF1X13A	9/15/94	13
LF1X13B	9/15/94	13
LF1Y13A	9/15/94	13
LF1Y13B	9/15/94	13
LF1X14A	9/16/94	14
LF1X14B	9/16/94	14
LF1Y14A	9/16/94	14
LF1Y14B	9/16/94	14
NWU1_28	9/26/94	24
LF1X28A	9/29/94	27
LF1Y28A	9/29/94	27
LF1XE	10/6/94	34
LF1XE2	10/6/94	34
LF1XR	10/6/94	34
LF1XR2	10/6/94	34
LF1BLA	10/16/94	44
LF1BRO	10/16/94	44
LF1GRY	10/16/94	44
LF1RED	10/16/94	44
POW1	10/26/94	54
GEN1	10/26/94	54

POW1	10/26/94	54
GEN1	10/26/94	54

Table A-2 Accessible-Head Testing Schedule for Shaft 2

File Name	Test Date	Concrete Age (days)
LF2X1A	09/03/94	1
LF2X1B	09/03/94	1
LF2Y1A	09/03/94	1
LF2Y1B	09/03/94	1
LF2X2A	09/04/94	2
LF2X2B	09/04/94	2
LF2Y2A	09/04/94	2
LF2Y2B	09/04/94	2
LF2X3A	09/05/94	3
LF2X3B	09/05/94	3
LF2Y3A	09/05/94	3
LF2Y3B	09/05/94	3
LF2X4A	09/06/94	4
LF2X4B	09/06/94	4
LF2Y4A	09/06/94	4
LF2Y4B	09/06/94	4
LF2X5A	09/07/94	5
LF2X5B	09/07/94	5
LF2Y5A	09/07/94	5
LF2Y5B	09/07/94	5
LF2X6A	09/08/94	6
LF2X6B	09/08/94	6
LF2Y6A	09/08/94	6
LF2Y6B	09/08/94	6
LF2Z7A	09/09/94	7
LF2X13A	09/15/94	13
LF2X13B	09/15/94	13
LF2Y13A	09/15/94	13
LF2Y13B	09/15/94	13
LF2X14A	09/16/94	14
LF2X14B	09/16/94	14
LF2Y14A	09/16/94	14
LF2Y14B	09/16/94	14
NWU2_28	09/26/94	24
LF2X28A	09/29/94	27
LF2Y28A	09/29/94	27
LF2XE	10/06/94	34
LF2XE2	10/06/94	34
LF2XR	10/06/94	34
LF2XR2	10/06/94	34
LF2BLA	10/16/94	44
LF2BRO	10/16/94	44
LF2GRY	10/16/94	44
LF2RED	10/16/94	44
[illegible]	[illegible]	54

LF2BLA	10/16/94	44
LF2BRO	10/16/94	44
LF2GRY	10/16/94	44
LF2RED	10/16/94	44
POW2	10/26/94	54
GEN2	10/26/94	54

Table A-3 Accessible-Head Testing Schedule for Shaft 3

File Name	Test Date	Concrete Age (days)
LF3X1A	09/01/94	1
LF3X1B	09/01/94	1
LF3Y1A	09/01/94	1
LF3Y1B	09/01/94	1
LF3X2A	09/02/94	2
LF3X2B	09/02/94	2
LF3Y2B	09/02/94	2
LF3X3A	09/03/94	3
LF3X3B	09/03/94	3
LF3Y3A	09/03/94	3
LF3Y3B	09/03/94	3
LF3X4A	09/04/94	4
LF3X4B	09/04/94	4
LF3Y4A	09/04/94	4
LF3Y4B	09/04/94	4
LF3X5A	09/05/94	5
LF3X5B	09/05/94	5
LF3Y5A	09/05/94	5
LF3Y5B	09/05/94	5
LF3X6A	09/06/94	6
LF3X6B	09/06/94	6
LF3Y6A	09/06/94	6
LF3Y6B	09/06/94	6
LF3X7A	09/07/94	7
LF3X7B	09/07/94	7
LF3Y7A	09/07/94	7
LF3Y7B	09/07/94	7
LF3X8A	09/08/94	8
LF3X8B	09/08/94	8
LF3Y8A	09/08/94	8
LF3Y8B	09/08/94	8
LF3Z9A	09/09/94	9
LF3X14A	09/14/94	14
LF3X14B	09/14/94	14
LF3Y14A	09/14/94	14
LF3Y14B	09/14/94	14
NWU3_28	09/26/94	26
LF3X28A	09/29/94	29
LF3X28B	09/29/94	29
LF3Y2A	09/29/94	29
LF3XE	10/06/94	36
LF3XE2	10/06/94	36
LF3XR	10/06/94	36
LF3XR2	10/06/94	36
LF3BLA	10/16/94	46
LF3BRO	10/16/94	46
LF3RED	10/16/94	46
LF3GRY	10/16/94	46
POW3	10/26/94	56

LF3XR2	10/16/94	46
LF3BLA	10/16/94	46
LF3BRO	10/16/94	46
LF3RED	10/16/94	46
LF3GRY	10/16/94	46
POW3	10/26/94	56
GEN3	10/26/94	56

Table A-4 Accessible-Head Testing Schedule for Shaft 4

File Name	Test Date	Concrete Age (days)
LF41A	09/01/94	1
LF41B	09/01/94	1
LF4Y1A	09/01/94	1
LF4Y1B	09/01/94	1
LF4X2A	09/02/94	2
LF4X2B	09/02/94	2
LF4Y2A	09/02/94	2
LF4X3A	09/03/94	3
LF4X3B	09/03/94	3
LF4Y3A	09/03/94	3
LF4Y3B	09/03/94	3
LF4X4A	09/04/94	4
LF4X4B	09/04/94	4
LF4Y4A	09/04/94	4
LF4Y4B	09/04/94	4
LF4X5A	09/05/94	5
LF4X5B	09/05/94	5
LF4Y5A	09/05/94	5
LF4Y5B	09/05/94	5
LF4X6A	09/06/94	6
LF4X6B	09/06/94	6
LF4Y6A	09/06/94	6
LF4Y6B	09/06/94	6
LF4X7A	09/07/94	7
LF4X7Y	09/07/94	7
LF4Y7A	09/07/94	7
LF4Y7B	09/07/94	7
LF4X8A	09/08/94	8
LF4X8B	09/08/94	8
LF4Y8A	09/08/94	8
LF4X14A	09/14/94	14
LF4X14B	09/14/94	14
LF4Y14A	09/14/94	14
LF4Y14B	09/14/94	14
LF4X15A	09/15/94	15
LF4Y15A	09/15/94	15
NWU4_28	09/25/94	25
LF4X28A	09/28/94	28
LF4X28B	09/28/94	28
LF4Y28A	09/28/94	28
LF4XE	10/06/94	36
LF4XE2	10/06/94	36
LF4XR	10/06/94	36
LF4XR2	10/06/94	36
LF4BLA	10/16/94	46
LF4BRO	10/16/94	46
LF4GRY	10/16/94	46
LF4RED	10/16/94	46

LF4XR2	10/06/94	36
LF4BLA	10/16/94	46
LF4BRO	10/16/94	46
LF4GRY	10/16/94	46
LF4RED	10/16/94	46
GEN4	10/26/94	55
POW4	10/26/94	55

Table A-5 Accessible-Head Testing Schedule for Shaft 5

File Name	Test Date	Concrete Age (days)
LF5X1A	9/1/94	0
LF5X1B	9/1/94	0
LF5Y1A	9/1/94	0
LF5Y1B	9/1/94	0
LF5X2A	9/2/94	1
LF5X2B	9/2/94	1
LF5Y2A	9/2/94	1
LF5Y2B	9/2/94	1
LF5X3A	9/3/94	2
LF5X3B	9/3/94	2
LF5Y3A	9/3/94	2
LF5Y3B	9/3/94	2
LF5X4A	9/4/94	3
LF5X4B	9/4/94	3
LF5Y4A	9/4/94	3
LF5Y4B	9/4/94	3
LF5X5A	9/5/94	4
LF5X5B	9/5/94	4
LF5Y5A	9/5/94	4
LF5X5B	9/5/94	4
LF5X6A	9/6/94	5
LF5X6B	9/6/94	5
LF5Y6A	9/6/94	5
LF5X7A	9/7/94	6
LF5X7B	9/7/94	6
LF5Y7A	9/7/94	6
LF5Y7B	9/7/94	6
LF5X8A	9/8/94	7
LF5X8B	9/8/94	7
LF5Y8A	9/8/94	7
LF5Y8B	9/8/94	7
LF5X13A	9/14/94	13
LF5X13B	9/14/94	13
LF5Y13A	9/14/94	13
LF5Y13B	9/14/94	13
LF5X14A	9/15/94	14
LF5X14B	9/15/94	14
LF5Y14A	9/15/94	14
LF5Y14B	9/15/94	14
LF5Y14C	9/15/94	14
NWU5_28	9/26/94	25
LF5X28A	9/29/94	28
LF5X28B	9/29/94	28
LF5y28A	9/29/94	28
LF5XE	10/6/94	35
LF5XE2	10/6/94	35
LF5XR	10/6/94	35
LF5XR2	10/6/94	35
LF5BLA	10/16/94	45
LF5BRO	10/16/94	45

LF5XE2	10/6/94	35
LF5XR	10/6/94	35
LF5XR2	10/6/94	35
LF5BLA	10/16/94	45
LF5BRO	10/16/94	45
LF5GRY	10/16/94	45
LF5RED	10/16/94	45
GEN5	10/26/94	55

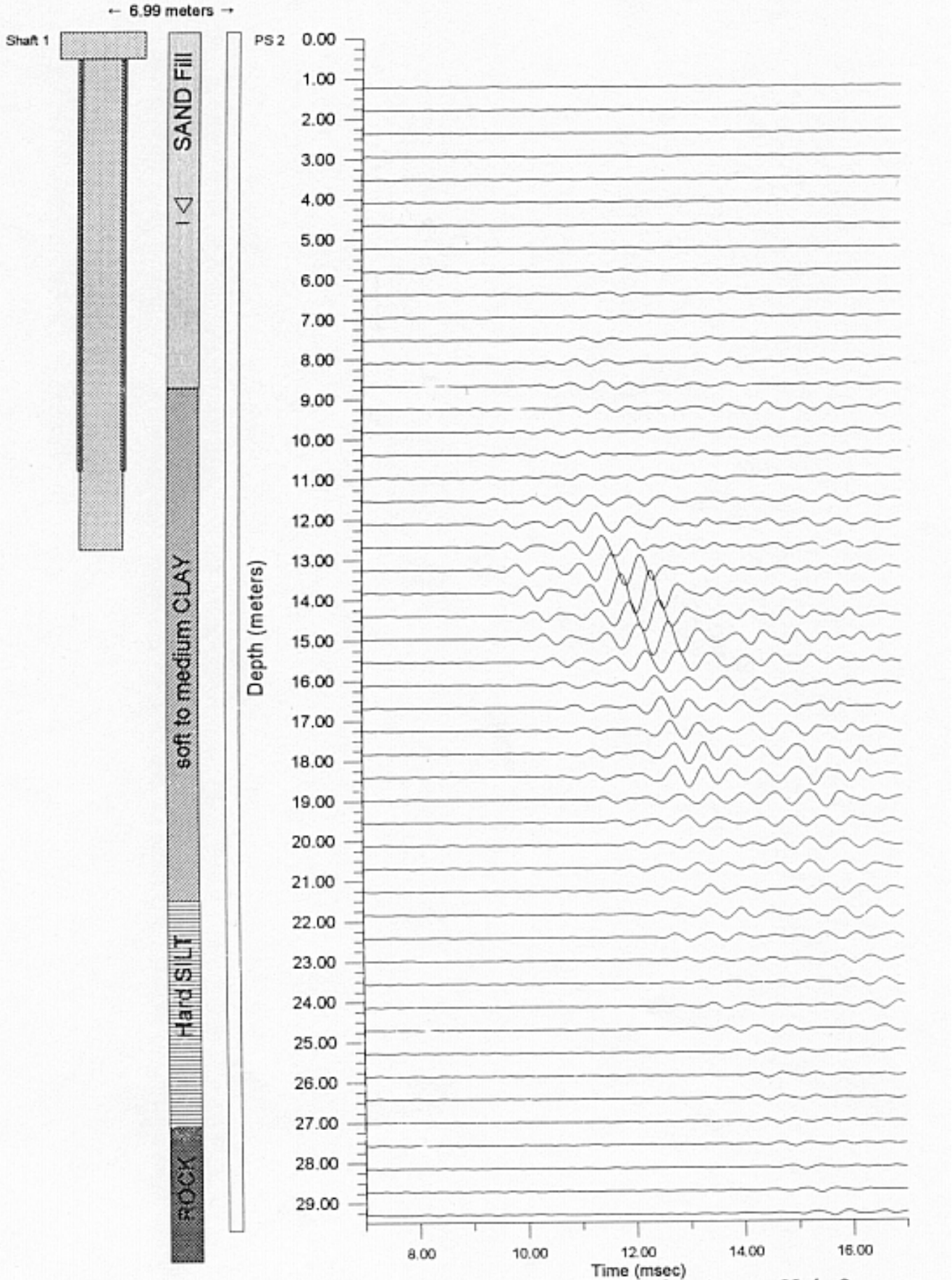

Figure B-1 Compiled Parallel Seismic Profile: Shaft 1 Access Hole 2

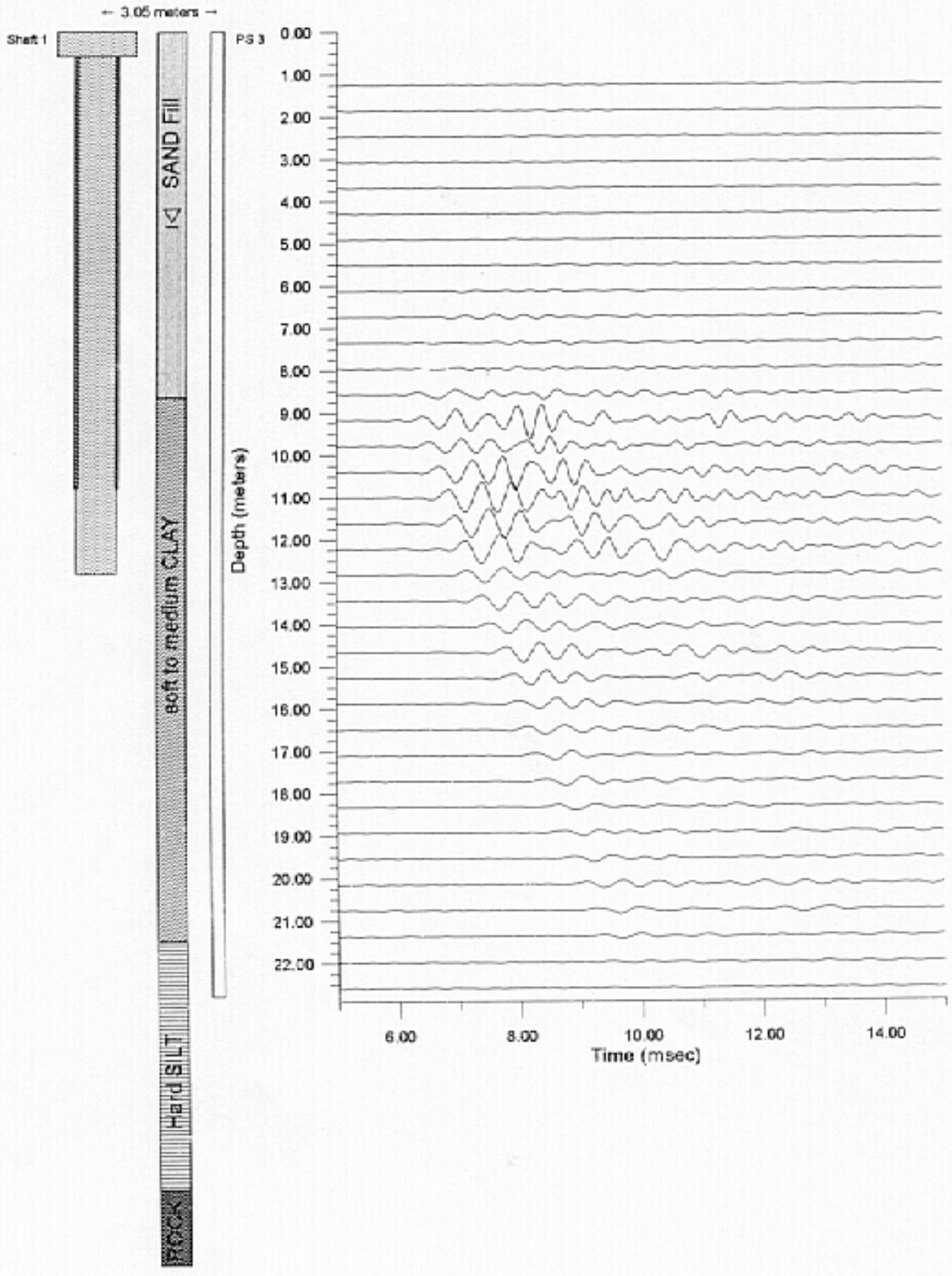

Figure B-2 Compiled Parallel Seismic Profile: Shaft 1 Access Hole 3

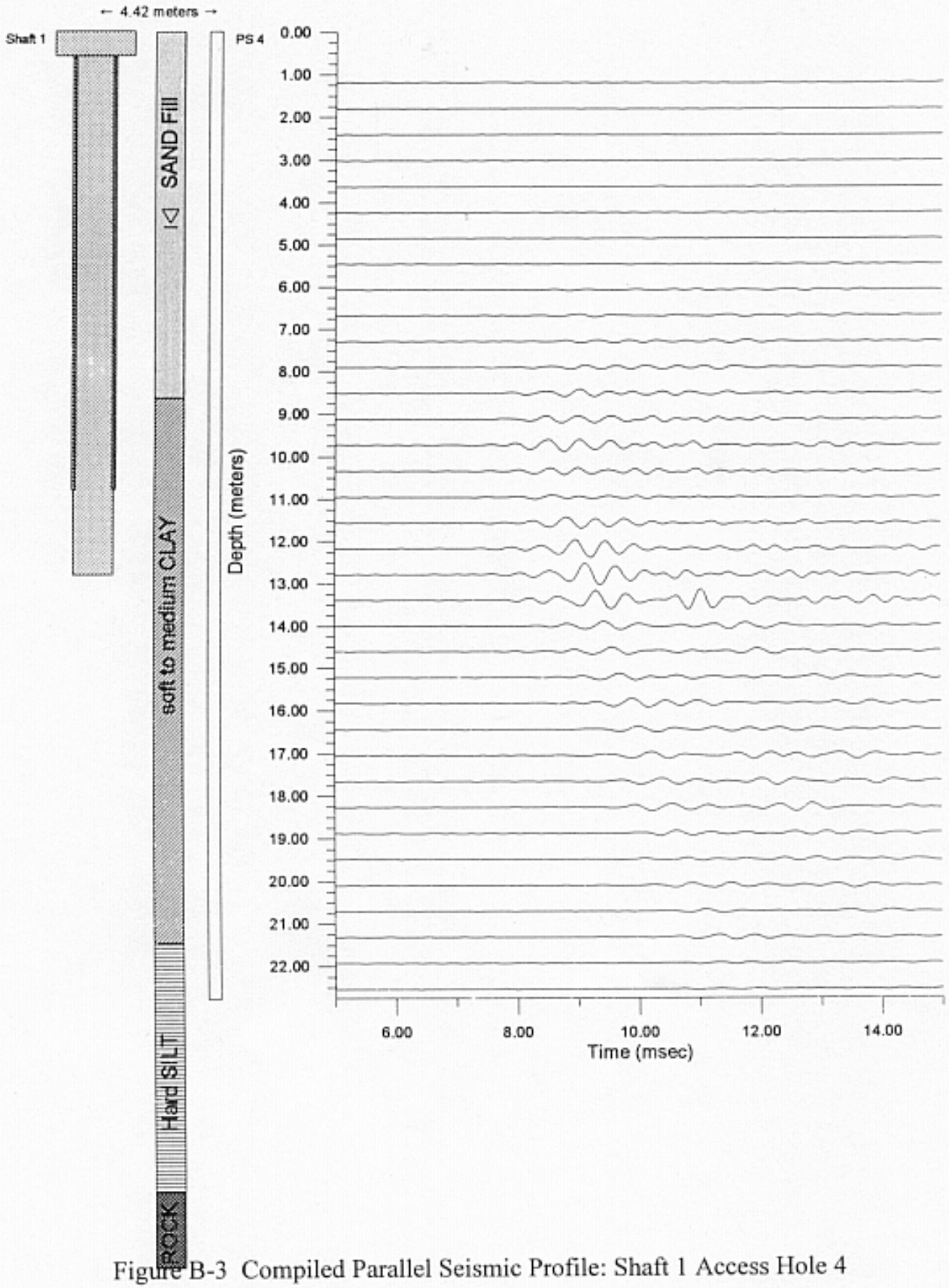

Figure B-3 Compiled Parallel Seismic Profile: Shaft 1 Access Hole 4

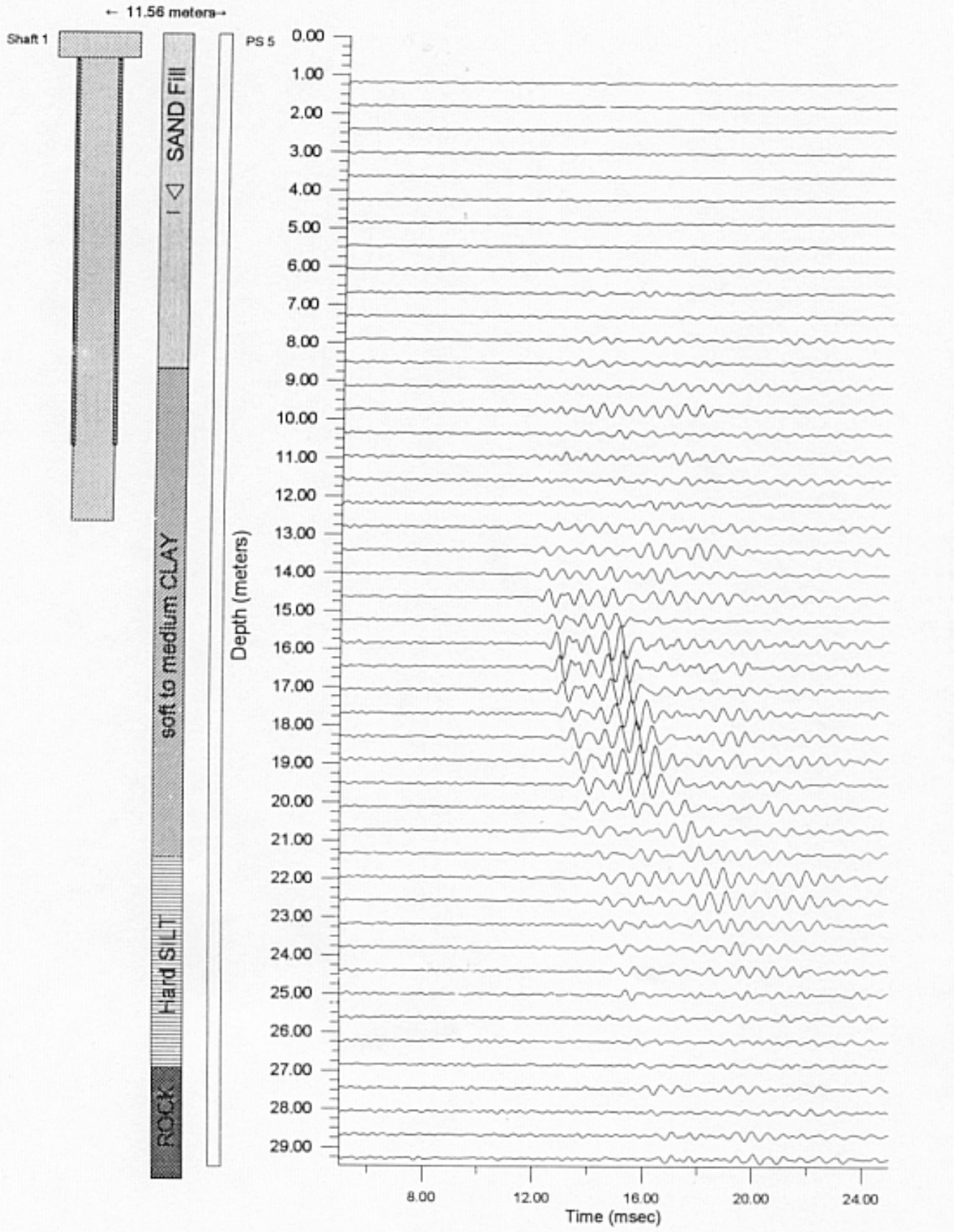

Figure B-4 Compiled Parallel Seismic Profile: Shaft 1 Access Hole 5

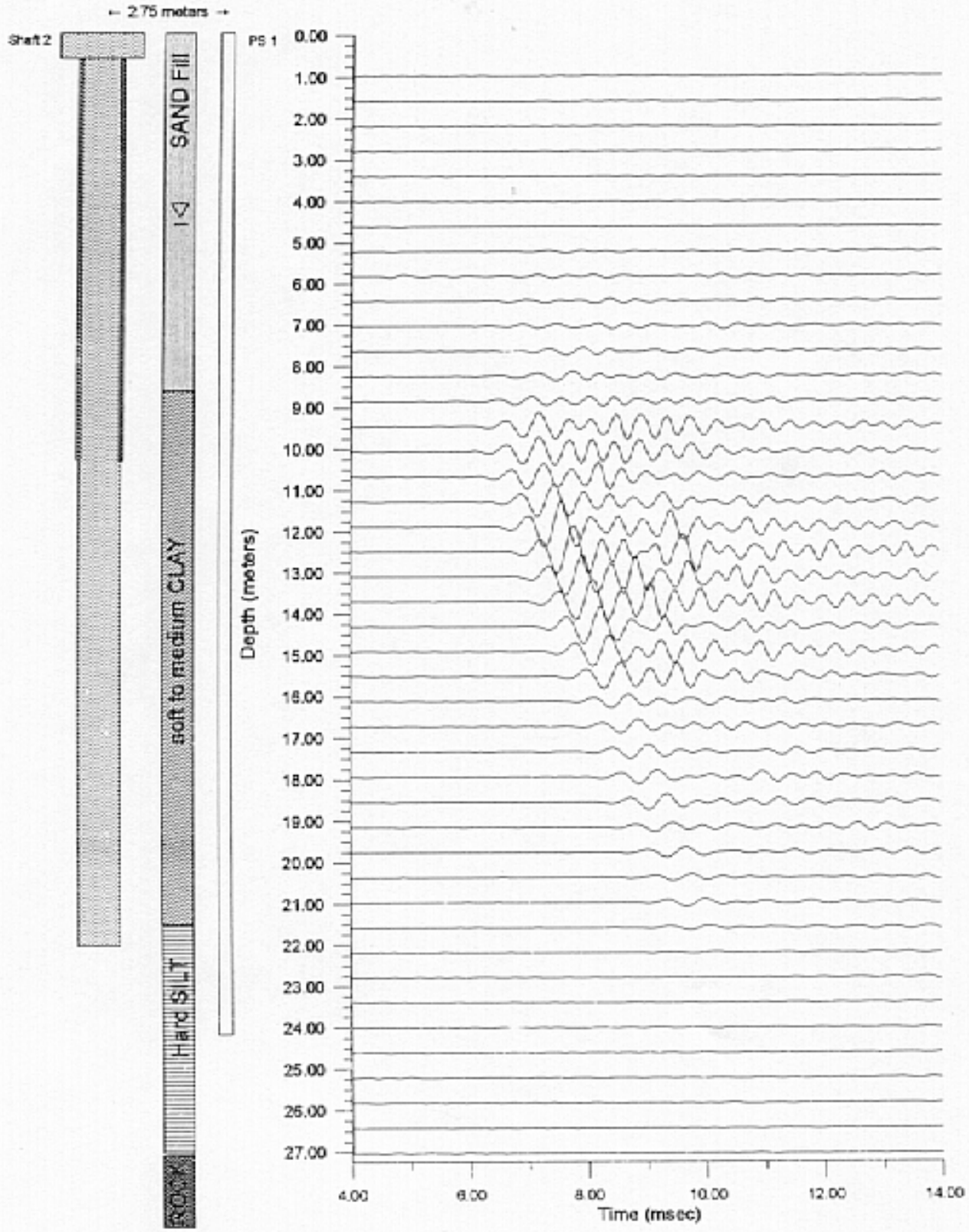

Figure B-5 Compiled Parallel Seismic Profile: Shaft 2 Access Hole 1

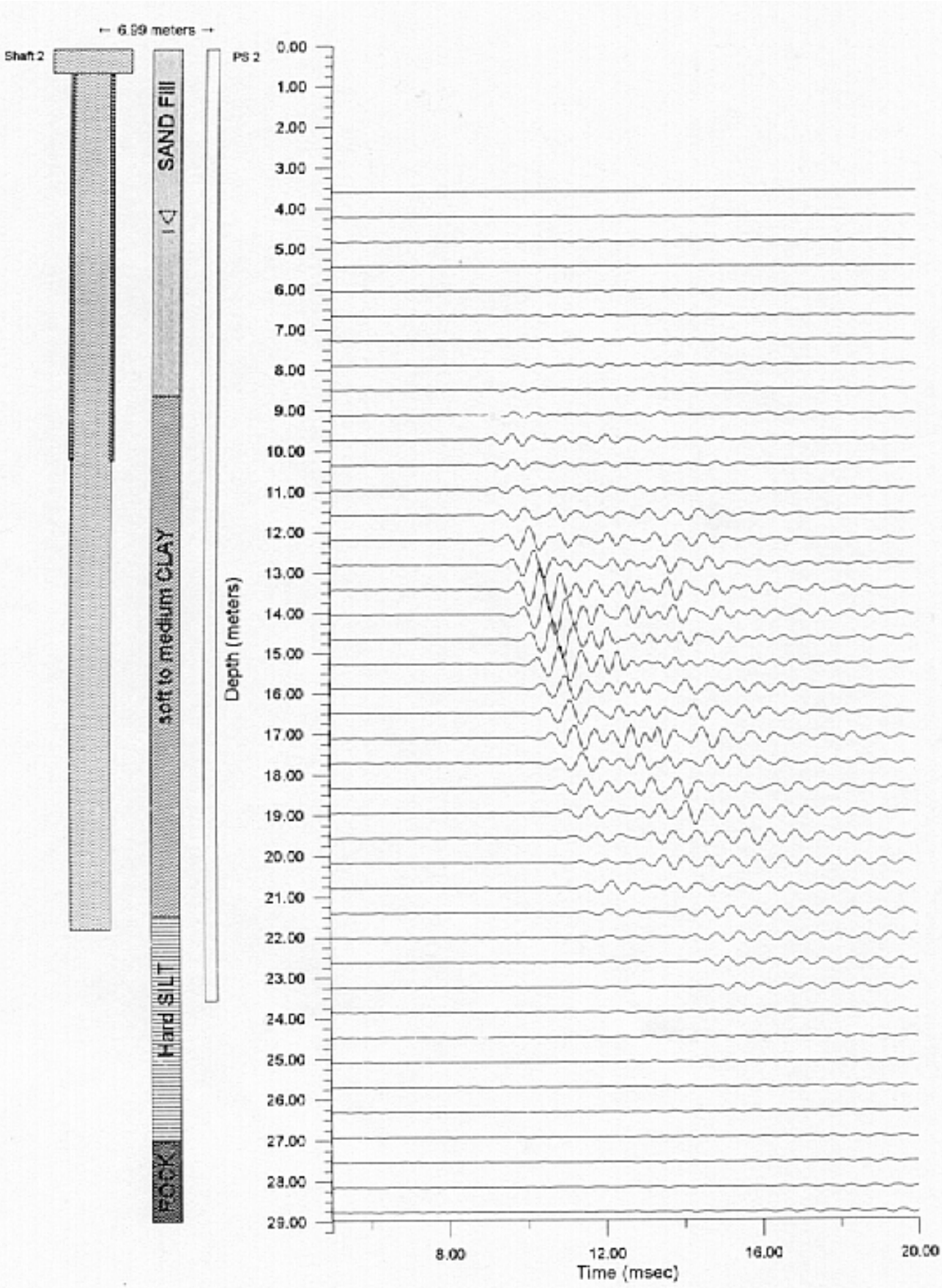

Figure B-6 Compiled Parallel Seismic Profile: Shaft 2 Access Hole 2

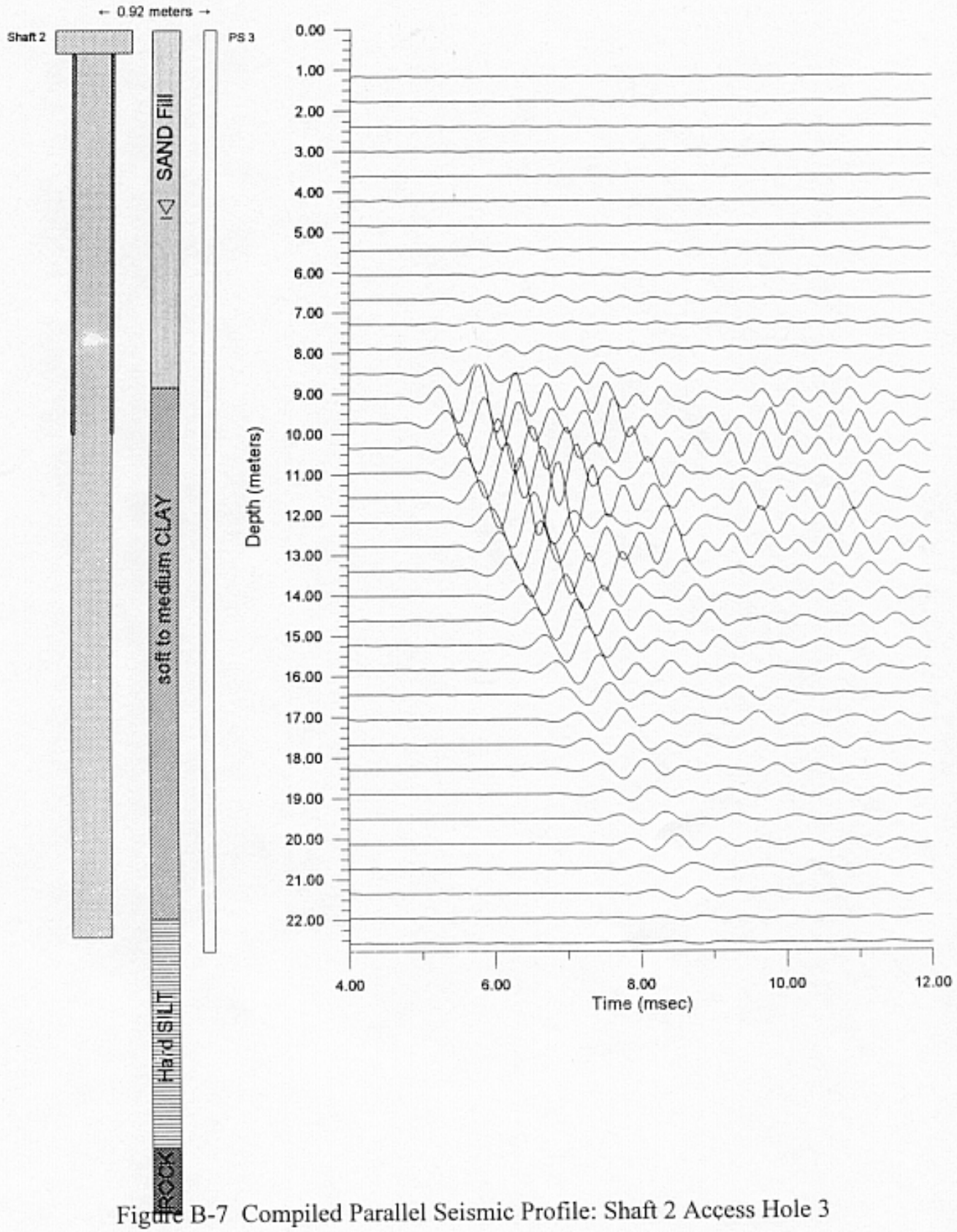

Figure B-7 Compiled Parallel Seismic Profile: Shaft 2 Access Hole 3

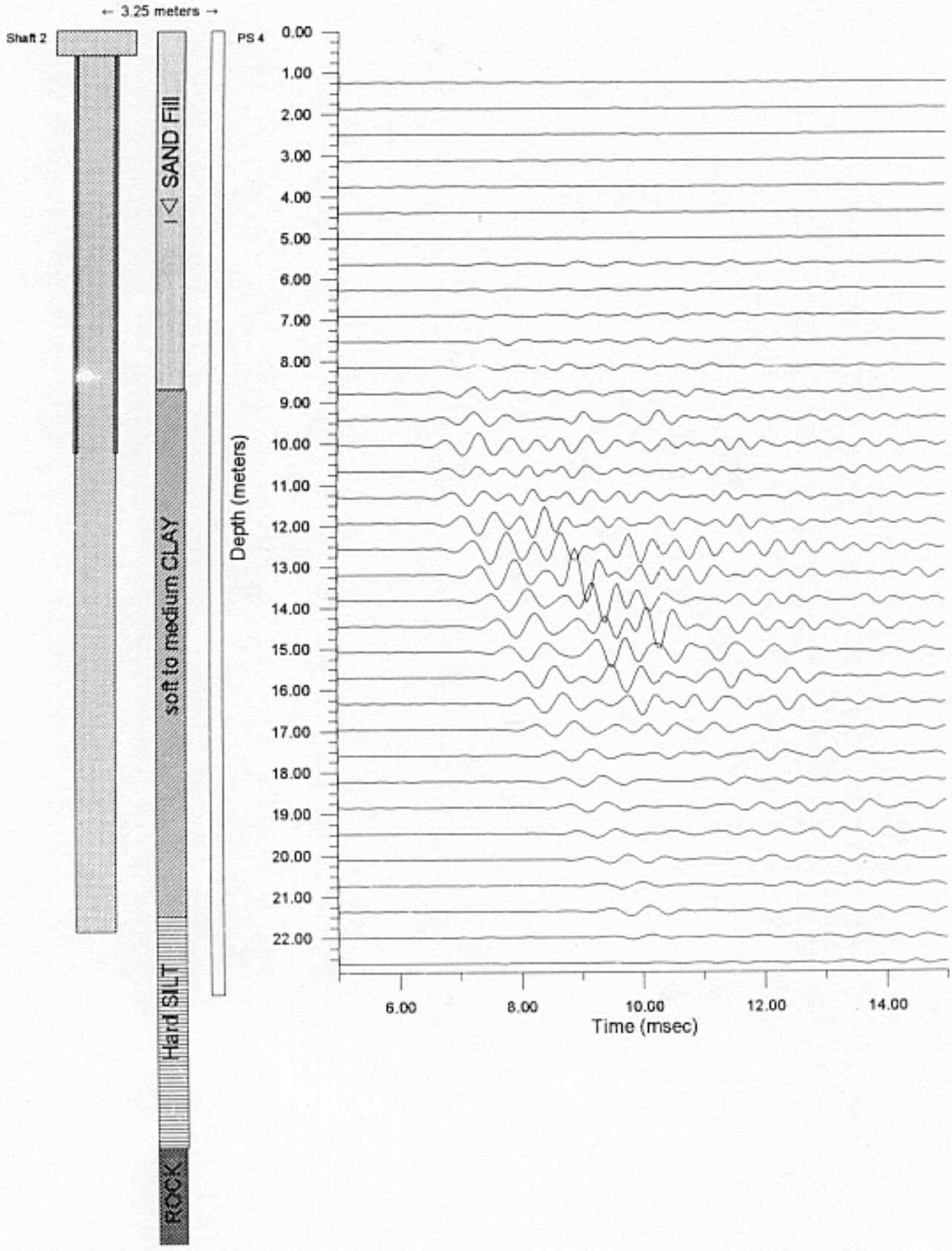

Figure B-8 Compiled Parallel Seismic Profile: Shaft 2 Access Hole 4

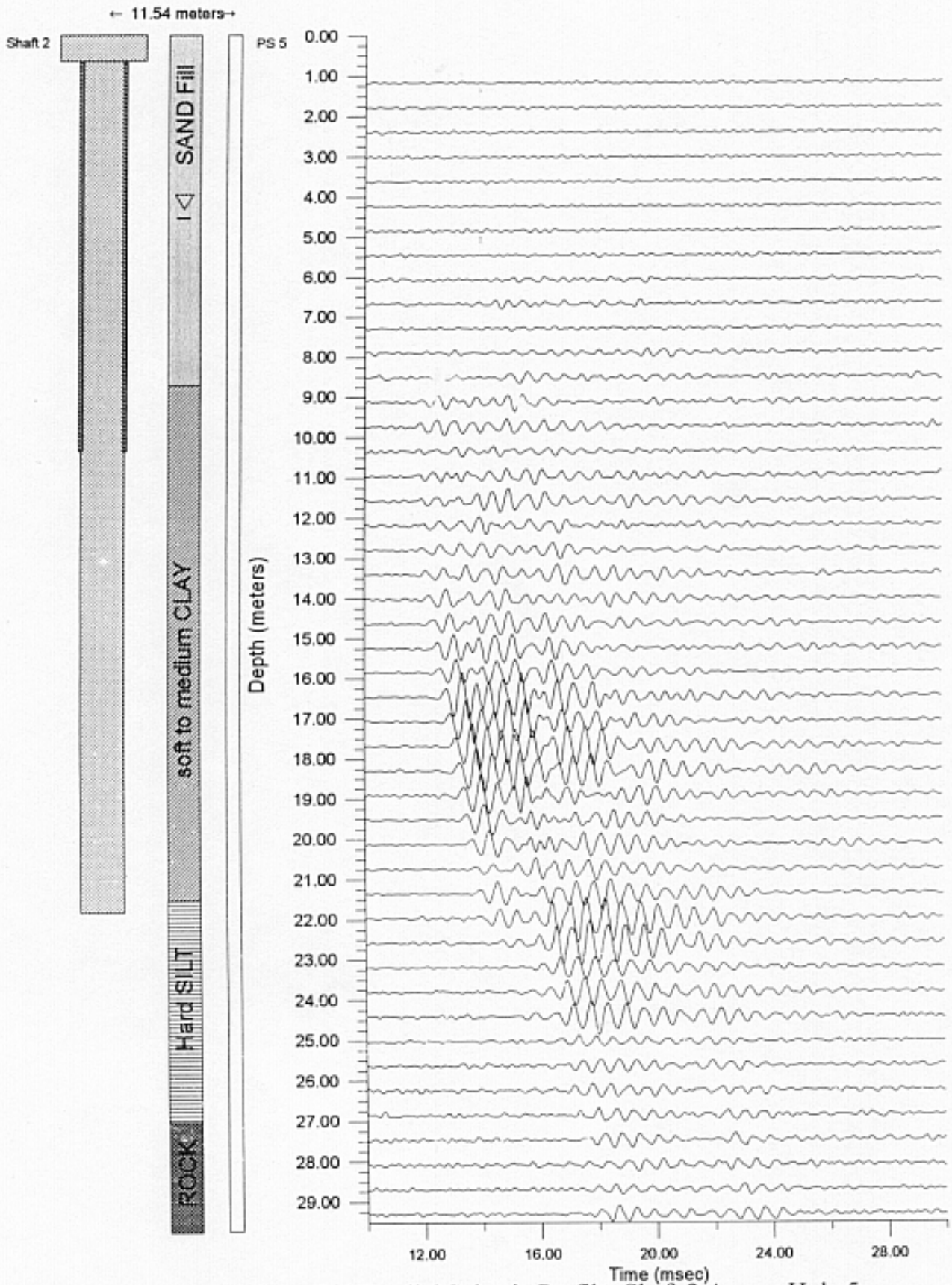

Figure B-9 Compiled Parallel Seismic Profile: Shaft 2 Access Hole 5

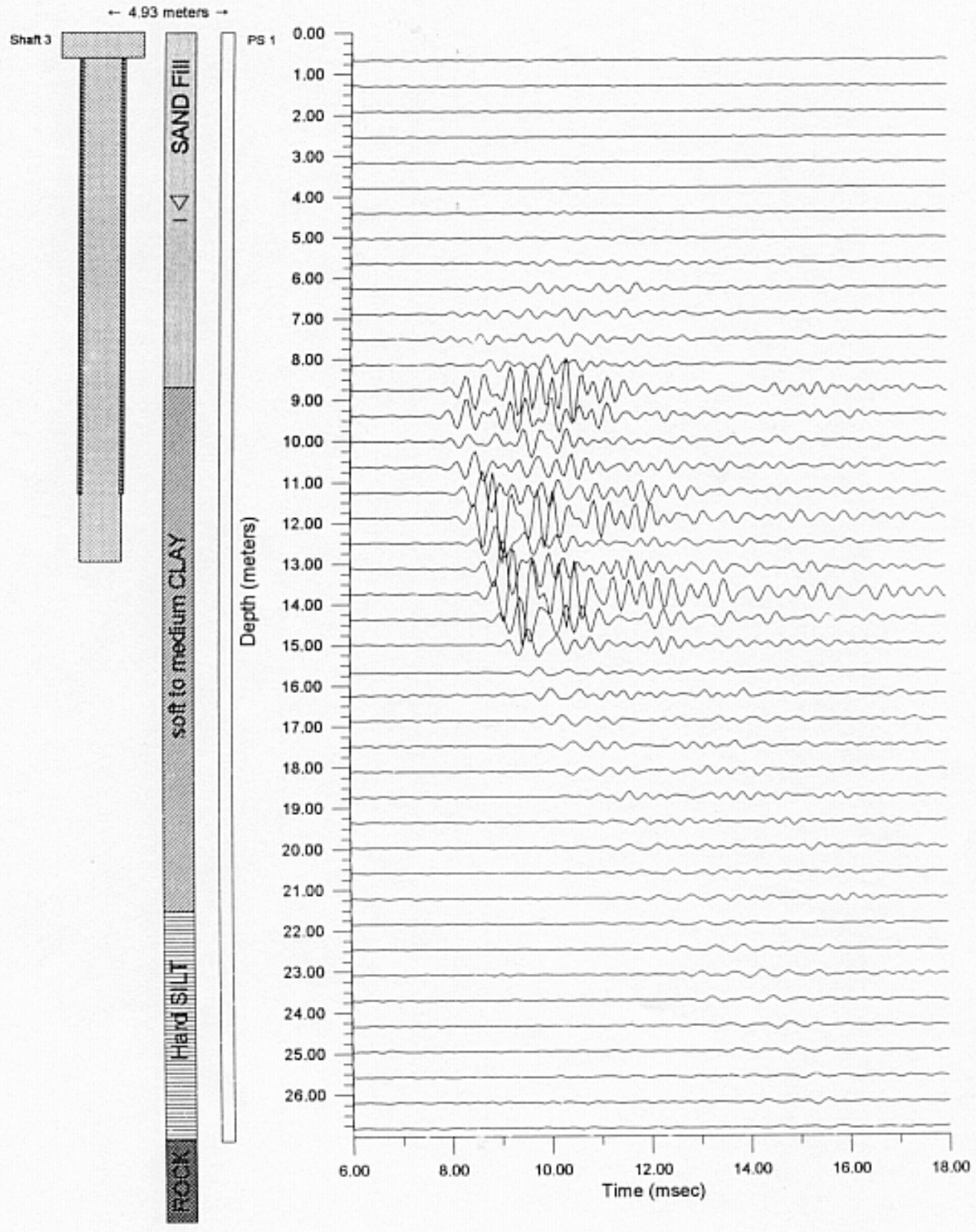

Figure B-10 Compiled Parallel Seismic Profile: Shaft 3 Access Hole 1

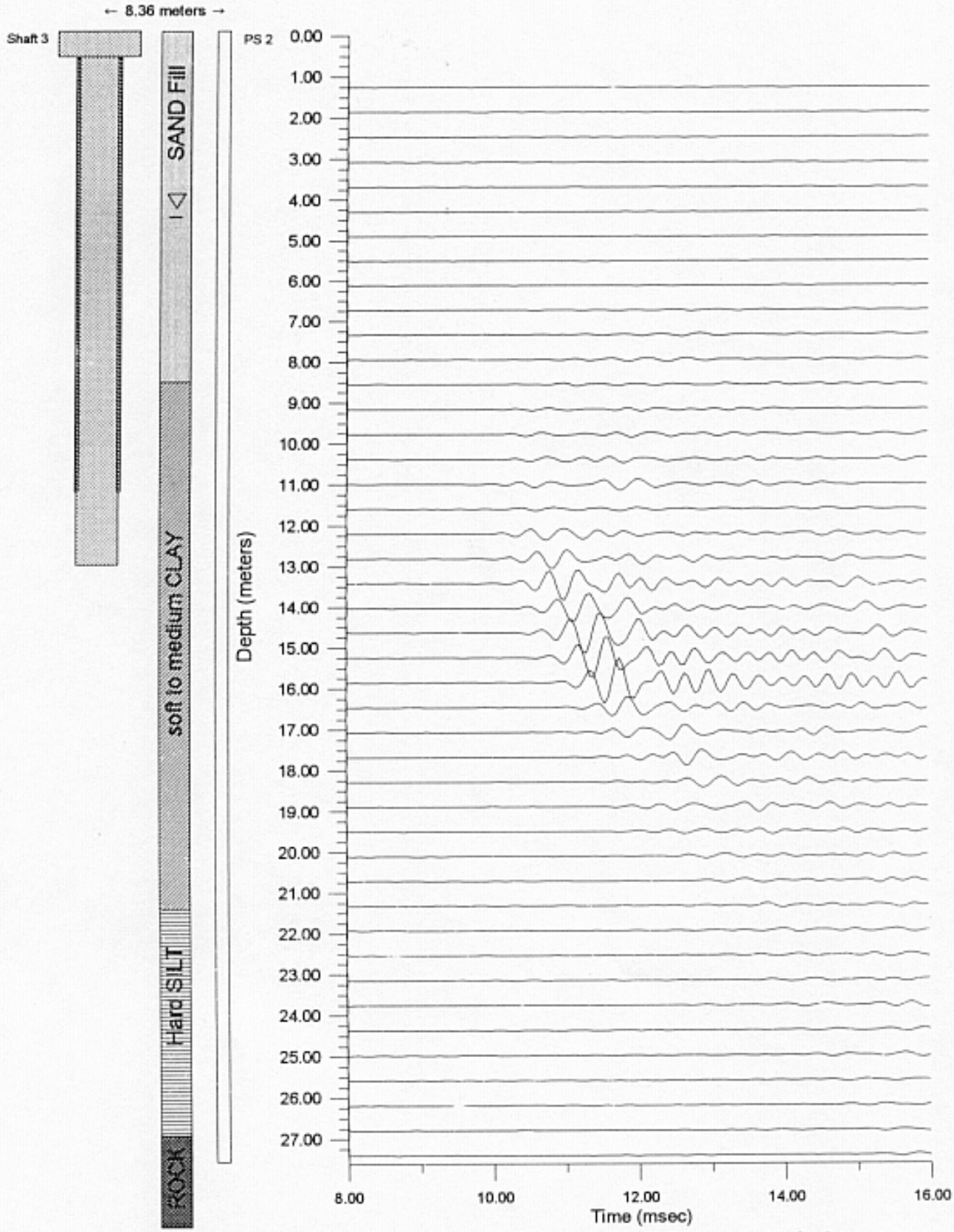

Figure B-11 Compiled Parallel Seismic Profile: Shaft 3 Access Hole 2

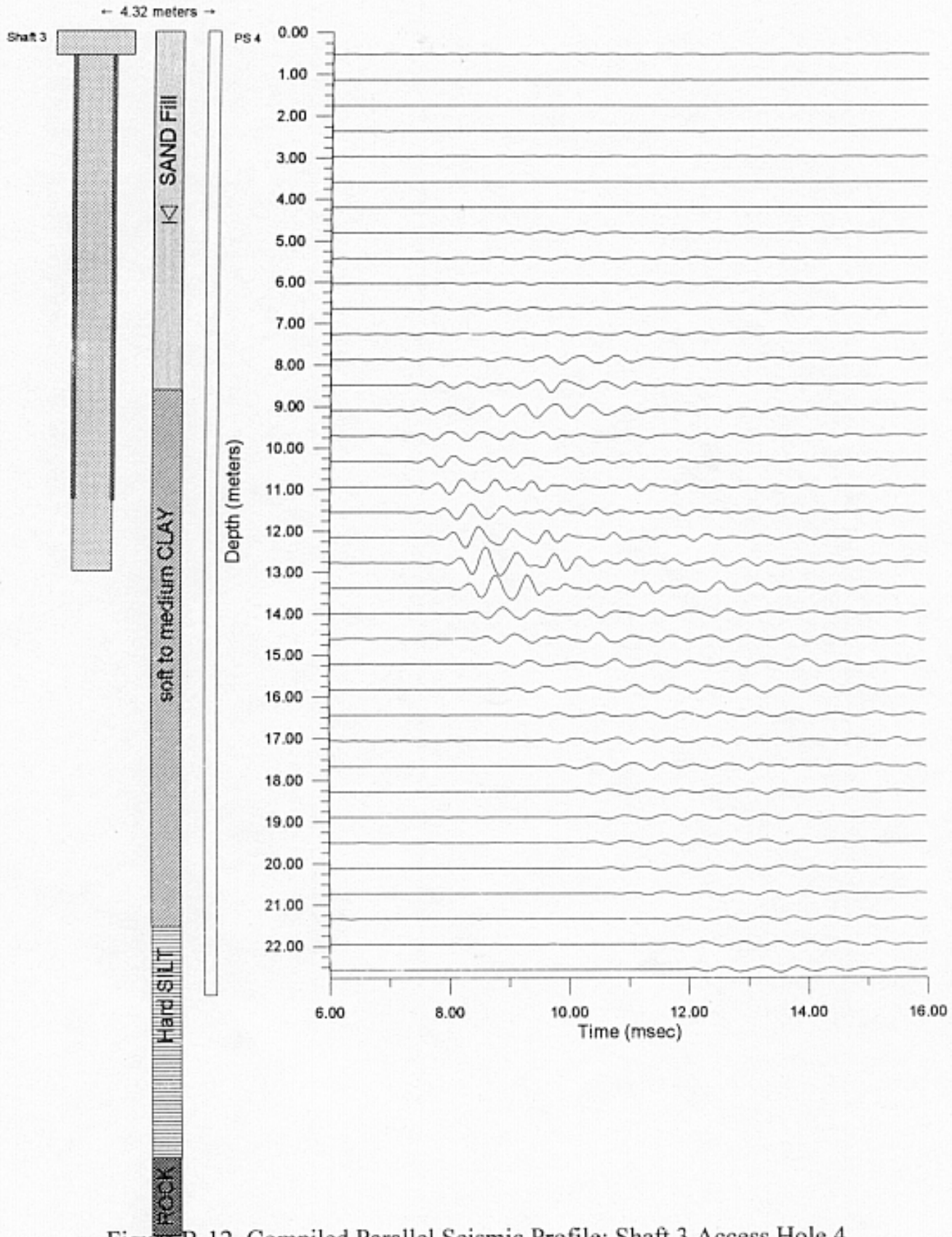

Figure B-12 Compiled Parallel Seismic Profile: Shaft 3 Access Hole 4

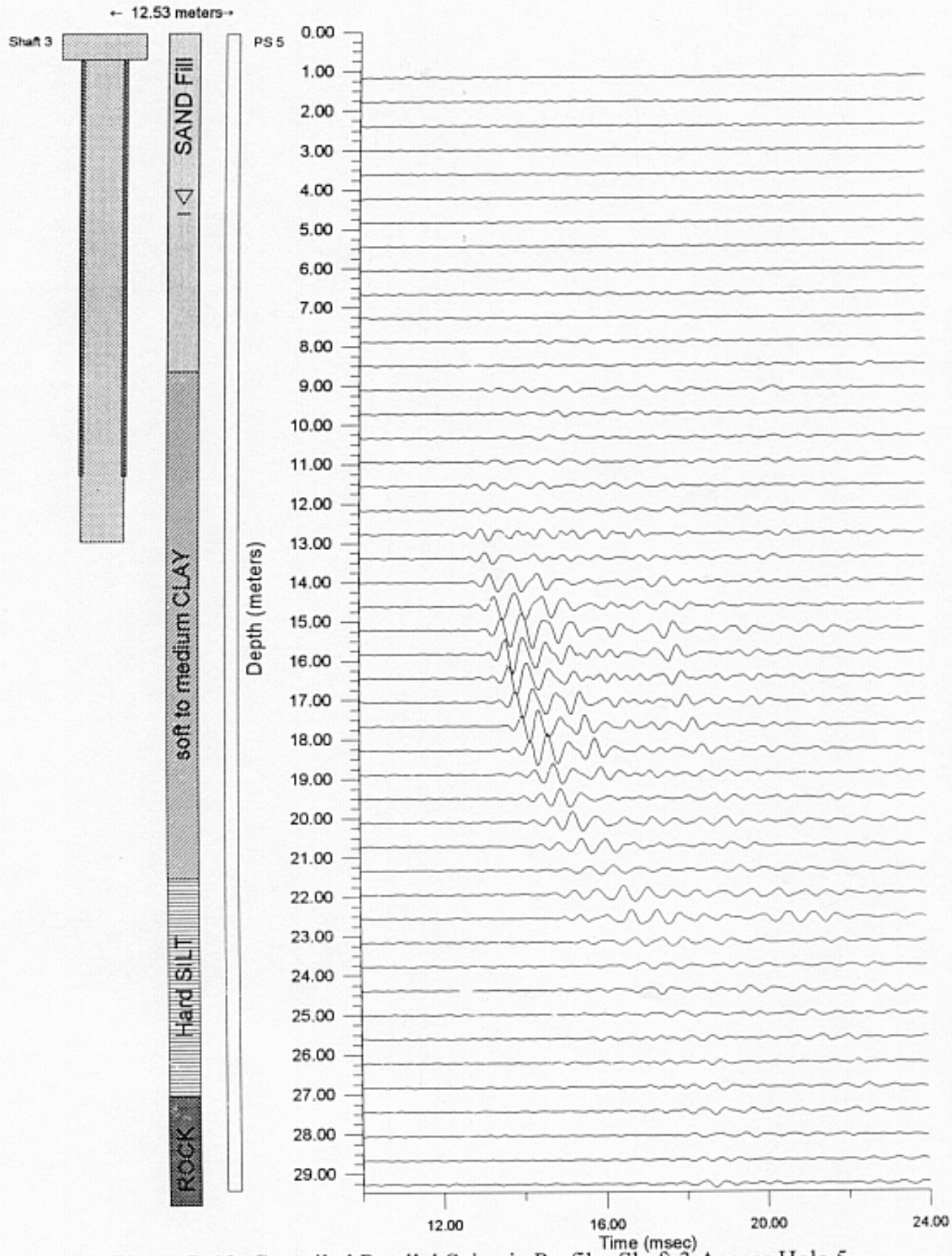

Figure B-13 Compiled Parallel Seismic Profile: Shaft 3 Access Hole 5

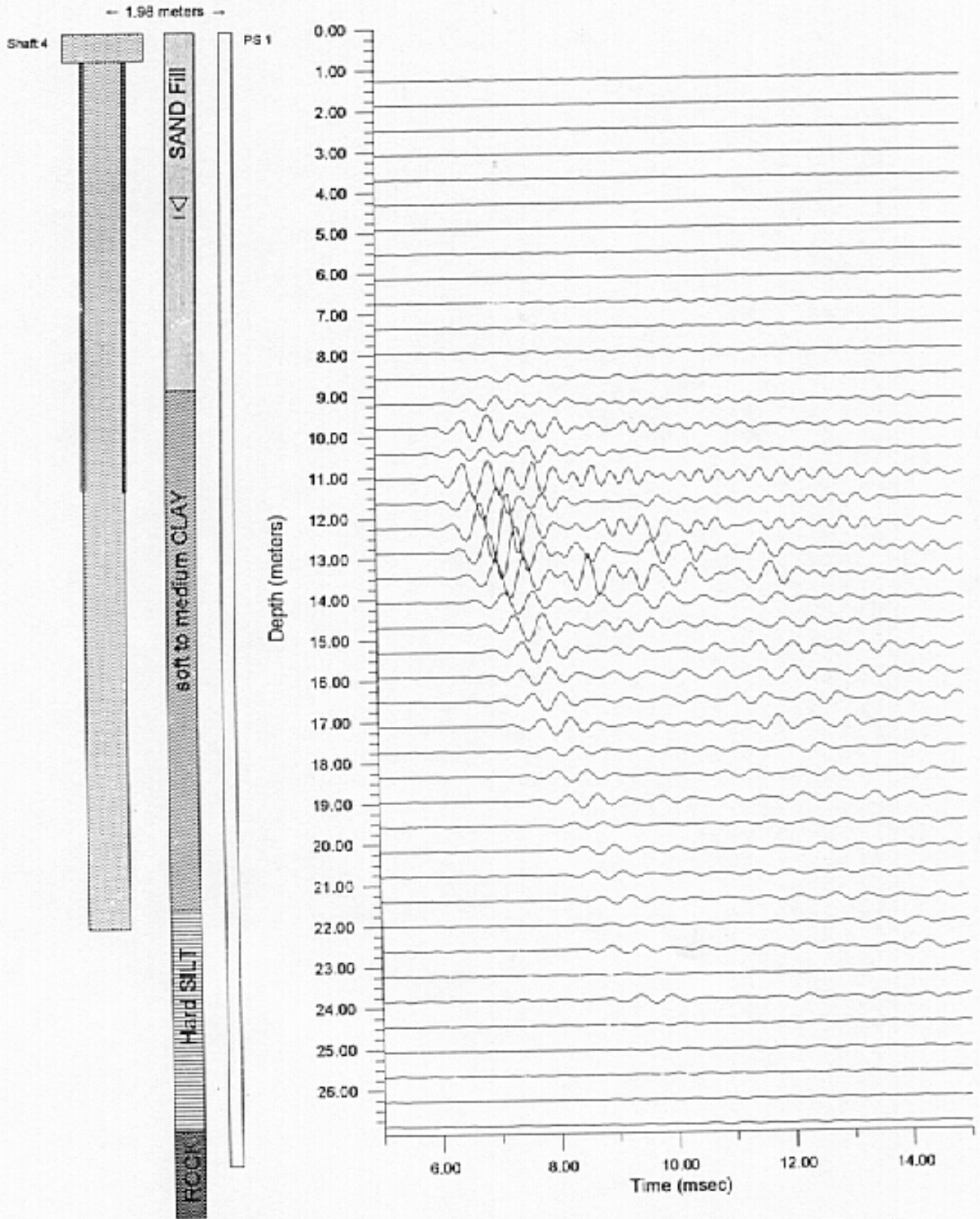

Figure B-14 Compiled Parallel Seismic Profile: Shaft 4 Access Hole 1

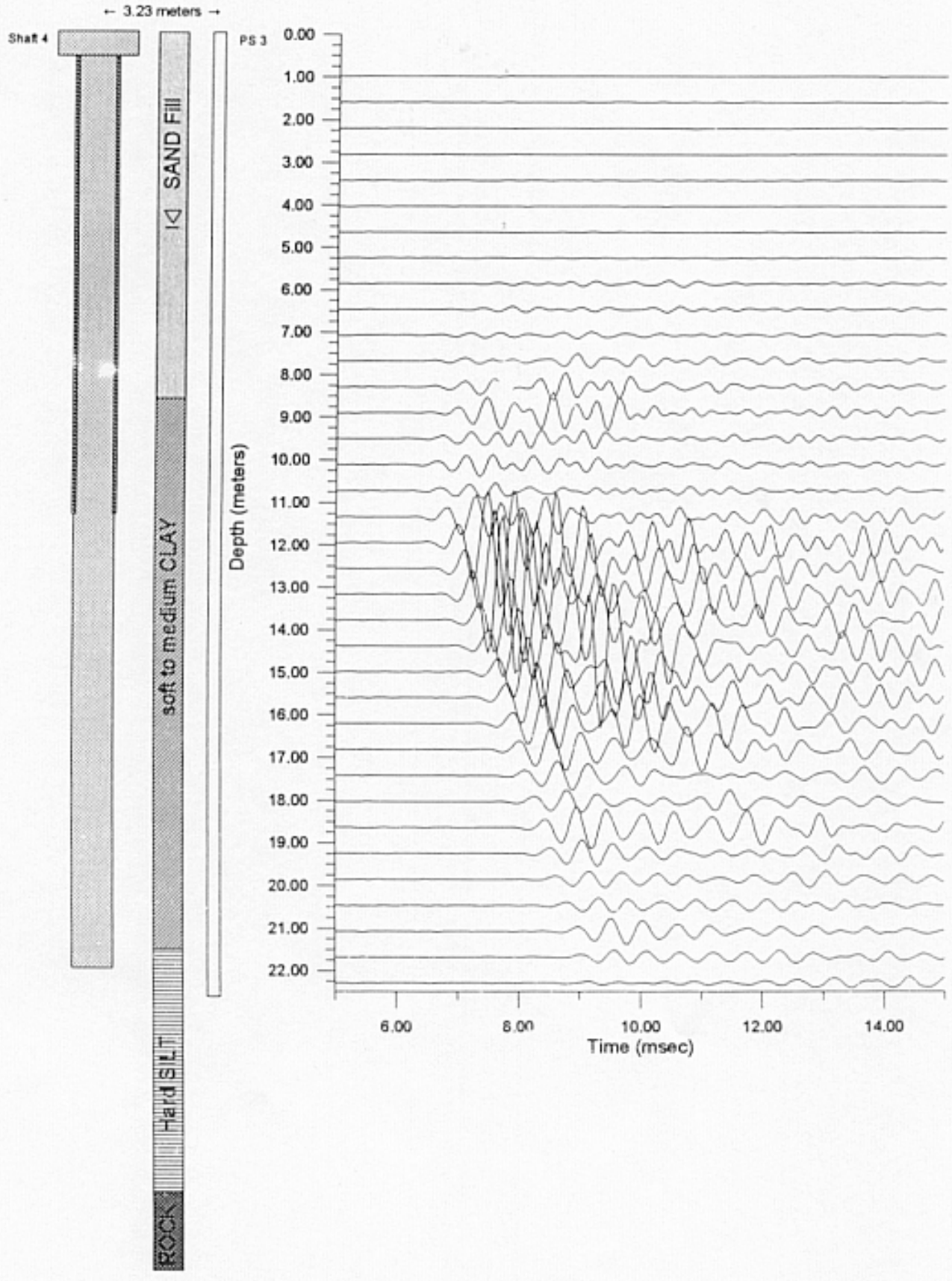

Figure B-15 Compiled Parallel Seismic Profile: Shaft 4 Access Hole 3

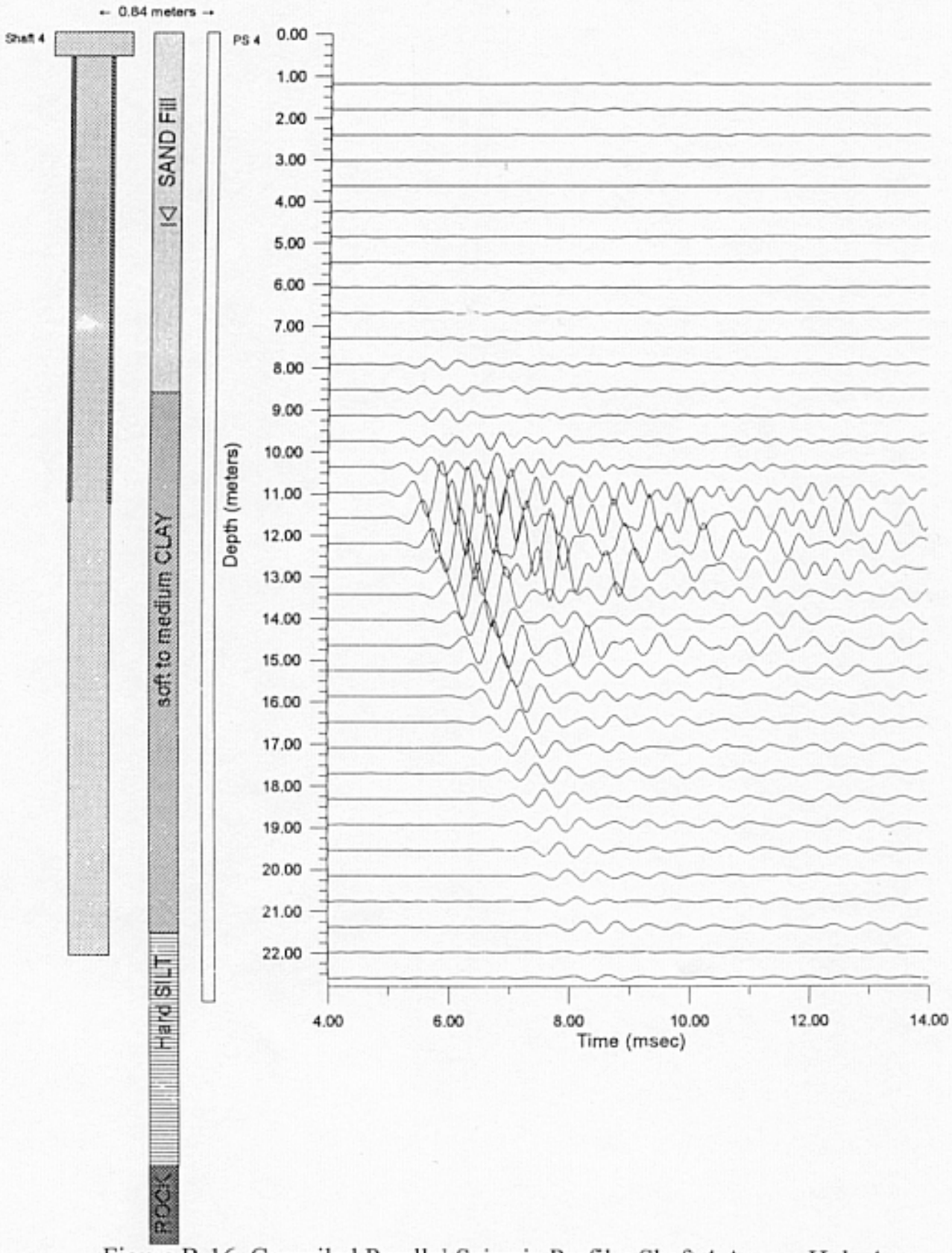

Figure B-16 Compiled Parallel Seismic Profile: Shaft 4 Access Hole 4

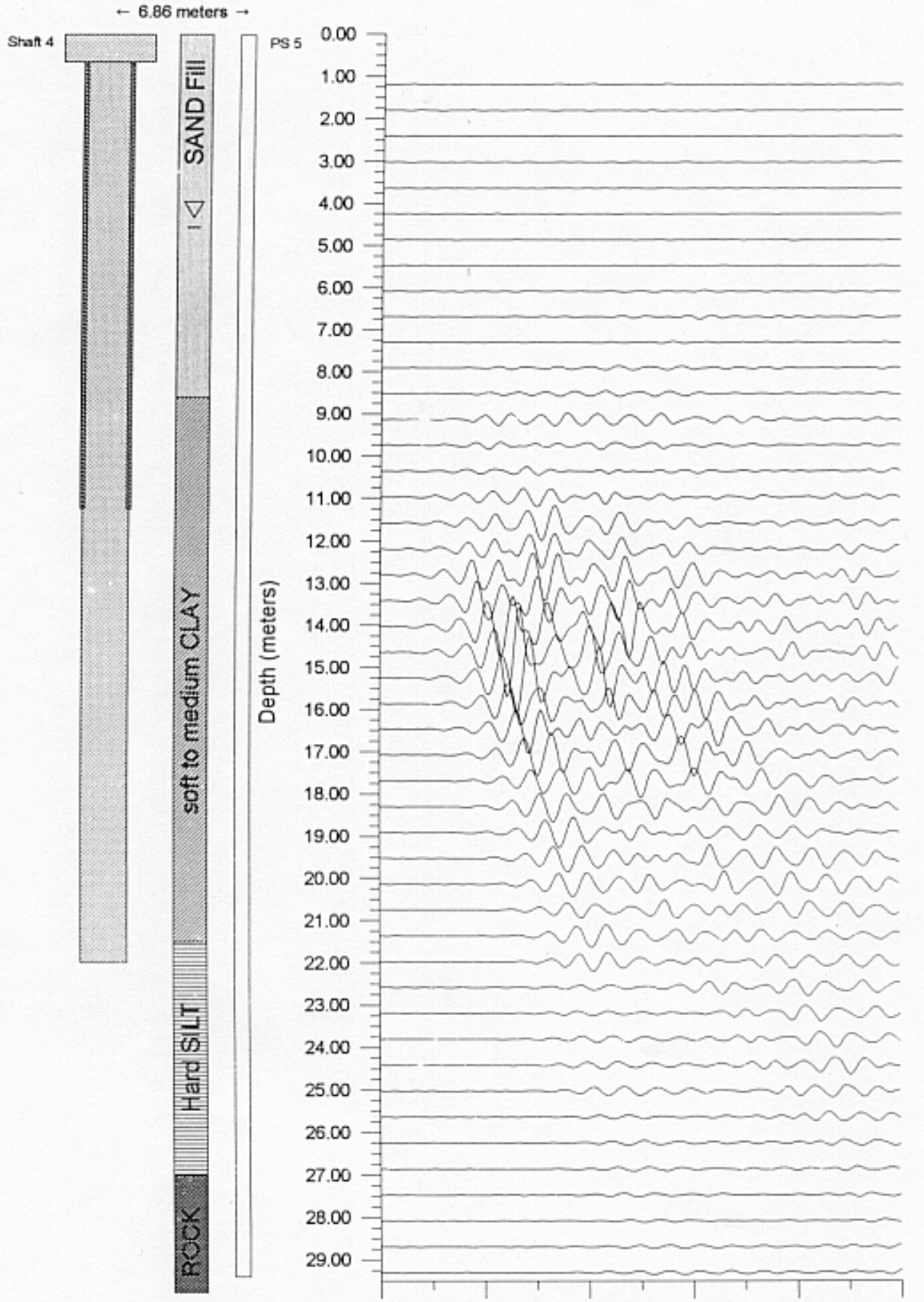

Figure B-17 Compiled Parallel Seismic Profile, Shaft 4 Access Hole 5

Figure B-17 Compiled Parallel Seismic Profile, Start Access Hole B

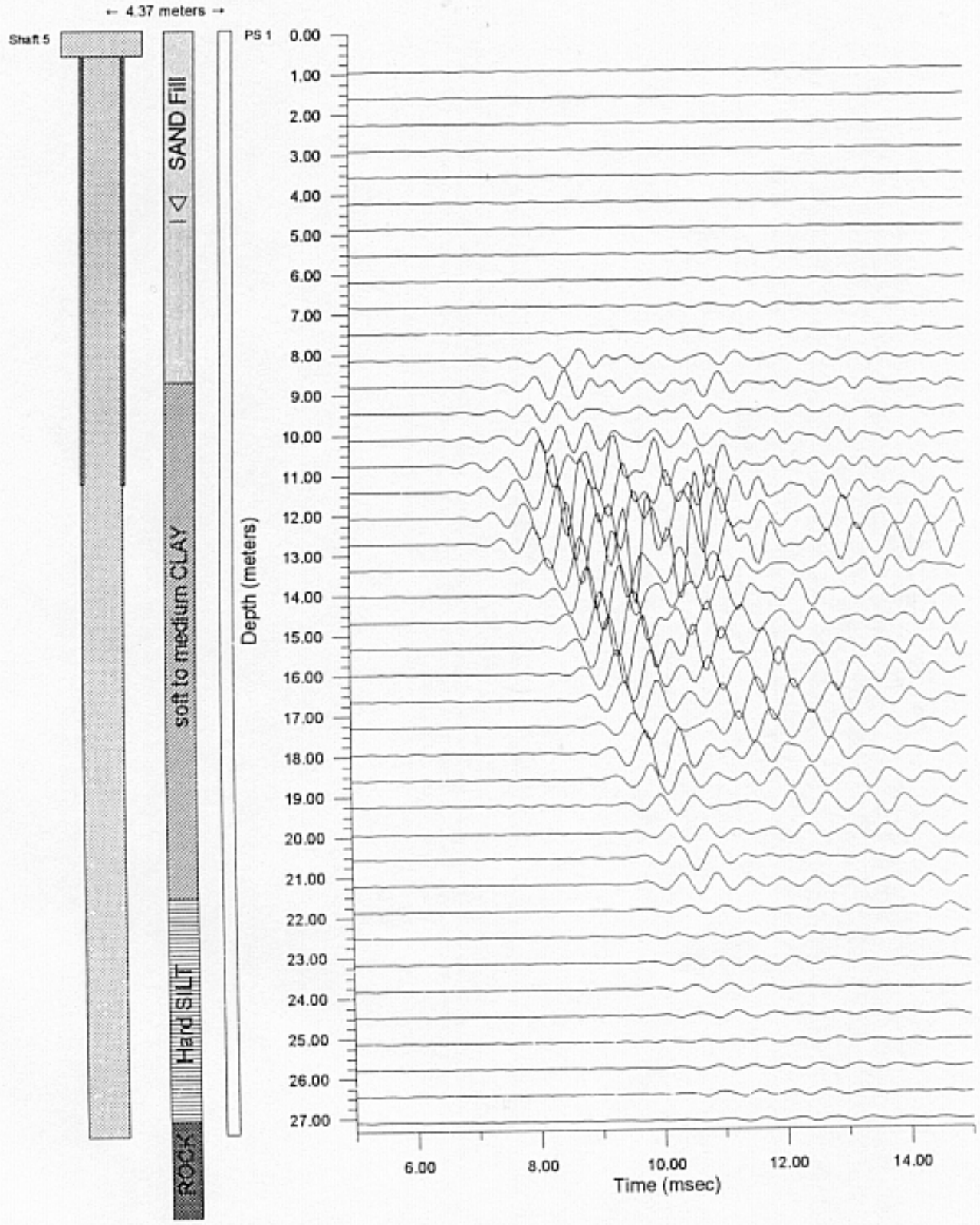

Figure B-18 Compiled Parallel Seismic Profile: Shaft 5 Access Hole 1

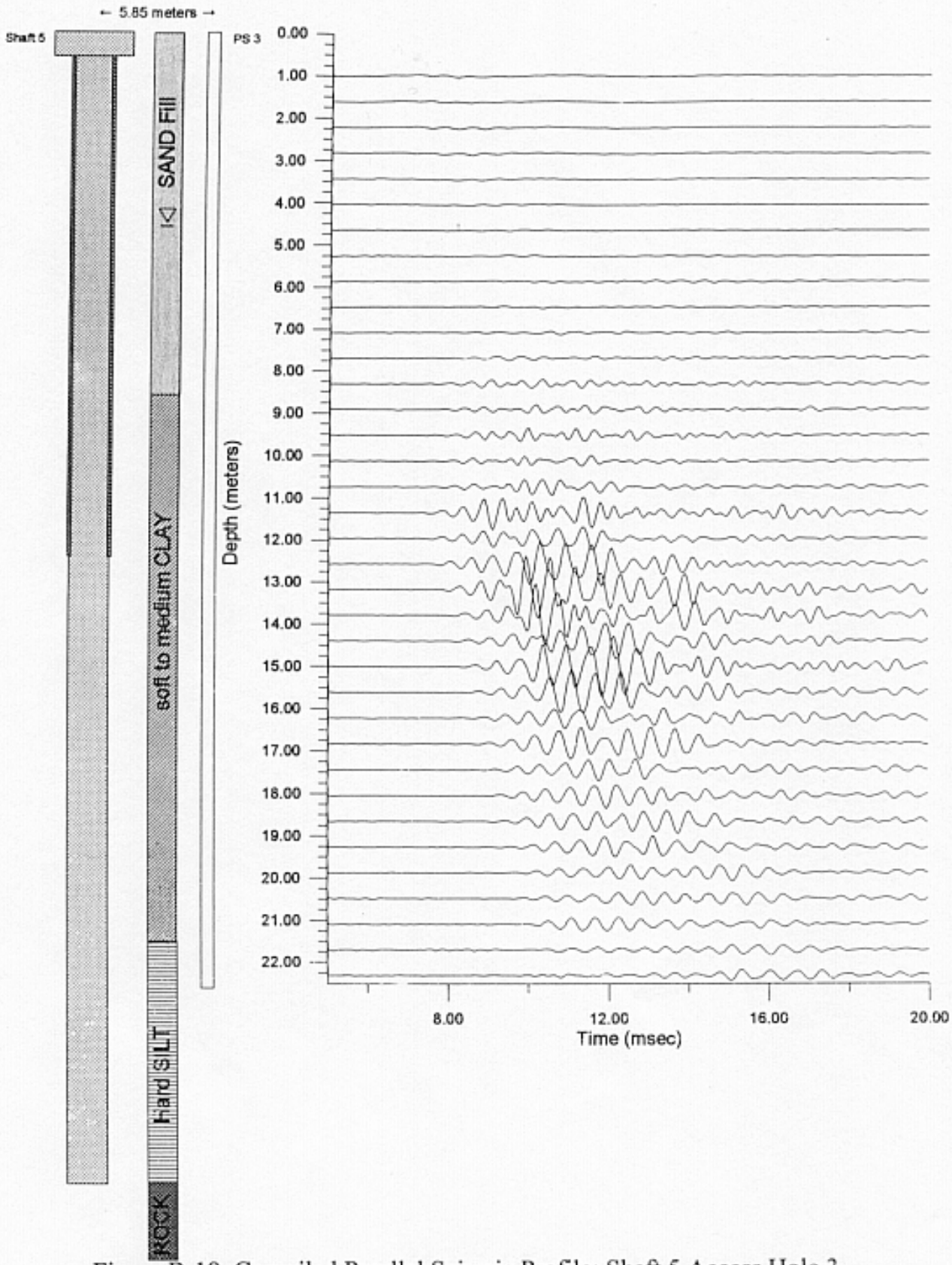

Figure B-19 Compiled Parallel Seismic Profile: Shaft 5 Access Hole 3

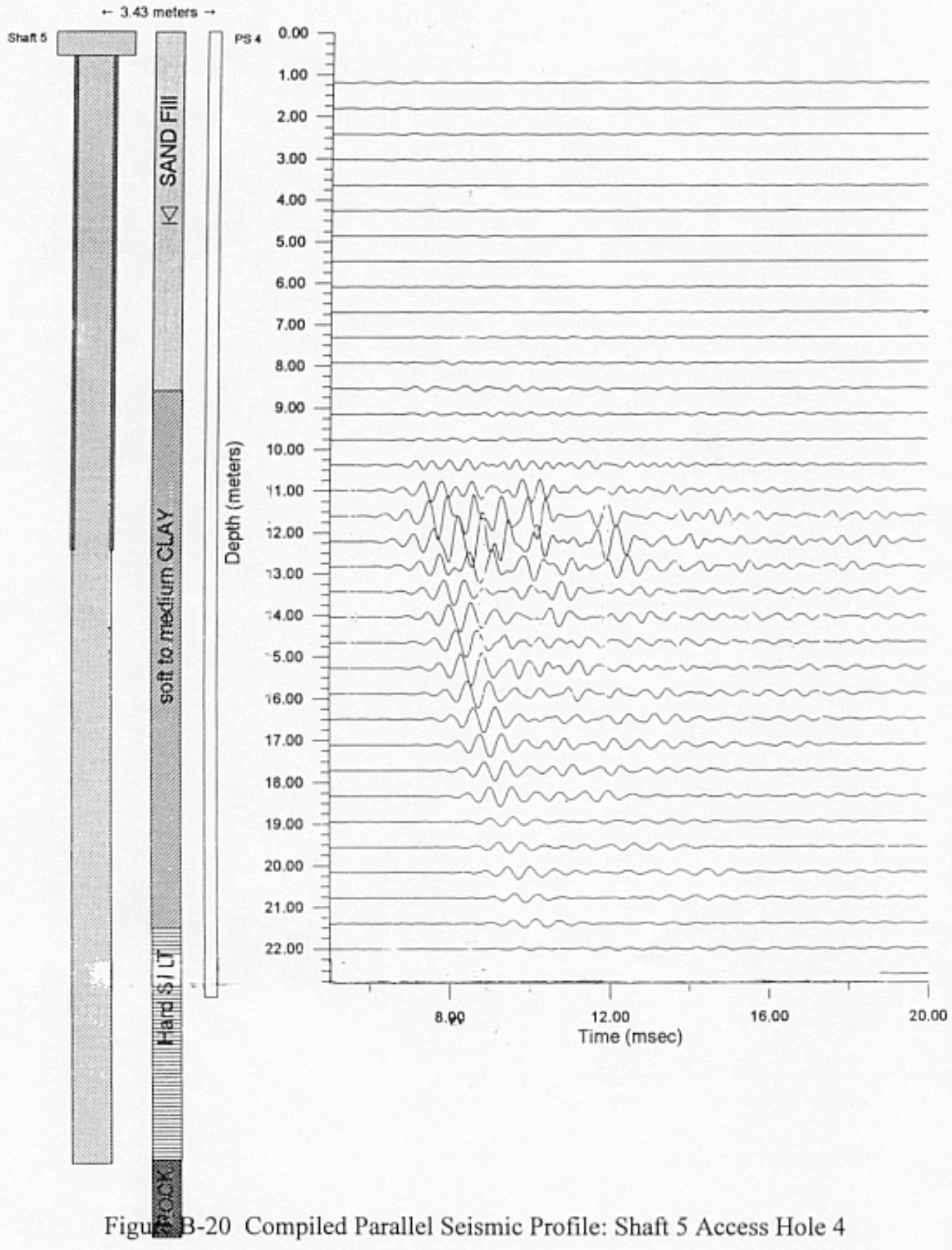

Figure B-20 Compiled Parallel Seismic Profile: Shaft 5 Access Hole 4

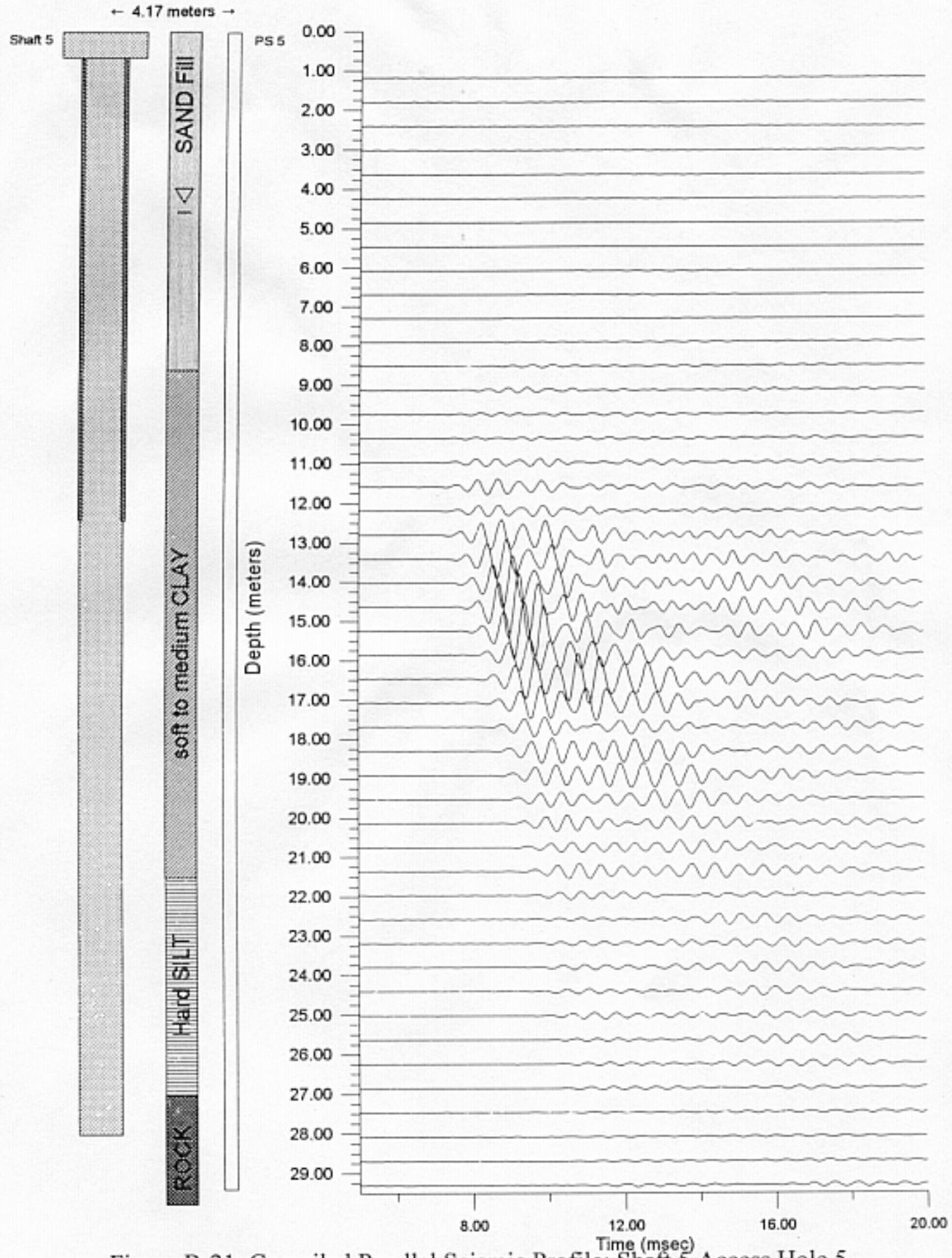

Figure B-21 Compiled Parallel Seismic Profile: Shaft 5 Access Hole 5